Ligand-Directed Heterogeneous Catalysis on Model Surfaces

Construction of Ultra High Vacuum Molecular Beams/ Infrared Apparatus

Investigation of Hydrocarbon Interaction with Pt(111)

vorgelegt von

Master of Science (M.Sc.)

Smadar Attia

von der Fakultät II - Mathematik und Naturwissenschaften

der Technischen Universität Berlin

zur Erlangung des akademischen Grades

Doktor der Naturwissenschaften

- Dr. rer. nat. -

genehmigte Dissertation

Promotionsausschuss:

Vorsitzender: Prof. Dr. Michael Gradzielski

Gutachter: Prof. Dr. Hans-Joachim Freund

Gutachter: Prof. Dr. Reinhard Schomäcker

Tag der wissenschaftlichen Aussprache: 28. Juli 2020

Berlin, 2021

ii

„People without fantasy don't do fantastic things"

-Shimon Peres-

Acknowledgment

I am glad to take the opportunity to express my deep gratitude to everyone who contributed directly or indirectly to the successful completion of this work.

Foremost, I wish to thank my supervisor Prof. Dr. Hajo Freund for letting me work in his department and supporting me in many ways during the last four years. Special thanks are also devoted to Prof. Dr. Swetlana Schauermann for great scientific co-operation and fruitful discussions.

I thank Prof. Dr. Reinhard Schomäcker for being my official second supervisor and receiving my thesis.

I wish to thank Jens Hartmann for his exceptional technical support during the machine construction and further on when it has been moved to Kiel. Without his qualified support and technical skills, it would not have been possible to complete the installation of a new, high quality, experimental set-up as that achieved.

I am also grateful to Prof. Schauermann's workgroup members for their help and support, interesting discussions, and for providing a pleasant working atmosphere. In particular, I would like to mention my colleagues Marvin Christopher Schmidt, Evan Spadafora and Carsten Schröder for their experimental contribution.

Many thanks to Klaus-Peter Vogelgesang for helping whenever he could. I wish to thank the technical staff at the Fritz-Haber Institute, particularly the electronic (ELAB) and mechanical workshops. I would like to express my sincere respect for their excellent craftsmanship: Georg Heyne, Patrick Schlect, Christian Teβmar, Christian Viezke and Wielko Ganz. I would also like to thank the mechanical workshop of CAU for the help and support in Kiel, and in particular to Timo Görgens for providing a technical support, and also a nice company during the long period spent in reassembling the machine in Kiel.

I also wish to thank Manuela Misch from the FHI for administrating all aspects of bureaucracy, for her kindness, and for checking on me when things turned complicated.

Abstract

In the common perception of catalysis, a catalyst should typically possess multiple functionalities in order to promote several individual reactions within a multi-step process. A promising way to approach this concept relies on functionalization of a catalytic surface with organic ligands, e.g. organic adsorbate or covalently bonded functional groups, to allow for a selective and controlled promotion of the desired reaction path via lateral reactant-ligand interactions. In such functionalized systems, the role of ligands can be multifold: it can either impose a geometrical constraint on the surface, hence affecting the interaction of the adsorbates with the underlying metal substrate, and/or undergo more specific intermolecular interaction, as in building a 1:1 complex with the reactant that affects its electronic structure or adsorption geometry. Despite ongoing vigorous progress in this field, the development of powdered heterogeneous catalysts of practical relevance, frequently relies on trial and error. For establishing a more rational approach towards synthesis of new advanced functionalized catalytic materials, the atomistic-level understanding of the mechanisms governing ligand-directed heterogeneous catalysis has to be significantly improved.

Towards this goal, a new experimental setup was designed and built which allows us to prepare and characterize ligand-modified model catalysts under well-controlled UHV conditions and investigate reactive surface processes across a broad pressure regime, from UHV and up to the near ambient. Integrative measuring techniques, capable of probing the mechanisms, kinetics and dynamics of such processes, namely molecular beams and infrared reflection absorption spectroscopy, were installed and applied in this work. Two case studies were performed by the newly built setup, aiming at exploring the lateral interactions between adsorbates on Pt(111) surface. Complementary, scanning tunneling microscopy was employed to obtain real space information on the distribution of the adsorbates. First, we show that a lateral interaction, mediated by hydrogen bonding between two adjacent acetophenone molecules, triggers the formation and stabilization of the normally unstable enol tautomer of acetophenone. This interaction is a crucial first step in the hydrogenation of the molecule. More importantly, we also provide a strong experimental evidence that confirms theoretical predictions that transformation of simple carbonyl compounds to their enol part enables low-barrier hydrogenation pathway of normally very stable C=O compounds. The second case reported in this dissertation involves a chiral modification of

the surface with *(R)-(+)-1-(1-naphthylethylamine)* (R-NEA) and its interaction with CO that was utilized as a simple proxy for carbonyl compounds. The combination of spectroscopic and microscopic observations shows that the R-NEA molecules are self-assembled into directed short chains, clearly suggesting an intermolecular interaction between individual molecules. The individual molecules in the chains are also strongly inclined with respect to the surface plane as established spectroscopically. The adsorption geometry of R-NEA was found to be greatly affected by co-adsorption of CO, and the observed spectral changes induced in this process are indicative of a strong intermolecular interaction between CO and adsorbed R-NEA molecules, most likely the amino-group.

Kurzzusammenfassung

Ein Katalysator sollte typischerweise mehrere Funktionalitäten besitzen, um mehrere Einzelreaktionen innerhalb eines mehrstufigen Prozesses spezifisch zu beschleunigen. Ein vielversprechender Ansatz beruht auf der Funktionalisierung einer katalytischen Oberfläche mit organischen Liganden. In solchen funktionalisierten Systemen kann die Rolle der Liganden vielfältig sein: Diese können entweder der Oberfläche eine geometrische Beschränkung auferlegen, wodurch die Wechselwirkung der Adsorbate mit dem darunter liegenden Metallsubstrat beeinflusst wird, und/oder diese können spezifische intermolekulare Wechselwirkungen eingehen, wie beim Aufbau eines 1:1-Komplexes mit dem Reaktanten, der die elektronische Struktur oder die Adsorptionsgeometrie beeinflusst. Trotz anhaltender Fortschritte auf diesem Gebiet beruht die Entwicklung pulverförmiger heterogener Katalysatoren von praktischer Relevanz häufig auf dem Prinzip des „Trial and Error". Um einen rationaleren Ansatz für die Synthese neuer funktionalisierter Katalysatoren zu finden, muss das atomistische Verständnis der Mechanismen für die ligandendirigierte heterogene Katalyse verbessert werden. Zu diesem Zweck wurde ein neuer Versuchsaufbau verwirklicht, der es uns ermöglicht, ligandenmodifizierte Modellkatalysatoren unter kontrollierten UHV-Bedingungen herzustellen und zu charakterisieren und deren reaktive Oberflächenprozesse über einen breiten Druckbereich (10^{-10} – 1000 mbar) zu untersuchen. In dieser Arbeit wurden zur Aufklärung der Mechanismen, Kinetik und Dynamik Molekularstrahlexperimente und Infrarot-Reflexionsabsorptionsspektroskopie durchgeführt. Es wurden zwei Fallstudien durchgeführt, um die lateralen Wechselwirkungen zwischen Adsorbaten auf der Pt(111)-Oberfläche zu untersuchen. Komplementär zu den oben genannten Messtechniken wurde die Rastertunnelmikropskopie eingesetzt, um Informationen über die tatsächliche Verteilung der Adsorbate auf der Substratoberfläche zu erhalten. Es konnte gezeigt werden, dass die laterale Wechselwirkung, welche auf Wasserstoffbrückenbindungen zweier benachbarter Acetophenon-Moleküle beruht, die Bildung und Stabiliserung des normalerweise instabilen Enoltautomers von Acetophenon auslöst. Diese beobachtete Wechselwirkung ist dabei ein entscheidender erster Schritt bei der Hydrierung des Moleküls. Darüber hinaus konnten aussagekräftige experimentelle Beweise geliefert werden, welche die theoretischen Vorhersagen bestätigen, dass die Umwandlung einfacher Carbonylverbindungen in das korrespondierende Enoltautomer einen energetisch günstigeren

Reaktionspfad für die Hydrierung der normalerweise sehr stabilen C=O-Gruppe darstellt. Die Zweite in dieser Dissertation beschriebene Studie betrifft eine chirale Modifikation der Oberfläche mit (R)-(+)-1-(1-Naphthylethylamin) (R-NEA) und dessen Wechselwirkung mit CO, das als einfachster Vertreter von Carbonyl-Verbindungen verwendet wurde. Die Kombination von spektroskopischen und mikroskopischen Beobachtungen zeigen, dass sich die R-NEA-Moleküle in gerichteten kurzen Ketten selbstanordnen, was eindeutig auf eine intermolekulare Wechselwirkung zwischen einzelnen Molekülen hindeutet. Spektropskopisch kann gezeigt werden, dass die einzelnen Moleküle in diesen Ketten in Bezug auf die Oberfläche stark geneigt sind. Es wurde festgestellt, dass die Adsorptionsgeometrie von R-NEA durch die Ko-Adsorption von CO stark beeinflusst wird und die beobachteten spektralen Änderungen weisen auf eine starke intermolekulare Wechselwirkung zwischen CO und adsorbierten R-NEA-Molekülen hin, höchstwahrscheinlich der Aminogruppe.

Abbreviations

R-NEA R-(1-naphthyl)ethylamine
MB Molecular Beam
EMB Effusive Molecular Beam
GCA Glass Capillary Array
SMB Supersonic Molecular Beam
ER Eley-Rideal
LH Langmuir-Hinshelwood
HREELS High-resolution Electron Energy Loss Spectroscopy
FT Fourier Transform
IR Infrared
IRAS Infrared Reflection-Absorption Spectroscopy
MCT Mercury-Cadmium-Telluride
MSSR Metal Surface Selection Rule
TR Time-resolved
LEED Low Energy Electron Diffraction
QCM Quartz Crystal Microbalance
APC Ambient Pressure Cell
GC Gas Chromatography
TCD Thermal Conductivity Detector
FID Flame Ionization Detector
MCA Multi-Channel Arrays
CEM Channeltron Electron Multiplier
EI Electron Impact
QMS Quadrupole Mass Spectrometry
STM Scanning Tunneling Microscopy
TDS Thermal Desorption Spectroscopy
TPD Temperature Programmed Desorption
TPRS Temperature Programmed Reaction Spectroscopy
UHV Ultra-High Vacuum
DFT Density Functional Theory
UPS Ultraviolet-Photoelectron Spectroscopy
NEXAFS Near Edge X-Ray Absorption Fine Structure
VdW Van-der-Waals
PES Potential Energy Surface
HB Hydrogen Bonding/ Hydrogen Bond

Table of Contents

Chapter 1

Introduction

Heterogeneous catalysis constitutes the basis of various commonly leading chemical technologies. Those include chemical manufacturing, the generation, conversion and storage of energy, as well as environmental technologies.[1, 2] Despite the traditional paradigm and the common literature view of catalysis, both focusing on relatively simple reactions of feedstocks to products and on the improvement of their conversion rates, the demand for new industrial processes has shifted the scientific interest towards improving the selectivity of the catalyst. Special emphasis is given in that regard to the preferential promotion of desirable reactions from complex manifolds of available pathways via more sophisticated, state of the art, synthetic processes.[3, 4] Many of these processes involve, for instance, selective synthesis of enantiopure chiral compounds for pharmaceutical and agricultural applications, as well as for food industry uses.[5, 6] Clearly, the concept of selectivity is being realized not only by excluding expensive separation steps and reducing the consumption of the reactants, but it also makes the industrial procedure more environmentally friendly. The growing emphasis on selectivity, however, adds significantly more strict requirements on the catalyst.[7]

Generally, two classes of properties which affect the overall activity of any catalytic surface may be accounted for: *(i)* the intrinsic activity of the metal in catalyzing the desired reaction pathway, and *(ii)* the ability of the surface to efficiently bind the reactants, stabilize the desired reaction intermediates and effectively release the products. While the latter is determined by the bond strength of the adsorbed surface species and by the relative thermodynamic stabilities of the reaction intermediates, for the former, it is in many cases not possible to promote a particular reaction by using one particular solid. Hence, the catalyst often requires the combination of multiple functionalities to promote several individual reactions through a multi-step process.[8] A multiple functionality may be assembled by tuning the electronic properties of a given phase, by using bimetallic or alloys[9, 10], or by adding to a given catalyst several active phases or promoters[11, 12], inhibitors or modifiers. Interestingly, the modest differences between the potential energy barriers of individual reactions comprising a multi-step process, practically govern their selectivity. Also, for reversible surface reactions, the overall reaction rate towards a desired

product, is determined, in addition to the difference in activation barriers, also by the relative rates of backward reactions, with the later depending on the relative stabilities of products on the surface.

It is therefore not surprising that most of the heterogenous catalysts employed nowadays are multi component. Moreover, the principal advantage that provides the ability to tune chemical and adsorption properties of a catalytic surface in order to optimize the activity and selectivity of specific reactions, lays in the compositional and structural complexity of these catalysts. At the same time however, the huge structural and chemical complexity realized in real catalysts, strongly restricts the ability to gain a detailed atomistic understanding of structure-reactivity relationships, and hence hinders rational and coherent control of new catalytic materials. In that sense, surface-sensitive methods hold the potential of providing detailed information on the surface structure and correlate it to catalytic activity. Nonetheless, surface science methodology cannot be applied in most cases to such complex materials as commercial heterogeneous catalysts. This, in turn, leaves the fundamentals of heterogeneous catalysis largely unexplored. The enormous complexity of industrial catalysts is, in fact, the primary impediment restricting the acquisition of such valuable information, thus precluding detailed structural studies by standard surface science techniques.[13] The greatest discoveries in this field, demonstrated on powdered materials, have often been based on great deal of fortuity and optimization by trial and error. This is not to say that there have not been fundamental studies directed at the basic understanding of the chemistry of catalysis. And yet, the introduction of new catalytic processes, altogether anticipates their mechanism on a molecular level.

As a novel strategy to overcome this problem, a model catalyst approach has been developed over the last two decades by several groups.[14-20] The concept is illustrated in Figure 1.1. Model studies propose a systematic structural variation of the model catalytically active surfaces, by employing both single crystalline metals and metallic nanoparticles (NPs) supported on well-defined planar oxide supports as heterogeneous catalysts.[14] Increasing the complexity of the models towards supported NPs, resembling a real disperse metal catalyst, allows one to uncover in the model some of the most important key aspects of selectivity and activity that cannot be captured by single crystals alone. These aspects were demonstrated in hydrogenation[21, 22] and oxidation[23, 24] reactions, synthesis of ammonia[25] and water-gas shift (WGS) reactions.[26] The most

important advantage of exploring the model catalyst approach, lays in the possibility to reproduce most crucial structural and electronic properties inherent to realistic catalysts in a very controlled way. It has been recognized early on in catalysis research, that the reduced dimensionality of metal particles and the presence of a support may have crucial influence on their electronic, structural and catalytic properties.[15, 27] The role of these particular features, which are considered to be responsible for the high reactivity of small supported metal clusters, can be investigated in great detail on well-defined supported model surfaces.
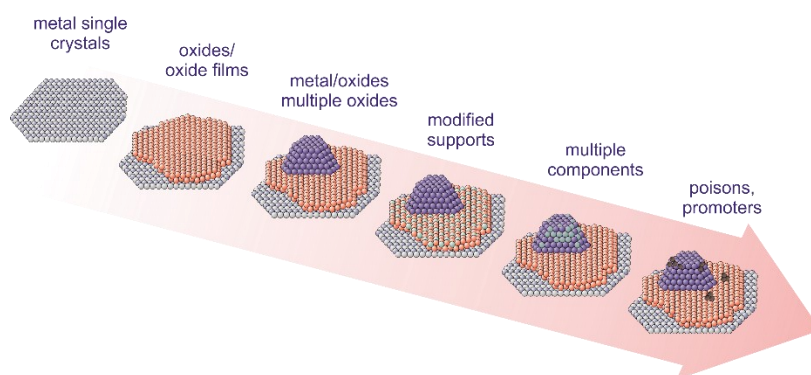
Figure 1.1: Schematic representation of the model catalyst approach, proposing systematic structural variation of the surface from single crystals to nanostructured systems of increasing complexity.

A desirable major task is to combine the model catalyst approach with detailed investigations on the kinetics and thermodynamics of reaction and adsorption processes. A unique way of performing detailed quantitative adsorption and kinetic experiments relies on molecular beam techniques. The possibility to study reaction kinetics under isothermal reaction conditions employing molecular beams, offers several advantages over the traditional experimental tools for studying reactivity on surfaces - temperature programmed reaction spectroscopy (TPRS). The biggest limitation of TPRS arises from the fact that the reactants can prematurely desorb from the surface, i.e. before undergoing any reaction.[16] According to a previous study of our group on butene hydrogenation[28], this problem is of particular relevance in hydrocarbons hydrogenation. Such problems may be avoided by applying a constant reactant supply at isothermal conditions, under which high hydrogenation rates may be achieved even under ultra-high vacuum (UHV) conditions. Furthermore, the thus obtained hydrogenation rates, can exceed those obtained at

ambient pressure, by as much as several orders of magnitude.[28] A second major advantage that is uniquely offered by using molecular beams, stems from the possibility to study transient reaction kinetics upon modulation of one of the reactants on a time scale of several milliseconds. Such transient experiments may provide valuable information on the reaction mechanisms as well as on the rate limiting steps, which is difficult to achieve in a steady state mode of operation.

Also, in regard to technological catalysts, it is often questioned if surface-sensitive investigations under UHV are relevant. A convincing evidence exists from former studies, that adsorbates may act to restructure the catalyst surface, and given the high pressures and temperatures employed in many chemical reactions, one may expect this effect to be even more pronounced. Consequently, adsorbed species present during a high-pressure reaction may differ from those observed at low pressure or in vacuum.[29, 30] Even in cases where the catalyst surface structure remains intact upon gas exposure, critical intermediates occurring at high-pressure catalytic reactions may not be present under low-pressure conditions. Weakly bound active species may only appear at high pressure once all the strongly adsorbing sites on the surface are occupied by the stronger bonded species.[31] Hence, dominant species of low pressure studies may turn out to be more spectators in high-pressure reactions. Thus, gaining further insights into the details of catalytic processes, particularly under the more practical and relevant ambient pressure conditions, requires detailed reactivity studies on well-defined model catalysts beyond the range of UHV pressures.

Considering the above-mentioned issues and the concepts suggested to address them, the first and most important objective of this thesis project was to design an applicable multi-tool setup, capable of studying the structure-reactivity-selectivity relationship in model catalysts (see chapter 3). The conceptual view of the current thesis project is illustrated in Figure 1.2. The apparatus allows to prepare and characterize model catalysts under well-controlled conditions in UHV, in order to obtain atomistic-scale insight into chemoselective chemistry ranging from UHV to elevated pressures. The new UHV system includes: *(i)* a *preparation chamber* provided with the experimental techniques required for preparation and structural characterization of single-crystal based model catalysts such as oxide supported metal particles or ordered oxide surfaces, and *(ii)* the *reaction chamber* comprising three molecular beams - two effusive and one supersonic, all having a joint crossing point on the sample surface, infrared reflection-absorption spectroscopy

(IRAS) for detection of surface-adsorbed species, and quadrupole mass spectrometry (QMS) for evolved gas analysis. The supersonic molecular beam is generated in a pulsed supersonic expansion and can be modulated via a variable duty-cycle chopper. The effusive molecular beams are produced by newly developed compact differentially pumped sources based on multichannel glass capillary arrays. Both effusive sources can be modulated by a vacuum-motor driven chopper and are capable of providing high flux and high purity beams. The apparatus contains an ambient pressure cell which is connected to the preparation chamber via an *in situ* sample transfer system; it offers a valuable experimental possibility to study the reactivity of well-defined nanostructured model catalysts in a broad range of pressures encompassing UHV to ambient pressures - with the gas phase analysis based on gas chromatography.
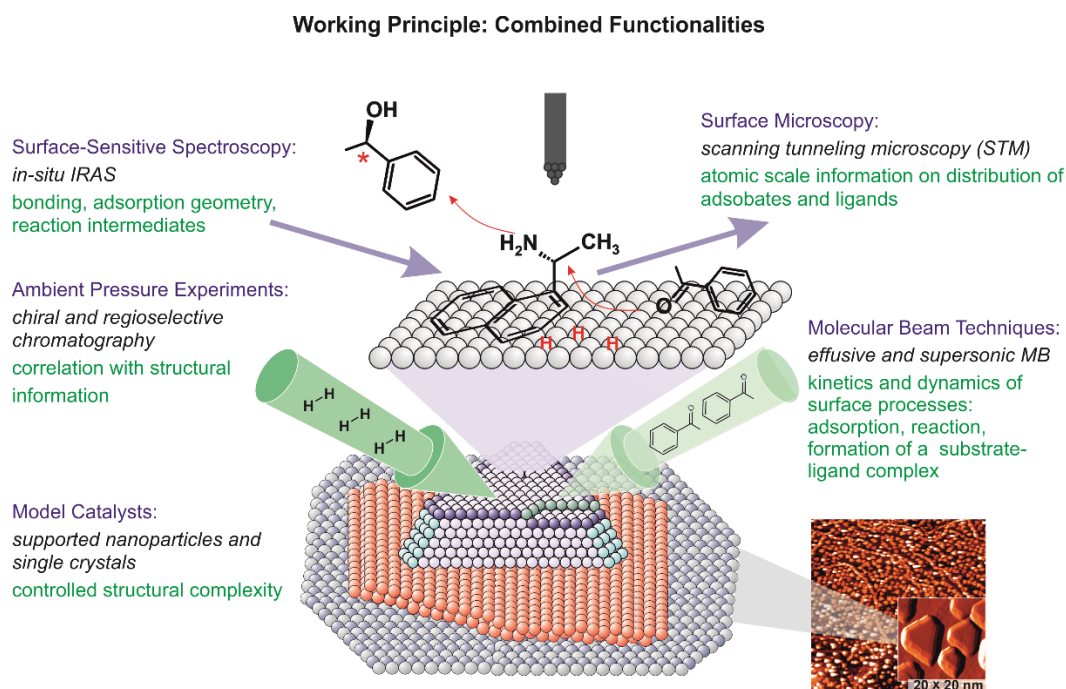
Figure 1.2: Conceptual view of the current thesis project. Kinetics and mechanisms of surface reactions are investigated on model systems of different levels of complexity, ranging from single crystal surfaces to complex supported catalysts. A combination of molecular beam techniques, in-situ infrared reflection absorption spectroscopy, scanning tunneling microscopy and ambient pressure experiments is applied to gain microscopic insights into surface chemistry on ligand-directed model catalytic materials.

The subtle differences between the potential energy barriers of individual reaction pathways, can be controlled not just by the interaction of the reactants and the reaction intermediates with the catalytic surface, but also by their intermolecular interactions with the surrounding adsorbates. The latter can significantly modify the overall energy landscape and, in turn, dramatically affect the selectivity towards individual reaction pathways.

While intermolecular interactions have been successfully employed in many homogeneous catalysts to control selectivity[32, 33], e.g. via modification of an active metal site with specific organic ligands, only a limited number of studies on heterogeneous catalysts relying on this principle was reported. Well exemplifying cases are related to enantioselective heterogeneous catalysis on surfaces functionalized with chiral adsorbates. In this type of catalysis, chiral modification can be produced by a selection of methods, including e.g. chiral templating by formation of long-range ordered patterns of chiral molecules on metal surfaces (chiral lattice templates),[34, 35] or adsorption of chiral organic molecules (chiral modifiers) that build a 1:1 complex with a prochiral substrate.[36, 37] The chiral modification exhibits enantiospecific interaction with a pro-chiral reactant, hence directing the catalytic process towards formation of only one enantiomeric form of the product.[5, 38-40]

Besides of enantioselective heterogeneous catalysis, in the last decade ligand-induced catalysis reactions for non-chiral systems gain increasing importance. In this type of surface processes, highly chemoselective catalytic surfaces can be obtained by specific adsorbate-adsorbate interactions which are induced by pre-absorbed surface ligand. Both steric and electronic effects can be efficiently used to tune catalytic properties of active metal sites. Recent studies demonstrate the important roles of surface ligands in creating metal-organic interfaces that can significantly improve both catalytic activity as well as selectivity of the catalytic surface.[41-44] For example, a dramatic enhancement in hydrogenation rate of the olefinic bond in 1-epoxy-3-butene, was reported on Pd nanoparticles in the presence of n-alkanethiol.[44] It was proposed that disordered thiol tails can block access of reactants to the active sites and increase the entropic barrier for adsorption of all reactive species. Over 90% selectivity towards C=O bond hydrogenation in unsaturated aldehydes, containing both C=C and C=O double bonds, were shown on PtCo nanocrystals in the presence of surface oleylamine arrays.[45] This finding has been ascribed to the steric effect of long-chain amines that favors adsorption of the substrate to the NPs via the end aldehyde groups rather than adsorption of the C=C bonds located in the middle of the molecule.

Towards this goal, model catalysis approach offers a unique opportunity to contribute to a deeper understanding of the ligand/adsorbate interactions, both on single crystalline metal surfaces as well as on more practically relevant nanostructured model surfaces. This was experimentally realized in recent mechanistic studies by our group on partial selective hydrogenation of acrolein towards unsaturated alcohol propenol over Pd model surfaces, in which we were able to show that the surface modification with a dense overlayer of organic ligands, particularly oxopropyl species, turns the Pd(111) surface 100% selective towards desired hydrogenation of the C=O bond.[46-49] In contrast, on Pd nanoparticles lacking this ligand-overlayer, only minor amounts of propanal, resulting from undesired hydrogenation of the C=C bond, were detected.

Despite the impressive and ongoing progress in the field, basic understanding of the intermolecular interactions between co-adsorbed molecular species on surfaces, is rather limited. Therefore, combining the model catalysts approach with their systematical functionalization by adsorption of different organic ligands by means of transient chemical modifications of specific parts of the molecules, can result in tremendous electronic and geometric effects that allow to independently address different ligand-related phenomena, and explore working principles of ligand-directed heterogenous catalysis.

As first steps towards this goal, we address lateral interactions between co-adsorbed molecules on surfaces, which can crucially affect the activity and selectivity of heterogeneously catalyzed reactions, and therefore be employed for purposeful functionalization of surfaces to improve their catalytic efficiency. Two case studies were investigated in the newly built setup: (i) the adsorption behavior of simple carbonyl compound acetophenone on Pt(111), and (ii) co-adsorption studies of one of the most efficient and well-studied chiral modifiers,[38] (R)-(+)-1-(1-naphtylethylamine) (NEA) and CO adsorbed on well-defined Pt(111).

The structure of this thesis is as follows. A theoretical background of the experiments conducted in the new experimental setup, is first discussed (chapter 2). Then, the experimental MB/IRAS setup, designed and built for the measurements, is thoroughly described (chapter 3). Apart from the considerations and special requirements regarding the incorporation of three molecular and infrared beams in the chamber, the design of the construction parts, as well as their performance

is presented and discussed. Chapters 4 and 5, discuss the obtained results of the investigated case studies.

In chapter 4 we present a mechanistic study on the details of intermolecular interactions between acetophenone adsorbates on well-defined Pt(111). We show that these interactions trigger an important reaction of keto-enol tautomerization, producing an enol reaction intermediate, which is envisaged to enable low-barrier hydrogenation of simple carbonyl compounds.[50-52] By combining surface sensitive techniques, including IRAS, scanning tunneling microscopy (STM) and molecular beam techniques, we found that enol can be formed on Pt(111) by building a ketone-enol dimer, in which one molecule is present in the enol form and is stabilized via hydrogen bonding to the carbonyl group of the second ketone molecule. This process is accompanied by the evolution of new vibrational bands detected by IRAS, which are related to the enol tautomer. We show that the enol can exists only if it is stabilized by the neighboring ketone molecule. The second observed type of surface dimers involves two ketone molecules. Surprisingly, the presence of large amounts of H on Pt was found to destabilize both types of dimers, leading to formation of acetophenone monomers in the ketone form. Additionally, based on the investigations of the co-adsorption behavior of acetophenone and hydrogen, we conclude that keto-enol tautomerization occurs in the intramolecular process and does not involve hydrogen transfer through the surface hypothesized previously.[53]

The interaction of acetophenone with Pt(111) was investigated in a broad range of temperatures. Several types of hydrogen-bonded oligomer species can be formed. Their evolution exhibits a strong temperature dependence, suggesting that oligomer formation promotes keto-enol tautomerization by lowering the activation barrier for hydrogen transfer from the methyl to the carbonyl group. Based on these observations, we conclude that this process occurs most likely in a concerted way, in which the energy barrier for hydrogen transfer can be compensated by formation of strong hydrogen bonds between enol and ketone species assembled in an oligomer. Additionally, we demonstrate an important role of hydrogen bonding between the ketone and the enol parts of surface-adsorbed oligomers, which stabilizes the otherwise unstable enol species, making them accessible for further reaction steps. We show that the target process – hydrogenation of the carbonyl group – occurs not in monomers but in the ketone-enol dimers and results in the formation of a partly hydrogenated acetophenone species attached via the hydrogen bonding to the

second acetophenone molecule. The results provide a strong experimental evidence that confirms the theoretical predictions that transformation of simple carbonyl compounds to their enol part enables low-barrier hydrogenation pathway of normally very stable C=O compounds. To the best of our knowledge, an experimental verification of this theoretical prediction was not yet provided.

The second study case involves the adsorption of chiral modifier, R-NEA, on Pt(111) (chapter 5). The spectroscopic results are supportive of a strongly inclined adsorption geometry of R-NEA molecules in accordance to previously reported data.[54] In addition, we found that the molecules form directed chains at intermediate coverage and self-assemble onto overlayers at coverages close to saturation. It is therefore suggested that the observed directed interaction between the individual R-NEA molecules involves the amine group of one molecule and the hydrogen of naphthyl-ring of the neighboring molecule.

In the next step, adsorption of CO on the Pt surface functionalized with R-NEA was investigated. CO was utilized as a simple proxy to study the interaction of simple carbonyl compounds with chiral modifiers. The spectroscopic results point to an intermolecular interaction of CO with the NEA-modified surface, as suggested by the strong shift and considerable broadening of the CO related bands compared to that one observed on a pristine surface. The latter observation is accompanied by a dramatic attenuation of the skeletal bands related to R-NEA, suggesting a less inclined geometry of the molecules with respect to the sample surface.
Finally, the most important key results of this work are summarized in chapter 6.

Chapter 2

Theoretical background and experimental techniques

This chapter provides an overview over dynamic and kinetic processes, which might occur on catalytic surfaces as well as the physical aspects of the major experimental and detection techniques implemented in this work.

2.1 Dynamics and kinetics on surfaces

To understand elementary reaction steps at a molecular scale in catalytic processes, it is of great importance to understand the kinetics and dynamics of gas-surface interactions. The rate constants of these elementary steps and their coverage dependence, determine the global reaction kinetics. Thus, unraveling the dynamics and kinetics of these steps is an essential question in kinetic studies.

In general, when a molecule collides with the surface, it can undergo several processes, as depicted in Fig. 2.1. Fundamentally, these processes are inevitably linked and are classified by the energy exchange of the species with the surface; it can gain or lose momentum or exchange the internal energy with the surface. Following the collision, some of the species will be *scattered* from the surface, but some of them lose sufficient momentum and cannot leave the gas-surface potential well. In such a case we say that the molecules are *trapped*. For the latter case, the molecules can be in a weakly bound state, and thermal motions of the surface can cause the molecule to *desorb*. If, however, a molecule stays on the surface for a significant time it can be converted to a more strongly bound state and it is said that the molecule *sticks*.

In the following, each elementary process will be described shortly. A more extensive summary of these processes can be found elsewhere.[55-58]
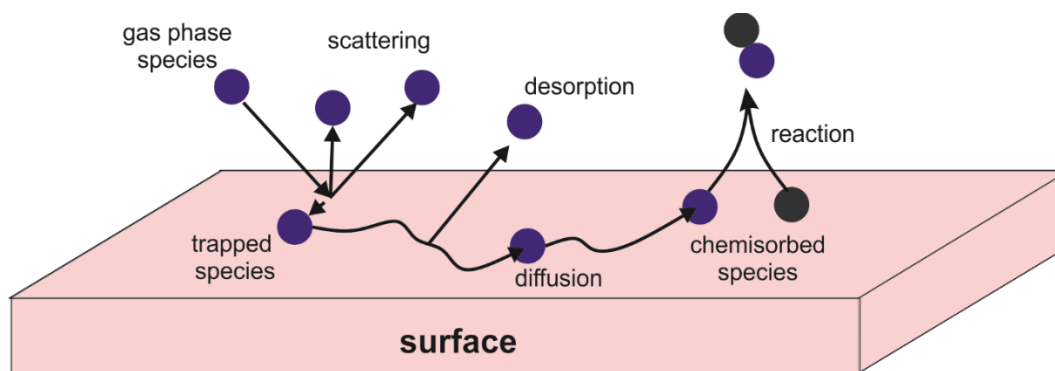
Figure 2.1: Schematic illustration of elementary surface processes.

1. **Scattering.** When a molecule or an atom collide with the surface, they can simply bounce from the surface without being trapped. The kinetic energy of these species can be either preserved i.e. elastic scattering, or the energy can be transferred in between the species and the surface i.e. inelastic scattering. While in the former event, incidence and scattering angles are equal, in inelastic scattering the species maintain their parallel momentum, but lose the perpendicular one. Gas-surface scattering experiments can provide valuable insights into the factors that determine the energy exchange and the nature of collision. For instance, the velocity and state distributions of the scattered species as a function of the angle, the energy and the quantum states of the incident species.[55]

2. **Trapping.** When a species loses sufficient momentum along the surface normal, it cannot leave the gas-surface potential well. There are few reasons for a species to be trapped; some of them are caused due to coupling of the normal momentum of the impinging species with the surface phonons or by thermal equilibration with the surface as a result of excitation of internal vibrations.[55] Temperature, mass and chemical structure of the species and other more parameters affect the trapping probability, and the events can be followed by desorption, also attributed as "trapping-desorption".[55, 59, 60]

3. **Adsorption**. Adsorption of species on a surface, originating from relatively weak dispersive forces (Van-der-Waals, VdW), is called physisorption. In this case the molecules preserve their gas phase electronic structure, although some distortion is still possible. The binding energy varies between few meV to eV while large organic molecules are adsorbed. Even though the contribution of each individual organic molecule is small, the attractive nature of VdW interactions can lead to a sizable adsorption energy which can be associated with chemisorption

(see next). If the interaction between the surface and the adsorbates is large, it is termed chemisorption. Chemisorption occurs when there is a significant overlap between the electronic orbitals of the surface and of the adsorbates. The electronic structure of the adsorbed molecule in this case is often not preserved on the surface with respect to that of the gas phase. The interaction can be classified as -molecular, -non-activated dissociative and -activated dissociative chemisorption,[61] and it often occurs after the adsorbate had passed through a more weakly bound precursor state. It should be noted that the strong interaction of the adsorbate with the surface is often associated with formation of a chemical bond. Yet, several cases have shown that even when significant hybridization with the surface occurs, the molecules can be only weakly adsorbed as was shown for water on graphene.[62]

The adsorption rate of a molecule depends on the flux of the incoming molecules impinging the surface (Z_A), the number of vacant adsorption sites (θ_*) and the sticking coefficient (S_A) according to the following equation:[58]

$$\frac{d\theta_A}{dt} = Z_A \theta_* S_A(\theta_A, \theta_B, \dots) \quad (2.1)$$

where,

$$Z_A = \frac{p_A}{\sqrt{2\pi m_A K_B T}}, \theta_* = (1 - \theta_A - \theta_B - \cdots) \quad (2.2)$$

$$S_A(\theta) = \frac{dN_{ads}}{dN} \quad (2.3)$$

with p_A and m_A the partial pressure and the mass of the adsorbing molecule respectively.

Generally, the sticking coefficient -$S_A(\theta)$ – decreases linearly with the density of empty sites and thus with surface coverage. Note however, that the sticking coefficient might stay constant and high until a relatively high coverage is reached if the molecule is trapped in a precursor-mediated state. According to this process, adsorbates can be trapped over sites that are occupied by chemisorbed species (extrinsic precursor) that allow them to diffuse along the covered surface until vacant sites for chemisorption are found. Intuitively, when the desorption probability of the extrinsic precursor is low, and the adsorption probability of the intrinsic precursor- the sites which are directly available for chemisorption- is high, the sticking

probability will increase.[63] For relatively large organic ligands (> 50 amu), such as those utilized in this thesis, it is mostly shown that the sticking probabilities are high up to high surface coverages, indicating low desorption rate from the extrinsic precursor state and high adsorption rate from the intrinsic precursor state.

4. **Desorption and Diffusion.** Following the adsorption process, the adsorbate can undergo either a desorption or it can diffuse across the surface. Both diffusion and desorption are activated processes, with the latter process being generally characterized with higher activation energies than the former process. Taking into account that both processes are driven by thermal fluctuations from the surface, the surface temperature critically controls the rates of diffusion and desorption. The adsorbate thus typically undergoes several diffusion steps prior the desorption process. Within the residence time of an adsorbate on the surface (t), the lateral isotropic diffusion (x) can often be described as a simple Brownian diffusion model:[58]

$$\bar{x} = 2\sqrt{Dt} \quad (2.4)$$

where D is the diffusion constant, described by an Arrhenius equation:

$$D = D_0 \exp\left(-\frac{E_{diffusion}}{k_B T_S}\right) \quad (2.5)$$

with D_0 and $E_{diffusion}$ being the pre-exponential factor and the diffusion activation energy respectively, and T_s represents the surface temperature. Note that the molecules can either diffuse freely in some sort of a Brownian motion-like if $RT_s \gg E_{diffusion}$, or they can move along the surface in a hoping motion if $RT_s \ll E_{diffusion}$. For the latter case, strongly bound species have to overcome a significant activation barrier between different adsorption sites.

Similarly to the Arrhenius model for diffusion, the rate of desorption $-\frac{d\theta}{dt}$ is given by

$$-\frac{d\theta}{dt} = \theta^n k_0^{des} \exp\left(-\frac{E_{des}}{k_B T}\right) \quad (2.6)$$

with θ the coverage, n the desorption order, k_0 the desorption pre-exponential factor and E_{des} the desorption activation energy.[55, 58] The pre-exponential factor for desorption, k_0^{des}, and the activation barrier for desorption, E_{des}, depend on the coverage θ. The desorption order depends on the type of desorption, e.g. recombinative or molecular, and it can be also influenced by adsorbate-adsorbate interactions, island formation and other effects.

Bimolecular reactions on surfaces

In principle, there are two types of mechanistic bimolecular reactions on surfaces: (i) Langmuir-Hinselwood (LH) mechanism and (ii) Eley-Ridel (ER) mechanism.[55] The former mechanism is more common on transition metal surfaces and proceeds via the reaction of two adsorbed species on the surface. For the latter mechanism, which was shown only in few cases[56], a gas phase molecule directly reacts with an adsorbed surface species.

Schematic illustration of the LH mechanism is shown in Fig. 2.2.

Figure 2.2: Schematic illustration of Langmuir-Hinselwood reaction mechanism.

The adsorption process of the reactants might follow the surface processes described previously, such as: diffusion between different adsorption sites, molecular or dissociative chemisorption or physisorption in a precursor state. If the reactants are A and B, forming the product AB, the formation rate $-\frac{d\theta_{AB}}{dt}$ is described by:

$$\frac{d\theta_{AB}}{dt} = k_0^{LH} \exp\left(-\frac{E_{act}^{LH}}{k_B T}\right) \theta_A \theta_B \qquad (2.7)$$

where θ_A and θ_B are the surface coverages of the species A and B, E_{act}^{LH} is the activation energy for the reaction, and k_0^{LH} is the pre-exponential factor.

2.2 Experimental and detection methods

2.2.1 Molecular beams

When a gas passes from a high-pressure vessel into an evacuated chamber through an orifice, a molecular beam is formed. As long as the mean free path of the gas is larger than the aperture diameter, the molecules will escape through the orifice free of collisions. In such a beam, said to be effusive, the velocity distribution and the distribution over the internal degrees of freedom (vibration and rotation) is the same as that in the vessel. By raising the pressure in the vessel or by increasing the diameter of the orifice, the mean free path of the gas becomes smaller than the orifice diameter. In this case, molecules passing through the orifice frequently collide, which results in adiabatic cooling of all degrees of freedom in the expansion area. Consequently, the total energy which is available per gas phase molecule in the vessel is converted into kinetic energy, leading to a supersonic beam of molecules which are internally cold.[64] The molecule of interest can be diluted in a mixture with a noble heavier gas in order to reduce the terminal temperature which is normally limited by formation of clusters in the beam. Supersonic beams can be operated in a pulsed mode to reduce the pumping requirements and for the use of millimeter range orifices. Pulsed beams allow translational temperatures below 1 K. Generally, the rotational temperature and the translational temperature in the beam are relatively close. However, that of the vibrational degrees of freedom cool significantly less. Several parameters may be used to control the beam velocity: (i) the mass of the carrier gas, (ii) the temperature of the source and (iii) the pressure of the source.[65] Pulsed beams are employed in a variety of deceleration experiments as well as Zeeman and Stark experiments. Slow molecular beams can be produced for instance by introducing the gas into a cryogenic buffer or by loading it into a magnetic trap.[66] Additionally, molecular beams can be slowed down mechanically such as in elastic scattering from a receding substrate.[67]

The end goal of a fundamental research in catalysis would be a well-defined micro-kinetic model that properly describes all elementary reaction processes (see, e.g.[68]). In UHV studies, dynamic aspects of gas-surface interaction and the focus on reaction kinetics, can be performed by employing molecular beam techniques. The following part provides an overview on molecular

beam techniques which were implemented in the newly built setup, and their applications to study reaction kinetics. Further details and general overview can be found elsewhere.[16, 69-72]

Applications of molecular beams in studies of model catalysts

The quantitative nature of molecular beam experiments, together with the well-defined conditions under which they are performed, allows to obtain detailed insights into the corresponding reaction kinetics. Various types of experiments were previously performed with particular focus on the microscopic understanding and on the micro-kinetic modeling on surfaces of supported catalysts (a comprehensive review is given in Ref. 16).

In the following, the major experimental options for the use of molecular beam techniques are summarized:

1. The possibility to study reaction kinetics under isothermal reaction conditions. One of the most important limitation of temperature programmed reaction spectroscopy (TPRS) lays in the fact that reactants can desorb from the surface prior they are undergoing a reaction. This problem is of particular importance for certain reactions such as hydrogenation of hydrocarbons.[28] Constant supply of reactants and isothermal reaction conditions allow to prevent such problems and to obtain high hydrogenation rates even under UHV conditions that can even excess the reaction rates observed at ambient pressure by several orders of magnitude.[28]

2. The possibility to study transient reaction kinetics upon modulation of one of the reactants on a time scale of several milliseconds. Such transient experiments provide valuable information on the reaction mechanisms and on the rate limiting steps, which is otherwise difficult to achieve in a steady state mode of operation.

3. Determination of absolute reaction probabilities. The surface event can be effectively determined, as the reactant molecules interact with the surface only once. This allows the determination of absolute reaction probabilities such as sticking probabilities.

4. Controlling the dynamic properties of beams, which can be achieved by adjusting the temperature and the pressure of the source. In other words, the kinetic and internal energy of the impinging beam can be controlled and preserved until it hits the surface.

5. The effective pressure of the reactant molecule at the sample position is few orders of magnitude higher than the UHV chamber background pressure. This allows collision–free

detection of scattered and desorbing molecules, which is advantageous, for instance, for determining the angular distribution of reactant molecules, their kinetic energy and their vibrational and rotational energy distribution.[71, 73, 74]

As discussed above, the application of molecular beams in gas-surface studies involves in practice two types of beam sources: supersonic and effusive. Considering the conditions of gas expansion, these two categories represent, in fact, two limiting cases that result in two specific types of molecular beams that differ in the energy distribution of their molecular components. To describe the nature of gas expansion, the Knudsen number, Kn, is usually accounted for, as it allows characterizing the nature of a system's dynamics, namely if it is statistical or continuum. Defined as λ/d, with λ the mean free path of the gas molecules and d the characteristic physical length scale of the beam source, namely its aperture dimension, low and high Kn values respectively classify MBs as supersonic (SMB) or effusive (EMB).

Supersonic source

The case of SMB is schematically illustrated in Fig. 2.3 which depicts, in sequence, the dynamical evolution of gas expanding under a given pressure difference through a nozzle.
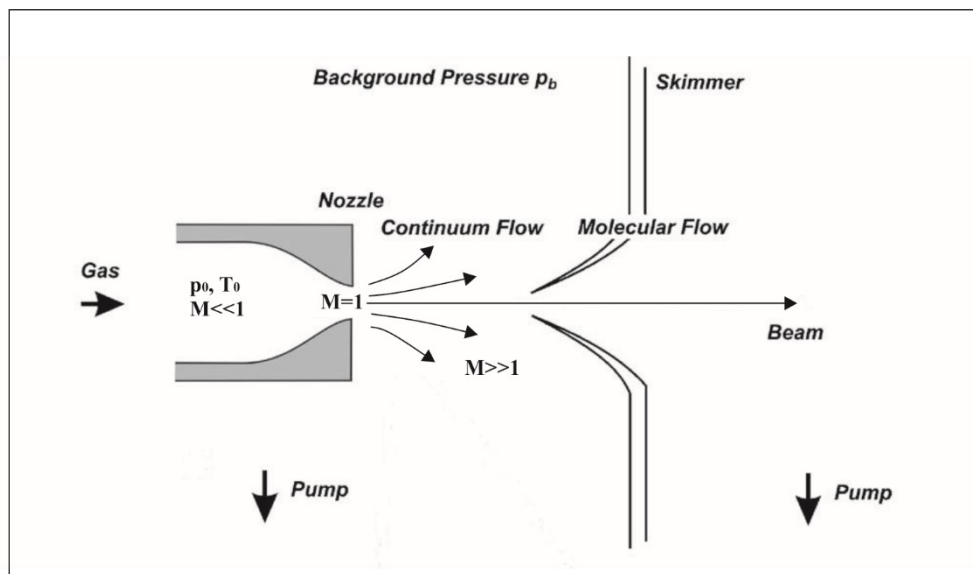

Figure 2.3: Schematic setup of the beam source. Adapted with permission from [16]. Copyright 2005, Elsevier.

Driven by a pressure difference, the gas accelerates from an initial stagnation state (Mach number, M <<1), and in extreme cases can exits the nozzle with a sonic velocity (M =1), which then increases to supersonic (M > 1) on further expansion. On distancing from the nozzle, the gas flow tends to readjust to the boundary conditions, however before such readjustment can be realized, a small solid angle of the expanding gas is sampled by means of a skimmer. In the expansion volume, the molecules frequently collide, resulting in an efficient cooling of external degrees of freedom (translational and rotational) whereby the velocity, v, of the molecules promptly approaches an asymptotic terminal value. The translational temperature hence decreases to the point where free molecular flow occurs. Under these conditions, the translational velocity along the beam direction is generally modeled by a shifted Boltzmann distribution, and all species composing the SMB, flow in a narrow velocity distribution and possess practically the same terminal velocity:

$$I_\parallel \propto v^2 exp\left(-\frac{M(v-v_\parallel)^2}{2kT_\parallel}\right) \qquad (2.8)$$

$$v_{\parallel,\infty} = \sqrt{\frac{2RT_0}{M}\frac{\gamma}{\gamma-1}} \qquad (2.9)$$

with $v_\parallel$ denoting the parallel flow velocity, M the molecular mass of the gas species in the beam, and γ the adiabatic exponent.

Such a situation provides advantageous unique possibilities as it allows one to prepare in advance a regulated gas mixture with inert gases, in the sense of achieving a fairly flexible degree of control over the kinetic energy of any species of interest. In practice, a broad scope of methods exists, that allow a controlled modification of energy distribution or selection of specific excited states in-flight, i.e. post preparation of the beam. Such features are crucial in studies of gas-surface dynamics, surface scattering and diffraction of fast transient kinetics.

Effusive source

Differently from SMBs, EMBs comprise large Kn values under which the number of intermolecular collisions between the gaseous species leaving the source is practically negligible. Hence, the energy distribution of all degrees of freedom is described by a T_0 stagnation state, with a Maxwell–Boltzmann velocity distribution:

$$I = N v^3 \exp\left(-\frac{Mv^2}{2kT_0}\right) \qquad (2.10)$$

The simplest configuration by which an effusive beam source may be realized experimentally, is based on expanding gas molecules through a thin-walled orifice into an evacuated chamber. In fact, only a small element of the solid angle needs to be extracted from the overall flux in order to form a beam, a requirement which is achieved by removing the utmost part of the gas by means of differential pumping. Moreover, to minimize collisions of beam gas molecules with those occurring in the background, the background pressure must be kept low, hence the beam intensity is usually restricted by the pumping speed in the expansion chamber. This, however, may be improved by utilizing alternative long channels instead of thin-walled orifices. Such an arrangement allows for a strong angle dependence of the transmission probability, which provides in turn, a unique capability of controlled flux collimation. In practice, the resulting angular distribution depends on l/r, being the ratio between the length of the channel to its radius.

The collimation effect is commonly characterized via a peaking factor, k, which reflects the ratio between the centerline intensity of the actual distribution, I(0), of a total flux N, and a cosine distributed flux of the same total N. For sufficiently long channels and in the low-pressure limit, k amounts approximately to 3l/8r. Under such conditions and typical l/r values, e.g. of ~40, k values of ~15 are achieved, to be compared with the case of supersonic expansions which comprise as low as 1.1 - 2.0 characteristic k values, depending on the type of gas.

On increasing pressure, the mean free path of the gas molecules becomes comparable to the channel length, whereby molecular collisions broaden the angular distribution hence causing the velocity distribution to deviate from that of Maxwell–Boltzmann. It hence follows that one may obtain a collimation effect at high total flux and high stagnation pressure by utilizing parallel arrays

of small channels. In practice, this is achieved by using glass capillary arrays (GCA). All in all, the key advantages of GCA effusive sources may be summarized as follows:

- Obtaining high-intensity peaks at a wide range of pumping conditions.
- Obtaining orders of magnitude range beam flux, without alteration of beam properties.
- Low stagnation state pressure which allows easy beam generation for reactants of low vapor pressure.
- Reduced gas consumption.

It hence follows that the use of effusive sources is advantageous in addressing most requirements of surface kinetics studies.

2.2.2 Infrared absorption spectroscopy

Infrared absorption spectroscopy is one of the most powerful spectroscopic techniques available for the characterization of catalytic systems. The technique provides key fundamental information about a variety of catalysts and catalytic reactions and allows several novel options for the acquisition of new information on both reaction mechanisms and the nature of the solids used as catalysts. With model systems such as those used in surface-science studies, the technique can be employed for studying specific aspects of catalytic processes in great details. The technique is non-intrusive, and it can be implemented in situ or in operando mode during catalytic reactions without perturbing the system.

IR absorption spectroscopy provides molecular insights into both adsorbates and surface sites that are otherwise difficult to obtain with other techniques; it can be used in conjunction with probe molecules to further explore catalytic ensembles, and can also be implemented in quantitative mode for surface titrations or for the estimation of turnover frequencies and other kinetic parameters. Despite the fact that IR absorption spectroscopy was one of the first spectroscopic techniques applied to the study of catalysts, it remains one of the most powerful, and continues to be developed with the goal of enhancing its ability to extract more detailed chemical information on ever increasingly complex systems.

General principle

When electromagnetic field of infrared radiation interacts with the oscillation dipole associated with a particular normal vibrational mode, molecules in adsorbed phase can be excited. This excitation manifests itself in the absorption of a proportion of the reflected radiation in the infrared experiment.

For wavelengths that are much bigger than the dimensions of the excited vibration, which is always valid for IR light, the electric field induced by the electromagnetic radiation can be described by the dipole approximation, so that the Hamilton operator H^1 is described as:

$$H^1 = -\vec{\mu} \cdot \vec{E} \qquad (2.12)$$

with $\vec{\mu}$ the electric dipole moment of the molecule, and $\vec{E}$ the electric field vector of the electromagnetic radiation.[75] According to Fermi's Golden Rule, the transition probability for excitation is given by:

$$W \propto <\psi_f|\vec{\mu} \cdot \vec{E}|\psi_i> \qquad (2.13)$$

where ψ_f and ψ_i being the eigenfunctions of the vibration in the excited and in the ground states. Based on the Born-Oppenheimer approximation, the wavefunction of the molecule can be broken into electronic and nuclear (vibrational) components that can be treated separately:

$$\psi = < \epsilon, v'_k|\vec{\mu}| \epsilon, v_k > \qquad (2.14)$$

From the equation above, the vibration will be infrared active, if it is associated with an oscillating dipole moment, i.e. if

$$\frac{\partial \vec{\mu}}{\partial \vec{Q_k}} \neq 0 \qquad (2.15)$$

The derivative $\frac{\partial \vec{\mu}}{\partial \vec{Q_k}}$ is denoted as a dynamic dipole moment of the molecule along the normal coordinate Q_k. Thus, only vibrations where the dynamic dipole moment changes along the normal coordinate of the vibration are excited (see for instance Refs. [75, 76] for further details).

Infrared reflection absorption spectroscopy

In IR absorption spectroscopy, a number of setups is available, by which the experiment may be adapted to the nature of the sample to be probed.[77-79] On metal surfaces, IR spectroscopy is typically performed in grazing incidence reflection geometry called infrared reflection absorption spectroscopy (IRAS). The technique allows not just to chemically identify molecules based on their absorption frequency, but also for obtaining detailed information related to the interaction of the molecules with the surface.[80-82] The surface morphology and the adsorption sites strongly affect the absorption frequency. For instance, CO can be used as a probe molecule to characterize the morphology of the surface. In addition to studying adsorbed molecules, the technique allows to study lattice vibrations and phonons.[83]

Figure 2.4 shows a typical IRAS setup. The IR beam comes in at grazing angles which are nearly parallel to the surface and partially absorbed by a highly reflective surface. The reminder of the beam is reflected by the surface towards a detector. Directing the IR beam onto- and from- the surface is optically performed by means of mirrors.
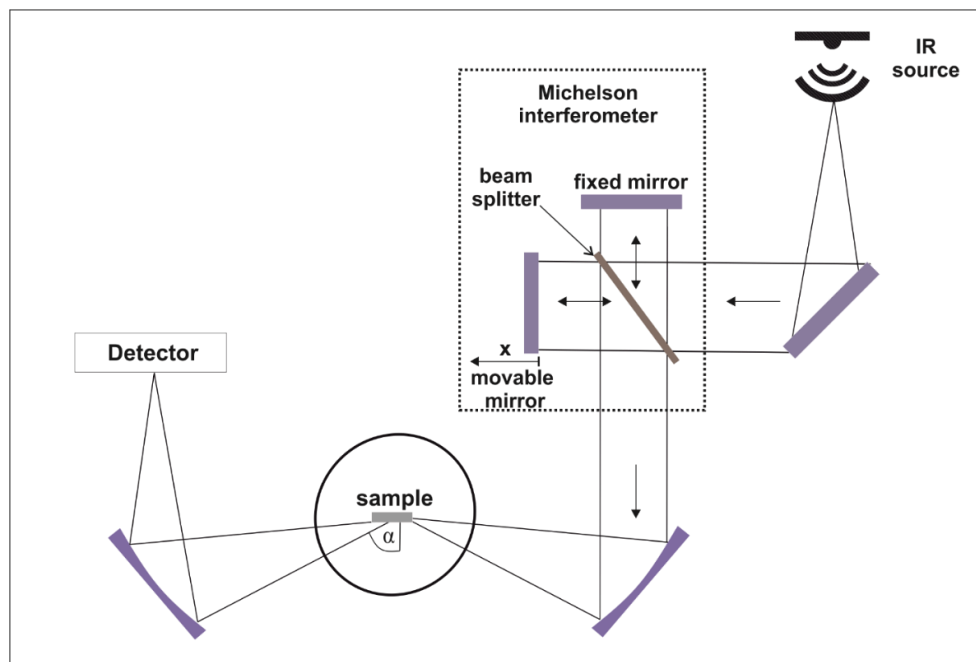

Figure 2.4: Schematic illustration of a typical IRAS setup with Michelson interferometer.

New generation infrared spectrometers consist of Fourier-Transform Infrared (FTIR) spectrometers operating on the principle of Michelson interferometer at which the entire spectrum

is obtained for each scan the interferometer makes. In comparison with old generation energy-dispersive type spectrometers, the sample is not exposed to monochromatic light but to a broad spectral region, resulting in much shorter collection time needed to measure a spectrum.

A common and simple configuration of Michelson interferometer is shown schematically in Fig. 2.4. Using a beam splitter, the light source is split into two paths after which the two partial beams recombine. The configuration typically consists of two mutually perpendicular plane mirrors; one at a fixed position (Fig. 2.4, fixed mirror), whereas the other can be moved along a specific axis (Fig. 2.4, movable mirror). The beam is partially reflected by the beam splitter to the fixed mirror and partially transmitted to the movable mirror. Each beam is reflected back to the beam splitter, where the superposition of both beams causing the interference. The resulting beam intensity is then measured by a detector as a function of the optical path difference, hence containing all the information accessible in the IR experiment, i.e. the interferogram. The single channel can be calculated by Fourier transformation. The treatment of the FTIR can be found elsewhere.[84]

It should be noted that the structure of a single channel spectrum is dictated by the thermal characteristics of the radiating source, but contains also other contributions, e.g. from the optical set up, detector response function, molecules adsorbed on the sample surface, etc. To account for those, the sample spectrum is divided by a reference spectrum that is acquired for the same conditions and optical setup, but without adsorbates.

Major Principles

The electromagnetic field experienced by the adsorbed molecule, is dominated by the dielectric response of the substrate at infrared frequencies, with which it is in a close spatial proximity relative to infrared wavelengths. Hence, it is possible to detect not only the first monolayer under the substrate influence, but also thicker films comprising multilayer. The observation of vibrational modes of adsorbates on metallic surfaces is subjected to the metal surface selection rules[80, 82, 85]. Only vibrations having projection of the dynamic dipole moment perpendicular to the surface plane, are detectable by IRAS. Those with parallel orientation are strongly attenuating due to mirror dipoles of the underlying metal. In addition, the phase of the incident light shifts upon reflection. The phase of the s-polarized light is shifted by 180°, irrespective of the angle of incidence. However, the phase shift of p-polarized light depends on the angle of incidence. Since only the p-polarized light may interact with dipoles on the surface, the experiments are performed

with p-polarized light at grazing incident angles. The major principles of IRAS are illustrated in Fig. 2.5.
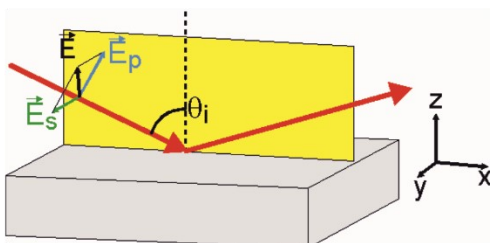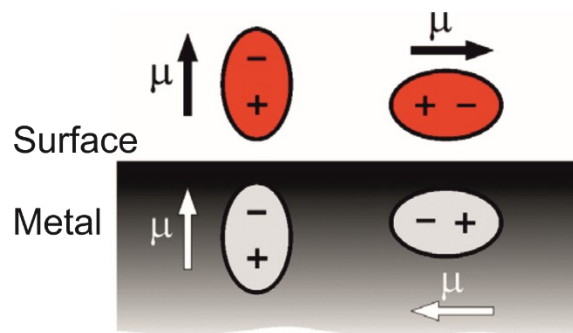
(a)   **(b)**

Figure 2.5: (a) Illustration of the IR electric field vector ($\vec{E}$). Ep and Es are the electric field vectors parallel and perpendicular to the plane of incidence respectively. Only the p-polarized component interacts with dipoles on the surface. (b) Illustration of the metal surface selection rule. Adapted from:http://www.fhi-berlin.mpg.de/acnew/department/pages/teaching/pages/teaching__wintersemester__2007_2008/sterrer_vibspec_091107.pdf.

Considering the selection rules mentioned above, IRAS experiments of adsorbed molecules on surfaces allow also to obtain insights related to the adsorption geometry of the molecule. By comparison of the submonolayer spectra to that obtained in the gas phase, some conclusions can be drawn based on the absence or the intensity distribution of vibrational bands.

When a molecule is adsorbed on a metal surface and does not interact with any other molecule, it experiences a frequency shift from the gas phase due to (i) *mechanical renormalization*, (ii) its *dipole image* and (iii) its *chemical bonding* to the surface.[80-82] Mechanical renormalization is caused due to the binding of a molecule to a rigid surface of a much higher mass, resulting in a shift to higher frequencies, i.e. a blue shift. In the second effect (dipole image), the adsorbate induces an image charge which consecutively alters the local electric field of the adsorbate and by this leads to a downward shift (red shift). Lastly, chemical shifts arise from changes in the electronic structure of the adsorbate as a result of charge transfer with the surface. This includes several contributions such as bonding configuration, coordination number, and the local chemical

environment. For the latter contribution, co-adsorbed species on the surface and the influence of neighboring molecules of the same species, particularly at high coverages, can significantly affect the frequency shift. Neighboring dipoles can interact with each other due to the local electric field of vibrations, or through the surface electrons. These effects, known as dipole coupling effects, result in frequency shift to higher wavenumbers, i.e. blue shift. Dipole image as well as chemical bonding influence the half-width, line shape, and intensities of the vibrational bands, in addition to coverage-dependent frequency shift.

Intensity changes: the adsorption geometry of adsorbed molecules can affect the observed intensities due to the Metal Surface Selection Rule (MSSR).

The intensity, which depends on the magnitude of the dipole moment along the surface normal, does not necessarily behave in a linear fashion with increasing coverage of the adsorbate; this is because dipole interactions between the adsorbates, and in particular at high coverage, can lead to depolarization. Consequently, the intensity either does not increase further or even decrease.

Another important contribution to the intensity of vibrational bands is related to a phenomenon called intensity borrowing. For two species comprising similar frequencies that are in close proximity, dipole coupling may result in intensity transfer from the low frequency species to the high frequent one, i.e. a blue shift.

2.2.3 Mass spectrometry

Principles

Mass spectrometry is an analytical technique in which molecules or atoms from a sample are ionized (usually positively), separated according to their mass-to-charge ratio (m/z), and then recorded. In contrast to other techniques such as IRAS, the method is destructive.

In this work, quadrupole mass spectrometer (QMS) was implemented in the new setup to investigate chemical surface reactions (for details see Chapter 3). Schematic representation of a typical QMS setup is shown in Fig. 2.6 which consists of an ionizing source, quadrupole analyzer to separate the produced ions, and a detector which counts the ions. In the following, the description of components and their working principle are described briefly. Further details can be found elsewhere.[86-88]
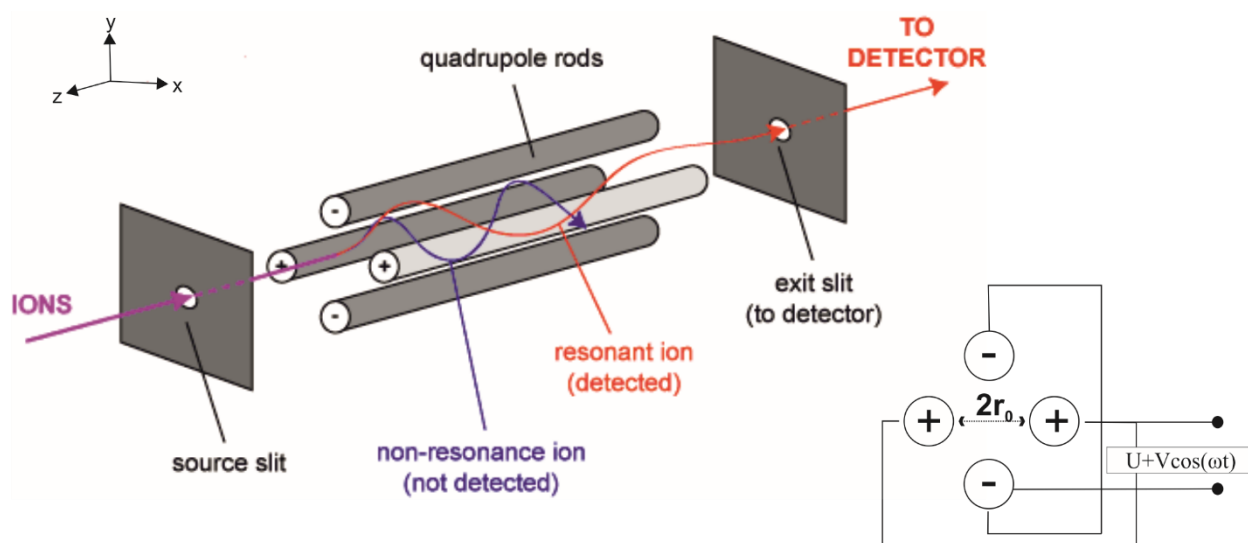
Figure 2.6: Schematic representation of QMS setup. Adapted from [89].

Ion source

The ion source produces gas phase ions of compounds by electron impact (EI):

$$M + e^- \rightarrow M^{\cdot+} + 2e^- \qquad (2.16)$$
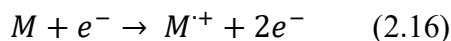
There are two possible fragmentation routes for the produced molecular ions; they can either undergo fragmentation to a radical and an ion with an even number of electrons, or to a molecule and a new radical cation. Note that the latter pathway typically occurs when an excess energy is transferred to the molecule as shown in the following:

$$M^{\cdot+} \rightarrow A^{\cdot+} + B \qquad (2.17)$$
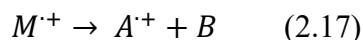
Each of the products have different chemical properties and can undergo further fragmentation and is detected according to their abundance to produce a mass spectrum. The molecular ion, as long as it is present, normally appears at the highest value of m/z and provides the molecular weight of the compound. To follow the temporal evolution of the molecules formed under the reaction conditions, it is advisable to use the apparent mass which provides a better signal to noise ratio.

Quadruple analyzer

The quadrupole analyzer consists of four rods with circular or hyperbolic section which are aligned in a parallel orientation. The traveling of the ions along the z-axis of the rods is subjected to the influence of a total electric field. Two opposite rods have an applied potential of (U+Vcos(ωt)) and the other two rods have a potential of -(U+Vcos(ωt)), where U is a dc voltage and Vcos(ωt) is an ac voltage. U and V are variables. The positive ions entering the space between the rods are drawn towards the negative rod. In case that the potential changes sign before it discharges itself on this rod, the direction of the ion will change.

Along the trajectory of the rods (z-axis), the ions maintain their velocity. However, the electric field induces forces which results in acceleration along the x and y axes. The latter axes determine the position of the ion from the center of the rods and subsequently determine if an ion will travel along the trajectory and be detected. The motion of the ions is simply described by Newton's equation. The relationship between the ion coordinates and the time was established by the physicist Matieu and is described in the following:

$$\frac{d^2x}{dt^2} + \frac{e}{m_i r_0^2}(U + V\cos wt)\,x = 0 \qquad (2.18)$$

$$\frac{d^2y}{dt^2} - \frac{e}{m_i r_0^2}(U + V\cos wt)\,y = 0 \qquad (2.19)$$

From the above discussion it can be realized that the quadrupole is used as a filter which can be tuned and controlled by simply varying the amplitudes of the voltages. To obtain the entire mass spectrum, the amplitude of the DC and the RF should be varied while fixing the angular frequency (w). For detection of a desired mass, which is often used for studying chemical reactions, the amplitude of the RF voltage should be varied. The resolution is varied electronically by adjusting the DC to RF ratio. Typically, U will vary from 500 to 2000 V and V from 0 to 3000 V (-3000 to +3000 peak to peak).

Detector

After passing the mass analyzer, the ion beam is transferred to the detector. In our setup, a channeltron electron multiplier detector is used. The working principle of such a detector is based on a continuous dynode. A negative potential of several kilovolts is applied on the first dynode with respect to the positive ion beam. The ion beam hits the first dynode and produces a stream of secondary electrons. The latter electrons are attracted to the second dynode ejecting more electrons in a snowball-like effect. The working principle of channeltron is the same as that of discrete dynode electrons. However, in the channeltron, the discrete dynodes are replaced by a tube containing drilled cylindrical channels, and electrons are bounced along the tube towards its exit. The channels are coated by semiconductor substance which emits electrons. This type of detector allows signal amplification of up to 8 order of magnitudes.

2.2.4 Scanning Tunneling Microscopy

Scanning Tunneling Microscopy (STM) is based on the quantum mechanical effect of tunneling which is used to investigate and image conductive surfaces with atomic resolution. The wave and particle nature of matter in quantum mechanics allows the tunneling of electrons through a barrier with a finite probability. This probability is used to quantify the local properties of the surface while there is no direct contact in between the tip and the sample.

Figure 2.7a shows schematically the general setup for STM imaging. Generally, a bias voltage (Vs) is applied between the sample and the tip with z-piezo. The tunneling current (I_T) and the height (z) produce a feedback loop which is controlled by a data processing unit.

The current of electrons tunneling through the vacuum barrier is caused by applying a bias voltage between an atomically sharp tip and the sample. This current depends on the tip-surface distance as well as the density of states (DOS) of the tip and the sample:

$$I_T(z) \propto U_s \rho_s \exp\left(-2z\frac{\sqrt{2m\phi}}{\hbar}\right) \qquad (2.20)$$

Where U_s is the sample bias, ρ_s is the local density of states, ϕ the work function of the sample, m the mass of the electron, and $\hbar$ the reduced Planck constant.

Owing to this dependence, the change in the tip-sample distance, strongly influences the measured tunneling current. For example, a reduction of tip-sample distance by 1 Å leads to an increase in current by approximately one order of magnitude. The technique is very useful for obtaining general surface morphology. Nevertheless, interpretation related to the geometry of adsorbates on the surface must be considered with further cautions and cannot be directly derived in case of changes in the local electronic structure.
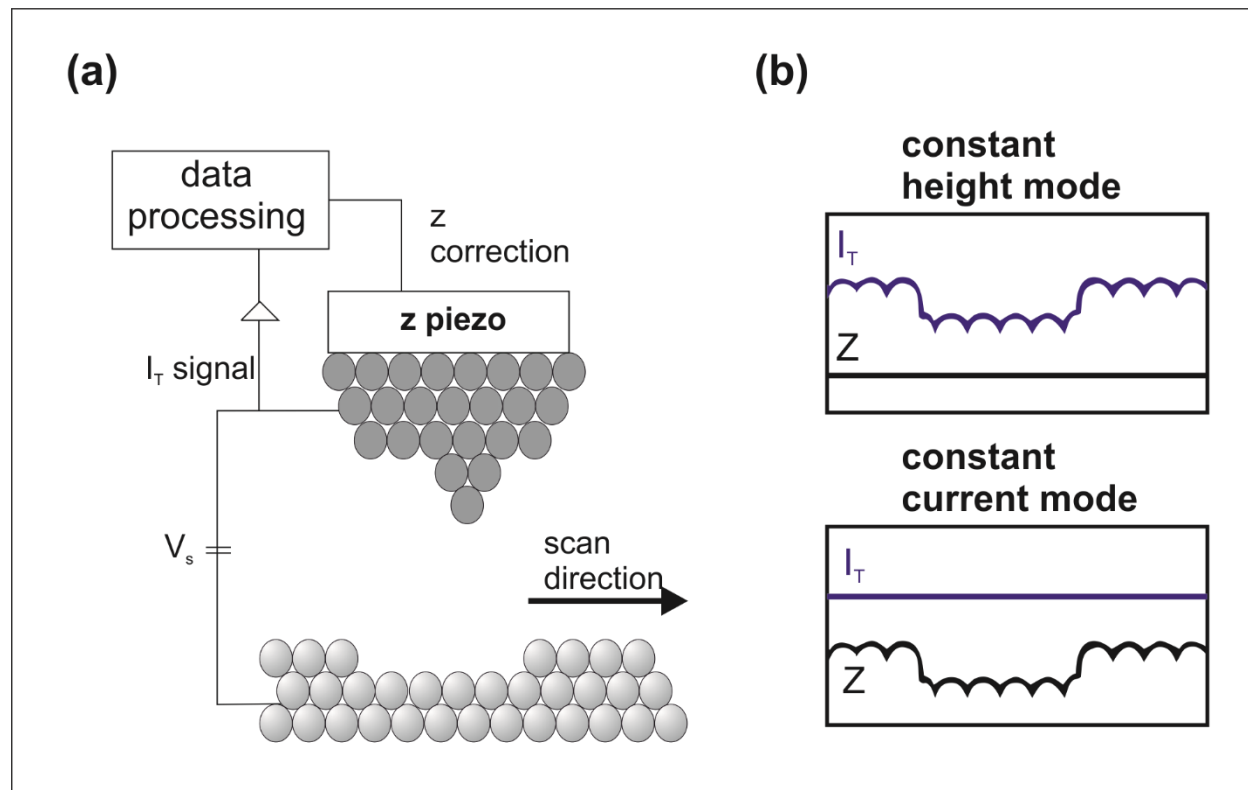
Figure 2.7: (a) General measurement principle for STM imaging and the STM main elements. (b) Corresponding line profiling in constant height (upper) and constant current (lower) modes. I_T represents the tunneling current and Z represents the height.

Two operational modes can be used with STM: (i) constant height mode and (ii) constant current mode. All of the experiments presented in this thesis were operated in constant current mode. Here, the two modes of operation are described briefly. Further details can be found elsewhere (for instance [90-92]).

Schematic representation of the two modes is shown in Figure 2.7b. In the first mode (upper panel, Fig. 2.7b), the tip is held at a fixed height over the surface whereas the change of the tunneling current is measured. In this mode, a quick scanning speed can be obtained. However, the tip and the sample – if the surface is not flat – can collide with each other as no feedback loop is applied. Practically, the applied bias voltage can be varied to change the sample-tip height and the change in the tunneling current is measured. This mode allows a local investigation of the electronic structure. In the second mode (lower panel, Figure 2.7b), the tunneling current is kept constant while scanning the tip over the surface and varying the tip-sample distance accordingly. This is done by a feedback mechanism, and thus prevents that the tip will touch the surface or the adsorbates. To ensure the quick response of the feedback loop, the scanning speed is relatively slower compared to the constant height mode. Note that the experimental quantity measured in the constant-current mode is the corrugation of the tip and not the tunneling current. The corrugation amplitude is defined as the difference between the largest and smallest tip-sample distance in a constant current experiment. Since there is an exponential dependence of the tunneling current on the tip-sample distance, this type of setup allows a high resolution with respect to the surface normal. As long as the experimental setup is sufficiently stable, e.g. having a sharp stable tip, one can reach atomic resolution for imaging ad-atoms and surface defects. Yet, the interpretation is often not so easy.

Chapter 3

Setup of a new molecular beam/IRAS UHV apparatus[¥]

In the course of this thesis project, a new UHV apparatus was planned and constructed. This chapter describes the experimental setup and the calibration and alignment procedures employed in this study. The equipment used for sample preparation and characterization is also presented. It provides an overview of the UHV chambers, and illustrates the application of molecular beam techniques and surface spectroscopy for studying the reactivity of hydrocarbon compounds by employing ligand-functionalized model catalysts. Note that our group combines experimental approaches for detailed characterization of the adsorbed ligands both with respect to their chemical nature as well as their spatial distribution on the surface. Thus, an additional apparatus containing STM was constructed. The design and arrangement of the STM apparatus is described briefly in Appendix I

3.1 Considerations and special requirements

We have specifically designed an apparatus that allows to prepare and characterize ligand-modified model catalysts under well-defined UHV conditions, and address the mechanisms, kinetics and dynamics of reactive surface processes across a broad range of pressure conditions, from UHV up to the near ambient pressure.

The specific requirements for such experiments may be summarized as follows:

1. *Sample preparation and characterization.* The preparation of model catalysts demands for a particular ability to deposit several metals for preparing different metal oxides and/or metal nanoparticles, as well as the ability to modify the surface by deposition of liquid or solid organic modifiers. To achieve that, the tools for preparation and characterization of a variety of model catalysts have to be integrated. Hence, in situ transferring of the sample from the

---

[¥] The following chapter is based on a manuscript published in the Journal *Review of Scientific Instruments*, reference 93.   Attia, S.; Spadafora, E. J.; Hartmann, J.; Freund, H.-J.; Schauermann, S. Molecular beam/infrared reflection-absorption spectroscopy apparatus for probing heterogeneously catalyzed reactions on functionalized and nanostructured model surfaces. *Rev.Sci Instrum.* 2019, 90 (5), 053903. The figures presented in this chapter are adapted or reprinted from reference [93], with the permission of AIP publishing.

preparation chamber into the reaction chamber under UHV conditions is imperative in order to correlate the kinetic and dynamic information with the structural features of the catalysts under the same, well-defined, conditions.

2. The *molecular beam source* should allow for fast variation of reactant fluxes over the widest possible range, and moreover, on a time scale of several milliseconds. This is essential for capturing transient kinetics which allows in turn for an accurate identification of the most relevant elementary reaction steps. The molecular beam must also be well-collimated and pulsed with a variable modulation frequency. Great care should be taken however to produce the pulsed molecular beam with only low intensity vibrations in the UHV chamber, because the infrared spectrometer and the Mercury-Cadmium-Telluride (MCT) detector are highly sensitive to mechanical vibrations. For reactivity and selectivity experiments, which require exposure to several reactants, it is necessary to integrate more than one beam source in order to avoid exposure from the background. The beam should also be suitable for using a wide choice of gases: both having high vapor pressure, e.g. CO and propylene oxide, or such comprising large molecules with low vapor pressures ($<10^{-2}$ mbar), typically used as surface modifiers.

3. *Surface species detection. In situ* detection and monitoring of different co-adsorbed surface species is a key requirement for establishing the correlations between the catalytic performance of the surface and its chemical and structural composition. In IRAS studies, the chemical nature of the adsorbates, as well as their orientation relative to the surface, can be determined. The latter can be deduced based on the metal surface selection rule[80]: vibrational modes exhibiting dynamic dipole moment parallel to the metal surface are invisible to IRAS, which in many cases allows for deducing the relative orientation of the various bonds with respect to the metal surface. Of particular importance is the possibility to explore variations in adsorption geometry with changing environment, such as adsorption of a second reactant (e.g. hydrogen), which may strongly affect the binding of organic molecules - both reactants and modifier-ligands or growing modifier-ligand coverage, etc. The experimental setup should be such that ensures chemical resolution as well as short acquisition time for chemical identification of the adsorbates, and *in situ* monitoring of the transformations occurring on the surfaces under the reaction conditions.

4. *In situ* calibration techniques for determining the absolute values of beam fluxes and its distribution must include a beam monitor for measuring the absolute reactant flux and beam profile. It should be possible to locate the beam monitor at position identical to that of the sample with respect to the molecular beams, in order to perform calibration and adjustment of the beam position.

5. *Gas phase detection in UHV*. The detection of gas phase must account integrally for both sticking and reaction probabilities. The detector should also provide temporal resolution in the microsecond to second range, typical of the reaction or scattering time scales.

6. *Gas phase detection in ambient pressure conditions*. To explore the catalytic performance under ambient pressure conditions, a dedicated Ambient Pressure Cell (APC) should be employed, such that it is separated from the preparation and measurement UHV chambers and can be run as an independent UHV system. Detecting the gas phase in the APC requires suitable detection methods that are compatible with ambient pressure conditions. Gas Chromatography (GC) is the method of choice which allows for a monitoring of the reactants and reaction products, with further capability of distinguishing between different chemical species of identical molecular masses (e.g. regio- or enantiomers), which are otherwise difficult to differentiate. The transfer system should also enable *in situ* transfer of the sample prepared under UHV from the preparation to the APC chamber without breaking the vacuum, in order to avoid exposure to air that might destroy or alter the catalyst surface.

Altogether, the UHV setup comprises molecular beam techniques, *in situ* surface spectroscopy, an ambient pressure cell, chamber for deposition of liquid and solid organic compounds and a portable transfer system. Such a setup allows to study surface reactions across a broad range of ligand-functionalized and nanostructured model catalytic systems prepared *in situ* under UHV conditions. In the following section the arrangement of such multi-molecular beam/surface spectroscopy apparatus is presented in detail. Additionally, to test the performance of the new apparatus against an already studied metal-ligand reference system, the adsorption behavior of one of the most efficient and well-studied chiral modifiers,[38] (R)-(+)-1-(1-naphtylethylamine) (NEA) adsorbed on Pt(111), was investigated. As a second independent check, acetophenone adsorption on Pt(111) was also studied in a broad range of temperature conditions. A short discussion regarding the key observations obtained for the above adsorption systems, is given in section 3.8

3.2 Overview

The key components of the new setup are schematically displayed in Fig. 3.1. The experimental setup, consisting of three major parts, namely a preparation chamber, a reaction chamber and APC, operates as a whole under UHV conditions. All parts are interconnected such that samples can be transferred *in situ* between the individual chambers with the aid of a specially designed integrated transfer system. The preparation chamber, the reaction chamber and APC are designed as three independent UHV systems. As already mentioned, the division of the apparatus into three separate UHV systems was necessary because of the complexity of the preparation procedures of supported model systems, requiring different preparation and characterization techniques, as well as due to spatial limitations that result from the necessity of incorporating simultaneously an infrared beam and three molecular beams on the sample surface.

The *preparation chamber* enables preparation and characterization of different types of catalytic surfaces by means of standard surface science tools. These samples range from single crystals to more complex nanostructured systems consisting of metallic nanoparticles supported on well-defined single crystalline thin oxide films, epitaxially grown on single crystalline metal supports.[14] For the latter class of surfaces, the size and the density of the metallic nanoparticles can be broadly varied by tuning the preparation conditions, such as metal flux, deposition time and temperature, as well as number of surface defects acting as nucleation centers for the growth of metallic nanoparticles. The quality and the structural properties of the thus prepared surfaces can be evaluated by standard surface characterization techniques available in the preparation chamber, including Low Energy Electron Diffraction (LEED), Auger Electron Spectroscopy (AES) and Temperature Programmed Desorption (TPD). Additionally, adsorption of small molecules, such as CO, can be employed in combination with IRAS (implemented in the *reaction chamber*, see below), to further address the structural and adsorption properties of the model systems.

The preparation chamber is connected to a small dedicated *deposition chamber*, in which liquid or solid organic compounds can be deposited by physical vapor deposition on the model catalyst surface. This procedure allows also for tuning the coverage and ligands distribution, which may be achieved by systematically varying the deposition parameters such as the molecular flux and deposition temperature. By that, formation of the intermolecular assemblies on the surface may be possibly affected, which may lead in turn to further valuable insights. It is possible to

incorporate in the *reaction chamber* three molecular beams (two effusive and one supersonic molecular beams) and *in situ* IRAS; a design which allows to study the reaction mechanisms, kinetics and dynamics of surface reactions on complex nanostructured model catalysts under UHV conditions. The evolution of the reaction products in the gas phase is monitored by a differentially pumped QMS, while simultaneous *in situ* monitoring of adsorbed surface species (reactants, ligand modifiers, reaction intermediates and products) evolving under the reaction conditions can be performed by means of vacuum Fourier Transform IRAS (FT-IRAS). An APC, connected to the UHV chamber, provides an experimental possibility for complementary reactivity studies on the same well-defined model surfaces under ambient pressure conditions, by utilizing sensitive gas phase detection via GC. Sample transfer between the different chambers is realized by a combination of two manipulators and two magnetic transfer rods.
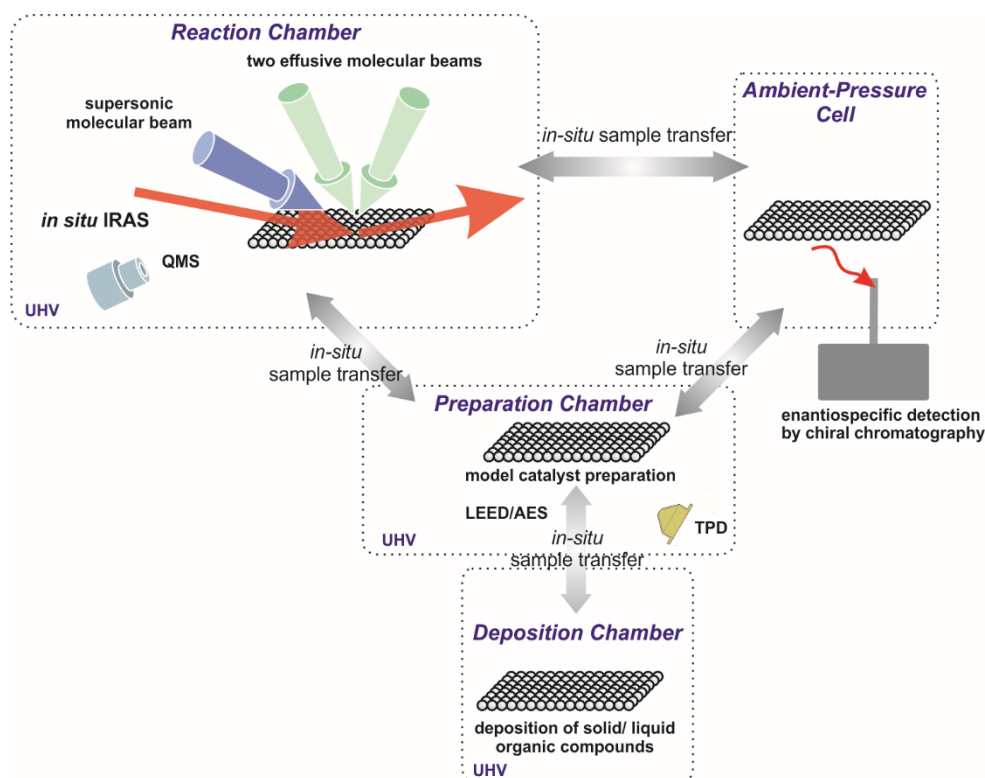
Figure 3.1: Schematic drawing of the main components of the experimental setup. The apparatus consists of preparation and reaction chambers, with the latter being equipped with two effusive and one supersonic molecular beams, IRAS, QMS, as well as an APC equipped with a GC for the gas phase detection of reaction products under ambient pressure conditions. The sample can be transferred *in situ* between all compartments of the apparatus. Adapted from [93], with the permission of AIP publishing.

3.3 Reaction chamber

After sample preparation, the sample is transferred *in situ* to the reaction chamber without breaking the ultra-high vacuum. The 300 mm inner diameter reaction chamber is designed for simultaneous IRAS, reactivity and sticking probability measurements. Figure 3.2 illustrates schematically the experimental arrangement of the reaction chamber. The exact incidence and detection angles of the main compartments are given in the inset of Fig. 3.2

Component	Incidence and detection angle [°] θ	α
(1) Effusive source 1	+35	-27
(2) Effusive source 2	+35	+27
(3) Supersonic source	0	+35
(4) IRin/out	0	+83/-83
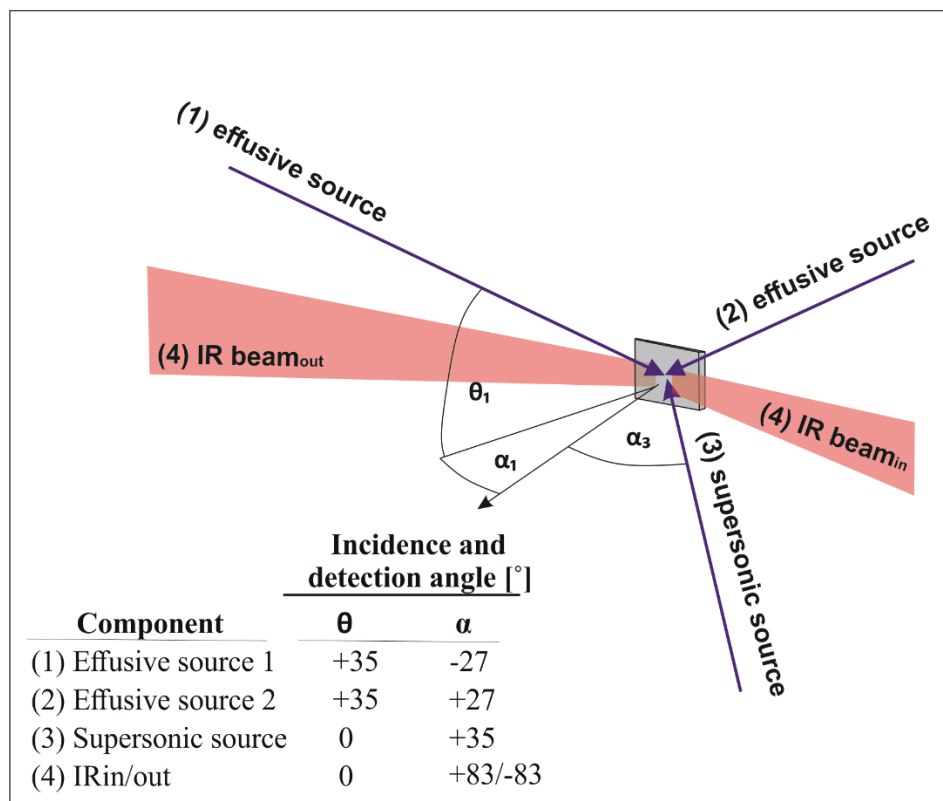
Figure 3.2: Schematic representation of the orientation of the molecular and infrared beams relative to the sample surface. Beam and detector geometries are given in the inset table. All angles are given with respect to the surface normal. Adapted from [93], with the permission of AIP publishing.

A 3D visual of the reaction chamber is given in Fig. 3.3. This chamber includes molecular beams: two high-flux effusive (Fig. 3.3 (1) and (2)), and one supersonic (3) molecular beams. Gas phase detection is performed by means of highly sensitive triple-filter QMS ((4), Hiden, Hal/3F 301 PIC (model type 553201). The QMS is additionally equipped with a differential pumping stage

(pumped by a TMP Leybold, Turbovac SL-80), and a gold-plated shutter (5), acting as a shield that avoids the QMS from detecting gaseous species that are directly scattered from the sample surface to the ionization cage of the mass spectrometer. A gold-coated shutter (Fig. 3.3 (6)) driven by UHV stepper motor ((7), AML, D35.1) can be placed in front of the sample for performing sticking coefficient measurements. IRAS experiments are performed by means of vacuum FT-IR spectrometer which has been modified to meet the special requirements of the beam experiment (Bruker, Vertex 80v, for further details see Fig. 3.7a (24)-(26)). It includes an external UHV adaptation chamber (Fig. 3.7a (25), Bruker, W109/UHV Vertex v80v) and a detector chamber (Fig. 3.7a (26)). The spectrometer (Fig. 3.7a (24)) is equipped with an internal detector- Deuterated L-alanine Doped Triglycerine Sulfate (DLa-TGS), Bruker, D301/B, which is accommodated inside the spectrometer compartment and is used as an internal reference for qualitative and quantitative sampling of the IR transmission signals in the spectrometry mode of operation. The spectrometer is pumped by a scroll pump (EDWARDS, nXDS10i), providing a < 1 mbar typical base pressure in the spectrometer chamber.

The original circular apertures in the IR spectrometer were replaced by 1.2×6 and 0.7×4 mm^2 rectangular aperture slits in order to adjust the beam profile at the sample position to the required geometry, namely one that fits the rectangular shape of the sample. Once the IR beam leaves the spectrometer, it enters the external chamber (Fig. 3.7a (25)) where it is focused onto the sample surface by a 250 mm focal length parabolic mirror, resulting in an incidence angle of 7° with respect to the sample surface plane. To improve the signal-to-noise ratio, only p-polarized component of the IR beam produced by the MIR p-polarizer (Bruker, F351) is used in the measurements. The reflected beam enters the detector chamber (Fig 3.7a (26)) where it is focused by an ellipsoid mirror of a 250 mm focal length onto a liquid-nitrogen (LN$_2$) cooled MCT detector. The detector chamber is pumped by a pumping station (Pfeiffer, HiCube 80 Eco with a backing diaphragm pump MVP-15-4) to minimize contribution of water ice that may irreversibly accumulate on the cooled MCT detector and introduce large perturbations to the measurements. The typical base pressure in the detector chamber is $5 \cdot 10^{-5}$ mbar. The reaction chamber is separated from the IR spectrometer and detector chambers by KBr windows (Fig. 3.3 (8) and (9)) and is sealed by Viton gaskets (Fig. 3.3 (10)). The spectrometer vacuum flanges, enclosing the UHV flanges of the reaction chamber (Fig. 3.3 (11)), act as a differential pumping stage. The reaction chamber is connected to the detector chamber and the external chamber of the

spectrometer via two Viton O-rings sealed flexible bellows (Fig. 3.7a (27), (28)). Both the spectrometer and the detector chambers are mounted on a stable movable Al-platform (Rose+Krieger) equipped with a xyz translator that enables quick removal and precise reconnection of the spectrometer and the detector.

Determining the sample-center position, i.e. spatial calibration of all four sample coordinates (x,y,z,θ), is achieved by specially designed adjustment pins (Fig. 3.3 (12)), for more details see section 3.4.1), and measurement of the distribution and absolute molecular flux of gaseous species, is performed by means of molecular beam monitor (Fig. 3.3 (13), for details see section 3.4.2).
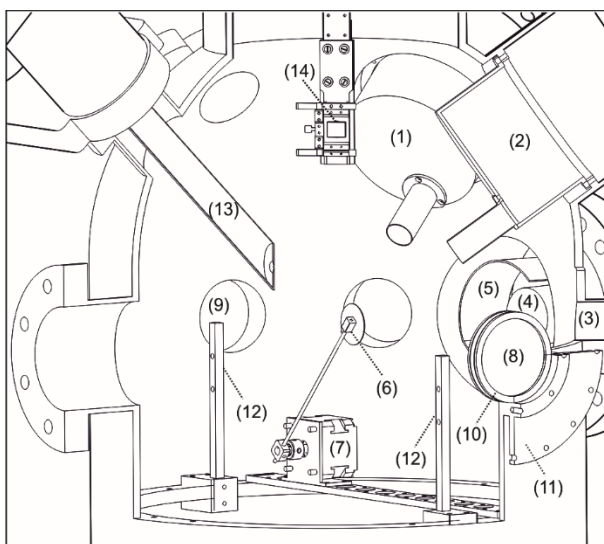
Figure 3.3: Schematic drawing of the reaction chamber: (1), (2) effusive sources no. 1 and 2 respectively, (3) flange for supersonic beam source, (4) quadrupole mass spectrometer, (5) Au coated shutter for QMS, (6) Au plate sample shutter, (7) stepper motor, (8), (9) KBr windows for IRAS assembly, (10) Viton gasket, (11) flange for bellow assembly (12) center-position alignment pins, (13) beam monitor, (14) movable sample plate and sample holder. Reprinted from [93], with the permission of AIP publishing.

3.3.1 Effusive beams

The reaction chamber contains two effusive molecular beams that are designed to provide well-defined, stable and homogeneous flux of gaseous molecules, and to allow fast and variable modulation of the beam flux on a time scale of a few hundreds of milliseconds. The most important requirement regarding the molecular beams in this setup, is their compact size, which allows to incorporate in one reaction chamber all required components, two effusive beams, one supersonic molecular beam, and the infrared setup.

Fig. 3.4a depicts the cross section of the effusive molecular beams, and Figs. 3.4b-d are actual photographs of the setup. The setup of the effusive molecular beam includes two DN 100 CF-F chambers which compose two differential pumping stages separated by a 15 mm circular aperture (1). The two differential stages, the first ((2)-inner pumping stage) and the second ((3)-outer pumping stage), are pumped, each, by a 260 l/s TMP (Pfeiffer, HiPace 300), mounted at flanges no. (4), and no. (5) respectively. The second pumping stage is constructed as an integral part of the reaction chamber (6); its role is to reduce the pumping speed and to minimize the distance to the exit beam orifice (not shown, see Fig. 3.3 (1) and (2)). The pressure of both differential stages is monitored by cold cathode pressure gauges ((7), Pfeiffer, IKR 361). Effusive expansion is produced by employing a Glass Capillary Array (GCA, (8), Collimated Holes Inc., holes size 50 µm, holes density $2 \cdot 10^6$ holes/cm^2, 1 mm thickness) which is mounted on the source tube and sealed by Teflon gaskets (9), and is connected via a stainless-steel hose to the gas inlet flange (10). The source tube is fixed to the inner walls of the first pumping stage via clamps (11), such that the centers of the GCA and of the aperture share a common axis. The distance of the GCA to the sample position can be adjusted by varying the position of the GCA in the tube. The GCAs of source 1 and 2 are positioned at 378 and 368 mm away from the sample surface respectively. The inner pumping stage is mounted on a flexible bellow (12) and can be adjusted by two orthogonally aligned translator-screws (13) operated by translation feedthroughs (14) which are used for beam alignment. After exiting the inner pumping stage through the 15 mm aperture, the molecular beam enters the outer pumping stage, where it can be interrupted or opened by means of a shutter (15). The beam shutter is a rectangular sheet of Al metal plate, driven by a UHV-compatible stepper motor ((16), AML, D35.1). The shutter is fully remote controlled (using LABVIEW software) and allows arbitrary opening times of at least 150 ms.

Finally, the GCAs typically require backing pressures of 0.001-1 mbar. Two gas lines which are part of a dedicated manifold gas system are connected to the tubes that deliver gas to the GCAs and can be evacuated through a TMP (Pfeiffer, HiPace 80) or a scroll pump (EDWARDS, nXDS10i). Each of the lines is provided with an electro pneumatic angle valve (novotek, 706142) allowing for fast switching of the gas (pure or mixture) used to generate the molecular beam. The pressure in the gas line is measured by a capacitance manometer (MKS Baratron 627D with readable pressure range of $5 \cdot 10^{-4}$ to 1 mbar) and is regulated and stabilized by a flow control valve (MKS 248 A) equipped with a PID pressure controller (MKS Type 250).
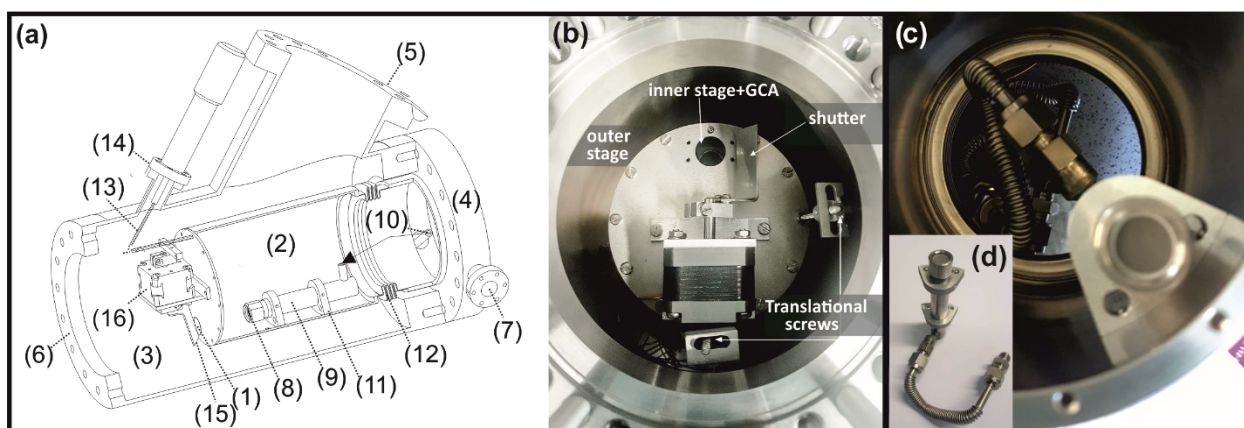
Figure 3.4: (a) Effusive beam source. For clarity, cross sections of the outer and the inner stage show only the back half of the source. The actual setup contains an additional translational screw and feedthrough, and a flange for pressure measurement of the inner stage. The labeled components are: (1) beam inner aperture, (2) inner pumping stage, (3) flange for TMP of the inner pumping stage, (4) outer pumping stage, (5) flange for TMP of the outer pumping stage, (6) flange connected to the reaction chamber, (7) pressure measurement, (8) GCA, (9) source tube, (10) gas inlet, (11) clamps for GCA assembly, (12) flexible bellow, (13) translational screw, (14) translational feedthrough, (15) shutter, (16) stepper motor. (b) Top view photograph of the effusive source (c) A photograph of the inner pumping stage with the GCA assembly (d) GCA assembly and the source tube. Adapted from [93], with the permission of AIP publishing.

3.3.2 Supersonic beam

Figure 3.5 shows a 3D scheme of the supersonic source. The source is an independent UHV system, separated from the reaction chamber via a gate valve ((1), see also Fig. 3.7a (28)). The source consists of an expansion chamber, which is pumped by a 2100 l/s turbo molecular pump ((2), Leybold, MAG integra), and two differential pumping stages pumped by 590 l/s and 65 l/s turbo molecular pumps ((3), (4) Leybold, MAG w 700, TURBOVAC 80 H). For backing, a rotary vane pump (25 l/s, Leybold, SOGEVAC® SV28 BI) is utilized. The supersonic expansion is generated from a solenoid type pulsed valve with a 100 µm orifice diameter ((5), Parker, General Valves Series 9). The pulsed source is driven by a controller allowing a minimum pulse width of approximately 150 µs. The pulse valve is mounted on a xyz- translator ((6), travel length 50 mm, MDC, EPSM-1502) allowing both vertical and horizontal alignment of the propagating jet with respect to the molecular beam axis as defined by the skimmer. From the expansion, a molecular beam is extracted by means of a 0.7 mm diameter Nickel skimmer ((7), Beam Dynamics, Inc). In the second differential pumping stage, the beam can be modulated by means of a beam shutter (8) and a mechanical chopper (9). The beam shutter is driven by a UHV compatible high-torque stepper motor (Oriental Motor, PKP268MD28B). The chopper wheel is machined from a 150 mm diameter Al disk and is mounted on a translation stage operated from the atmospheric side ((10), VAb, ML 16-50). The chopper wheel is driven by a 400 Hz ac synchronous motor ((11), Globe motors, 75A1008-2), which is controlled by an ac frequency transformer. The motor assembly is clamped into a water-cooled Cu bronze block which keeps constant temperature operation conditions (12). The chopper can be modulated with varying duty cycles for delivering 5%, 20% or 50% of the original beam flux.

For reducing pulse width and improving pulse shape in pulsed valve operation, the rotating wheel chopper can be synchronized with the solenoid valve. This is done by dividing the synchronization signal by a 1/N counter to meet the desired pulsing frequency and externally triggering the valve controller following a delay time which is chosen such that a suitable portion of the pulse is cut out by the chopper wheel. In the current design, the chopper to sample distance is 637 mm. Before hitting the sample surface, the beam passes through a square aperture, which determines the beam shape at the sample position. Its location is chosen in between the second and third differential pumping stages for reducing the gas load in the third pumping stage. Three

different square apertures, of 2.5, 3.5, and 4.5 mm side lengths, on a Cu bronze blade (13), may be chosen. Aperture positions are adjusted from the air side by moving the blade via a linear translator ((14), VAB, ML 16-50). The 35° incidence angle imposes a rectangular beam profile of a 1.2 axial ratio. The beam size can be chosen on demand, to be smaller, equal or larger than the sample size.

Finally, for generating the supersonic expansion, typical pressures of 1200-5000 mbar are delivered to the pulse solenoid valve through a 6 mm tube (15). The tube is connected to the manifold gas system and pressure readings are acquired by an absolute capacitance manometer (10000 mbar, MKS, 722B14MFE2FA).
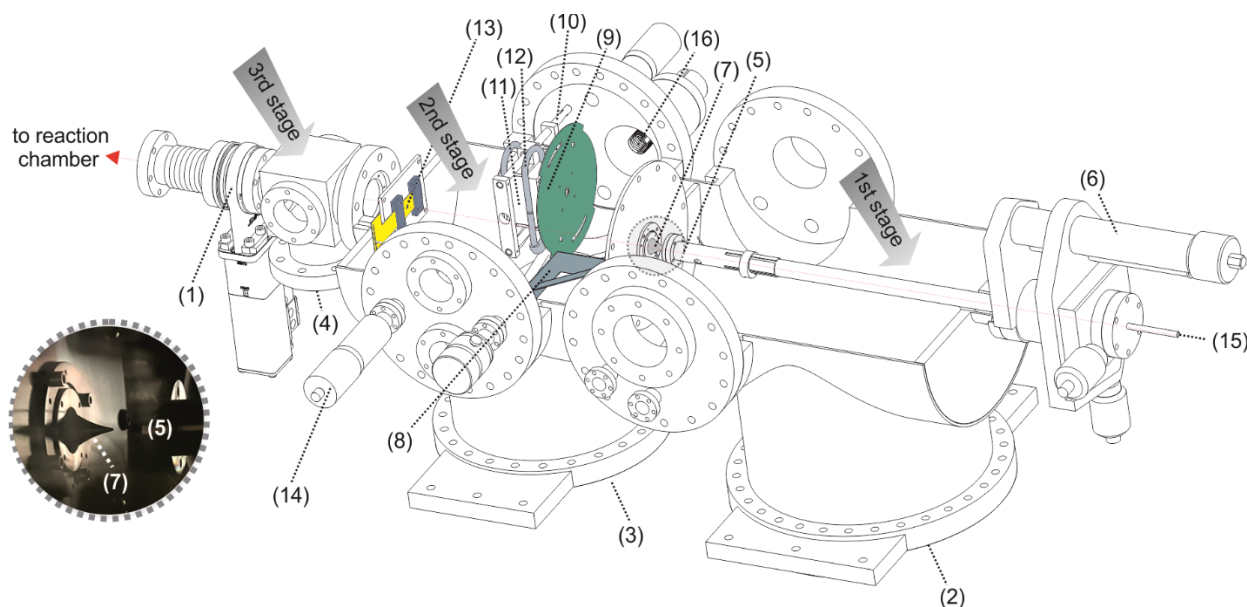
Figure 3.5: Supersonic beam source. The labeled components are: (1) gate valve, (2)-(4) flanges for TMPs, (5) pulse solenoid valve assembly, (6) XYZ-translational stage of the supersonic jet, (7) skimmer, (8) shutter, (9) chopper, (10) chopper translational stage, (11) chopper motor, (12) chopper cooling housing, (13) apertures, (14) aperture translational stage, (15) gas inlet, (16) pressure gauge. Encircled: photograph of the labeled components nos. (5) and (7). Adapted from [93], with the permission of AIP publishing.

3.4 Adjustment tools and calibration procedures

To enable simultaneous kinetic and spectroscopic measurements, the infrared and all molecular beams should intersect at the same spatial point on the sample surface. This is achieved by installing two adjustment and calibration tools: *(i)* adjustment pins for determining both the sample center and the molecular beam monitor positions, and *(ii)* molecular beam monitor for adjusting the positions of the molecular beams and for the determination of their spatial distribution and molecular flux.

3.4.1 Sample position adjustment tools

To adjust the sample position inside the reaction chamber, four cuboid metal-pins were introduced on a narrow ring welded to the chamber along its internal perimeter. In front of each pin, a viewport is installed. The combination of these pins allows to build two optical axes with a 45° relative alignment, which intersect at the center of the chamber and allow for calibration of all four coordinates of the sample in space, including the x,y,z positions as well as the angle with respect to the position of the infrared beam. One pair of the pins, which constitutes an optical axis parallel to the surface plane of the sample, is shown in Fig. 3.3 (12).

The relative positions of the IR spectrometer and detector, with respect to each other and to the reaction chamber, are determined by a support frame, at which both parts of the spectrometer are installed. The spectrometer and the detector chambers are connected to the chamber via Viton O-rings sealed flexible bellows. Tuning the position of the infrared beam is performed by adjusting the mirrors of the spectrometer to maximize the signal reflected from the sample, which is installed at the center position of the reaction chamber. Rough primary alignment can be achieved by using visible light, while the final fine adjustment of the mirror positions is performed by employing an infrared source.

3.4.2 Adjusting the molecular beams and molecular flux

Molecular beam monitor

A molecular beam monitor is employed for two purposes: (1) directing the three molecular beams to the correct spatial position, ensuring they all intersect at the sample center; (2) determining the absolute molecular flux and the beam profile, which contain the information regarding the spatial distribution of gaseous species entering the reaction chamber.

The molecular beam monitor used in this work (Fig. 3.3 (13)) is an accumulation sensor which is, in fact, an adaption of a previously described beam monitor.[72] It contains a high accuracy ion gauge (Granville-Phillips, 370 Stabil-Ion) mounted to a 490 mm long / 14 mm diameter stainless steel tube. At its front end, the tube is provided with an orifice in the form of a stainless-steel plate having a 1 mm diameter central hole. The orifice directs the incoming gas such that it expands into the central inner space of the tube. The pressure rise upon the expansion process, monitored by the pressure gauge, is in fact a measure of the absolute flux of the molecular beam as hereby described. The whole assembly is mounted on a manipulator with three translational degrees of freedom (travel length 50 mm, MDC, EPSM-1502) that allows to bring the molecular beam monitor – or more specifically, the orifice – into exactly the same position. By that, the working position of the beam monitor is determined, at which the incoming molecular beam enters the orifice of the beam monitor in 45° with respect to the orifice plane. Once the working position is calibrated (in the same way as it is done for the sample position (see section 3.4.1), it is possible, by moving the molecular beam monitor in space, to measure the distribution of the beam intensity at different points within the chamber, from which the beam profile can be extracted. Vice versa, by measuring the beam profile, the current position of the molecular beam in space can be determined. In order to adjust the beam position at the chamber's center point at which the sample is located, and to reach homogeneous distribution of the gaseous species over the sample, the inner pumping state of the effusive beams (Fig. 3.4a (2)), including the glass capillary array (Fig. 3.4a (8)), can be moved with respect to the outermost beam aperture (Fig. 3.3 (1) and (2)), by using two orthogonally arranged translational screws (Fig. 3.4b) operated via translational feedthroughs (Fig. 3.4a (13) and (14)).

In case of the supersonic molecular beam, the adjustment procedure involves initially the adjustment of the position of the pulsed source from the skimmer along the beam line. The precise

distance is not a crucial parameter, however it must be far enough to ensure the transition to a molecular flow at the skimmer front, as well as the reduction of perturbing effects such as backscattering from the skimmer.[94] While the skimmer is fixed at the exit of the first pumping stage (Fig. 3.5 (7)), the pulsed source is movable; its assembly is mounted on a manipulator having three translational degrees of freedom allowing to set the position of the pulsed source along the beam within the desired precision. The horizontal and vertical alignments of the pulse valve are optimized by maximizing in situ the detected beam intensity by using the beam monitor. To direct the beam to the center point of the chamber, the beam monitor is placed at the center in the same way as done for positioning the sample. The supersonic beam setup is positioned on movable support frame, and a flexible bellow links it to the reaction chamber. Its position relative to the center can be maneuvered by four translational screws. Lastly, a fine adjustment is performed to set the position of the beam apertures located at the exit of the second pumping stage with respect to the center position (Fig. 3.5 (13)). For this, the frame carrying the aperture plate, can be linearly moved inside the molecular beam by using a linear translational feedthrough connected to the frame (Fig. 3.5 (14)).

Altogether, an optimal adjustment of all three molecular beams should result in a homogeneous and symmetric distribution of the gaseous species at the sample position.

The molecular beam entering the aperture causes a pressure rise inside the detector volume. Following equilibration of the incoming/outgoing effusive flux to/from the detector volume, the pressure attains a constant value that can be used to evaluate the absolute beam flux by applying the following relation:[69]

$$Flux = \frac{dN_{out}}{Adt} = \frac{p}{\sqrt{2\pi M k_B T}} \qquad (3.1)$$

with N*out*, the number of molecules traveling through the beam monitor aperture with cross sectional area A, p is the pressure rise in the detector volume, M, the molecular mass, k_b, the Boltzmann constant, and T, the temperature of the test gas. The high stability pressure gauge has an accuracy of 4% and a repeatability of 3%. The typical background pressure in the detector is about 2×10^{-8} mbar, from which a minimum detectable pressure rise of $\sim 8 \times 10^{-10}$ mbar may be estimated. Such a pressure rise, in case of Ar, corresponds to a flux resolution of about 2×10^{11} molecules $cm^{-2}s^{-1}$.

3.5 Sample preparation and organic molecules deposition chambers

Figure 3.6 and Figure 3.7a are draws of the side and top views of the apparatus. For the clarity of discussion, they are presented as cross sections through different planes of the apparatus, hence not all the parts of the apparatus are visualized. The components described in this section are labeled in a numerical order, and are indicated also in the captions of Figs. 3.6 and 3.7a. Both side and top view drawings include the preparation ((1) in Figs. 3.6 and 3.7a) and reaction ((2) in Figs. 3.6 and 3.7a) chambers. The chambers are independent UHV systems, separated by a gate valve ((3) in Figs. 3.6 and 3.7a, VAT, 10836-CE01) and are pumped, each, by a 560 l/s turbo molecular pump (TMP, Fig. 3.6 (4), Leybold, Turbovac 600 C). The TMPs are equipped with magnetic suspension, which reduces vibrations that might potentially interfere with the IR measurements. Typical base pressures in both chambers are $2 \cdot 10^{-10}$ mbar. Two manipulators (preparation chamber- manipulator I, Fig. 3.6 (5), VAB, PM 12-600, and reaction chamber- manipulator II, Fig. 3.6 (6), VAB, PM 12-200 SZ2), having one rotational and three translational degrees of freedom, are placed in the center of each chamber. The former (manipulator I, Fig. 3.6 (5)) is of a 600 mm travel length, and the latter (manipulator II, Fig. 3.6 (6)) is of a 200 mm travel length and it is also equipped with a translational stepper motor for manipulating the sample along the z-direction. In combined, the two manipulators and the magnetic translational rod ((7) in Figs. 3.6 and 3.7a), VAB, MDS 40-1200) provide a capability for transferring the sample between the preparation and reaction chambers. The large travel length of manipulator I (Fig. 3.6 (5)) allows the transfer of the sample to the deposition chamber, inside which organic compounds may be deposited on the sample in either liquid or solid phase (Fig. 3.6 (8)).
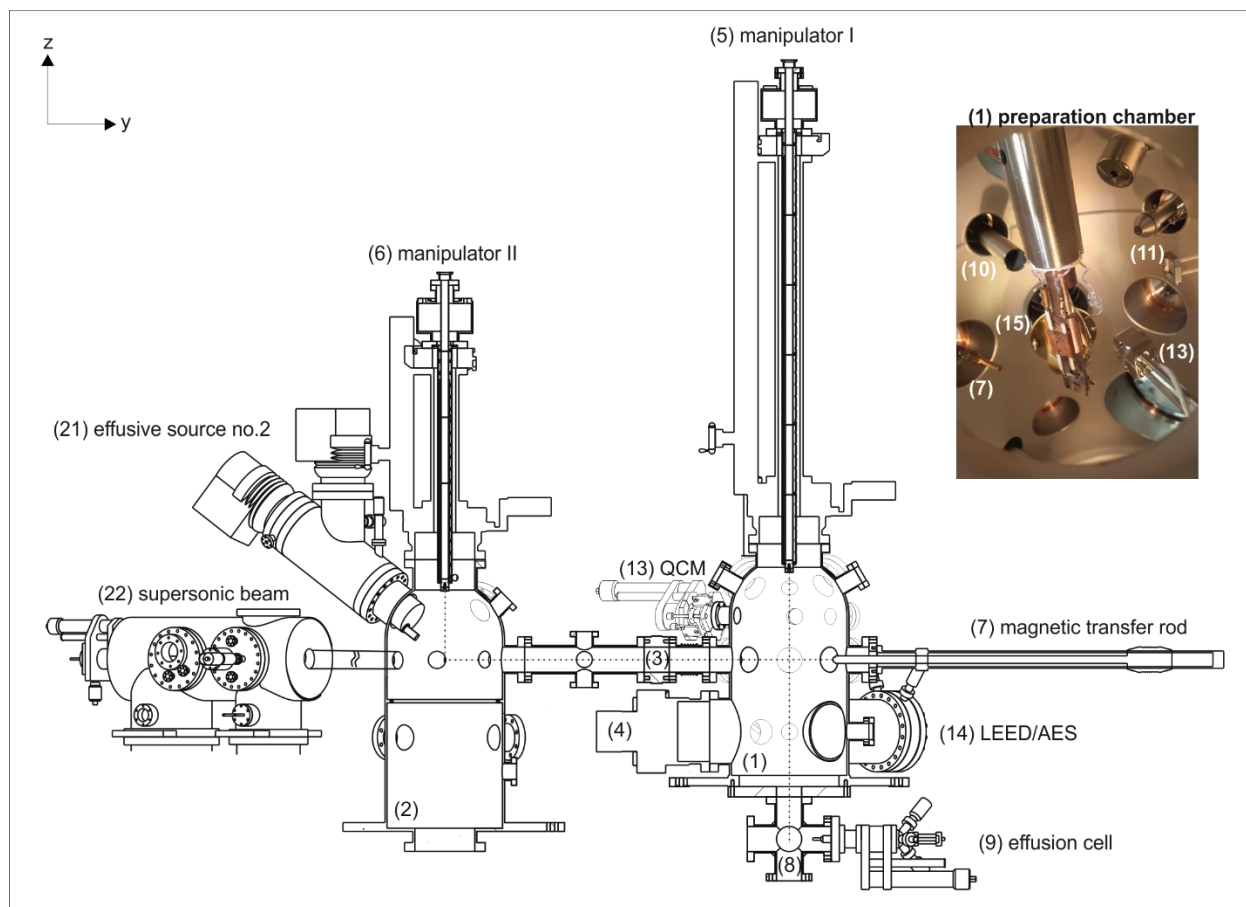
Figure 3.6: Side (y,z) cross sectional view of the experimental setup. The section is along the plane of the transfer rod and manipulators, and only the back half of the chambers is shown. The labeled components are: (1) preparation chamber, (2) reaction chamber, (3) gate valve, (4) turbomolecular pump of the preparation chamber, (5) sample manipulator I, (6) sample manipulator II, (7) magnetic transfer rod, (8) deposition chamber, (9) effusion cell for deposition of organic molecules, (10) gas doser, (11) metal evaporator, (13) quartz crystal microbalance (QCM), (14) LEED/AES, (15) QMS in the preparation chamber, (21) effusive source no. 2, (22) supersonic source. The inset shows a photograph of the preparation chamber assembly. Adapted from [93], with the permission of AIP publishing.

The assembly of the preparation chamber (Fig. 3.6 (1)) is divided into two parts. The upper part of the chamber contains all standard facilities for preparing complex nanostructured model catalysts, including an ion gun (SPECS, IQE 11/35), gas doser (Fig. 3.7a (10)), two metal

evaporators (Fig. 3.7a (11) and (12), Omicron, EFM3-EVC 300) and quartz crystal microbalance (QCM) for calibration of the metal fluxes ((13) in Figs. 3.6 and 3.7a, tectra, QMB-im-mod). The lower part of the preparation chamber contains structural characterization tools, including LEED/AES ((14) in Figs. 3.6 and 3.7a, SPECS, ErLEED 150 4-grids) and QMS (Fig. 3.7a (15), Hiden, Hal/3F 301 PIC system type 553201). The preparation chamber is connected to a deposition chamber (Fig. 3.6 (8)), which is separated by a shutter operated with a rotary motion feedthrough (Fig. 3.7a (16), MDC, BRM-133) and pumped with 65 l/s TMP (not shown, Leybold, TURBOVAC SL 80). The deposition chamber contains a low temperature effusion cell (Fig. 3.6 (9), MBE components, NTEZ 40-2-16-S-SF) for deposition of solid organic compounds, and a gas doser for deposition of liquid organic compounds (not shown). The preparation chamber is equipped with an additional transfer rod (magnetic transfer rod - Fig. 3.7a (17), VAB, MDS 40-700) which allows to transfer the sample to the APC (Fig. 3.7a (18)). The APC is separated from the preparation chamber by a gate valve (Fig. 3.7a (19), VAT, 10836-CE01) and pumped with a pumping station (not shown, Pfeiffer, HiCube 300H Eco). The details on the setup of the APC are given in section 3.7.

Along the course of preparing the model catalysts, great care must be taken to reduce the background pressure rise upon gas dosing. Therefore, a gas doser ((10) in Fig. 3.7a and 3.6) was implemented in the preparation chamber. It is equipped with a manually operated leak valve (VAT, 59024-GE01) and a linear translator (linear travel 101.6 mm, MDC, E-LMT-154, no. 665511). During gas dosing, the gas phase is monitored by the QMS. The distance between the gas doser and the sample can be adjusted from 7 to 60 mm.

For the preparation of complex model catalysts under UHV conditions, the experimental setup allows for two different metals to be deposited onto the sample surface by physical vapor deposition, by employing two individual electron beam evaporators (Fig. 3.7a (11) and (12)). Damaging of the sample by ions thus produced in the electron beam evaporator source, is avoided by applying to the sample during preparation, a retarding voltage equal to the acceleration potential of the evaporator (typically 800 V) which decelerates those ions. The evaporator fluxes are calibrated using a QCM ((13) in Figs. 3.6 and 3.7a). An ion gun and a LEED/AES ((14) in Figs. 3.6 and 3.7a) are used for sample cleaning and for characterization of the single crystal and the crystallinity of the model oxide films. Temperature-programmed desorption can be performed in

the preparation chamber by means of a QMS equipped with a gold-coated aperture (Fig. 3.7a (15)). A PID based temperature ramp generator (Eurotherm, 2148) allows heating rates of up to 10 K/s.
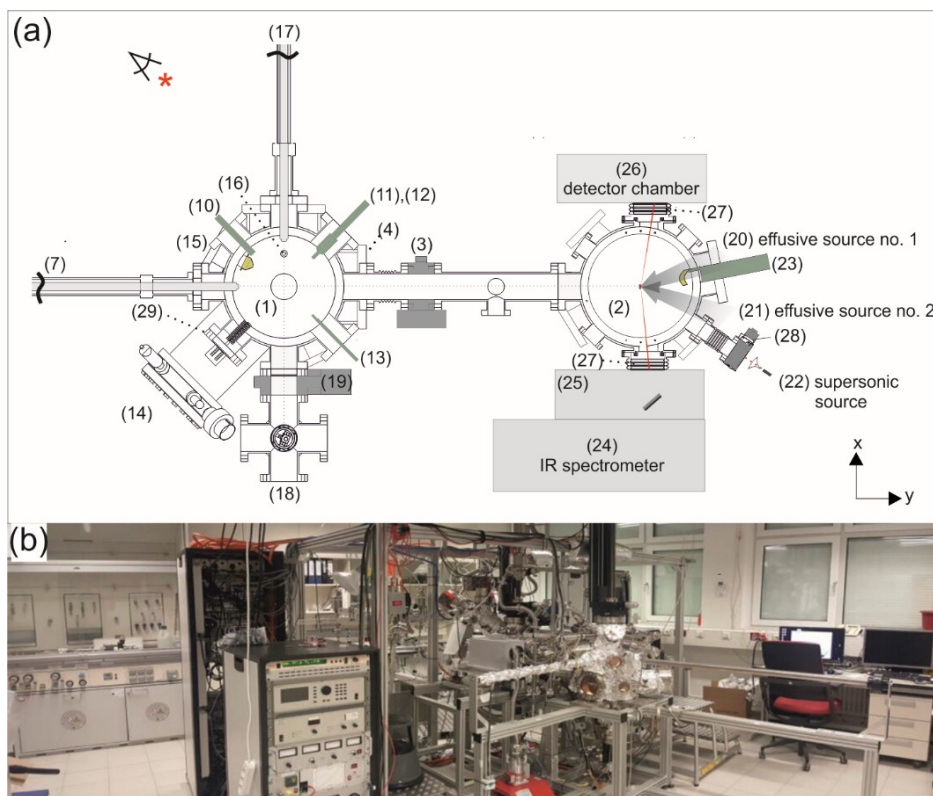
Figure 3.7: (a) Schematic cross sectional top view (x,y) of the experimental setup showing the preparation chamber, the reaction chamber and the APC. The section was done slightly above the plane determined by the transfer rods, and for clarity, the lower part is shown. The labeled components are: (1) preparation chamber, (2) reaction chamber, (3) gate valve, (4) connecting flange for TMP (7) magnetic transfer rod, (10) gas doser, (11),(12) metal evaporators, (13) QCM, (14) LEED/AES, (15) QMS in the preparation chamber, (16) shutter assembly (17) magnetic transfer rod, (18) APC, (19) gate valve, (20) effusive source no. 1, (21) effusive source no. 2 (22) supersonic source, (23) QMS in the reaction chamber, (24) IR spectrometer, (25) external UHV adaptation chamber of the IR spectrometer, (26) IRAS detector chamber, (27) flexible bellows for IRAS assembly, (28) gate valve, (29) ion gauge. The effusive sources are shown schematically with perspective arrows (20),(21) as they are inclined and positioned above the cross sectional plane. (b) A photographic overview of the entire experimental setup (photo perspective is indicated in Figure 3.7 (a)). Reprinted from [93], with the permission of AIP publishing.

3.6 Sample transfer system and holder design

The movable sample plate designed for this apparatus allows for a quick transfer of the sample between different chambers. The sample can be heated and cooled across a broad range of temperatures (115 - 1400 K), which is required for the preparation of a variety of model catalytic surfaces, including metal single crystals as well as epitaxially grown thin oxide films. Each of the manipulators implemented in each of the three UHV chambers is equipped with a sample holder allowing effective cooling or heating with a precise temperature control. Temperature measurement is realized by K-type thermocouples. The sample can be additionally connected to the high voltage supply, which is required for deceleration of the metal ions during metal evaporation onto the sample surface. The sample holders in the preparation and reaction chambers are identical, in the sense that in both, electron beam heating is used for temperature control. This method of heating is incompatible with the APC since it operates at ambient pressure conditions. Hence, the design of its sample holder was altered, and a ceramic button heater was implemented into it instead (for more details, see section 3.7).

Figure 3.8a shows drawings of the side- back- and front- views of the *movable sample plate*, the movable compartment which is directly attached to the sample. Figure 3.8b shows a front view drawing of the sample holder, the fixed assembly attached to the manipulators in the different chambers. The dashed framed area in Fig. 3.8b (10) denotes the *sample holder adaptor*.

In the *movable sample plate* (Fig. 3.8a), a single crystal sample (1) is mounted on a Mo supporting plate (2). Metal single crystal samples are cut into 1-2 mm thick 10×10 mm^2 squares, then spot welded to the Mo supporting plate via tantalum foils (3). Accessing the back side of the sample is provided by a 8.5 mm diameter central opening in the Mo supporting plate. A rectangular ceramic plate containing six in-line holes (4) is attached at its center (its two central holes) to the front side of the supporting plate by molybdenum screws (5) and a trapezoid pin (6). The remaining two pairs of holes are used for the installation of Chromel-Alumel thin thermocouple sheets from both front sides of the supporting plate (7),(8) via additional screws and trapezoid pins. The ceramic plate ensures an electric insulation between the thermocouple pair and the Mo supporting plate. The trapezoid shape of the pins was carefully chosen to provide a sandwich-like

arrangement, in which the probability of a parasite electrical contact caused by thermal expansion of individual trapezoid pins during heating, is minimized (side view, Fig. 3.8a (6)).

Thermocouple wires are pressed with molybdenum screws against the K-type thermocouple sheets ((7),(8) and are spot welded to the edge of the single crystal from the front side of the supporting plate (not shown in Fig. 3.8a). This assembly allows for a specific accurate temperature measurement on the single crystal (1) without interferences from the supporting plate (2) of the *movable sample plate*.

The sample holder (Fig. 3.8b) includes four identical tangential trapezoid pins (9), each containing two threads. Such arrangement of pins and screws is employed for fixing the *movable sample plate* to the *sample holder adaptor* (10) for manipulators I and II (see Fig. 3.6a (5) and (6) or Fig. 3.9a (12) for the manipulator of the APC). For this purpose, the *movable sample plate* slides into the space between the thin tantalum foil (11) attached by the tangential trapezoid pins (9) to the *sample holder adaptor* (10), while the thermocouple sheets ((7) and (8) attached to the Mo supporting plate (2), Fig. 3.8a) slide into the thermocouple sheets ((12) and (13) installed on the sample holder adaptor (10)). The latter contact allows for the temperature control of the sample. To ensure temperature measurement, which is specific only to the sample, two ceramic plates are inserted in between the sample holder adaptor (10) and the thermocouple sheets (12), (13). Finally, the *movable sample plate* can be attached to the *sample holder* using magnetic transfer rods (VAB, MDS 40-1200, VAB, MDS 40-700, see Fig. 3.7a (7) and (17)) containing an adaptor with rotating locking mechanism which is attached to the clamp of the *movable sample plate* (14). A photograph of the *movable sample plate*, already inserted into the *sample holder* of the manipulator in the reaction and preparation chambers, is shown in Fig. 3.8c with the same labelling of the components shown in Fig. 3.8a and b.

Figure 3.8d shows a schematic drawing of the *sample holder* mounted onto the manipulator (of either the reaction or preparation chamber). Since the manipulator has an electrical contact to the UHV chamber, the *movable sample plate* must be electrically insulated from the chamber. This is achieved by employing an electrical insulator in the form of a sapphire plate (15), which is also a fairly good thermal conductor. The sapphire plate is introduced between the copper platform (16) mounted on the bottom part of the manipulator and the *sample holder adaptor* ((10), see also Fig. 3.8b and c).
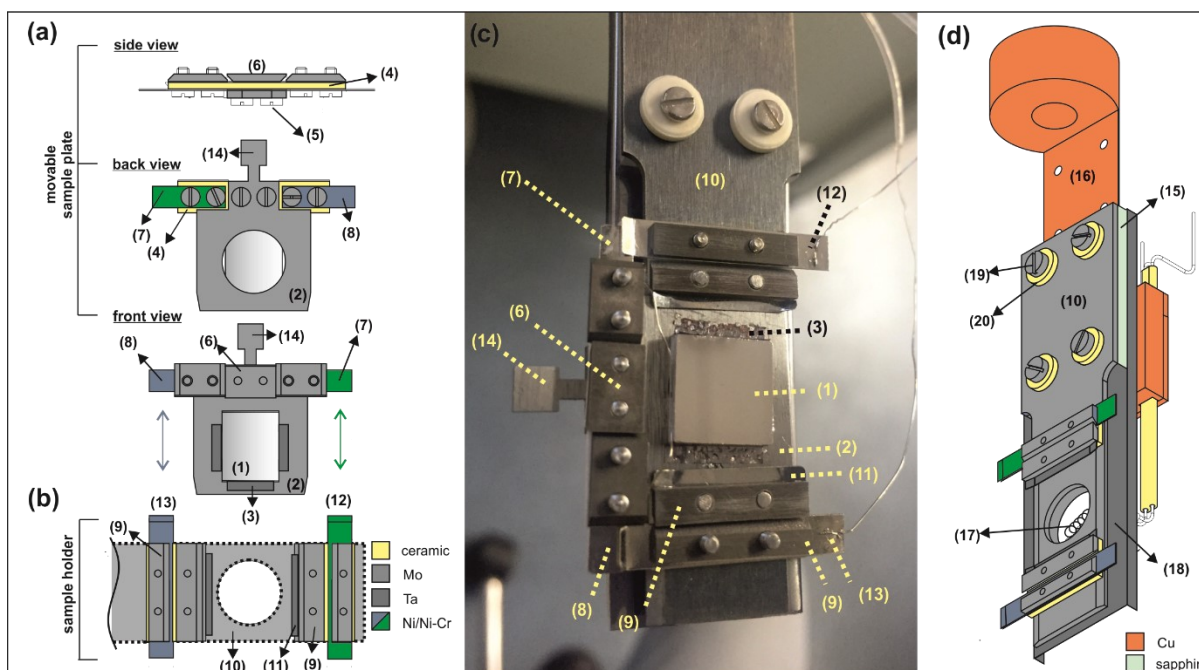
Figure 3.8: **(a)** schematic drawing of the *movable sample plate* from different perspectives and **(b)** the *sample holder* (top view), which is used to fix the *movable sample plate* on the manipulators (of the reaction and preparation chambers). The legend indicates the color-coded materials of the sample plate and holder. **(c)** a photograph of the *movable sample plate* and the *sample holder* mounted on the manipulators. (a)-(c) *__movable supporting plate__*: (1) single crystal (sample), (2) Mo sample supporting plate, (3) foil for sample assembly to the supporting plate, (4) rectangular plate containing six in-line holes, (5) screws, (6) trapezoid pins, (7),(8) thermocouple thin sheets installed on the ceramic plate; *__sample holder__*: (9) tangential trapezoid pins, (10) *sample holder adaptor*, (11) thin foil for *movable sample plate* assembly, (12),(13) thermocouple thin sheets installed on the *sample holder adaptor*. **(d)** schematic drawing of the *sample holder* installed in the preparation and reaction chambers. Color-coded materials are the same as shown in (b) and additional colors are indicated in the legend. The labelled components are: (15) insulating plate, (16) platform attached to the manipulator, (17) sample heating filament, (18) shield to minimize unwanted heating of the sample holder, (19) screws for adaptor assembly, (20) hat-shape washers. Reprinted from [93], with the permission of AIP publishing.

Heating of the sample in the reaction and preparation chambers is performed by electron bombardment or thermal radiation from a handmade filament ((17) Thoriated tungsten, Goodfellow), situated approximately 10 mm behind the *sample holder* and aligned parallel to the sample to ensure heating homogeneity. To ensure that only the sample is heated and minimize undesired heating, a Ta shield (18) is mounted on top of the copper platform of the manipulator and is attached to the *sample holder adaptor* via the sapphire plate. It contains the same central opening as those of the sample holder and plate, and it is positioned in such a way that all openings are aligned. Finally, electron bombardment is generated by applying high voltage onto the sample via Ta wire which is pressed against the adaptor ((10), see also Fig. 3.8b and c) using Mo screws (19). The latter are electrically insulated from the chamber by hat-shape ceramic washers (20). In this setup, sample temperature exceeding 1400 K can be obtained upon heating via electron bombardment. Also, when LN_2 flows through the coils in the manipulation stage, heat is efficiently removed from the sample and a temperature as low as 115 K may be reached. The radiative heater in this setup can heat the sample up to 500 K.

3.7 Ambient Pressure Cell (APC)

The body of the APC (Fig. 3.9) is a 6-way cross (DN 63 CF-F), which is separated from the preparation chamber by a gate valve (see also (3) in Figs. 3.6 and 3.7a). It is pumped by a pumping station (Pfeiffer, HiCube Eco 300H) equipped with a turbomolecular pump (HiPace 300H, 260 l/s) backed with a 3-stage diaphragm pump (MVP 030-3DC). The base pressure is measured with dual gauge (Pfeiffer, PKR 361). Figure 3.9a overviews the APC and flange housing. An enlarged cross-sectional 3D view is shown in Fig 3.9b. The APC consists of a platform (Fig. 3.9a (1)) mounted onto the upper flange of the 6-way cross (2) via 3 mm stainless steel tubes (3). The platform fulfills two rolls: *(i)* it serves as a reservoir for liquid nitrogen that can be filled through the tubes (3) from the air side, and *(ii)* it serves as a support for the *sample holder adaptor* (4). The bottom flange of the 6-way cross contains all electric feedthroughs (5) that are in electrical connection with the sample heating assembly (6). *The sample holder adaptor* has a hat-like shape and it is positioned on top of the platform and fixed with screws (Fig. 3.9b (7)). It has a 8.5 mm diameter central opening from which the back side of the sample may be accessed. Resistive heating of the sample up to 1200 K is realized via a ceramic button heater ((8), Heat Wave Labs, 102273 Ø.320"

O2 Heater), which can be operated both under UHV and ambient pressure conditions. The sample is positioned directly on top of the heating ceramic button. The heating plate is made of catalytically inert ceramic material, capable of operating under ambient pressure conditions. Prior to catalytic studies, reference experiments with inert samples must be performed in order to quantify effective contributions from the chamber walls to the overall reaction rate. The back part of the sample holder contains a custom flange accommodating the thermocouple and power feedthrough ((9), Ideal vacuum products, 108065, DN 16 CF-F). Finally, the sample can be transferred from the preparation chamber directly into the sample holder of the APC by a magnetic transfer rod. Once the *movable sample plate* is inserted into the *sample holder* of the APC, the cell can be sealed. This is realized by approaching an internal metal cup (10) towards the *sample holder* and pressing against a Viton sealing (11). The latter allows pressurizing the APC while maintaining a high vacuum in the surrounding 6-way cross chamber (Fig 3.9a (2)). The metal cup is connected to a manipulator which is mounted on the upper DN 63 CF-F flange of the 6-way cross ((12), VAb, LDK 40-50). The metal cup is also connected to two 3 mm tubes serving as gas outlet and inlet (13). When used in the batch mode, they are connected to a metal bellow recirculation pump (Gasmet Ansyco, MB-41E,). The recirculation loop is interfaced with GC (Agilent 7890B) through a pneumatic sampling valve. The GC is equipped with electronic pneumatic regulation inlet (Split/Splitless 0–100 PSI EPR Inlet, G4352-60502) and thermal conductivity and flame ionization detectors. To detect different types of hydrocarbons, the GC is additionally equipped with a fused silica capillary column (MACHERY-NEGAL, LIPODEX A, model 723360.50, I.D. 0.25 mm, length 50 m). The batch mode, being the typical choice for studies on low surface area model catalysts, allows an easier detection of the products due to the increased reactants conversion with reaction time.[95,96] Gas pressure is measured using two absolute pressure transducers (full range 10 mbar and 1000 mbar, MKS, Baratron 627D).
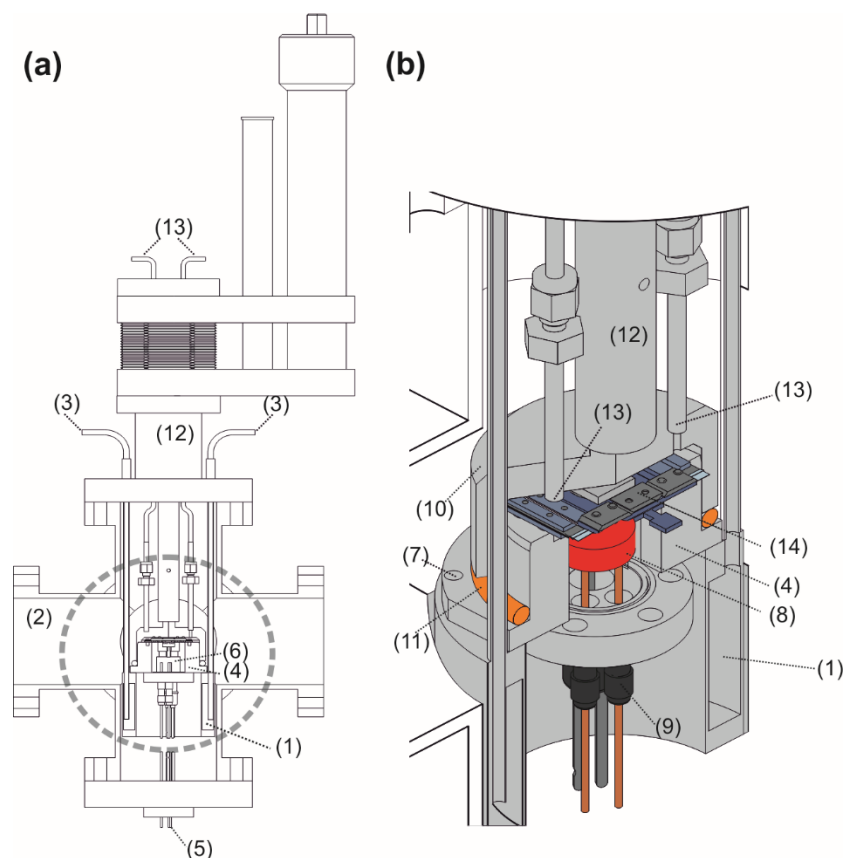
Figure 3.9: (a) Cross-section of the APC setup. The experiments consist of a two-level system that combines an outer UHV chamber with an inner elevated pressure reactor (encircled). (b) Enlarged 3D view of the encircled part of (a). The labeled components are: (1) platform for *sample holder* assembly (2) 6-way cross, (3) inlet/outlet platform cooling (4) *sample holder adaptor*, (5) electrical feedthroughs, (6) sample heating assembly, (7) screws of sample holder assembly, (8) button heater, (9) electrical feedthroughs, (10) metal cup, (11) Viton seal, (12) metal cup manipulator, (13) gas inlet/outlet, (14) movable sample plate. Reprinted from [93], with the permission of AIP publishing.

3.8 Implementation and test measurements

3.8.1 Performance of the molecular beams

Effusive beams

Prior to testing the performance of the molecular beams, alignment of the beam to the sample center position was conducted as described in section 3.4.1. Measuring the molecular flux and its spatial distribution, requires a reliable measurement of the beam intensity and its profile. Figure 3.10a shows a top view photograph of the reaction chamber during beam intensity and distribution measurements.

Figure 3.10(b) and (c) show contour beam profiles of effusive source no. 1 and 2 respectively at backing pressure of 7.0×10^{-2} mbar of Ar. For this measurement, the beam monitor was placed in the center position and moved in a plane parallel to the sample position (xz plane, see Fig. 3.6). The color map illustrates the pressure gradient measured with the beam monitor across the xz plane, and the dashed black rectangular indicates a 10×10 mm^2 area at the center of the reaction chamber, at which the sample is to be positioned.

To obtain a homogenous exposure during reactivity and IR absorption measurements, the outer beam was chosen to have a slightly larger diameter (12 mm) than the sample area (10×10 mm^2). The two beams of Fig. 3.4 are shown to have an ellipsoid shaped profile due to their inclination with respect to the sample surface plane (see inset of Fig. 3.2). Taking into consideration the symmetric arrangement of the beams in space relative to the center position, the beam profiles should appear symmetric in this representation, which is indeed observed experimentally.

When the beam monitor is moved during the measurement to scan the beam profile along the central plateau, the variation of the beam intensity corresponds to the declared 3% repeatability of the gauge, suggesting that a stable homogeneous flux of gaseous species is formed in the effusive expansion. In practice, the experimentally measured variation of the beam intensity along the central axes of the sample amounted to approximately 4%.
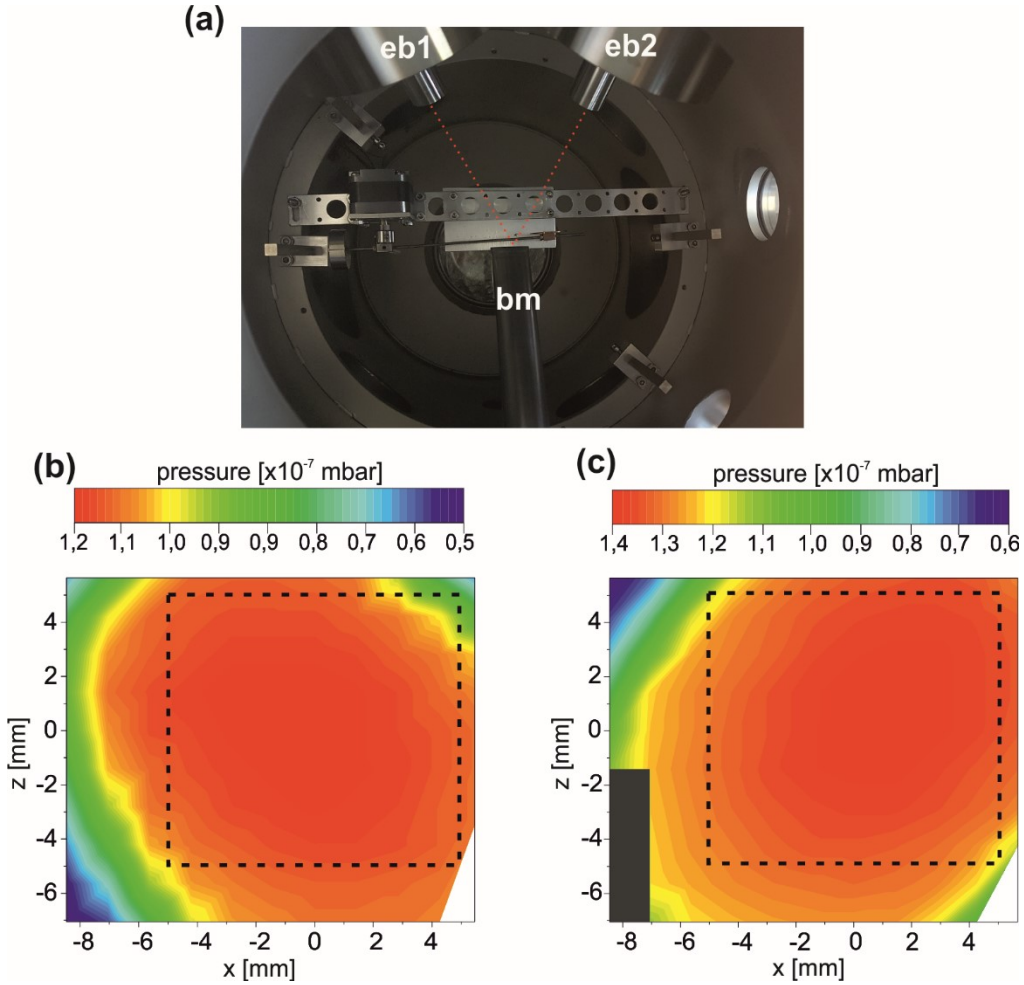
Figure 3.10: (a) A photograph of the setup for beam profiling and flux measurements. All beam sources are aligned with respect to the sample position. (b) and (c) Molecular beam profiles at the center position of source no. 1 and 2, obtained at the backing pressure of Ar amounting to 7×10^{-2} mbar. The dashed rectangles show the sample position with respect to the molecular beam. The sample position is parallel to the xz plane. Reprinted from [93], with the permission of AIP publishing.

A variable molecular beam flux may be obtained by varying the backing pressure of the beam source. Figure 3.11 shows the dependence of the centerline intensities of the two effusive sources on the backing pressure, as recorded for Ar. For this measurement, the molecular beam monitor is placed exactly at the sample position. The intensities of the effusive sources were measured as a function of the beam sources backing pressure (by varying it over several orders of magnitude). The source pressures of sources no. 1 and no. 2 were measured with capacitance

manometers with a full-scale range of 1 mbar (red rectangles, black circles). To test the pressure limit of the effusive source employed in our beam setup, the source pressure of source no.1 was additionally measured with a capacitance manometer of 10 mbar range (MKS, Baratron 627D, green triangles).

It should be noted that the effusive beam expansion starts from low pressure conditions with nearly no interaction between gas phase particles, so that this type of expansion is practically nearly gas independent. In a backing pressure range from 1×10^{-2} to 1 mbar, the molecular flux increases linearly with pressure. In this range, the source pressure intensity behaves practically identical for the two beams. The distances between the beam orifice, installed in the center position, and the GCAs amount to 378 and 368 mm for sources no.1 (Fig. 3.10 (b)) and no.2 (Fig. 3.10 (c)) respectively, which accounts for the slightly different molecular flux at the same backing pressure of the effusive sources. Above 1 mbar, scattering losses result in decreasing intensity,[69] and the flux levels off at a value of ~9.6×10^{14} molecules $cm^{-2}s^{-1}$. This intensity corresponds to a deposition of about 1.3 ML of CO molecules on Pt(111) per second. In principle, there is no lower limit to the beam intensity. It is nonetheless indirectly limited by the components of the source pressure regulation (the capacitance manometer) which limit the range of controllable values of the molecular flux. In practice, a modulation of 0.1% monolayer can be obtained. It should be pointed out that in the current setup, the background pressure in the molecular beam detector limits the minimum detectable pressure change to ~2×10^{11} molecules $cm^{-2}s^{-1}$. Variable time modulation of the molecular flux by means of a mechanical shutter allows the production of beam pulses of arbitrary length with a minimum pulse length of 150 ms. When the molecular beam is blocked by the shutter, a leakage of about 3% of the unblocked beam intensity is observed using the QMS, which is caused by the increased background pressure in the outer pumping stage.
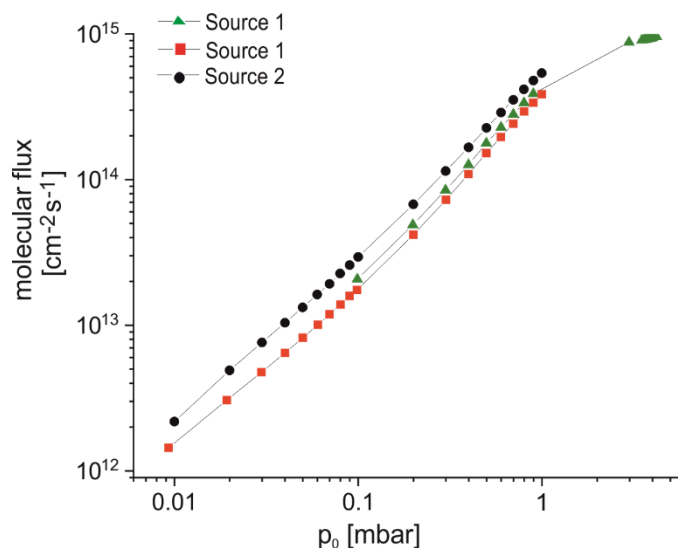
Figure 3.11: Effusive beams intensity (measured for source no. 1-red and no.2 -black using a 1 mbar full scale capacitance manometer) versus Ar backing pressure at 298 K. The pressure limit of source no. 1 was additionally tested with a 10 mbar full scale capacitance manometer (green). Reprinted from [93], with the permission of AIP publishing.

Supersonic beam

The supersonic source is operated by a pulsed solenoid valve (see section 3.3.2). On generating a current pulse through the solenoid, a magnetic field evolves, which lifts a plunger from the valve orifice, hence opening the valve. Typical voltage of 220 V and current of 0.4 A were used to activate the valve, resulting in 200-300 μs opening periods. The nozzle-skimmer distance of 185 mm was installed. The repetition rate of the pulsed valve results in a maximum working pressures of $2 \cdot 10^{-6}$ and $2 \cdot 10^{-8}$ mbar in the first and second stages respectively. The aligning procedure for the supersonic beam includes *(i)* aligning the propagating jet with respect to the molecular beam axis defined by the skimmer, which is realized by installing the solenoid valve on an xyz-translational stage, thus providing a possibility to change the valve's position in three dimensions ((6) in Fig. 3.5), and *(ii)* aligning the jet that passed the skimmer with respect to the sample's center position in the reaction chamber. The latter alignment procedure is realized by adjusting the positions of the translational screws mounted on the platform supporting the supersonic beam. The molecular beam profile and beam intensity were measured by the molecular beam monitor, which

was placed at the center position of the reaction chamber, where it can be moved along the axes of the sample surface plane. The obtained 3D beam profile along the sample surface, employing a 4.5 mm diameter inner aperture, is shown in Figure 3.12a. Measured horizontal beam profiles for the three different apertures are shown in Figure 3.12b. The beam intensity at the center position amounts to $\sim 2 \cdot 10^{13}$ molecules$\cdot$cm^{-2}s^{-1} for a back Ar pressure of 1.710 bar at 298 K and a 305 μs average pulse interval. Upon moving the beam monitor during the measurement to scan the beam profile along the central plateau, the variation of the beam intensity corresponds to the declared 3% gauge repeatability. This observation suggests a stable a homogeneous flux of gaseous species formed in a supersonic expansion.

Depending on the nature of the experimental requirements, the beam can be chosen to either fit, exceed or subceed the sample size by choosing one of three inner apertures (see Fig. 3.5 (13)). The tails occurring at the sharp beam edges, shown in Fig. 3.12b for different apertures, result from a convolution of the beam monitor aperture (1 mm) with the actual beam profile.

(a)

(b)
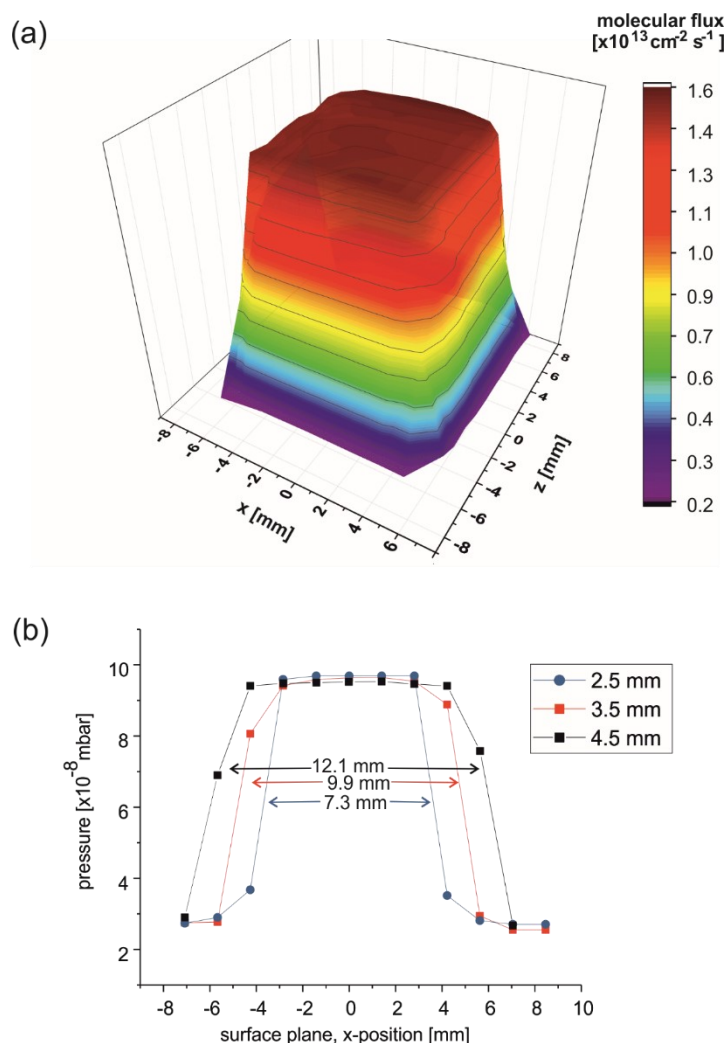
Figure 3.12: (a) Beam profile at the center position, obtained at Ar backing pressure of 1.710 bar and employing the 4.5 mm inner aperture. (b) Horizontal beam profile for different aperture sizes. Reprinted from [93], with the permission of AIP publishing.

3.8.2 Test measurements: adsorption of acetophenone and (R)-(+)-1-(1-naphthylethylamine) on Pt(111)

The performance of the new multi-molecular beam/spectroscopy apparatus was tested by studying in detail the interaction of two adsorbates, namely *acetophenone* and *(R)-(+)-1-(1-naphthylethylamine)* (R-NEA), with Pt(111) as a function of coverage. Literature data, available for these two compounds from former comprehensive adsorption studies on either powdered materials or single crystals, serve as a reference data for testing the present results.

Prior to acetophenone exposure, the Pt(111) sample was first cleaned in the preparation chamber by cycles of a stepwise procedure that consists of Ar sputtering (20 minutes, beam energy 1kV at $5 \cdot 10^{-6}$ mbar Ar), subsequent annealing at 850 K in O_2 ($5 \cdot 10^{-6}$ mbar, 20 minutes), and a consecutive shorter high temperature annealing under UHV conditions (1300 K, 2 minutes). The last cleaning cycle included reduction with CO ($5 \cdot 10^{-6}$ mbar) at 400-450 K and subsequent flashing to 600 K. The surface structure and cleanliness level of the sample surfaces were examined by LEED and AES. In addition, IR spectra of adsorbed CO were obtained to check the availability and distribution of the different adsorption sites on the Pt(111) surface.

Adsorption of acetophenone: characterization of high vapor pressure adsorbates

Acetophenone was deposited via an effusive molecular beam onto Pt(111) at 115 K, while simultaneously recording IR spectra. Figure 3.13 shows a sequence of IR spectra obtained at 115 K for acetophenone coverages between 0.1 and 10 ML (a), together with a NIST reference IR spectrum of gaseous acetophenone[95] (b). The measured spectra clearly depict a continuous growth of intensities of all acetophenone fundamental frequencies with increasing exposure, which confirm the formation of acetophenone ice. Multilayer coverage IR spectra may be viewed as reflecting that expected for molecular adsorbates that are largely unperturbed by the underlying metal support, as those occurring in the uppermost layers.

Relying on the literature vibrational bands assignments of gaseous acetophenone,[96] most of the vibrational bands, recorded for the acetophenone multilayer, can be accordingly identified. The most intense band at 1683 cm^{-1} is assigned to the C=O stretching vibration. The bands at 1598 and 1583 cm^{-1} are assigned to the in-plane C-C stretching modes of the aromatic ring. The bands at 1431 and 1362 cm^{-1} are related to the antisymmetric and symmetric methyl deformation, respectively. The strong absorption band at 1276 cm^{-1} is assigned to the x-sensitive benzene mode.[96, 97] The band at 958 cm^{-1} is related to the mix modes comprising the $-CH_3$ rocking and the aliphatic C-C stretching.

Having identified the vibrational bands related to the unperturbed molecules in the multilayer, we may now proceed to assign the bands measured for the sub-monolayer coverages. Those however, have the potential of being strongly perturbed by the interaction with the Pt surface, which in turn might alter the observed vibrational structure compared to the reference one. For this purpose, a detailed coverage dependence of the IR spectra was extracted from Fig. 3.13a,

allowing to follow the evolution and possible frequency shifts of all bands when reducing the coverage from multi- to sub-monolayer range.
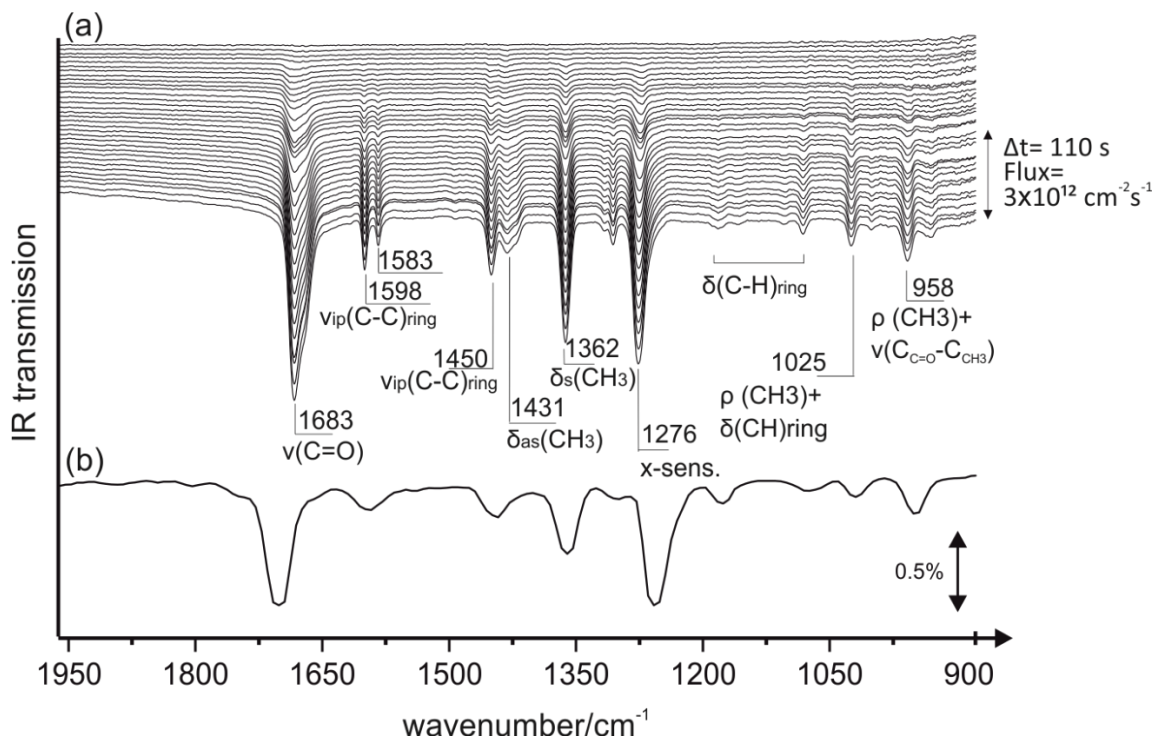
Figure 3.13: (a) IR spectra of acetophenone recorded at 115 K during its deposition onto Pt(111) by the effusive beam of source 2. The spectra in downwards direction correspond to increasing molecular coverage from 0.1 to 10 ML. (b) NIST reference IR spectrum of gaseous acetophenone.[95] Reprinted from [93], with the permission of AIP publishing.

It can be clearly seen that the spectra obtained for the sub-monolayer coverages generally produce the same vibrational bands as those of the multilayer, yet, show a strong intensity dependence on the coverage. This dependence stems from a specific adsorption geometry of acetophenone at the metal surface, which affects the relative ratio of the intensities due to the metal surface selection rule.[80] A detailed discussion related to the interaction of acetophenone with Pt(111) at sub-monolayer coverage is presented in chapter 4.

Adsorption of R-NEA: characterization of low vapor pressure adsorbates

R-NEA was utilized to test the new apparatus and the experimental setup for deposition and spectroscopic characterization of low vapor pressure adsorbates that in practice cannot be deposited by molecular beams. After cleaning, the Pt crystal was transferred to the deposition chamber (bottom part of the preparation chamber, see Figure 3.6(8)). R-NEA was dosed on Pt(111) at 155 K via backfilling, after which the sample was transferred to the reaction chamber for IR acquisition.

The basic instrumental requirement of integrating a deposition chamber dedicated solely for the deposition of low vapor pressure organic compounds, as posed by the necessity to keep the reaction chamber as clean as possible, rises a fundamental question regarding the stability of the measurement and background signals. A background spectrum is a single channel spectrum that is acquired for the pristine metal surface to account for all instrumental and environmental contributions to the measured signals. In a standard procedure, normally applied for relatively high vapor pressure compounds, the background is collected prior to data acquisition with the sample being already situated at the center position, after which the adsorbates of interest are dosed at the sample by the molecular beams. Here, moving the sample is not required, and hence, the resulting spectra exhibit stable background. In contrast, since deposition of low vapor pressure compounds cannot be realized with molecular beams, the sample must be moved back and forth to the deposition chamber. However, altering the sample location after collecting the background spectrum, inevitably introduces instability to the baseline which consequently becomes wavy, hence falsifying the peak information.

In order to overcome these limitations, we conceived a new procedure by which high quality IR spectra can be obtained even for low vapor pressure compounds. In this procedure, the sample is first cleaned in the preparation chamber, after which the adsorbates of interest are deposited onto the sample in the deposition chamber. The sample is then transferred to the reaction chamber and the IR spectrum is acquired. This spectrum is a single channel spectrum which contains the background information. In the next step, the sample, still at the center position, is cleaned by oxidation cycles for 10 minutes at 800 K, carried out by a O_2 effusive source ($1 \cdot 10^{14}$ $cm^{-2}s^{-1}$), and successively reduced with CO ($1 \cdot 10^{14}$ $cm^{-2}s^{-1}$) at ca. 400 K for 5 minutes. Finally, after flashing the sample to 600 K and cooling it down to the desired temperature, the background is collected

on the clean Pt(111) surface and is further used to calculate the net IR spectrum. During the above cleaning procedure, the evolution of O_2, CO, CO_2 and the apparent mass is monitored. The oxidation-reduction cycle time can be optimized according to CO_2 desorption from the sample.
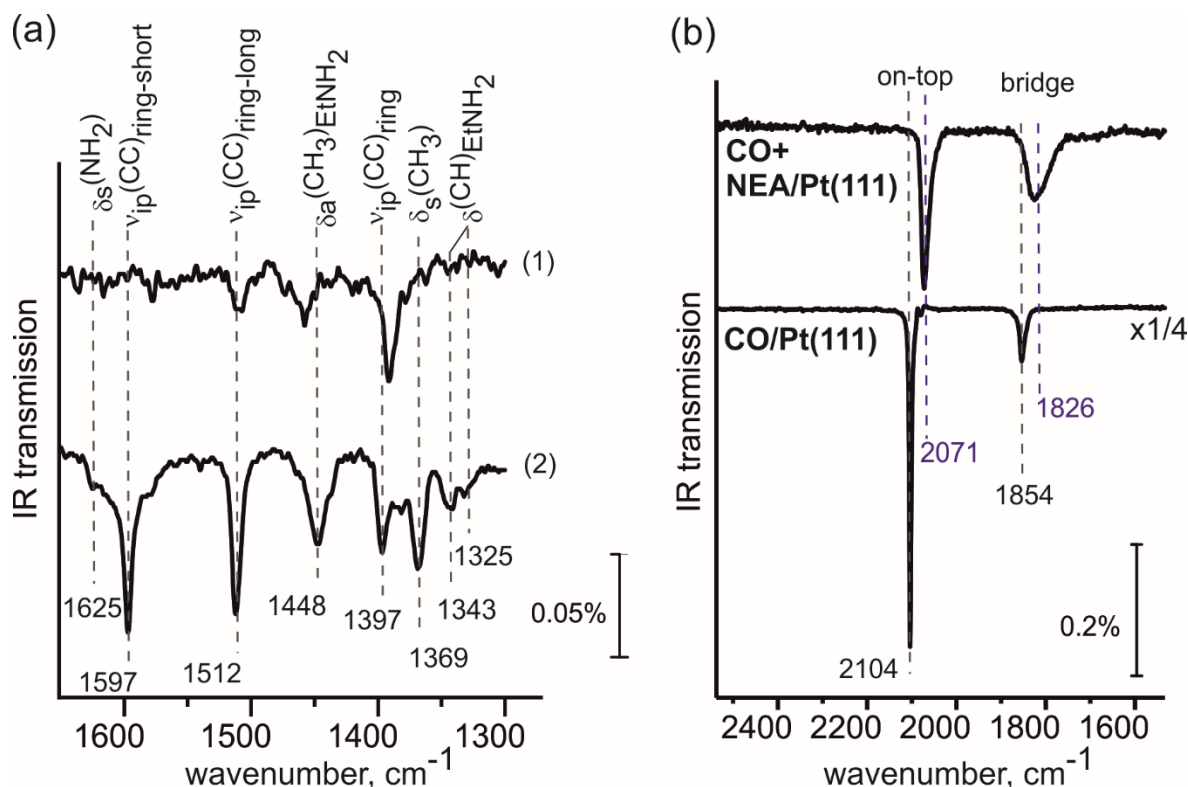
Figure 3.14: (a) IRAS spectra of *R*-NEA adsorbed on Pt(111) at 155 K: exposure to 5×10^{-8} mbar for (1) 2 and (2) 10 minutes. (b) IRAS spectra of CO adsorbed on pristine Pt(111) and *R*-NEA/Pt(111) recorded at 155 K, CO exposure: 6×10^{14} molecules cm^{-2}. The R-NEA-covered surface corresponds to *R*-NEA exposure of 5×10^{-8} mbar for 2 minutes at 155 K. Reprinted from [93], with the permission of AIP publishing.

To assess the sample cleanliness obtained by the above described cleaning procedure, the CO IR spectrum was recorded on the cleaned surface. The CO/Pt(111) spectrum is presented by the bottom measurement of Figure 3.14b. Two vibrational bands, at 2104 cm^{-1} (on-top sites) and 1854 cm^{-1} (bridge sites), were obtained. These frequencies as well as their intensities nicely comply to a IR spectrum previously recorded on a clean Pt(111) surface.[98]

Figure 3.14a shows the IRAS spectra of R-NEA on Pt(111) at 155 K at two different coverages. The spectrum, obtained for a ~30 L exposure (2), corresponds to a multilayer adsorption of R-NEA and displays a distribution of vibrational bands that is characteristic of largely unperturbed molecules, resembling those measured for gas or condensed phase.[99] By comparison to the literature data, the vibrational modes at 1512 and 1597 cm^{-1} are assigned to in-plane stretching of the naphthyl ring along the long and short axes respectively. The broad peak at ~1448 cm^{-1} is assigned to the asymmetric deformation of the methyl moiety of the ethyl amine, and the peak at 1369 cm^{-1} is assigned to the symmetric deformation of methyl group.[36, 54, 99-101] The IR spectra obtained for sub-monolayer R-NEA coverages, exhibit strong changes in the peak relative intensities, hence reflecting a change in the adsorption geometry. The absence of the peak at 1597 cm^{-1} and the relatively small intensity of the in-plane deformation of the naphthyl ring along the long axis, suggests that at submonolayer coverages the molecules adopt a tilted geometry of the naphthyl ring with respect to the surface plane. At this surface coverage, the tilt is more pronounced along the long axis. The tilted geometry of the naphthalene ring at sub-monolayer coverages is consistent with IRAS and NEXAFS studies previously reported by Zaera and Lambert.[36, 54] Some discrepancy regarding the assignment of the vibrational bands is evident from a comparison to that reported by McBreen and co-workers.[101, 102] This discrepancy calls for resolution in further studies which are presented in chapter 5.

In the next step, adsorption of CO on the Pt surface functionalized with R-NEA was investigated. Figure 3.14b shows the IRAS spectrum of CO adsorbed on R-NEA/Pt(111) at 155 K. The spectrum clearly shows that the peaks of adsorbed CO on NEA-modified surface are both shifted and broadened compared to the pristine surface: the CO adsorbed at the on-top sites is red-shifted by 33 cm^{-1}, whereas the band related to CO adsorbed at the bridge sites is red-shifted by 28 cm^{-1} as compared to the pristine Pt(111) surface. Additionally, the latter band shows a considerable broadening (FWHM = 100 cm^{-1}). These two observations could suggest an intermolecular interaction of CO with the adsorbed R-NEA molecules. Exploring their exact nature, requires further studies which are presented in chapter 5.

3.9 Conclusions

A new compact multi-molecular beam/surface spectroscopy experimental setup allowing fundamental-level reactivity studies on ligand-functionalized model (nanostructure) surfaces, is introduced. The new apparatus consists of three chambers, which can be operated as independent UHV systems, and of a unique combination of tools including two effusive and one supersonic molecular beams, IRAS for spectroscopic identification of adsorbed surface species, QMS for gas phase analyses, as well as tools required for preparation and structural characterization of complex nanostructured model catalysts based on thin oxide films epitaxially grown on metal single crystals. These include LEED/AES, TPD, metal evaporators as well as calibration methods. Additionally, a dedicated deposition chamber is implemented allowing to functionalize the catalytic surface with low vapor pressure compounds. The apparatus contains an ambient pressure cell that provides an experimental possibility to carry out reactivity studies in a broad range of reaction conditions, up to the ambient pressure conditions.

In this chapter we present the constructional details of this setup and its preliminary performance tests. In particular, we show that the new compact design of effusive beams allows for achieving high molecular fluxes typically required in reactivity studies. In the test studies on catalytically relevant materials, adsorption of two different adsorbates, acetophenone and R-NEA, was investigated by employing IRAS and molecular beam techniques, and a brief discussion on the observed phenomena is accordingly provided.

Chapter 4

Acetophenone adsorption on Pt(111)[ψ]

In this chapter, both molecular beams/IRAS and STM setups are employed to investigate the adsorption of the prochiral molecule acetophenone on Pt(111).

Prior the discussion of the experimental data, the principal vibrational bands in the IR spectrum of acetophenone ice will be introduced (section 4.1). In the next section, we will focus on the adsorption geometries of the molecule on the surface (section 4.2). The third section (section 4.3) provides atomistic-level insights into the mechanisms of keto-enol tautomerization of acetophenone over Pt(111). It will be shown that enol can be formed on the surface by building a ketone-enol dimer, in which one molecule is present in the enol form and is stabilized via hydrogen bonding to the carbonyl group of the second ketone molecule. We achieved a clear spectroscopic identification of the ketone-enol dimers and showed that the enol can exist only if it is stabilized by the neighboring ketone molecule. Special attention will be paid to the influence of co-adsorbed hydrogen on the acetophenone adsorption and the mechanisms of keto-enol tautomerization on Pt(111), which allow us to develop new concepts for rational design of new catalytic materials. The fourth section (section 4.4) focuses on the adsorption behavior of acetophenone at different surface temperatures. The tautomerization reaction was found to be temperature sensitive. The amount of enol is growing with increasing temperature and can exist only if stabilized by the neighboring ketone molecule. It will be shown spectroscopically that the vibrational frequency of the C=O group reflects the strength as well as the chemical nature of the hydrogen bonding with

---

neighboring surface species. The temperature evolution of the molecular surface species is complementary detected and distinguished microscopically, and a summary of the various surface species is provided. The last section (section 4.5) focuses on the influence of co-adsorbed hydrogen on the acetophenone tautomerization at different temperatures. We show that the target process – hydrogenation of the carbonyl group – occurs not in monomers but in the ketone-enol dimers, and results in the formation of a partly hydrogenated acetophenone species attached via the hydrogen bonding to the second acetophenone molecule. Possible mechanisms responsible for the dimer-induced hydrogenation of the carbonyl group are discussed, based on the spectroscopically derived reaction intermediates.

4.1 Assignment of vibrational modes of acetophenone

The assignment of acetophenone vibrations was done based on the frequencies for acetophenone in the gas and condensed phases[96], and in the form of adsorbates on powdered Pt-based materials[97, 106]. Additionally, via isotopic labeling experiments combined with IRAS, fundamental vibrational modes of acetophenone multilayers are assigned along with ab initio MP2 theoretical calculations in the gas phase.

The adsorption of acetophenone on Pt(111) was investigated in the 115-300 K temperature range under well-defined UHV conditions by IRAS. To obtain a reference for an unperturbed molecule, the IR spectra are first recorded at multilayer coverages in which most of the adsorbed molecules do not directly interact with the surface. These reference spectra can be compared with those obtained at sub-monolayer coverages to investigate the perturbation of chemical bonds by the interaction with Pt(111). According to the metal-surface selection rule,[80] only vibrations having non-zero projection of the dynamic dipole moment perpendicular to the surface are visible in IRAS spectra, whereas vibrations parallel to the surface are strongly attenuated by formation of an image dipole in the underlying substrate. Thus, we can obtain insights into the adsorption geometry of the adsorbate from the characteristic IR intensity distributions at sub-monolayer coverage. In former studies, vibrational properties of acetophenone have been investigated in the gas phase[96], liquid phase and solution,[107, 108] as well as in the adsorbed form on powdered Pt-based materials[97, 106]. To address the multilayer regime of acetophenone adsorption, and identify the associated vibrational bands, the experimental spectra is compared with previously published spectra.[96]

Additionally, to assign the measured experimental frequencies to specific vibrations of the molecule, we performed isotope labeling experiments and single molecule calculation in vacuum.

Frequencies calculation of an acetophenone molecule in vacuum was performed with MP2 functional using the Gaussian09 software[109]. To get a reasonable description of the virtual orbitals, aug-cc-pVQZ basis set was used. Isotope labeling experiments are performed with ^{13}C-carbonyl acetophenone, and the resulting vibrational frequencies are then compared with the corresponding estimated frequency shift in the scope of the harmonic approximation.[110]

Figure 4.1a displays the IR spectrum of acetophenone multilayers on Pt(111) at 156 K. At this coverage regime, constantly growing intensities of all vibrational features are observed, that confirm the formation of acetophenone multilayers. For comparison, the bottom curve in Fig. 4.1 shows the NIST gas phase IR spectrum[95] (c) and the middle spectrum represents the calculated IR vibrational frequencies (b). The frequencies of the latter are scaled by a factor of 0.975 with an origin at 1683 cm^{-1} to show best agreement with experimental data. Most experimentally resolved IR active vibrations are correctly described in the calculation; calculated and measured vibrational frequencies show relatively good agreement, while in the case of relative IR intensities the agreement is less accurate, but qualitatively satisfactory. Altogether, the above comparison demonstrates that MP2/aug-cc-pVQZ is a reliable method for calculating the vibrational frequencies of acetophenone and is therefore employed in the further analysis.
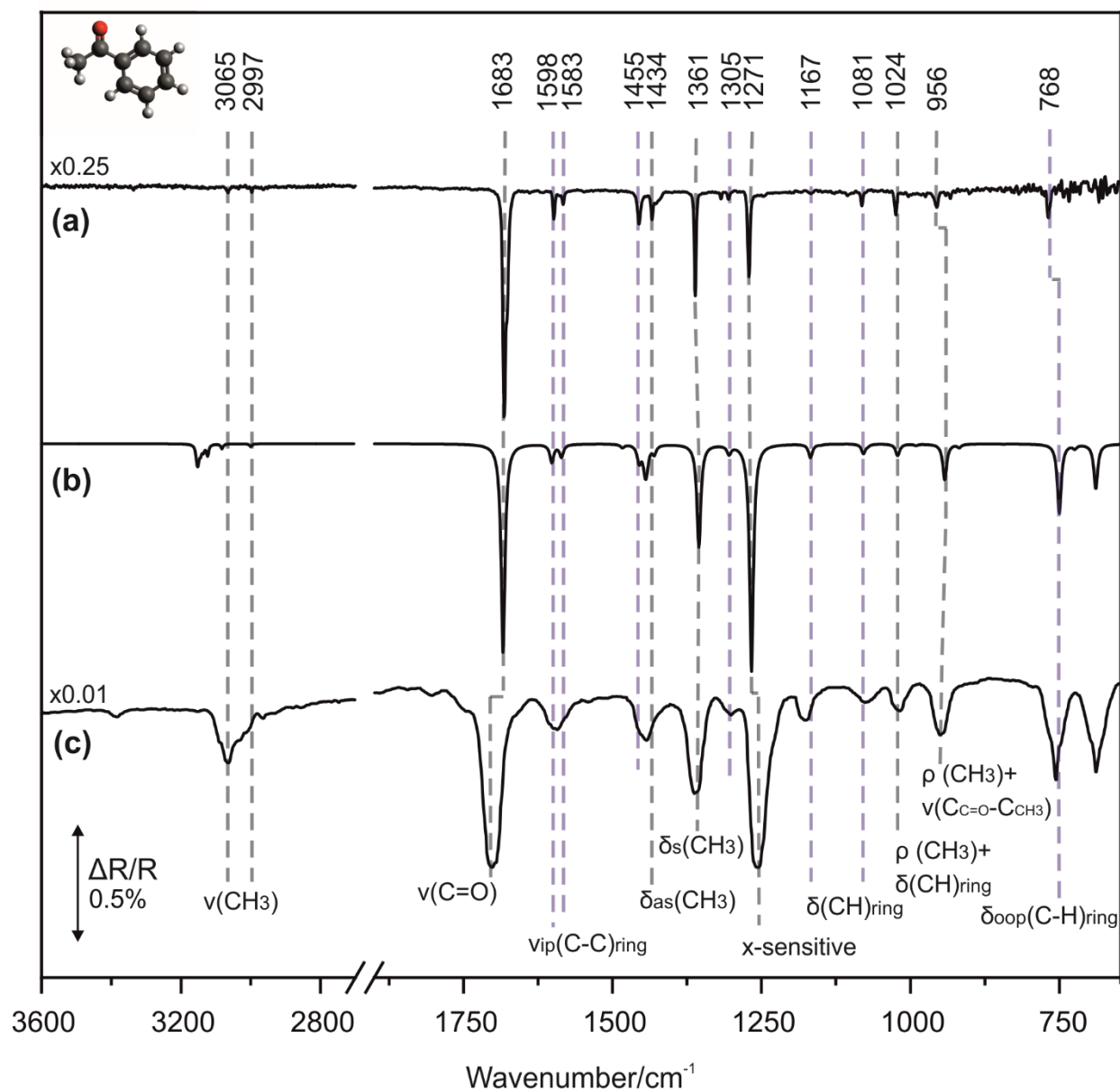
Figure 4.1: (a) IR spectrum of acetophenone ice on Pt(111) at 156 K; (b) Calculated gas phase spectrum of acetophenone at the MP2/aug-cc-pVQZ level of theory; (c) Experimental IR spectrum of acetophenone in the gas phase from NIST database.[95] The labeled bands refer to the experimental multilayer spectrum of acetophenone on Pt(111).

Assignments of the observed vibrational bands were made by comparison to previously published experimental data,[96] as well as by isotope labeling experiments performed with ^{13}C-carbonyl acetophenone and by accounting for those calculated for the gas phase. Here, a large number of IR absorption modes can be identified. In the C–H stretching region, IR vibrations are observed at 2997 cm^{-1} and 3065 cm^{-1}. These vibrational bands can be assigned to the CH$_3$ asymmetric and symmetric stretching modes respectively. The band at 1683 cm^{-1} is the most intense vibration in the spectrum and it is assigned to the C=O stretching. Note that the position of this band is about 25 cm^{-1} lower than the C=O stretching frequency determined in NIST database in the gas phase (1708 cm^{-1}).[95] The bands at 1598, 1583, 1455 and 1318 cm^{-1} are assigned to the in-plane C-C stretching modes of the aromatic ring, and the bands at 1305, 1082 and 1025 cm^{-1} are assigned to the C-H ring bending modes. The bands at 1434 and 1362 cm^{-1} are assigned to the antisymmetric and symmetric methyl deformation respectively. The strong absorption band at 1271 cm^{-1} is assigned to the X-sensitive benzene modes[96, 97] which is a C(aromatic)-C(substituted group) stretching mode whose intensity and wavenumber position is greatly influenced by the nature of the substituted atom.[111] The peak at 956 cm^{-1} is assigned to mix modes comprising the –CH$_3$ rocking and the aliphatic C-C stretching. Lastly, the peak at 768 cm^{-1} is assigned to the out-of plane C-H bending modes. The corresponding assignment for this peak is only weakly evident since the infrared detector used to collet these spectra is not very sensitive in this region.

Even though the spectrum obtained for acetophenone at multilayer coverages exhibits generally the same vibrational bands as the gas phase spectrum, it shows slightly different intensity distribution. It is therefore assumed that even for acetophenone multilayers at low temperature, the molecules may still adopt a preferential orientation.

In relation to the above, one of the advantageous features of IRAS is that it can provide information on molecular orientation, both in the monolayer and multilayer regions, as shown for various organic thin films on oxide supported materials (see for instance Ref. [112-114]). A detailed analysis of the orientation of acetophenone multilayers on Pt(111) is beyond the scope of the present study. Nevertheless, to determine the orientation of the molecule on the surface at submonolayer coverages, the spectra should be compared to a reference spectrum. The multilayer spectrum would be thus a more suitable reference in case of a random orientation.

Acetophenone was continuously deposited onto Pt(111) at 115 K – the lowest obtainable temperature in the experimental setup – while IR spectra was recorded simultaneously during the

exposure. The spectra are shown in Fig. 4.2. Above $4.9 \cdot 10^{15}$ molecules·cm^{-2} ($3 \cdot 10^{12}$ molecules·cm^{-2}, 1650 s), constantly growing intensities of all vibrational features are observed that confirm the formation of acetophenone multilayers. For comparison, the bottom part of Fig. 4.2 shows IR spectrum in the gas phase from the NIST database.[95]
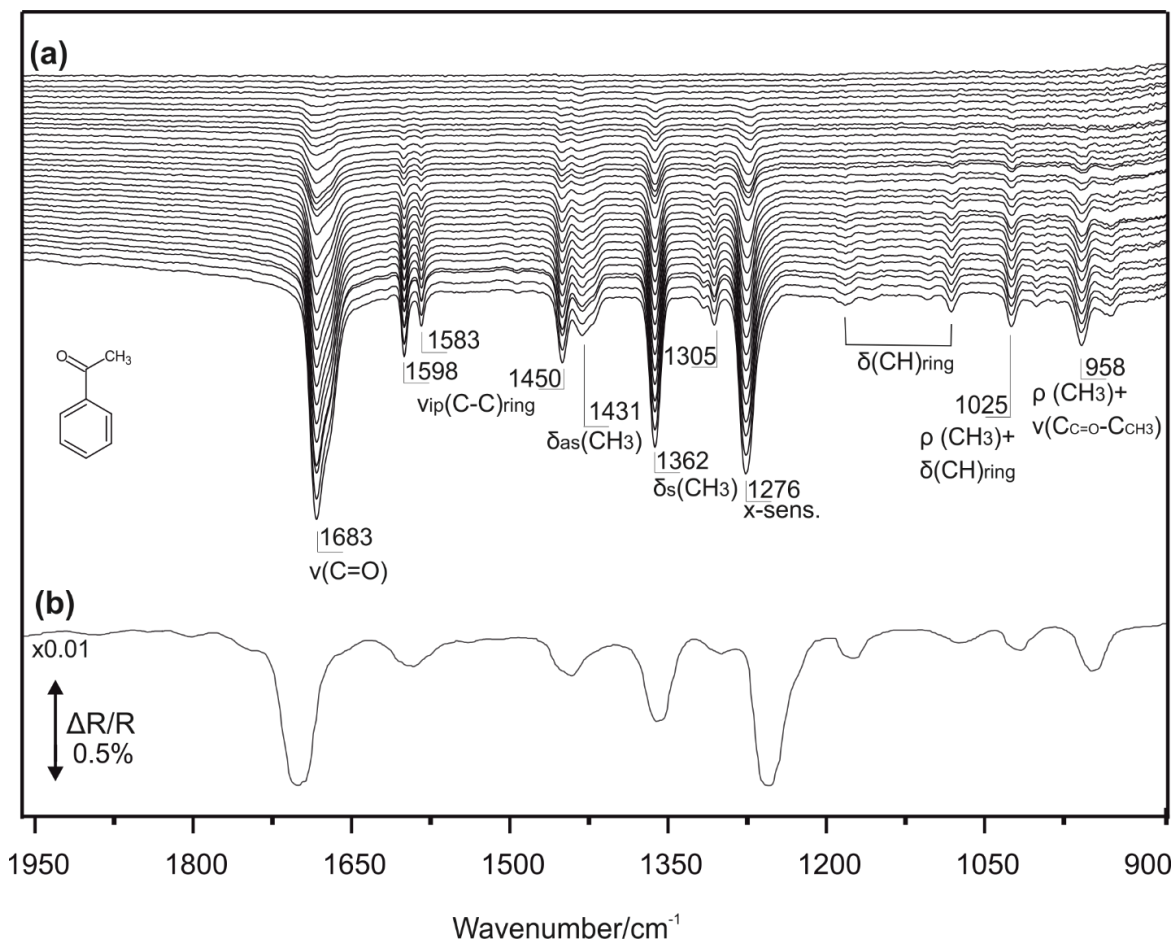
Figure 4.2: (a) IR spectra of acetophenone on Pt(111) as a function of exposure time of acetophenone beam (beam intensity 3×10^{12} cm^{-2}s^{-1}, $\Delta t = 110$ sec) from sub-monolayer to multilayer coverage recorded at 115 K (b) Experimental gas phase spectrum taken from NIST.[95]

The spectrum obtained at 115 K at multilayer coverages is in fair similarity to the experimental gas phase spectra, particularly in terms of relative intensities. Therefore, a random orientation of the molecules in the multilayer at 115 K can be better assumed. This spectrum is thus a rather

suitable reference to be compared with the spectra obtained at sub-monolayer coverages to investigate the perturbation of chemical bonds by the interaction with Pt(111).

The corresponding literature data and our experimentally measured frequencies of acetophenone multilayer are displayed in Table 4.1.

Frequency cm^{-1}			Assignment[a]	Ref.
Multilayer	MP2/aug-cc-pVQZ scaled	Gas phase NIST [95]		
3065	3082	3067	$\nu(CH_3)$	[96,97]
2997	3000			
1683	1683	1708	$\nu(C=O)$	[96,97,106-108]
1598	1602	1598	$\nu_{ip}(CC)_{ring}$	[96,97]
1583	1585		$\nu_{ip}(CC)_{ring}$	[96,97]
1450	1445	1446	$\nu_{ip}(CC)_{ring}$	[96,97]
1431	1429		$\delta_{as}(CH_3)$	[96,97]
1362	1355	1366	$\delta_{s}(CH_3)$	[96,97]
1318	1304		$\nu_{ip}(CC)_{ring}$	[96,97]
1305		1303	$\nu_{ip}(CH)_{ring}$	[96,97]
1276	1267	1263	$\nu_{ip}(CC)_{ring-acetyl}$	[96,97]
1167	1168	1182	$\delta_{ip}(CH)_{ring}$	[96,97]
1081	1078	1080	$\delta_{ip}(CH)_{ring}$	[96,97]
1024	1022	1024	$\delta_{ip}(CH)_{ring} + \rho(CH_3)$	[96,97]
956	943	952	$\rho(CH_3) + \nu_{ip}(CC)_{carbonyl-methyl}$	[96,97]
768	750	757	$\delta_{oop}(CH)_{ring}$	[96,97]

a) Modes: ν= stretching, δ= deformation, ρ=rocking. Subindices: ip= in-plane, oop= out-of-plane, s= symmetric, as= anti-symmetric, ring= aromatic ring, acetyl= H_3C-$C=O$

Table 4.1: Assignments of vibrational modes of acetophenone.

The effect of the annealing temperature on a surface pre-covered by multilayers of acetophenone at 115 K, is displayed in Fig. 4.3. These experiments were performed by heating to the indicated temperature for a period of 2 s and allowing the sample to cool once again to 115 K, following which the infrared spectrum was recorded.

While a small change is observed upon slowly warming the surface to 135 K, a noticeable distinct transition occurs in the 135–153 K region, revealing a spectrum of narrower bands as well as different intensity distribution. The broad, rounded peaks of the spectrum recorded at 115 K,

are typical of those known for amorphous multilayers, whereas the sharper narrower features of the two upper most spectra (e.g. 153 and 170 K) suggest a crystalline multilayer.[115] The results might point to crystallization of the initially amorphous ice. Determination of acetophenone molecule at sub-monolayer coverages presented in this study is thus based on comparison of IR spectra of multilayers of acetophenone obtained at 115 K.
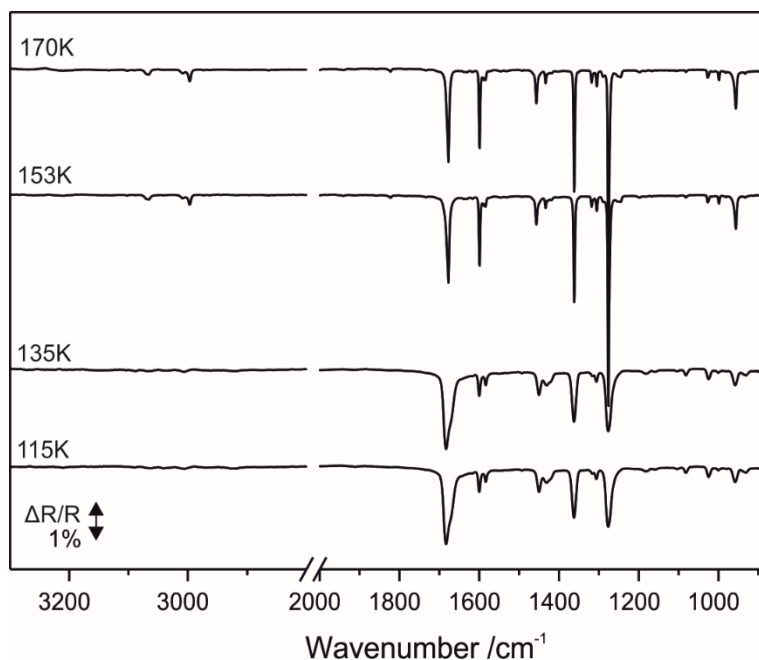
Figure 4.3: IRAS spectra of multilayers of acetophenone adsorbed on clean Pt(111) as a function of annealing temperature. The annealing temperatures are marked adjacent to the corresponding spectra. All spectra were recorded at 115 K.

To further establish the assignments of bands, adsorption of multilayers of acetophenone isotopically labelled with ^{13}C-carbonyl was investigated by IRAS. Figure 4.4 shows the IR spectra obtained for two acetophenone isotopes on Pt(111) at 115 K. The vibrational band at 1683 cm^{-1} related to the C=O stretching vibration, is red-shifted by 36 cm^{-1} upon isotopic labelling, in a good agreement with a shift of about 38 cm^{-1}, expected within the scope of the harmonic approximation.[110] The vibrational band at 1276 cm^{-1} related to the so called "x-sensitive" mode[96, 97], is red shifted by 26 cm^{-1} with the labeled compound. The latter red shift is in a good agreement with an isotopic shift factor expected for an exchange of [12]C[12]C to [13]C[12]C, i.e. 1.019.[110] The band

at 958 cm^{-1} is a mixed mode comprising the aliphatic C-C stretching and the -CH$_3$ rocking[96]. The shift of this band by only 8 cm^{-1} seems to support the assignment of different relative contributions. Finally, the bands comprising the -CH$_3$ group (1431, 1362 cm^{-1}) and the ring stretching modes (1450, 1583 and 1598 cm^{-1}) exhibit no change in the vibrational frequencies. The results are a further support to the previously reported assignments of acetophenone. The multilayer assignments reported herein are in good agreement with previously reported experimental data,[96, 97, 106] and are further evident with isotopically labeled experiments, as well as by our calculated gas phase spectrum.

Figure 4.4: IR spectra of (^{13}C-carbonyl)-acetophenone (1) and acetophenone (2) multilayers adsorbed on pristine Pt(111) at 115 K. Vibrations related to the bands greatly affected by isotope labeling are indicated in grey. Reprinted with permission from [105].

4.2   Adsorption geometries of acetophenone on Pt(111) at sub-monolayer coverages
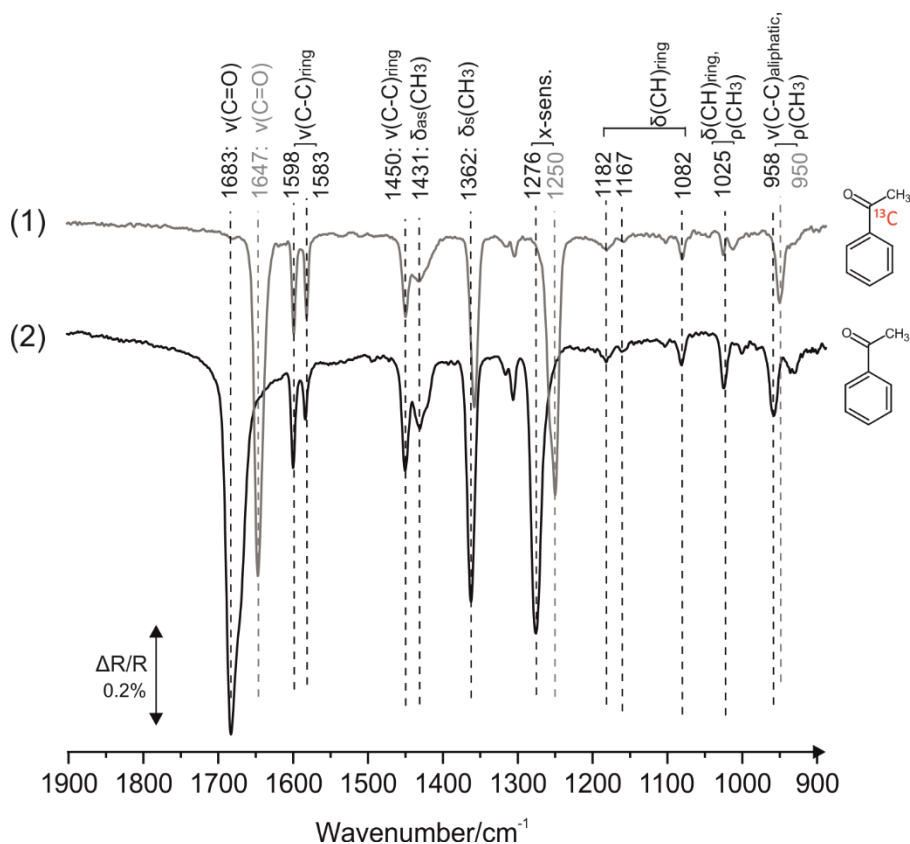
As mentioned before, we can obtain insights into the adsorption geometry of the adsorbate from the characteristic IR intensity distributions at sub-monolayer coverage. To determine the orientation of acetophenone on the clean Pt(111) surface, a series of IR spectra was obtained at different sub- to multi- layer coverages in the 115-300 K temperature range.

In the submonolayer regime, further pronounced changes occur as compared to unperturbed acetophenone. Figures 4.5a and b show two sets of coverage-dependent IR spectra obtained for two acetophenone isotopes. In these spectra two vibrational regions are displayed for simplicity: the region of the C=O and C-C (ring) stretching vibrations (~1700-1600 cm^{-1}), and that of the -CH$_3$ deformation as well as the ring stretching vibrations (~1450-1350 cm^{-1}). Note that for the determination of the orientation of the molecule on the surface, we will focus only on these vibrational regions, since they exhibit the most prominent changes of the intensity distribution and are relevant for the further discussion.

The evolution of the IR spectra investigated as a function of acetophenone coverage, suggests that there are different peaks in the C=O stretching region that likely result from ketone species with different molecular geometries: (i) at low coverage, the acetophenone molecule adopts a flat-lying geometry with the aromatic ring oriented parallel to the surface plane, and (ii) at high coverages, a transition from flat-lying to tilted-oriented molecule occurs.

At the lowest coverage (1 in Fig. 4.5a), vibrational frequencies of the C=O stretching at 1683 cm^{-1}, the -CH$_3$ symmetric deformation at 1362 cm^{-1} and the –CH$_3$ anti-symmetric deformation (1431 cm^{-1}) are detected. The intensity of the latter band increases with increasing coverage and finally saturates. In spectrum (2), the onset of the band at 1450 cm^{-1} can be detected. The intensity of this band increases rapidly with increasing coverage and eventually exceeds the intensity at 1431 cm^{-1}, as shown in spectrum (4). Consistently, this band is accompanied with the consecutive evolution of the C-C ring stretching modes at 1598 and 1583 cm^{-1}, and with the appearance of the band at 1690 cm^{-1} which simultaneously grows with increasing coverage and finally saturates. Finally, in spectrum (5), the onset of the multilayer growth is detected. Note that at this coverage regime, constantly growing intensities of all vibrational features are observed, which confirm the formation of acetophenone ice. A similar coverage-dependent trend is observed in the spectra

shown in Fig. 4.5b for the isotopically labelled acetophenone comprising the ^{13}C=O stretching vibration at 1643 cm^{-1}, followed by a saturation of the band at 1650 cm^{-1}, with the latter defining the onset of multilayer adsorption. Given the strikingly different intensity distribution of the coverage dependent spectra compared to that obtained for acetophenone ice, two types of ketone species can be identified: (i) species exhibiting a combination of vibrational bands prior the saturation of the band at 1431 cm^{-1}, as depicted in spectrum (1) in Figs. 4.5a and b (**species S1**; vibrations characteristic: 1431+ 1683 cm^{-1}), and (ii) species exhibiting a combination of vibrational bands following the saturation of the band at 1431 cm^{-1} but prior the saturation of the band at 1690 or 1650 cm^{-1} of the labeled compound, as depicted in spectra (2)-(4) (**species S2**; vibrations characteristic: 1450 + 1690 cm^{-1}). The latter species can be assigned to surface species growing within the monolayer at high coverage. Alternatively, it can be assigned to a second layer of acetophenone occurring prior the formation of acetophenone ice (multilayers).
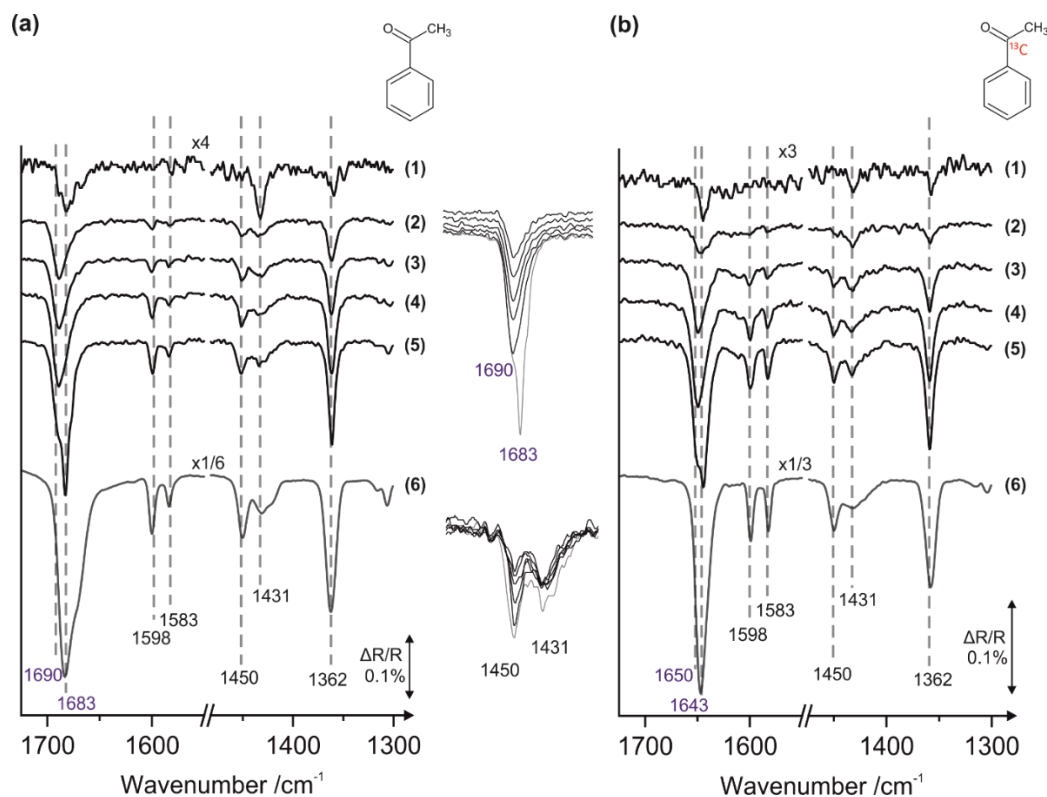
Figure 4.5: IR spectra of (a) acetophenone and (b) acetophenone isotopically labelled with ^{13}C-carbonyl recorded at different exposures at 155 K, correspondingly. Acetophenone exposure (a) (1): $1.4 \cdot 10^{15}$, (2): $4.6 \cdot 10^{15}$, (3): $5.5 \cdot 10^{15}$, (4): $7.3 \cdot 10^{15}$, (5): $9.1 \cdot 10^{15}$ molecules·cm^{-2}, (6): the spectrum of a multilayer. (b) (1): $4.9 \cdot 10^{14}$, (2): $1.4 \cdot 10^{15}$, (3): $2.4 \cdot 10^{15}$, (4): $3.8 \cdot 10^{15}$, (5): $5.2 \cdot 10^{15}$ molecules·cm^{-2}, (6): the spectrum of a multilayer. The inset shows the evolution of selected bands intensities with deposition time (a(2)-(6)).

The interaction of carbonyl compounds with model systems have been extensively studied in the past.[38] Among them, acetone is one of the simplest model to study interactions of simple carbonyl compounds with metal surfaces. Two types of bonding configuration were previously reported for acetone on Pt(111)[116]; a majority of more weakly bound "end-on" η^1(O)-ketone species, that is bonded to the surface through the loan pair electrons of the oxygen, and a minority of strongly bound "side-on" η^2 (C,O)-ketone species that is bonded to the surface via both O and C atoms of the C=O group. Semi-empirical Hückel theory calculations have shown that the preferred adsorption configuration of acetone on Pt(111) is η^1(O)-ketone on a top site position as

opposed to η^2 (C,O)-ketone in a di-σ mode on Pt(110) and Pd(111).[117] A recent theoretical study performed by Jeffery et al. have shown that the calculated vibrational frequency of "end-on" η^1(O)-ketone species agrees well with the literature data.[118] Nevertheless, this species is adsorbed rather stronger on the surface compared to the alternative parallel adsorption of η^2 (C,O)-ketone form. The energy difference was explained by the steric hindrance of the-CH$_3$ group while interacting with the surface, and it is likely to occur with any substituted ketone adsorbed parallel to the surface. For the η^2 (C,O)-ketone species on Pt(111), unambiguous spectroscopic evidence has not yet been obtained. Experimental spectroscopic assignments of η^2 (C,O)-ketone species suggested by Ibach's group[119] were doubtlessly disproved by Jeffery and coworkers and were explained theoretically by considerable C-O bond elongation of the ketone compared to the gas phase with correspondingly lower C-O frequency by hundreds of wavenumbers.[118] The C-O bond length in η^2 (C,O)-ketone was actually reported as equal to that of C-OH bond in the gas phase of enol species. It is worth mentioning that the reported calculated most stable form of enol species of acetone on Pt(111) involves bonding configuration through C=C in di-σ mode in which the C atom of the -C-OH group and the C atom of the -CH$_2$ group are exclusively bonded to the surface. The O atom is not bonded to the surface, as commonly perceived for η^2 (C,O)-ketone configurations involving both C and O atoms. Bonding configuration of the C-O group in the low wavenumber region, e.g. 1050-1250 cm^{-1}, will be discussed in detail in section 4.3.

The C=O related frequencies shown in Fig. 4.5a at 1683 and 1690 cm^{-1} (or 1643 and 1650 cm^{-1} of the labeled acetophenone, Fig 4.5b) are indicative of a double C=O bond as suggested by the similar C=O frequency observed for unperturbed molecules in the ice form. Bonding configuration via η^2 (C,O) should result in a considerably longer C-O bond compared to unperturbed molecule with a correspondingly lowered C-O stretch.[118] This means that experimental assignments of these bands to η^2 (C,O), via either π-interactions or in di-σ mode, can be ruled out. Therefore, the adsorption configuration of both acetophenone species points to a η^1(O)-ketone species. It appears that any other bonding configurations of ketone species cannot be stabilized on the surface due to steric repulsion between the -CH$_3$ group and the surface, in accordance to published theoretical data.[118] Note, however, that the frequency of the C=O stretching vibration obtained in our study, allows us to safely exclude the formation of η^2(C,O) and suggest a η^1(O)-ketone configuration, based on the proximity to the gas phase value. Yet, the spectroscopic observation can be also consistent with η^1(C)-ketone configuration with C bonded

to the surface and O pointing away, as well as non-bonding interaction of the carbonyl moiety with the surface.[120]

In spectrum (1) of Figs. 4.5a and b there is a significant signal in the –CH$_3$ anti symmetric deformation (1431 cm^{-1}), however there is essentially no signal for the in-plane C-C ring stretching modes (1598 and 1583 and 1450 cm^{-1}). This intensity distribution is in sharp contrast to the situation found for acetophenone ice ((6) in Figs. 4.5a and b), where the intensities of the ring stretching modes (1598, 1583 cm^{-1}) are comparable to that one observed for the antisymmetric deformation of the -CH$_3$ group (1431 cm^{-1}). The absence of absorption bands in the ring stretching region indicates that the aromatic moiety of the first surface species – species S1– is oriented parallel to the surface and therefore cannot be seen most likely due to the MSSR.[80] Obviously, parallel orientation of the C=O bond of these species does not occur on this surface. This result can be most likely explained by the steric repulsive interaction of the -CH$_3$ group with the surface, resulting in its orientation away from the surface. In the gas phase molecule, the C=O group and the aromatic ring are lying in the same plane. Illustration of this plane is shown schematically in Fig. 4.6 (xy plane).
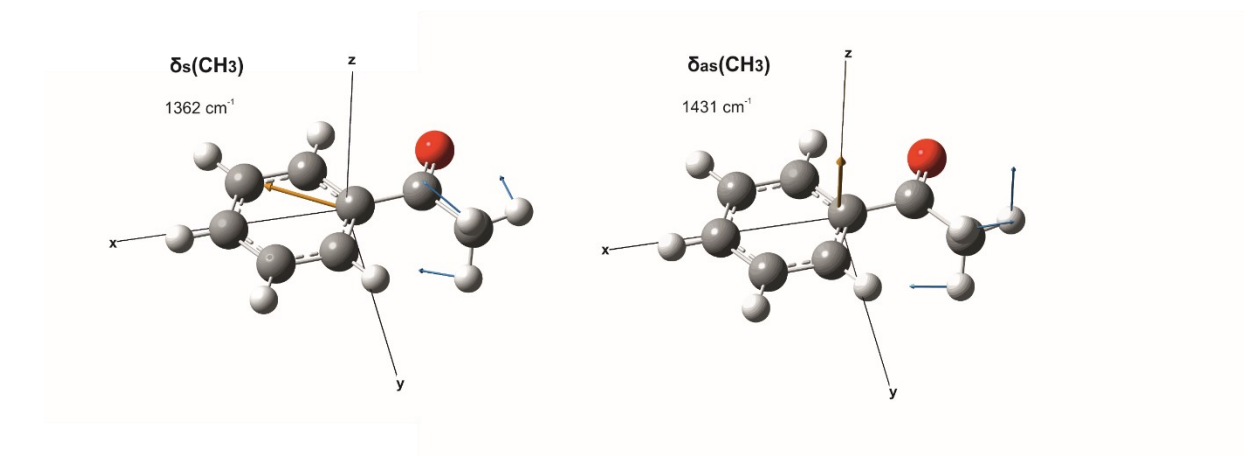

Figure 4.6: Graphical illustration of vibrational modes of the -CH3 group of acetophenone in the gas phase using Gaussview 05 (see text for details); blue arrows: the nature of the vibrational mode; orange arrows: the orientation of the dynamic dipole moment. The origin of the orange arrows was chosen to be in the molecule's center of mass.

It can be viewed as when approaching a gas phase molecule towards the surface in parallel adsorption, two possible scenarios can be considered to minimize the steric repulsion of the -CH$_3$ group with the surface: (i) the C=O group can be tilted with the O atom pointing towards the surface, such that the molecular plane of the gas phase structure is preserved; that is, both C=O group and the aromatic ring are uniformly tilting, or (ii) the C=O group alone is tilted and the geometry of the gas phase is not preserved. Since the aromatic ring can be strongly anchored to the surface via π interactions in a flat-lying geometry, it can be speculated that the C=O group will rather tilt towards the surface than an alternative tilting of both C=O and aromatic groups. The latter scenario will likely result in less anchoring point of the molecule with the surface. It should be pointed out that species S1– the flat-lying species– exhibits both $\delta_{as}(CH_3)$ and $\delta_s(CH_3)$ bands with higher intensity of the former vibration. Illustration of the two deformation modes as depicted in a non-perturbed molecule is given in Fig. 4.6. Their dynamic dipole moment is indicated by orange arrows. Note that the origin of each arrow is chosen at the molecule's center of mass and does not mean any particular vibration involves the atom, at which the arrow begins.

In the gas phase, the dynamic dipole moment of the $\delta_{as}(CH_3)$ is oriented perpendicular to the C_{ring}-$C_{(C=O)}$-$C_{(CH3)}$ plane, whereas the one of the $\delta_s(CH_3)$ is oriented parallel to that plane. If the molecular plane would lye parallel on the surface, the $\delta_s(CH_3)$ would not be detected due to the MSSR. The IR results thus indicate that the -CH$_3$ group adopts a slight upright orientation with respect to the surface plane. Such species, combining flat-lying geometry of the aromatic ring, an attractive nature of the C=O group and steric hindrance of the -CH$_3$ group with the surface, most likely establish itself in geometrically distorted species whose acetyl group is rotated with respect to the aromatic plane in which the C=O group is pointing towards the surface and the -CH$_3$ group is pointing away from the surface.

In spectrum (2), species S2 is detected. The appearance of the corresponding in-plane stretching modes is associated with a change in the molecular orientation and indicates a strong tilting of the aromatic ring with respect to the surface plane. In line with these observations, the intensity of the band assigned to the -CH$_3$ symmetric deformation (1362 cm^{-1}) sharply increases with increasing coverage, whereas the band comprising the -CH$_3$ antisymmetric deformation is saturated (1431 cm^{-1}). This indicates that these tilted species adopt a geometry in which the dynamic dipole moment of the $\delta_{as}(CH_3)$ is oriented fully parallel with respect to the surface plane – the C_{ring}-$C_{(C=O)}$-

$C_{(CH3)}$ plane – while the one of the $\delta_s(CH_3)$ modes is oriented fully perpendicular to this plane. This can be realized by adsorption of the C=O group nearly perpendicular to the surface plane.

As mentioned above, in a gas phase molecule the aromatic ring and the C=O group are lying in the same plane. Considering a uniform lifting of the molecule with respect to the surface plane, the relative intensities $\nu(C=O)$: $\nu(C-C)_{ring}$ are expected to be close to that one observed in a gas phase molecule (from reference [95] relative intensities $\nu(C=O)$: $\nu(C-C)_{ring} \approx 6$). The corresponding relative intensities $\nu(C=O)$: $\nu(C-C)_{ring}$ observed in spectra (4) of Figs. 4.5a and b amount to approximately ≈ 3. Therefore, it can be speculated that species S2, or more specifically, the tilted species is geometrically less perturbed than species S1 and is more similar to that observed for acetophenone ice.
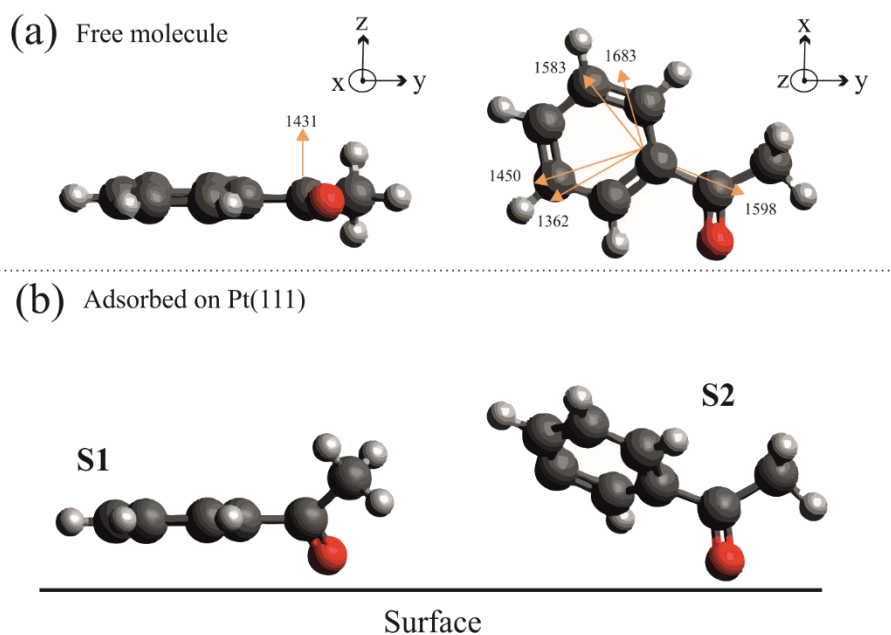
Figure 4.7: (a) Drawing of acetophenone in the gas phase. The dynamic dipole moment of selected modes is shown schematically. (b) Schematic representation of proposed adsorption geometries of acetophenone on Pt(111) as deduced with IR: S1: flat-lying species; S2: tilted species.

Based on these observations, we suggest two different structures of ketone species as shown schematically in Fig. 4.7b: (i) species adopting a flat-lying geometry of the aromatic ring, with the -CH$_3$ group pointing away from the surface – as suggested by the prominent appearance of the

$\delta_{as}(CH_3)$ and the absence of the bands comprising the in-plane stretching modes of the aromatic ring (**species S1**; vibrations characteristic: 1431+ 1683 cm^{-1}) – and (ii) species adopting a tilted orientation of the aromatic ring, as suggested by the prominent appearance of the bands comprising the ν(C-C) modes of the aromatic group (**species S2**; vibrations characteristic: 1450+ 1690 cm^{-1}). Distinguishing between the two species should not be misunderstood as referring to the same surface species merely exhibiting different vibrational frequencies due to dipole coupling effects, but rather to two different adsorption geometries which grow on the surface as a function of coverage. These species co-exist on the surface and do not interconvert to each other.

Based on comparison of the vibrational frequencies related to the C=O stretch at sub-monolayer coverage with those observed in multilayers of acetophenone, it can be safely assumed that the C=O bond of both species appears to be not strongly perturbed by the interaction with the metal and the main difference between the two species relies on their geometrical structures.
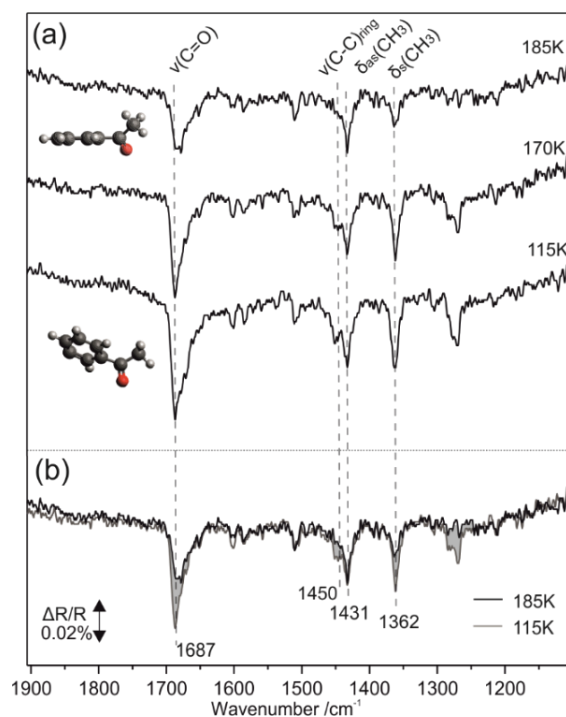
Figure 4.8: (a) IR spectra of acetophenone adsorbed on clean Pt(111) as a function of annealing temperature. The annealing temperatures are marked adjacent to the corresponding spectra. All spectra were recorded at 115 K. (b) Comparison between the IRAS spectra recorded at 115 and 185 K.

Figure 4.8 shows IR spectra of acetophenone at sub-monolayer coverage recorded at 115 K following heating to various temperatures. At 115 K, the two carbonyl species exist on the surface which were previously designated as species S1 (flat-lying) and S2 (tilted). The peak at 1431 cm^{-1}, assigned to the antisymmetric deformation of the methyl, is almost not affected by heating the surface to ~185 K. However, there is a significant diminution in intensity of the bands at 1362 and 1687 cm^{-1}. The latter vibration is also accompanied by a redshift to 1678 cm^{-1}. Also, by ~185 K, the band at 1450 cm^{-1} has completely disappeared. The attenuations of the bands at 1687, 1362 and 1450 cm^{-1} with increasing temperature is likely related to the disappearance of species S2. Three possible scenarios may be considered to explain such disappearance upon heating. The first is a chemical transformation of the acetophenone molecule. In this case, new vibrational modes should appear in the spectrum upon heating the surface whereas the intensities of those related to acetophenone molecule would likely diminish. The spectrum obtained at 185 K does not show any appearance of new vibrational bands. Therefore, chemical transformation of the acetophenone upon heating the surface to 185 K seems unlikely here. A second explanation may be related to interconversion of species S2 to S1. This can be associated with a change in adsorption geometry, such as for instance, tilted → flat interconversion and/or a change in the bonding configuration, such as for instance, interconversion of η^1 to η^2 (C,O). Conversion of η^1 to η^2 (C,O) of carbonyl compounds on metal surfaces has been previously suggested on both single crystals[119, 121] and real catalysts,[106] and was found to occur around the onset of the monolayer desorption when open sites become available.[119, 121, 122] It should be pointed out though, that such interconversion, being related to either a change in the adsorption geometry or the bonding configuration, would result in increasing intensities of the characteristic bands of species S1, that is the bands related to the δ_{as}(CH$_3$) at 1431 cm^{-1} and the ν(C=O) at 1683 cm^{-1}. The spectrum obtained at 185 K shows no intensity change of the band at 1431 cm^{-1} thus interconversion of species S2 to S1 can be likely ruled out. Lastly, attenuation of the characteristic bands related to species S2 may be associated with desorption of weakly bound tilted species from the surface above 185 K, leaving essentially only the species S1. Such energy difference between the two species can be explained by a stronger adsorption of species S1 due to predominant adsorption via the aromatic ring. Considering all the above-mentioned arguments, it is suggested that the tilted species (S2) is fully desorbing from the surface at temperatures near or above 185 K, leaving essentially only the flat-lying species (S1) on the surface.

4.3 Surface-driven ketone-enol tautomerization of acetophenone on Pt(111)[¥]

Tautomerization of simple carbonyl compounds to their enol counterparts on metal surfaces is theoretically predicted to enable an easier route for normally very difficult hydrogenation of the C=O bond on metal surfaces.[50, 51, 123] Specifically, once the carbonyl compound transforms to the enol form, the newly built C=C bond can be much easily hydrogenated than the C=O bond. This should result in a substantial acceleration of the overall reaction rate. Many experimental studies carried out on powdered catalysts put forward this predicted scenario to rationalize the experimental observations.[124-126] However, a detailed atomistic-level understanding of the enol formation and – probably even more important – enol stabilization on the metal surfaces, are largely missing, specifically for simple carbonyl compounds containing only one carbonyl group. In order to explore the feasibility of enol stabilization on metal surfaces, which is a difficult and the most crucial reaction step and explore the possibilities for rational design of new catalysts with tailor-made properties for enol formation and stabilization, a detailed atomistic-level understanding of the underlying surface processes is required, which is at the moment nearly completely missing.

Towards this goal, we studied keto-enol tautomerization for acetophenone adsorbed on clean Pt(111) with surface sensitive methods by employing a combination of IRAS and STM. The STM experiments presented in this section were performed by Marvin Schmidt at the Christian-Albrecht University of Kiel.

Figure 4.9 shows the STM image of acetophenone on Pt(111) following exposure at 200 K. A tendency of the acetophenone molecules to form dimers on the surface is clearly revealed. Two types of dimers were identified on the surface; the first type which is more abundant on the surface (82% of the dimer species; D1) shows symmetric species consisting of two identical elongated protrusions with a bright feature at their one end. The second type of dimer which is less abundant on the surface (18% of the dimer species, D2), is imaged as two asymmetric species: an elongated

---

[¥] The results of this section are adapted from work published in the *Angewandte Chemie*, reference 103: Attia, S.; Schmidt, M. C.; Schröder, C.; Pessier, P.; Schauermann, S. Surface-Driven Keto–Enol Tautomerization: Atomistic Insights into Enol Formation and Stabilization Mechanisms. *Angew. Chem. In. Ed.* 2018, 130 (51), 16901-16906.

protrusion with a bright spot at the end – as in the D1 dimer – next to an elongated protrusion lacking a bright spot.
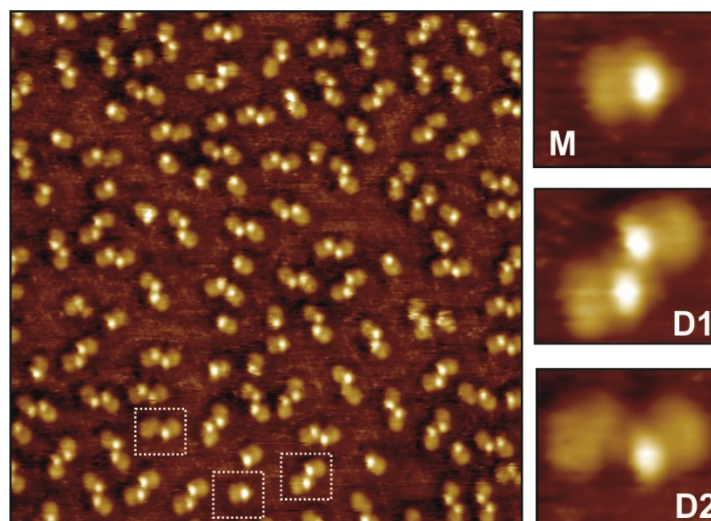
Figure 4.9: (left) STM image of acetophenone on pristine Pt(111) (exposure at 200 K; acquisition temperature 115 K; 1V, 0.29 nA, 15×15 nm^2); (right) Close-up images of a monomer (M) and two types of dimers (D1 and D2). Adapted with permission from [103].Copyright 2018, John-Wiley & Sons, Inc.

As observed by the STM image (Fig. 4.9), the acetophenone monomers obviously undergo some sort of interaction with each other. To clarify the chemical nature of the imaged species, we performed an IRAS study.

Figure 4.10 shows the IRAS spectra of acetophenone adsorbed on Pt(111) at 170 K at sub-monolayer coverages (1), (2). The bottom trace in the figure (3) displays the infrared spectrum of ~ 19 ML of acetophenone on Pt(111), and their frequencies and their assignments are shown correspondingly. The same vibrational frequencies that exist in the multilayer are also observed in the spectra obtained at sub-monolayer coverages (marked by vertical lines), pointing to a weak interaction of the acetophenone molecule with the Pt surface (for details see section 4.2). Besides, two new prominent bands at 1663 and 1203 cm^{-1} appear at sub-monolayer coverages. These bands are present neither in the multilayer, nor in the gas phase spectra of acetophenone[96], hence they cannot be related to any distinctive vibration of intact acetophenone molecules. Typically, vibrational bands in the range 1700-1640 cm^{-1} are characteristic of stretching vibrations of

conjugated C=O bond, whereas vibrational bands in the range 1250-1050 cm^{-1} are typical of stretching vibrations of C-O bond in alkoxy groups and alcohols.[127, 128] Considering a feasible keto-enol tautomerization reaction of various carbonyl compounds, it is primarily assumed that the band at 1663 cm^{-1} is assigned to the C=O bond of ketone form of acetophenone, and that the band at 1203 cm^{-1} is assigned to C-O bond of the enol form of acetophenone.
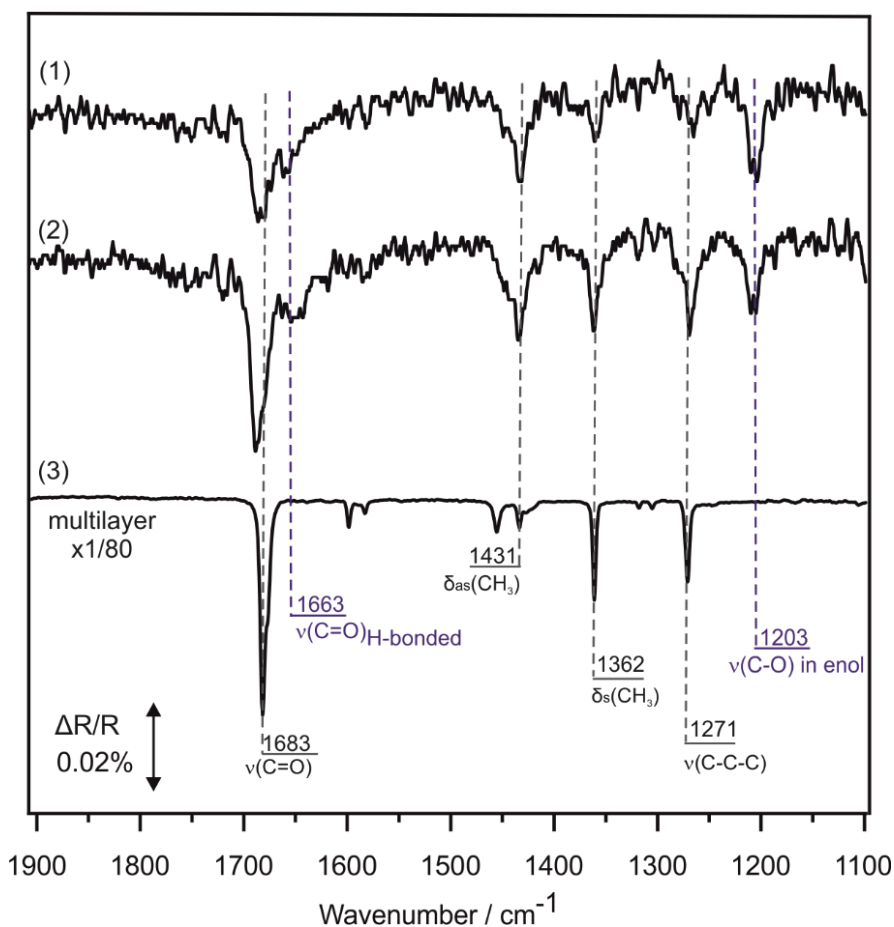
Figure 4.10: IR spectra of acetophenone adsorbed on pristine Pt(111) at different sub-monolayer coverages at 170 K; Acetophenone exposure (1): 4.5·10^{15}, (2): 6.1·10^{15} molecules·cm^{-2}, (3): the spectrum of a multilayer. Reproduced with permission from [104]. Copyright 2019, American Chemical Society.

The evolution of the IR spectra of acetophenone on Pt(111) was investigated at 190 K as a function of coverage, as depicted in Fig. 4.11. At the lowest coverage, following exposure of 1.8·10^{15} molecules·cm^{-2} shown by the upper most spectrum (1), there is almost an exclusive

formation of the two new bands at 1663 and 1203 cm^{-1}. These bands are simultaneously growing with increasing coverage, and saturate following exposure to $6.8 \cdot 10^{15}$ molecules·cm^{-2}. In spectrum (2), the onset of the band at 1683 cm^{-1} is detected; this band then further grows in intensity and finally dominates the spectra. Whereas the appearance of the two new bands and their intensities are strongly correlating with each other, the band at 1683 cm^{-1} does not correlate with these bands and develops independently- it has the lowest intensity at low coverage and the highest intensity at high coverage. Based on the coverage dependent IRAS spectra, it can be concluded that at least two types of acetophenone species exist on the Pt surface: (i) species exhibiting a combination of the vibrational bands at 1663 and 1203 cm^{-1}, and (ii) species showing vibration characteristics of largely unperturbed acetophenone molecules with the most prominent band at 1683 cm^{-1}.
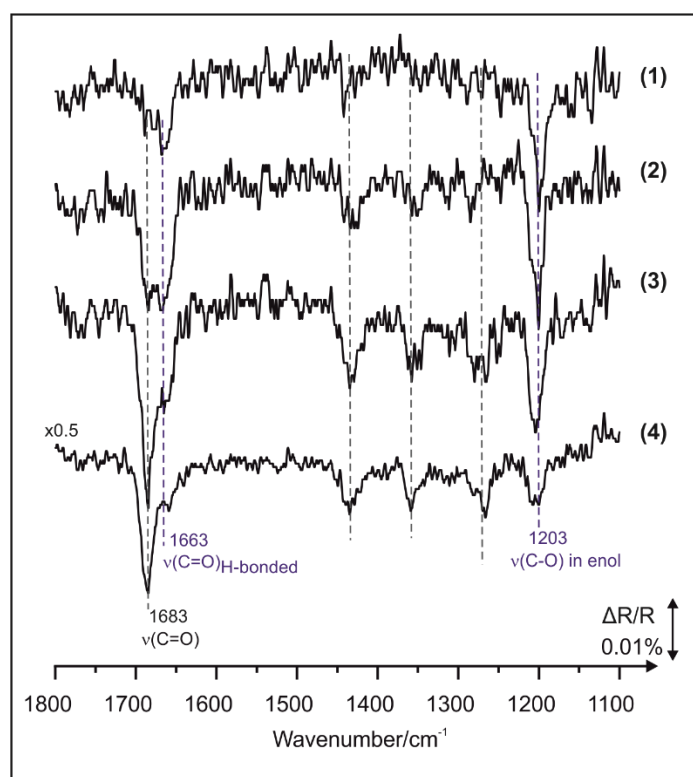
Figure 4.11: IR spectra of acetophenone adsorbed on pristine Pt(111) recorded at 190 K at different exposures: (1): $1.8 \cdot 10^{15}$, (2): $6.8 \cdot 10^{15}$, (3): $1.0 \cdot 10^{16}$, (4): $1.4 \cdot 10^{16}$ molecules·cm^{-2}. Adapted with permission from [103].Copyright 2018, John-Wiley & Sons, Inc.

Considering the observation that most of the acetophenone molecules are combined in dimers as previously imaged by the STM (Fig. 4.9), and spectroscopically two types of surface species were identified on the surface, it is suggested that at least two types of dimers exist on the surface; one of these dimer species consists of one ketone molecule and one enol molecule which are likely interacting via hydrogen bonds between the -C=O of the ketone molecule and the -OH of the enol molecule. The band at 1663 cm^{-1} is assigned to the C=O stretch of the ketone molecule and the band at 1203 cm^{-1} is assigned to the C-O stretch of the enol molecule. The assignment of the band at 1203 cm^{-1} to the stretching vibration of C-O single bond, is in an excellent agreement with previous theoretical and experimental studies on enol formation for a broad class of carbonyl compounds including acetone, diketones and ketoesters.[129, 130]

The second type of dimer consists of two ketone molecules which are likely interacting via hydrogen bonds in between the C=O group of one molecule to the -CH$_3$ group of the other. The vibrational frequency at 1683 cm^{-1} is assigned to the C=O stretch of the ketone molecules. As the related vibrational frequencies of this type of surface species coincide with that formerly obtained for acetophenone ice, it can be assumed that the intermolecular interaction in this dimer does not strongly affect the C=O frequency. In contrast, ketone-enol dimers featuring -COH---O=C, show a strong weakening of the C=O bond, resulting in a red-shift of the C=O frequency to 1663 cm^{-1}. A schematic illustration of the suggested surface species is depicted in Fig. 4.12.
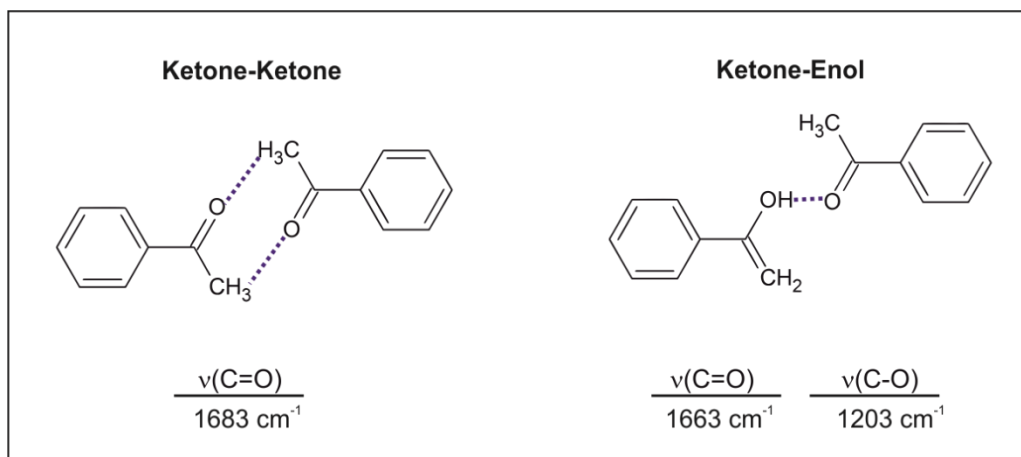
Figure 4.12: Schematic drawings of the suggested structures of two types of surface dimers; the hydrogen bonds are indicated by dotted lines. The characteristic stretching vibrations of the carbonyl group are marked adjacent to the corresponding structures.

Promising prototypes for studying the effect of hydrogen bonding on the carbonyl group are di-keto compounds. These compounds tend to undergo tautomerization reaction in which a chelated ring-like keto-enol tautomer can be formed with one of the carbonyls being transformed to a -C-O(H) entity, and the other carbonyl participating in the stabilization of the enol part of the molecule via hydrogen bonding between the -C=O and (H)O-C- functional groups.[129, 131-134]

The vibrational band close to 1663 cm^{-1} was previously assigned to the C=O stretch of chelated keto-enol species in various types of dicarbonyl and ketoesters compounds.[129, 135-137]

There are two reasons for the frequency down-shift of the carbonyl group in dicarbonyl compounds: (i) intramolecular H-bonding between the -O-H and the C=O groups in the enol tautomer, and (ii) mixing of the C=O and C=C stretching and C-OH deformation vibrations, which was theoretically predicted to downshift the C=O vibrational band to 1660 cm^{-1}.[136] The first phenomenon may be understood by the strength of the H-bonds between the two functional groups; the stronger is the acidity of the H-bond donor, the larger is the frequency shift of the H-bond acceptor. Actually, this trend is well shown in solutions[108, 138]; specifically, strong evidences for H-bonding formation of acetophenone with phenol were conferred experimentally and theoretically in which the C=O stretching frequency was reported at 1664 cm^{-1}, closer to that of acetophenone dissolved in water (1663 cm^{-1}).[108] Similar effect with the same vibrational frequency was reported for o-hydroxyacetophenone featuring carbonyl chelation through intramolecular H-bonds with OH substituent.[107]

For the single carbonyl compounds, the mechanism of intramolecular stabilization of the enol form is not possible. However, a similar mechanism can be realized via the formation of dimers, in which one molecule in the enol form can be potentially stabilized by H-bonding with the carbonyl group of the second molecule in the ketone form. Since the individual acetophenone molecules are not covalently bonded to each other in the dimers, the red-shift of the C=O group most likely originates from C=O---H-O H-bonds and not due to mixing between the C=O and C=C vibrations as calculated for chelated keto-enol dicarbonyls.[136] If dimers are formed on the pristine surface, the enol species is stabilized by the possibility of the formation of dimers via H-bonding between the OH group of the enol species and the C=O group of the ketone species. As H of the hydroxyl group is more acidic than that of the methyl group, H-bonds featuring C=O---HO interactions may be expected to have a more substantial effect on the C=O frequency than H-bonds featuring C=O---H$_3$C.

In line with these arguments, several groups have reported involvement of C_{sp2}-H and C_{sp3}-H donors in C-H---O HBs in solution, without noticeable frequency shift or intensity change of the C-H modes.[138-140] From a surface science perspective, the behavior of C-H bonds of adsorbed aromatic rings on metal surfaces as a result of HBs formation is in most cases impossible to characterize, as the aromatic plane tends to lay flat on the surface and hence cannot be detected with IR due to the MSSR. Nevertheless, the observation that this band is not visible cannot be used in order to rule out the existence of HB interactions. Therefore, indication for HBs formation of aromatic hydrogen with a C=O group is shown via the C=O stretch behavior. For instance, Mcbreen's group has reported a red shift of the C=O stretch of 7 cm^{-1} in acetone upon HBs formation with benzene on Pt(111).[141] Using Raman and IR studies, Nolasco et al. reported a red shift of 11 cm^{-1} of the C=O stretch in cyclohexenone dimers featuring C=O ---H-Aryl HBs. Their theoretical predictions have shown that the C=O stretching frequency is only slightly affected by hydrogen bonding, with a maximum calculated red-shift of 4 cm^{-1}.[138] In acetophenone, the H of the -CH$_3$ group is less acidic than the aromatic hydrogen, thus the frequency shift of the C=O group is expected to be small upon interaction with the -CH$_3$ group and slightly larger when it is hydrogen-bonded to e.g. a H of a phenyl group.

The two new observed bands at 1663 cm^{-1} and 1203 cm^{-1} are assumed to involve the C-carbonyl position of acetophenone. To further verify the assignments of these bands, the adsorption of acetophenone isotopically labelled with ^{13}C-carbonyl was investigated by IRAS. Shown in Figure 4.13 IRAS spectra of normal (a) and ^{13}C-carbonyl (b) acetophenone adsorbed on Pt(111) at 170 and 155 K as a function of coverage. In these spectra two vibrational regions are displayed for simplicity: the region containing the C=O and C-C (ring) stretching vibrations (~1700-1600 cm^{-1}), and that including the C-O single bond stretching vibrations (~1100-1300 cm^{-1}). On the top of Figs. 4.13a and b, the multilayer spectra of acetophenone on Pt(111) are depicted as a reference. The assignment of the IR vibration at 1683 cm^{-1} is straightforward and it corresponds to a stretching vibration of a C=O bond as previously discussed. This band is red-shifted by 40 cm^{-1} with the labeled compound, in good agreement with the theoretical (1.0228) as well as experimentally (1.023) observed isotopic shift factor expected for a ^{12}CO /^{13}CO exchange, i.e. 37 and 38 cm^{-1} respectively[110, 142]. The same red-shift of 40 cm^{-1} is also observed for the band at 1663 cm^{-1} with the labeled compound. This observation additionally supports the assignment of the band at 1663 cm^{-1} to the stretching vibration of a C=O group. Based on the spectroscopic and

microscopic observations, the combination of the bands at 1203 and 1663 cm^{-1} are assigned to a dimer that comprises one enol form and one ketone form of acetophenone which are interacting via H-bonds. The vibrational band at 1663 cm^{-1} is likely assigned to the H-bonded C=O of the ketone-form in a ketone-enol dimer, and the band at 1203 cm^{-1} is assigned to the C-O (single bond) of the enol-form.
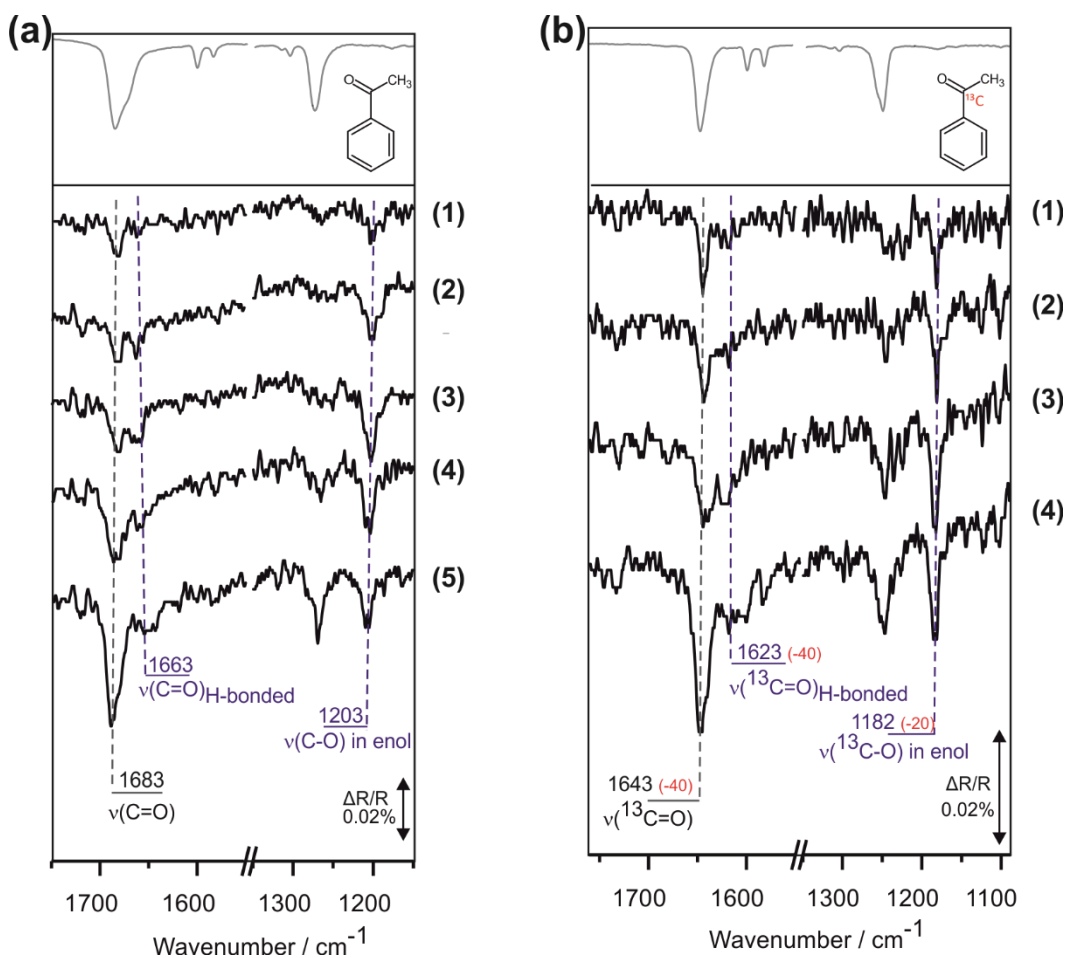
Figure 4.13: IR spectra of (a) acetophenone and (b) acetophenone isotopically labelled with ^{13}C-carbonyl recorded at different exposures at 170 and 155 K, respectively. Acetophenone exposure (a) (1): $2.1 \cdot 10^{15}$, (2): $3.5 \cdot 10^{15}$, (3): $4.3 \cdot 10^{15}$, (4): $5.3 \cdot 10^{15}$, (5): $6.2 \cdot 10^{15}$ molecules·cm^{-2} ; (b) (1): $4.9 \cdot 10^{14}$, (2): $5.9 \cdot 10^{14}$, (3): $8.9 \cdot 10^{14}$, (4): $1.4 \cdot 10^{15}$. On the top, multilayer spectra of acetophenone and ^{13}C-carbonyl acetophenone on Pt(111) are depicted as a reference.

The IRAS data of acetophenone on Pt(111) shown in Fig. 4.13 were obtained in the full accessible frequency range, 1000 –3800 cm^{-1}. Figure 4.14a shows IR spectra in the full frequency range. The intensities of the C-H vibrations, lying typically between 2800 and 3000 cm^{-1}, are hardly seen in these spectra related to sub-monolayer acetophenone coverages (enlarged view of this region can be seen in Fig. 4.14b). Two possible reasons can be responsible for this observation: the small dipole moment of the C-H bonds results in low intensities, which can be additionally strongly attenuated by the metal-surface selection rule for vibrations exhibiting a dynamic dipole moment parallel to the surface plane. Secondly, the sensitivity of the MCT detector used in the newly built setup is quite low in the frequency range characteristic of the C-H stretching vibrations (2800 – 3000 cm^{-1}). Usually, a different type of detector – the InSb detector – is used to obtain higher sensitivity in this vibrational range.

Experimental detection of the O-H group is also highly challenging for several reasons. First, the O-H vibrations, which are involved in H-bonding, are usually highly broadened[80] and therefore hardly visible in the spectra. Second, the O-H vibration in the enol form of acetophenone is expected to be parallel or nearly parallel to the surface, which should result in a strongly attenuated or completely missing intensity due to the metal surface selections rule. Also, the low absolute coverage of the enol species hinders detection of this vibration by IRAS. The reported frequencies of the O-H vibrations in alcohols span the range between 3690 (for gaseous species) and 3200 cm^{-1} (for solids), see .e.g. Ref. 143. Figure 4.14a shows the IR spectra in the range characteristic of O-H stretching vibration close to 3200- 3700 cm^{-1}. This region is dominated by a broad band in the range 3050–3500 cm^{-1}, which is an artifact originating from accumulation of molecular water ice during the measurement, not at the sample surface but rather at the cold (90 K) MCT IR-detector (placed outside the UHV chamber, see Chapter 3). This is a well-known phenomenon which is significantly reduced by an additional pumping of the detector chamber down to $5 \cdot 10^{-5}$ mbar using a turbo molecular pump. However, this artifact is very difficult to eliminate completely as some water is still present at $5 \cdot 10^{-5}$ mbar and unavoidably adsorbs at the cold surface of the detector. This water-related background changes can additionally hinder the observation of an O-H bond, which should appear in an overlapping frequency range. As it can be seen from the spectra shown in Fig. 4.14a, no individual OH vibration, which should have a significantly narrower width – 10-20 cm^{-1} as opposed to 450 cm^{-1} typically observed for water ice accumulated at the MCT detector – can be detected in these spectra. It seems like the most feasible reasons for the missing

OH band are the attenuation of the O-H vibration due to the metal surface selection rule as well as the strong broadening due to involvement into hydrogen bonding. Nevertheless, the missing OH vibration does not disprove the formation of enol species, as the other strong band characteristic for enol species – the C-O single bond – can be very clearly observed in the spectra.
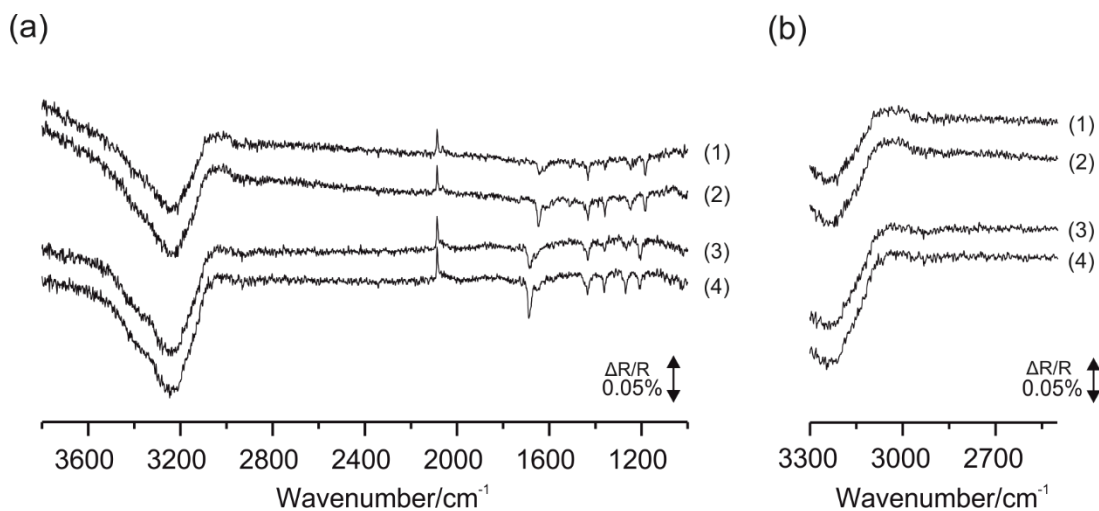
Figure 4.14: (a) Full scale spectra shown in Fig. 4.13: spectra (1)-(2) and (3)-(4) correspond to the two bottom spectra shown in Figure 4.13(b) and (a) respectively. (b) The same spectra shown in the vibrational range 3300– 2500 cm^{-1} characteristics for the CHx stretching vibrational region.

Combining the spectroscopic and microscopic information obtained by the IR and STM studies, the first type of dimer (denoted as D1 in Fig. 4.9) consists of two largely unperturbed ketone species, such that the intermolecular interaction between them does not strongly affect the C=O frequency. Most likely, this type of dimer consisting of the same building blocks -i.e. two identical protrusions with a bright spot- can be ascribed to the species consisting of two ketone molecules. The second type of dimer (denoted as D2 in Fig. 4.9) consists of one ketone species and one enol species, where the intermolecular interaction of the OH group with the C=O group strongly affects its vibrational frequency. The chemical structure of such a ketone-enol dimer, consisting of two different forms of acetophenone, most likely establishes itself in non-symmetric dimers, as displayed in Figure 4.15.
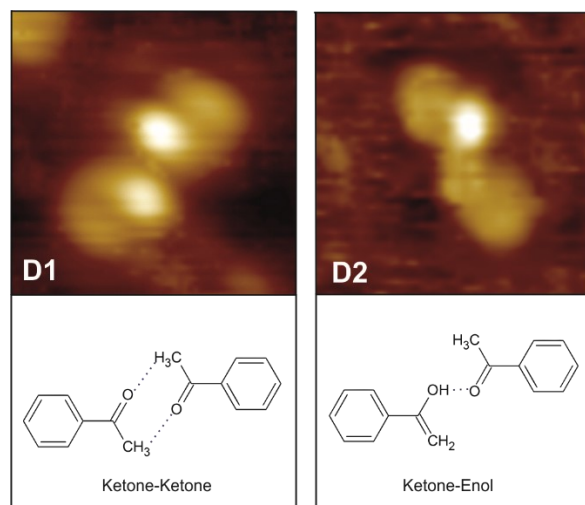
Figure 4.15: Close-up STM images of two types of surface dimers from Fig. 4.9 (top) and the corresponding suggested structures (bottom); D1: ketone-ketone dimer; D2: ketone-enol dimer. The hydrogen bonds are indicated by dotted lines. Adapted with permission from [103].Copyright 2018, John-Wiley & Sons, Inc.

It can be speculated that the dark protrusion in the D1 dimer is ascribed to the phenyl group, while the bright protrusion is attributed to the acetyl moiety, most likely to the methyl group. STM images of acetophenone adsorbed on Pt(111) recorded as a function of bias voltage over the same spatial region of the Pt surface did not show any change in image contrast. Therefore, it can be speculated that the physical topography, rather than the electronic structure, is the factor dominating the contrast in the STM image. Since the methyl group is assumed to be located much higher on the surface than the phenyl group (for details see section 4.2), the delocalized π-electron system of the latter appears as a dark spot in the STM image. Note that time-lapse sequences of the STM images of acetophenone on Pt(111) performed in our research group, have shown that the bright protrusion of monomers occasionally changes position from one side of the molecular backbone to the other as opposed to the constant distinct feature of the dimers. The fluctuations in the current of the bright protrusions in the monomers, can be most likely ascribed to molecular motion induced by the tunneling electrons. Regardless the observation that this effect was quenched in the dimers, pointing to the confined adsorption of the dimers on the surface, it can be concluded that the phenyl group featuring delocalized π-electron system cannot be ascribed to the bright spot which occasionally changes its shape, contrast and position over a time scale of minutes

and at a constant bias. In the dimer type D1, the two monomeric species are interacting via the ends containing the bright spots. As the interaction between two phenyl groups seems rather unphysical, in particular for flat-lying aromatic ring, as suggested by the IR data (Figs. 4.5a and b), we tentatively assign the darker protrusion to the phenyl group and the brighter protrusion to the acetyl moiety.

The formation of dimers and trimers of acetophenone on Pt(111) at room temperature was previously reported by Mcbreen[53]. The surface species were exclusively assigned to enol-enol oligomers. According to their hypothesis, enol formation involves hydrogen transfer through the surface, in which a C-H bond in the methyl group dissociates, followed by H diffusion via the Pt surface to the C=O group to form the enol tautomer.[53] The authors discussed the probability of enol formation as being related to the lifetime of a free hydrogen atom on the metal surface.

To clarify the feasibility of this mechanism, we investigated keto-enol tautomerization on hydrogen-precovered Pt(111). Figure 4.16a shows the STM image obtained for acetophenone on Pt(111) surface saturated with hydrogen. Remarkably, only monomers could be observed on this surface by STM, which appear as elongated protrusions with a bright spot at one end.

The effect of pre-adsorbed hydrogen was further investigated by IRAS measurements that were conducted at 115-300 K on Pt(111). Prior to the exposure of acetophenone, the Pt(111) surface was exposed to 900 L of D_2. At such exposure, hydrogen forms a saturated layer of surface adsorbed D species with a formal stoichiometry of D:Pt 0.8:1, positioned at 3-fold hollow sites.[144] [145] The corresponding IR spectra for acetophenone at 170 K are depicted in Fig. 4.16 (grey traces). While the spectra of a (^{13}C-carbonyl)- acetophenone multilayers on pristine and hydrogen precovered Pt(111) are similar, significant differences are observed at submonolayer coverages. For comparison, the IR spectra of acetophenone adsorbed on clean Pt(111) are also displayed (black traces). The total intensities of the CH_3 bending features (1431 and 1362 cm^{-1}) were found to be similar both on clean and hydrogen pre-covered Pt(111) at different acetophenone exposures. This observation might be considered as an indication that similar acetophenone coverages are formed on both surfaces. Remarkably, when hydrogen is co-adsorbed, only vibrational bands related to the unperturbed ketone form of acetophenone were detected, while the vibrations characteristic of ketone-enol dimers (1203 and 1663 cm^{-1}) did not appear. These findings clearly indicate that formation of enol species is inhibited by D adatoms. Obviously, the stabilization of the enol form by hydrogen bonding with a neighboring ketone does not occur at this surface. It

becomes also apparent that enol formation cannot be related merely to the availability of H (D) on the surface because if that was the case, a substantial amount of enol species would have to be observed on the H-containing Pt(111). This finding shows that enol formation does not follow the dissociative mechanism suggested by Mcbreen relying on H transfer through the surface and its abundance[53] but rather relies on the intramolecular process, in which a H atom is transferred to the carbonyl group to form a C-O-H entity and this enol form is stabilized by the intermolecular interaction with the neighboring ketone molecule via strong H-bonding. With this, the enol formation and stabilization mechanism of simple carbonyl compounds on surface is similar to that one occurring in the intramolecular process in dicarbonyl compounds.

Note that the monomers observed in all data sets, on either pristine or H-precovered surfaces, can be quite safely assigned to the ketone form of acetophenone since no stabilization mechanism for enol is available for the monomeric species. This observation additionally supports the assignment of the D1 species to a ketone-ketone dimer, as it consists of the same building blocks as the ketone monomeric species (M, Fig. 4.9).
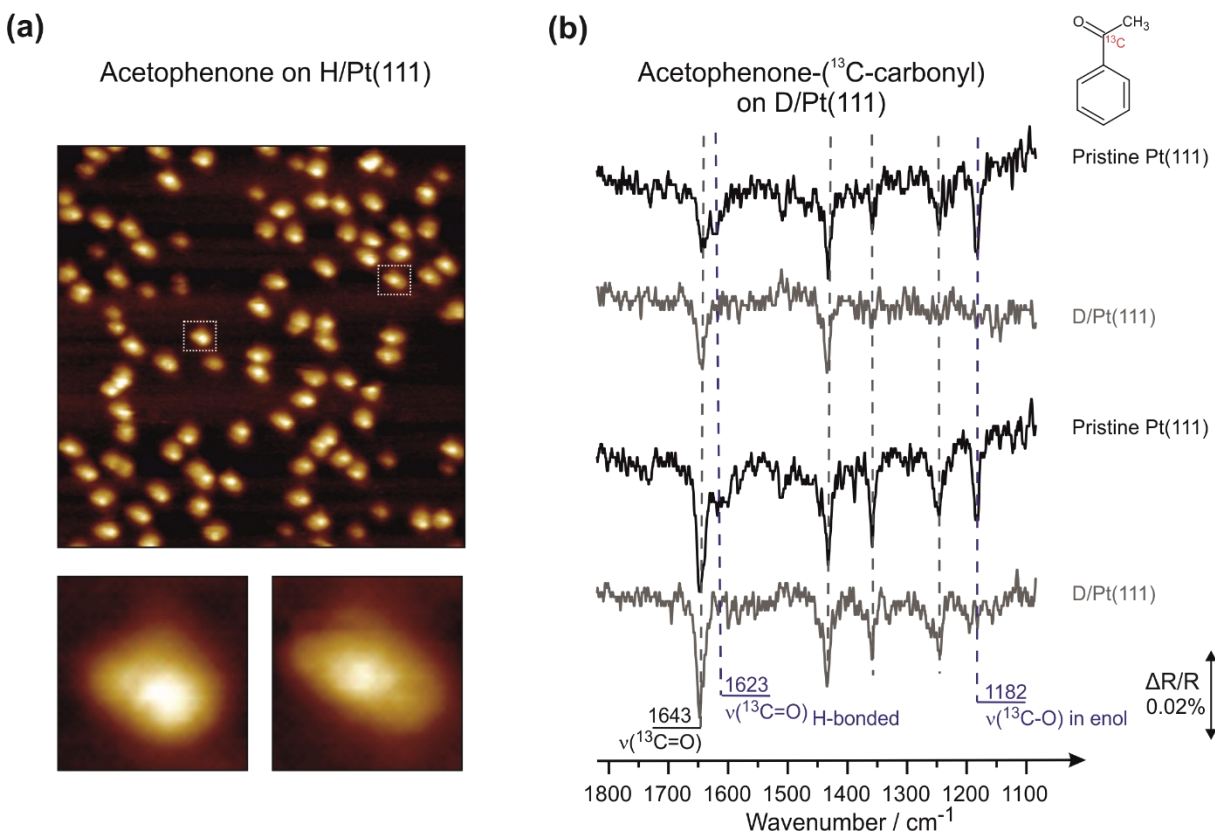
Figure 4.16: (a) STM image of acetophenone adsorbed at H-precovered Pt(111) (hydrogen exposure at 150 K; acetophenone exposure at 175 K; acquisition temperature 115 K, 1V, 0.29 nA, 15×15 nm^2); (b) Grey lines: IR spectra of (^{13}C-carbonyl)-acetophenone adsorbed on D-precovered Pt(111) obtained at two different submonolayer coverages; black lines: IRAS spectra of (^{13}C-carbonyl)-acetophenone adsorbed on pristine Pt(111). Spectra were recorded at 170 K. Adapted with permission from [103].Copyright 2018, John-Wiley & Sons, Inc.

The results indicate that the suppression of dimer on the surface, caused by the presence of adsorbed H, is the reason for the absence of the enol tautomer. Two general phenomena may be responsible for the appearance of the enol-form of acetophenone on surfaces, which are related either to *(i)* stabilization of otherwise unstable enol form via formation of surface dimers through H-bonding between OH and C=O groups, and/or *(ii)* facilitation of enol formation (i.e. decreasing the barrier for the H transfer to the carbonyl group).

The first phenomenon – stabilization of the enol form of acetophenone by dimer formation – might be related to the fact that the enol form can be rather unstable and – even if formed – quickly converts back to the ketone form, in the same known for many carbonyl compounds in the gas and liquid phases. On the surface, however, it is quite possible that the enol form can be stabilized by strong H-bonding to a carbonyl group of a neighboring ketone molecule. In that case, the surface acts as a support, at which both molecules can approach each other and form the dimer, consequently stabilizing the enol form. Stabilization of enol form is in fact well-studied for the dicarbonyl compounds (β-diketones and ketoesters), but not for the single carbonyl species. As discussed previously, these compounds form a chelated ring-like ketone/enol tautomer with one of the carbonyls being transformed to a -C-O-H entity, whereas the other carbonyl participates in the stabilization of the enol part of the molecule, via hydrogen bonding between the -C=O and H-O-C- functional groups.[129, 131-134, 146]

For single carbonyl compounds, a mechanism of intramolecular stabilization of the enol form is not possible. However, a similar mechanism can be realized via the formation of dimers, in which one molecule in the enol form can be potentially stabilized by H-bonding with the carbonyl group of the second molecule in the ketone form. The role of the surface in this case is related to bringing both acetophenone molecules in close vicinity to enable intermolecular interaction.

There are two feasible mechanisms that may act in the second scenario – hydrogen transfer to the carbonyl group can be feasibly facilitated due to formation of dimer species. Second, reduction of the activation barrier for H-transfer from the methyl to the carbonyl group.

Hydrogen transfer to the carbonyl group can be feasibly facilitated due to formation of dimer species. Previous experimental and theoretical gas-phase studies of β-cyclohexandione[52] and cyclopentanone[147] have shown that the barrier for intramolecular keto-enol tautomerization is high, while it is much reduced in the case of a C-H---O=C H-bonded dimer. In light of this, the suppression of dimer formation may be the reason why no enol-tautomers are observed in the presence of adsorbed H (or D). To the best of our knowledge, no computational predictions or experimental observations are available so far for surface-adsorbed dimers that would shed light on this mechanism; despite that, this possibility cannot be ruled out. In this case, the surface governs this process by bringing the individual molecules close to each other, thereby assisting dimer formation.

Reduction of the activation barrier for H-transfer from the methyl to the carbonyl group, can be also realized by means of weaken C-H bond due to the interaction of the methyl with the underlying metal. In such a case, the barrier for H-transfer from methyl-group to oxygen to form enol can be lowered. Previously, clear experimental evidences for the weakening of the C-H bonds were reported, e.g. for alkanes showing "softened" C-H stretching vibrational modes upon interaction with the underlying metal.[148] These prominent softened modes are not observed in our IR spectra as shown in Fig. 4.14b, however, it is very likely that the perturbation of the electronic structure of acetophenone due to interaction with the metal can potentially result in a significant weakening of the C-H bonds.

Further, it should be pointed out that all of the above discussed phenomena can be potentially acting in the studied surface chemistry: *(i)* formation of surface dimers can stabilize the enol form by hydrogen bonding with the second ketone molecule, *(ii)* formation of surface dimer species can lower the activation barrier for the intramolecular H-transfer, and *(iii)* the surface can weaken the C-H bond and with this reduce the barrier for intramolecular H-transfer. The degree of the contribution of these feasible individual mechanisms cannot be reliably estimated based on the available datasets. It can be quite surely claimed that the first and/or the second mechanisms related to dimer formation should be acting since the enol form can be observed only in surface dimers and not in the alone standing molecules. In order to be able to estimate the contribution of these phenomena to the formation and stabilization of the ketone form of acetophenone, a comprehensive theoretical study needs to be performed focusing on the analysis of different contributions. Nevertheless, the main conclusion of the study related to enol formation on surfaces, which is enabled and/or stabilized by intermolecular interaction with the ketone molecule in the dimer, can be very convincingly drawn based on the combination of the spectroscopic and microscopic data presented herein.

It should be pointed out that the second and the more abundant type of dimers – ketone-ketone dimers – are not formed on the H-precovered surface. This observation let us to conclude that adsorbed H must prevent H-bonding between the carbonyl group of one ketone molecule and the methyl group of the other ketone. We also speculate that the interaction of the carbonyl group of the ketone with adsorbed H_{surf} hinders the H-bonding to the neighboring molecules, and by that effectively prevents dimers formation. It is feasible that a similar effect plays also a role in the H-bonding between a ketone and an enol molecule in ketone-enol dimers. In such a case, the role of

H might be multiple: preventing enol stabilization by hindering H-bonding between the ketone and the enol form of acetophenone in ketone-enol dimers, as well as diminishing the activation of the C-H bond by the metal, which results in hindered intramolecular H transfer to form the enol form of acetophenone.

4.4 Formation and stability of enols through multiple hydrogen bonding: a mechanistic study in the 115-300 K temperature range.ς

The results presented in the previous section (section 4.3) have shown that the enol form of acetophenone on Pt(111) exists only in dimers. We did not detect enol species in a monomer form. It should be noted in that regard that the ketone form of mono-carbonyl compounds is more stable than its enol form,[149] thus the formation of enol species usually requires stabilization by for example, H-bonding as shown for various ketoesters and dicarbonyl compounds.[129, 135-137]

While the stabilization of enol is well understood for compounds comprising two carbonyls, much less is known about the formation and stabilization of enol for the case of mono-carbonyls, for which intramolecular stabilization via H-bonds is not feasible.

Involvement of the enol form of carbonyl compounds in the hydrogenation of a C=O double bond is a subject of ongoing discussion in the catalytic literature in the last two decades. The reason behind this persistent interest, lays in the fact that numerous theoretical calculations predict an alternative pathway based on keto-enol tautomerization as a first step to produce an enol, which can be hydrogenated on the C=C bond with a significantly lower activation barrier than in the case of direct hydrogenation of the C=O bond in the ketone form.[50, 51, 123] This mechanism was frequently invoked in catalytic studies on real powdered materials.[124-126] Thus, the problem of involvement of enol species into hydrogenation of carbonyl compounds is an intensively discussed topic in the broader catalytic community, regarding both experimental and theoretical perspectives.

To this day, no clear experimental proof regarding the theoretically predicted enol-related hydrogenation pathway exists. This is related to the problem that reaction intermediates on surfaces are very difficult to detect – especially under the reaction conditions in a short living state – and such detailed mechanistic studies generally require very well-defined and clean environment, such as UHV conditions and the incorporation of microscopic and spectroscopic tools on single crystalline-based or similarly well-defined surfaces. With the development of surface science methodology, it becomes possible to address such complex systems as e.g. presented in this study, and obtain new and valuable atomistic-level insights into the related processes.

This section presents one of the first studies, in which the mechanisms of chemical transformations of carbonyl compounds were addressed under high temperature conditions, allowing to monitor in-situ surface processes that are related to the initial stages of hydrogenation, by utilizing simultaneously spectroscopic and microscopic techniques.

The problem of enol-based hydrogenation of carbonyl compounds involves two independent key questions: (1) how the normally very unstable enol species can be stabilized on surfaces, and the reverse process of back-tautomerization to ketones can be avoided?, and (2) how adsorbed H atoms interact with enols and whether this interaction can facilitate hydrogenation.

This section deals with the first part of the problem – stabilization of enol species via interaction with the neighboring ketone molecule. This is a crucial question, because if enol molecules cannot be stabilized in the enol form, all the following steps of the suggested mechanism cannot occur. The second part of the problem will be addressed in section 4.5.

In the following, we will separate the discussion to formation of surface species of *(i)* largely unperturbed ketone species that can be related to ketone monomers (M) and/or ketone-ketone dimers (D1), and *(ii)* ketone-enol dimers (D2). The species exhibiting the prominent band at 1683 cm^{-1} (M or D1) can be safely assigned to the largely unperturbed ketone form of acetophenone as the related vibrational frequencies coincide with that obtained for acetophenone ice. In order to form a **ketone-ketone dimer (D1)**, two largely unperturbed ketone monomers should diffuse on the surface, bringing each other in close vicinity to enable intermolecular interaction. Note that the individual molecules in dimer D1 are connected at the positions containing the bright spots, and due to the fact that the vibrational frequency of the C=O bond is hardly affected by dimer formation, we believe that the two ketone molecules interact through H-bonding between the

carbonyls and H atoms of the methyl group. As discussed in section 4.3, rather weak hydrogen bonding is expected between the C=O and the methyl groups, resulting in a negligible effect on the C=O vibrational frequency. Therefore, vibrational bands showing frequency characteristic of acetophenone ice, such as the band related to the C=O stretching at 1683 cm^{-1}, can be referred to either ketone monomers or ketone-ketone dimers. The latter can be formed if the thermal energy of the ketone monomer is high enough to overcome the diffusion barrier on the surface.

As for the formation of **ketone-enol dimers (D2)**, two boundary cases should be considered: (i) the rate limiting step (i.e. exhibiting the highest activation barrier) of the overall process would be keto-enol tautomerism of individual adsorbed monomers, followed by an easier attachment of the formed enol to the carbonyl group of the ketone; or (ii) the rate limiting step of the overall process would be a concerted process in which the barrier for the intramolecular H-transfer from the -CH$_3$ group to the -C=O group is reduced due to the formation of dimers interacting via hydrogen bonding as was recently shown for gaseous dimers such as β-cyclohexandion[52] and cyclopentanone.[147] Obviously, both cases must fulfill two additional requirements: (i) the species should diffuse on the surface and can be brought in close vicinity to enable intermolecular interaction. For the case of tautomerism of an individual adsorbed monomer, this refers to the diffusion of both enol and ketone species, while for the case of the concerted process, this refers to diffusion of ketone species, i.e. ketone-ketone dimers (D1) must be initially formed. (ii) The enol form is stabilized via intermolecular H-bonding with ketone species, i.e. -OH group of the enol form with -C=O group of the ketone form.

We carried out a mechanistic study on acetophenone adsorption and chemical transformation over Pt(111) in a broad range of temperature conditions, in order to obtain these microscopic insights. Figure 4.17 shows the IR spectra of acetophenone adsorbed on Pt(111) at 115 K at different coverages in the submonolayer range; additionally, the bottom curve shows for comparison, a multilayer spectrum. The spectra obtained at sub-monolayer coverages of acetophenone exhibit generally the same vibrational bands as the spectrum obtained for the multilayer, yet they show a slightly different intensity distribution. This difference in the intensities results most likely from a specific adsorption geometry of acetophenone at the metal surface, which affects the relative ratio of the intensities due to the MSSR.[80]

Similarly to the trend observed in the spectra at 155 K at low coverage (for details see section 4.2, (1) in Figs 4.5a and b), there is a prominent appearance of the band comprising the $\delta_{as}(CH_3)$, whereas the bands related to the in-plane stretching modes of the aromatic ring (1450, 1583 and 1598 cm^{-1}) are missing. This situation is in sharp contrast to the intensity distribution found in acetophenone ice (Fig. 4.17, bottom curve, multilayer). The results indicate that at 115 K, up to exposures of $2.0 \cdot 10^{15}$ molecules·cm^{-2}, the acetophenone molecules adopt a geometry of a flat-lying aromatic ring, with the CH$_3$ group most likely pointing away from the surface.
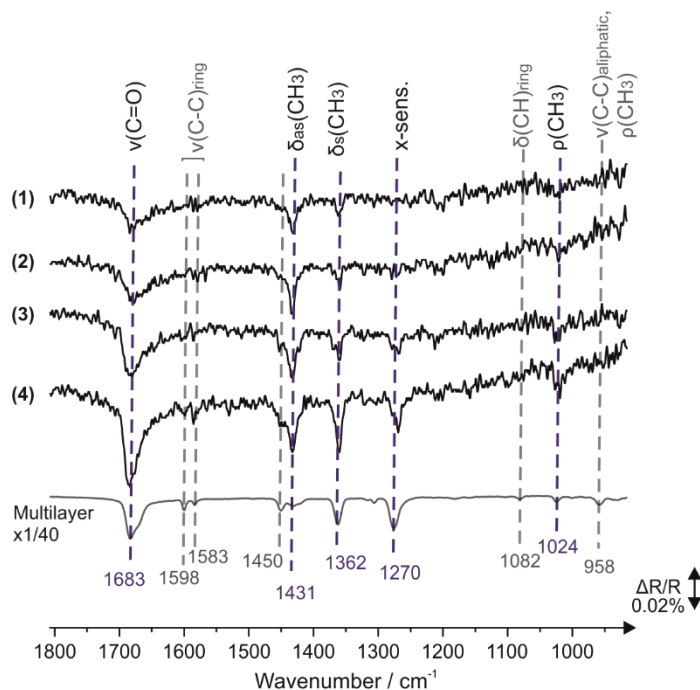
Figure 4.17: IR spectra of acetophenone adsorbed on pristine Pt(111) at different exposures (1): $1.1 \cdot 10^{15}$, (2): $1.4 \cdot 10^{15}$, (3): $2.0 \cdot 10^{15}$, (4): $2.3 \cdot 10^{15}$ molecules·cm^{-2} recorded at 115 K; all spectra are related to sub-monolayer coverages. The multilayer spectrum is shown at the bottom for comparison.

Importantly, no new bands, particularly at the frequencies 1203 and 1663 cm^{-1}, are observed at sub-monolayer coverages at 115 K. Only bands related to unperturbed ketone species (monomer and/or ketone-ketone dimers) are observed, whereas those related to enol species and/or ketone-enol dimers are missing at this temperature. Note that at this temperature acetophenone is present on the surface only as a monomer species as evidenced by STM (not shown). Given the fact that the band at 1203 cm^{-1} is completely absent, we can conclude that the enol tautomer is not stable

on this surface and even if formed, it quickly converts back to the ketone form as shown for many simple mono-carbonyl compounds.
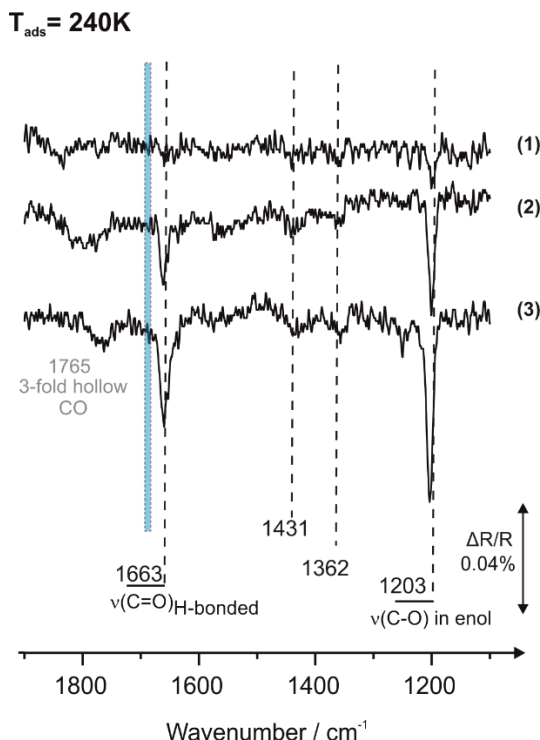
Figure 4.18: IR spectra of acetophenone adsorbed on pristine Pt(111) at different exposures (1): $1.3 \cdot 10^{14}$, (2): $2.7 \cdot 10^{14}$, (3): $4.0 \cdot 10^{14}$ molecules·cm^{-2} recorded at 240 K; The frequencies region related to unperturbed ketone species is indicated by the blue rectangle.

Figure 4.18 shows the IR spectra of acetophenone on Pt(111) at 240 K as a function of acetophenone exposure. Spectrum (2), corresponding to the exposure of $2.7 \cdot 10^{14}$ molecules·cm^{-2}, shows a prominent appearance of bands at 1663 and 1203 cm^{-1}. The intensities of these bands simultaneously increase with increasing coverage as depicted in spectrum (3). Note that spectrum (3) corresponds to a saturation coverage of acetophenone as no further growth of any of the bands were observed upon a further continuous deposition of acetophenone with the effusive molecular beam.

Similarly to the spectra obtained at 190 K (for details see section 4.3, Fig. 4.11) showing strong correlation of the bands at 1663 and 1203 cm^{-1}, here the two bands strongly correlate with each other. It becomes also apparent that the intensities ratio of the bands at 1663 and 1203 cm^{-1} in

spectra (2) and (3) remain roughly the same (5:3) with the most prominent band at 1203 cm^{-1}. The coverage dependent IR spectra suggest that at 240 K the bands at 1663 and 1203 cm^{-1} are related to the same surface species in a similar way shown previously for the spectra recorded at 190 K; that is the bands at 1663 and 1203 cm^{-1} are characteristics of ketone-enol dimers interacting via H-bonding in between the C=O group of one ketone molecule to the OH group of a second enol molecule. Importantly, at this temperature the band at 1683 cm^{-1} is not detected (denoted by the blue shaded rectangle in the IR spectra, Fig. 4.18). This indicates that at 240 K, most of the surface species are likely ketone-enol dimers. The species related to unperturbed ketone species in either monomer or dimer are obviously not formed on this surface at this temperature. The fact that the ketone species (monomer and/or ketone-ketone dimer) can undergo tautomerization and form ketone-enol dimer indicates that the acetophenone molecules have enough energy to overcome the tautomerization barrier. We cannot determine at this stage if at this temperature tautomerization occurs at all types of ketone species; that is individual adsorbed ketone monomers are being transformed to the enol form, or that ketone-ketone dimers are first formed and then transformed to ketone-enol dimers in a concerted process. Yet, it can be quite safely claimed that enol can be formed only if stabilized via H-bonding in ketone-enol dimers and not as monomers; as we show spectroscopically by the strong correlation of the bands at 1663 and 1203 cm^{-1} being related to the same surface species. This might point to the low stability of the enol monomer on the surface; a behavior similar to the situation found for acetophenone in the gas phase where the enol form is undoubtedly less stable than the ketone form.[150, 151] In other words, the enol monomer- even if formed, quickly converts back to the ketone form. Its formation on the surface can be realized by dimer formation in which the C=O group of the ketone species stabilizes the OH group of the enol species via H-bond.

It should be pointed out that the IR results of acetophenone on Pt(111) obtained at 190 K (see section 4.3, Fig. 4.11) have shown formation of both ketone species (monomer and/or ketone-ketone dimer) and ketone-enol dimers. Comparison between the spectra obtained at 190 and 240 K shows that the former exhibit a combination of ketone species (monomer and/or dimer) and ketone-enol dimers, whereas the latter shows an exclusive formation of ketone-enol dimers. This raises the question why not all surface dimers are transformed to ketone-enol dimers and some of them still exist as ketone-ketone dimers at 190 K, whereas at 240 K all species are undergoing this transformation and exist exclusively as ketone-enol dimers. One possible explanation for such

observation, in particular at lower temperatures, is that the dimers are adsorbed on different adsorption sites in which the activation barrier for tautomerization on one adsorption site can be overcome, whereas on the other one not. Nonetheless, with increasing temperature, the tautomerization barrier can be overcome for all adsorption sites accommodating the surface dimers. It should be pointed out that the main conclusion of the study related to enol formation on the surface, which is completely enabled at 240 K and stabilized by the intermolecular interaction with the ketone molecule in the dimer – can be very convincingly drawn based on the results presented herein.

The band at 1765 cm^{-1} is related to CO molecules adsorbed from the background prior to acetophenone deposition. Note that the intensity of this band is very low, corresponding to <0.01 CO molecules per Pt surface atoms (<1·10^{13} CO molecules·cm^{-2}). This will be discussed in more details in section 4.5.

Figure 4.19a shows STM image of acetophenone on Pt(111) at 285 K. The image shows formation of features that assemble into a variety of trimer and dimer configurations. This observation was noticed previously by the group of Mcbreen.[53] The blurring of the molecular image can be attributed to the high mobility of the molecules on the surface; a process that occurs on a timescale much faster than the feedback loop settings, which control the tip movement. Nevertheless, the formation of dimer and trimer on the surface can be clearly seen.

Some examples of the imaged species are indicated with dash rectangles and their close-up image is shown at the bottom correspondingly.

Figure 4.19b shows the IRAS spectra of acetophenone on Pt(111) at 280 K at submonolayer coverages (1)-(3). At submonolayer coverages, vibrational bands at 1663, 1634 and 1203 cm^{-1} are detected. Note that these bands are present neither in the multilayer nor in the gas phase spectra.[96] The bands at 1663 and 1203 cm^{-1} were assign in the previous section to ketone-enol dimers and were shown to strongly correlate with each other; they developed simultaneously with increasing coverage. Here, the band at 1634 cm^{-1} appears for the first time, and the band related to unperturbed ketone species (monomer and/or ketone-ketone dimer) -e.g. at 1683 cm^{-1}, is completely absent.

At the lowest coverage (1), there is almost an exclusive formation of the bands at 1634 and 1203 cm^{-1} whose intensities simultaneously increase with increasing coverage. Thus, the coverage dependent IR spectra suggest that at 280 K, an additional surface species exists on the surface; those exhibiting a combination of the vibrational bands at 1634 and 1203 cm^{-1}.

Furthermore, in spectrum (2) the band at 1634 cm^{-1} is saturated but the band at 1203 cm^{-1} is growing. Note that the lowermost spectrum (3) corresponds to the saturation coverage of acetophenone species at this temperature. In view of the strong correlation between the bands at 1663 and 1203 cm^{-1} observed previously at 190 and 240 K, we suggest that the consecutive growth of the bands at 1663, 1634 and 1203 cm^{-1} is a result of at least two types of surface species comprising the band at 1203 cm^{-1}: (i) species exhibiting a combination of the vibrational bands at 1634 and 1203 cm^{-1} and (ii) species exhibiting a combination of the vibrational bands at 1663 and 1203 cm^{-1}.

Inspection of the differences between the STM images obtained at 285 K (Fig. 4.19a) and 200 K (Fig. 4.9, section 4.3) shows that trimers are formed on the former image whereas monomers are missing, and the latter image shows no formation of trimers whereas monomers are present. In line with this observation, the spectroscopic data shows that at 190 K there is a prominent band at 1683 cm^{-1} being related to ketone species (monomers and/or ketone-ketone dimers), but no band is detected at 1634 cm^{-1} whereas at 280 K, the band at 1683 cm^{-1} is completely absent and the band at 1634 cm^{-1} is present. This temperature-dependent trend of the C=O frequencies is even more pronounced while comparing the IR spectra shown in Figs 4.17 and 4.19a obtained for acetophenone at 115 K and 280 K, with the former being related to an exclusive formation of unperturbed ketone species.

It is therefore suggested that trimer species formed at 285 K exhibit vibration characteristics that are related to the band at 1634 cm^{-1}. Additionally, the coverage dependent IR spectra show that the bands at 1634 and 1203 cm^{-1} are related to the same surface species.
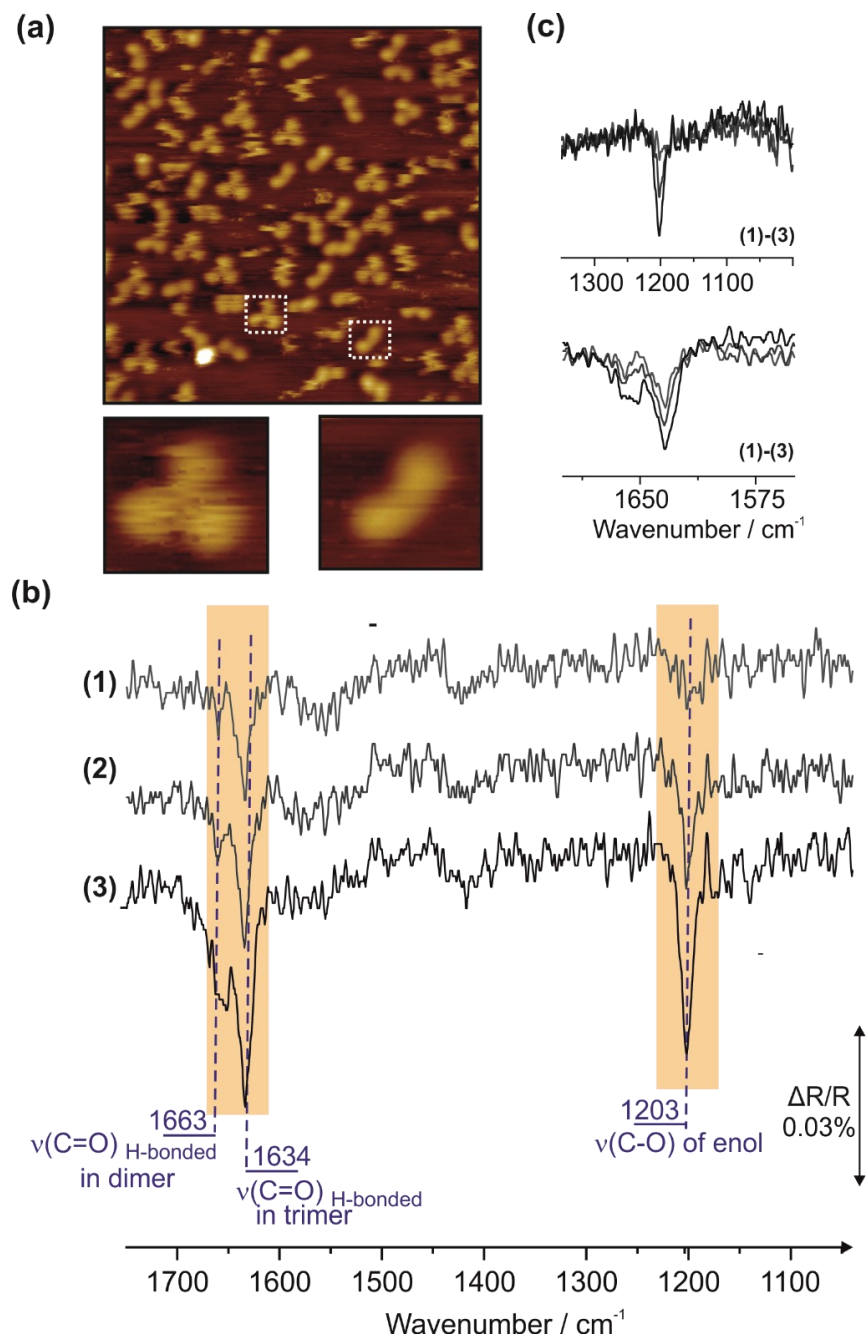
Figure 4.19: (a) top: STM image of acetophenone on pristine Pt(111) (exposure at 285 K; acquisition temperature 285 K; 1V, 0.29 nA, 15×15 nm^2); bottom: close-up images of a trimer and one type of dimer; (b) IR spectra of acetophenone adsorbed on pristine Pt(111) at different exposures of the acetophenone beam : 1.3·10^{14}, (2): 2.7·10^{14},(3): 9.0·10^{14} molecules·cm^{-2} recorded at 280 K. The C=O and C-O stretching frequencies are illuminated with orange rectangles; (c) spectra in Fig. 4.19b superposed. Adapted with permission from [104]. Copyright 2019, American Chemical Society.

A previous study by Demers-Carpentier et al[53] for acetophenone on Pt(111) have shown experimentally an appearance of a band at 1640 cm^{-1} which was assign to ν(C=C) mode of the enol. The interpretation was supported by HREELS spectra which showed the appearance of an intense band at 1640 cm^{-1} and the attenuation of a band at 1665 cm^{-1} upon heating from 180 K to RT. As the band at 1640 cm^{-1} was assigned to C=C stretch, and the band at 1665 cm^{-1} was assigned to a C=O stretch, they proposed that the structures observed on Pt(111) surface at RT are ascribed to H-bonded enol-enol structures. It should be noted that C=C stretching vibrations are expected to be very low in intensity compared to that of C=O stretching vibrations, with the former exhibiting a smaller dynamic dipole moment. Hence, assignment of the intense band at 1640 cm^{-1} to C=C stretching vibration seems unlikely here.

We have shown in section 4.3 that the extent of the frequency shift of the C=O group depends on the H-bond strength in these intermolecular H-bonded systems. Species forming H-bonding between the C=O group of ketone species and the OH group of enol species are expected to have a larger red-shift of the C=O frequency than for example H-bonds with less acidic group such as H of -CH$_3$ group.[108]

The band at 1634 cm^{-1} can be most likely assigned to the C=O stretching mode. A vibrational band close to 1634 cm^{-1} was previously observed in experimental studies on anthracendione derivative compounds.[152] This type of compounds consists of three conjugated aromatic rings with two keto groups located on the central ring. When two aromatic hydrogen atoms are replaced by OH groups, an interesting molecular structure can be observed, in which one C=O group participates in intramolecular hydrogen bonding with two OH groups and the second C=O group does not exhibit any intramolecular H-bonds. Such molecular structure is shown in Fig. 4.20. The C=O group which is interacting via intramolecular H-bonds with the OH groups was reported to exhibit a vibrational band in the IR spectra at 1627 cm^{-1}, whereas the intact C=O group exhibits the band at 1680 cm^{-1}.[152]
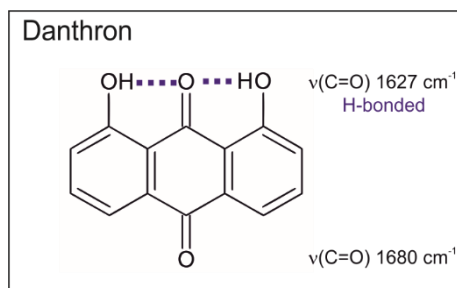
Figure 4.20: Molecular structure of Danthron revealing intramolecular hydrogen bonding. The vibrational frequencies of intact and H-bonded C=O groups are indicated[152]. Adapted with permission from [104]. Copyright 2019, American Chemical Society.

For acetophenone tautomers, the -OH group of the enol form is likely the most acidic H-bond donor in this system. The C=O band of the ketone form will thus exhibit the largest frequency shift while interacting with the OH group of the enol form. For a singular H-bond between C=O and OH groups in ketone-enol dimers, the IR data have shown a red shift of the C=O frequency by 20 cm^{-1} compared to the unperturbed ketone species (1683 cm^{-1}, monomer and/or ketone-ketone dimer, for details see section 4.3). Here, the frequency shift of the C=O group is significantly larger-ca. 50 cm^{-1}. Such a large frequency shift can be explained if the C=O group is involved *not in one* but in *two* H-bonds with -OH groups. This hypothesis agrees well with the STM image of acetophenone measured at 285 K (Fig. 4.19a) which shows that some of the molecules are combined in trimers. Spectroscopically we observed an additional surface species comprising the bands at 1634 and 1203 cm^{-1}. Therefore, we suggest that the trimer species are likely comprising one ketone molecule and two enol molecules in which the C=O group of the ketone molecule is interacting via H-bonds with OH group of two enol molecules. Figure 4.21 shows the most feasible model for dimer and trimer structures, which are consistent with the experimental observations.

Note that the dimer observed in this image, can be assign to ketone-enol dimers, as no vibrational bands related to the unperturbed ketone molecule were obtained. This is consistent with the IR results obtained at 240 K showing no vibrational bands related to unperturbed ketone species.

It should be pointed out though, that since we did not obtain an intramolecular resolution in the STM image (Fig. 4.19a), there might be some differences in the intermolecular alignment of the

imaged structures. The suggested structures are thus illustrated to show the *type* of the H-bond donor and acceptor (acidity and basicity); that is the C=O group of ketone species is involved with H-bonding of -OH group of one or two enol molecules. The trimer is likely assigned to one ketone molecule and two enol molecules, as the H-bond donor– the OH group of the enol– can form only a single H-bond. The H-bond acceptor – C=O group of ketone form of acetophenone – can possibly accept two H-bonds as shown for many single carbonyl compounds interacting via H-bonding with hydroxyl compounds.[153]
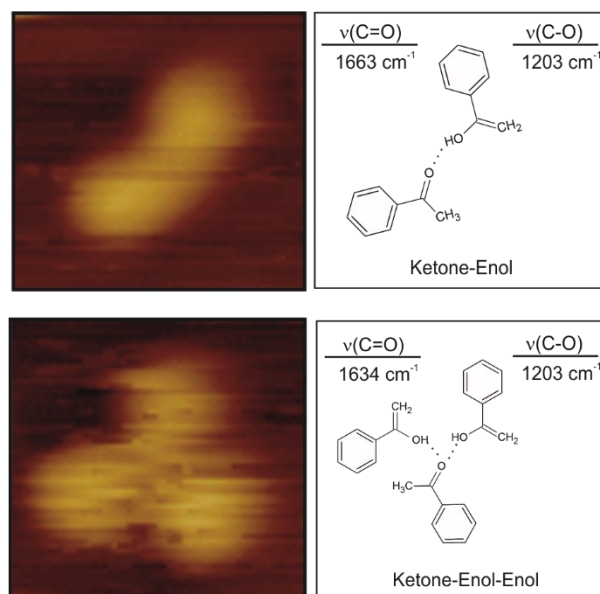
Figure 4.21: Close-up STM images of a dimer (top left) and a trimer (bottom left) from Fig. 4.19; corresponding suggested structures of ketone-enol dimer (top right) and ketone-enol-enol trimer (bottom right); the hydrogen bonds are indicated by blue dotted lines. The vibrational frequencies of the intermolecular H-bonded C=O group and the single bond C-O group are shown.

In summary, the evolution of the IR spectra of acetophenone investigated as a function of temperature suggests that different surface species can be formed on the surface at different temperatures: *(i)* the species showing the bands characteristic for largely unperturbed acetophenone with the most prominent band at 1683 cm^{-1}; *(ii)* the species exhibiting a combination

of the bands at 1203 and 1663 cm^{-1}; and *(iii)* the species exhibiting a combination of the bands at 1634 and 1203 cm^{-1}.

Figure 4.22 shows the IR spectra of acetophenone obtained at different temperatures. Two vibrational regions are displayed in the spectra for simplicity: 1750-1550 cm^{-1}, showing the region of the C=O stretching vibrations, and the 1275-1075 cm^{-1} region, showing vibrational bands related to C-O single bond stretching vibrations.[i]
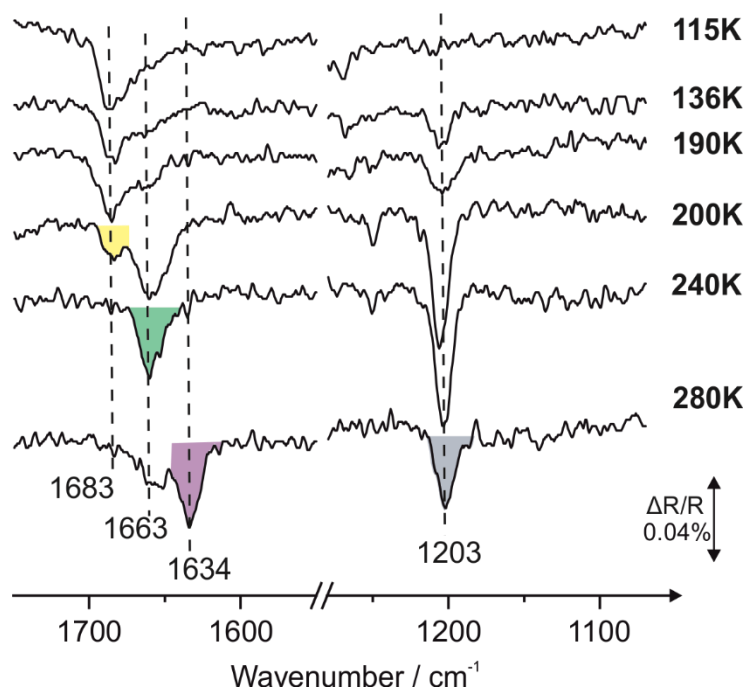
Figure 4.22: IR spectra of the C=O and C-O stretching region for acetophenone on Pt(111) as a function of temperature. The colored shaded areas under the IR curves in this figure are to guide the eye for the C=O and C-O related features (C=O; 1683 yellow, 1663 green, 1634 purple. C-O; 1203 blue). All spectra are related to sub-monolayer coverages. Acetophenone exposures (115 K): $2.3 \cdot 10^{15}$, (136 K): $3.8 \cdot 10^{14}$, (190 K): $1.0 \cdot 10^{16}$, (200 K): $6.5 \cdot 10^{14}$, (240 K): $4.0 \cdot 10^{14}$, (280 K): $9 \cdot 10^{14}$ molecules·cm^{-2}. Adapted with permission from [104]. Copyright 2019, American Chemical Society.

---

[i] The spectra were obtained at different exposures; chosen such to better represent the formed species. The spectra obtained at 115-190 K exhibit roughly the same relative intensities of the band at 1683 cm^{-1} and the spectra obtained above 190 K are shown at saturation coverage of acetophenone at a given temperature. This comparison allows to evaluate the intensity distribution in between the different surface species evolving at different temperatures.

At 115 K, only the band at 1683 cm^{-1} is detected, whereas the bands related to the ketone-enol dimers, i.e. 1663 and 1203 cm^{-1}, are missing. As previously mentioned, at this temperature acetophenone is present on the surface only as monomer species. Starting from 136- 190 K, two new bands evolve- at 1663 cm^{-1} which appears first as a shoulder, and at 1203 cm^{-1}- pointing to formation of ketone-enol dimers. The latter bands gain in absolute and relative intensity with increasing temperature and become the most prominent across the 200-240 K temperature range. It should be noted that at least up to 200 K, not only ketone-enol dimers are formed but also ketone-ketone dimers are present on the surface as was shown in the previous section by IRAS and STM (Fig. 4.9-4.11, section 4.3). In the temperature range 240-280 K, the vibrational band at 1634 cm^{-1} evolves, pointing to the formation of ketone-enol-enol trimers, which co-exist with the ketone-enol dimers as suggested by the combination of IRAS and STM findings.

The evolution of the IR data as a function of temperature shows that increasing the surface temperature upon acetophenone deposition results in formation of new species with red-shifted C=O frequency as compared to the unperturbed ketone species (monomer and/or ketone-ketone dimer); distinguishing between the new species should not be misinterpreted as referring to the same surface species that merely exhibit different vibrational frequencies due to dipole coupling effects, but rather to different surface species which grow on the surface as a function of temperature and show red-shifted frequency of the C=O group.

In the following, we will discuss the intensities distribution of the bands at 1683, 1663 and 1203 cm^{-1} in three temperature regions: 190-200 K, 200-240 K and 240-280 K.

Upon heating the surface from 190 to 200 K, the intensities of the bands at 1663 and 1203 cm^{-1} are increasing, whereas that of the band at 1683 cm^{-1} is decreasing. Such a change can be related to an interconversion of the unperturbed ketone species (i.e., 1683 cm^{-1}; monomer and/or ketone-ketone dimer) into ketone-enol dimer (1663+1203 cm^{-1}). Upon heating the surface from 200 to 240 K, the intensities distribution of the bands at 1663 and 1203 cm^{-1} remain roughly the same. Nevertheless, the band at 1683 cm^{-1} is vanishing. This might point to desorption of the unperturbed ketone species (monomer and/or dimer), leaving essentially only the ketone-enol dimer on the surface. Another possible explanation can be related to the interconversion of all unperturbed ketone species into ketone-enol dimer accompanied by a geometry change. In other words, the orientation of the C=O bond of the ketone as well as the C-O single bond of the enol is changed such that their projections along the surface normal become smaller. However, their absolute

concentration on the surface is increasing. Thus, the two opposite effects might exhibit a near zero change in the intensities of the bands at 1203 and 1663 cm^{-1}.

Upon heating the surface from 240 to 280 K, the intensities of the bands at 1663 and 1203 cm^{-1} are decreasing, and at the same time, the band at 1634 cm^{-1} is evolved. If the band at 1634 cm^{-1} is associated with trimer and increasing the surface temperature results in interconversion of dimer to trimer, the band at 1203 cm^{-1} is expected to grow in intensity upon heating the surface from 240 to 280 K, whereas the band at 1663 cm^{-1} is expected to decrease in intensity. This expectation agrees well with the intensity behavior of the band at 1663 cm^{-1} yet showing the opposite trend for the band at 1203 cm^{-1}. We therefore suggest that the decreased intensity of the band at 1203 cm^{-1} is likely associated with a change in the adsorption geometries of the molecular species. In other words, the orientation of the C-O single bond of enol is changed such that its projection along the surface normal becomes smaller thus exhibiting lower intensity of the band at 1203 cm^{-1}. It is very likely that species consisting of two different forms of acetophenone with at least two H-bonds in trimer establish itself in a strong change of the molecular orientation. Another possible scenario for the intensity change can be ascribed to desorption of the surface species at 280 K.

A summary of the temperature-dependent surface species of acetophenone on Pt(111) and the related vibrational bands is presented in Table 4.1, with the corresponding proposed surface species shown at the bottom.

Temperature/K	C=O Wavenumber/cm^{-1}	C-OH Wavenumer/cm^{-1}	Molecular structure	Proposed structure
280^a	1634	1203	trimer	KEE
	1663	1203	dimer	KE (1), KE (2)
240	1663	1203	dimer	KE (1)
200	1663	1203	dimer	KE(1)
	1683	-	unp. Ketone	K, KK
170	1663	1203	dimer	KE
	1683	-	unp. Ketone	K, KK
136^b	1663	1203	dimer	KE
	1683	-	unp. Ketone	K, KK
115^b	1683	-	unp. Ketone	K, KK

Subindices: unp. ketone= unperturbed ketone species (monomer and/or ketone-ketone dimer). a) no intramolecular resolution was obtained with STM. b) Based on IR data.
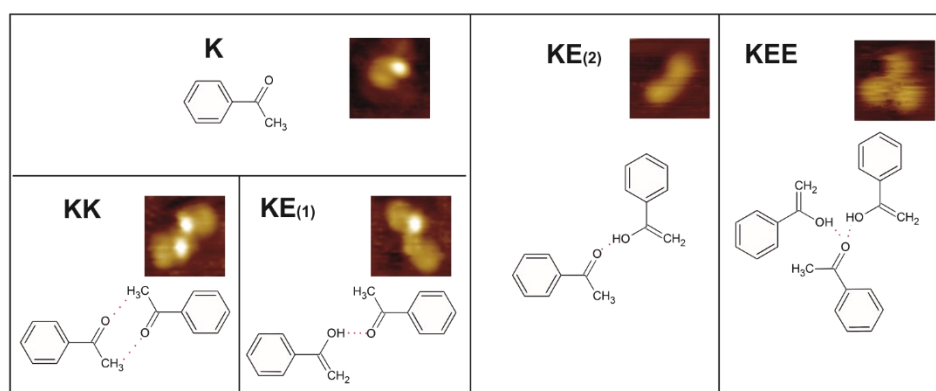
Table 4.1: Assignment of the C=O and C-O stretching frequencies of acetophenone tautomers on Pt(111) as a function of temperature. The suggested structures of the surface species are shown correspondingly (further details can be found in section 4.3); K: ketone monomer, KK: ketone-ketone dimer, KE: ketone-enol dimer, KEE: ketone-enol-enol trimer.

Based on the strong temperature dependence observed for the evolution of the ketone-enol(s) dimers and trimers on Pt(111), and considering the above discussion on the possible pathways of ketone-enol(s) oligomer formation, it can be concluded that the kinetic effect play most likely the major role in this process. Obviously, a kinetic barrier for tautomerization must be overcome in order to form the enol species. This becomes possible above ca. 136 K (as evidenced by IRAS) to

form the first enol species involved in a ketone-enol dimer, and at around 280 K to form the second enol molecule involved in a ketone-enol-enol trimer. The difference in the temperatures for the formation of the first and second enols accommodated in a dimer and in a trimer, correspondingly, indicates that tautomerization occurs in a concerted process within a complex of molecules (dimers or trimers) and not in an individual acetophenone monomer adsorbed on the surface. If the latter scenario was the actual case, similar activation barriers for dimers and trimers formation are expected which strongly contradicts the experimental observations. In contrast, the concerted process suggests the formation of a surface dimer (trimer), in which the simultaneous formation of H-bonds between the OH group of enol and the C=O group of ketone compensates the high energy costs for H-transfer from the methyl to the carbonyl group. This means that different activation barriers are expected for dimer and trimer formation because different reacting species are involved: two individual monomers for the formation of ketone-enol dimer compared to dimer and monomer species for building ketone-enol-enol trimer. In the latter process, formation of a trimer is expected to have a higher overall activation barrier since the formation of a second hydrogen bond – between a second enol and a carbonyl group of the ketone-enol dimer– might compensate for the low barrier most likely only to a low extent since the C=O bond is already involved in H-bonding with the first enol molecule. On the contrary, the formation of ketone-enol dimers involves strong hydrogen bonding of the enol to a non-bonded carbonyl group, which can compensate for the energy barrier for H transfer to a larger extent, and thus might result in a lower apparent activation energy.

Note that this study needs computational support from density functional theory calculations which can help to confirm or disapprove the suggestions put forward based on experiments e.g., a potential mechanism of how single ketone can stabilize multiple enols, or how hydrogen bonding helps to reduce the activation barrier for enol formation on Pt(111).

4.5 The role of keto-enol tautomerization in hydrogenation of acetophenone.

In this section, we demonstrate the crucial role of keto-enol tautomerization in hydrogenation of acetophenone over Pt(111) surface. Keto-enol tautomerization of simple carbonyls to their enol form is theoretically predicted to enable a low-barrier pathway for hydrogenation of normally very stable C=O bond. In the scope of this anticipated mechanism, the reaction can proceed via two consecutive steps, including formation of enol followed by a H insertion into the enolic C=C bond, and exhibits a significantly lower activation barrier than a direct H insertion into the carbonyl group. However, the experimental verification of such theoretical prediction is missing so far. Observed phenomena provide important atomistic-level insights into the mechanisms of heterogeneously catalyzed hydrogenation of simple carbonyl compounds and can be employed for purposeful modification of catalytic surfaces with functional groups capable of stabilizing the enol species and by this enable the low-barrier reaction pathway.

Molecular H_2 dissociatively adsorbs on Pt(111) to give a saturation coverage of nearly one H atom per Pt surface atom at low surface temperatures[145, 154]. The literature reports suggest three-fold hollow sites for H atoms on Pt(111) [see e.g. [155, 156]], but with negligible differences in the adsorption energy from other sites [see e.g. [157]]. Previously, H adsorption on Pt(111) surface was comprehensively studied by temperature-programmed desorption (TPD); the review by Christmann summarizes the most important conclusions of this study.[145, 154] Briefly, H forms two distinct states on Pt (111) – the weakly-bound β_1-H state, exhibiting the maximum of the desorption rate at about 225 K, and the strongly bound β_2-H state, desorbing at approximately 325 K. The filling of the β_1-state starts already at low coverages, before the filling of the β_2-state is completed, which was interpreted in terms of incomplete equilibration between these two states. The data for Pt(111) were analyzed in terms of two-states model, where the surface was assumed to be energetically homogeneous and the binding energy was influenced by lateral interactions between the adsorbed atoms. As a consequence, the activation energy for desorption was found to be constant (~9 kcal/mole) up to medium coverages and then to decrease continuously, which was found to be in fair agreement with the evaluation of the isosteric heat of adsorption from the adsorption isotherms.[145, 154] Based on their TDS spectra, adsorption into the β_1 state proceeds

before complete filling of the tighter bound β_2 state. However, during the course of the desorption program, it was shown that the two states desorb independently.[145, 154]

While the reported values of saturation coverage of H on Pt(111) are mostly between 0.8 and 1.0 [145, 157, 158], an absolute surface coverage of 1 has been reported following an excessively large exposure of ~2×10^4 L of molecular H_2 at 155 K.

In our experiments, we presaturated the Pt(111) surface with hydrogen at 150 K with a constant flux of 9×10^{14} molecules·cm^{-2}·s^{-1} for 3 min generated by one of the effusive beam sources (for details see chapter 3). These deposition conditions were preliminary used in all experiments to ensure saturation coverage of at least 0.8 H atoms per Pt atom in which both β_1 and β_2 states have been filled prior to acetophenone adsorption in accordance to previously reported data.[145] It should be noted that the desorption temperatures and the relative peak intensity of the two states reported by Christmann et al are slightly different than other experimental results[159] most likely due to different adsorption temperatures and heating rates. Based on the TDS spectra reported by Christmann[145], we can estimate the coverage as lying between 0.8-1 atoms per Pt atom in which both β_1 and β_2 states have been filled prior to acetophenone adsorption. Following the saturation exposure, the β_2 desorption peak is centered around 300 K, and the β_1 desorption peak occurs roughly at ~225 K. In order to understand how the nature of adsorbed hydrogen affects the adsorption and reactivity behavior of acetophenone, co-adsorption of acetophenone species was studied on two types of surfaces: *(i)* Pt(111) containing both β_1- and β_2-H states, and *(ii)* Pt(111) precovered with the β_2-H only. The latter surface was produced by adsorbing hydrogen at 150 K, at which both states are populated, followed by heating the surface to 240 K, at which the weakly-bound β_1-H desorbs, while the stronger bound β_2-H remains on the surface.

The interaction of acetophenone with adsorbed H on Pt(111) was further investigated with STM. The STM experiments presented in this section were performed by Marvin Schmidt at the Christian-Albrecht University of Kiel.
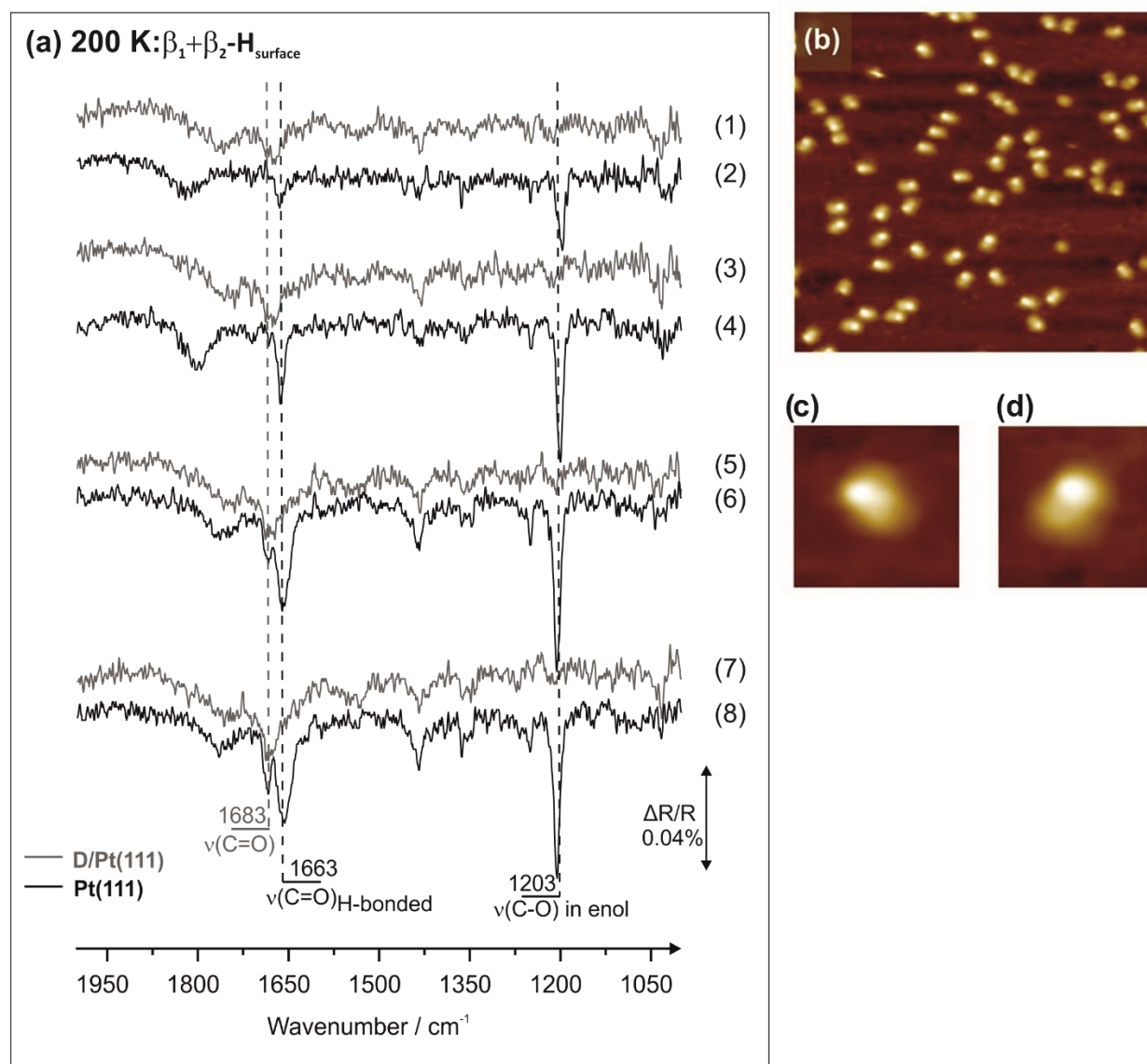
Figure 4.23: IR spectra of acetophenone adsorbed on pristine (black lines) and D-precovered (gray lines) Pt(111) obtained at different sub-monolayer coverages recorded at 200 K. Acetophenone exposure (gray lines) (1): $3.1 \cdot 10^{14}$, (3): $5.8 \cdot 10^{14}$, (5): $2.0 \cdot 10^{15}$,(7): $3.9 \cdot 10^{15}$ molecules·cm^{-2}; (black lines) (2): $1.7 \cdot 10^{14}$, (4): $2.1 \cdot 10^{14}$,(6): $6.5 \cdot 10^{14}$,(8): $1.2 \cdot 10^{15}$ molecules·cm^{-2}. (b)-(d) STM images of acetophenone adsorbed on H-precovered Pt(111) (H$_2$ exposure at 150 K; acetophenone exposure at 190 K; acquisition temperature 115 K, 1V, 0.29 nA, (b): 23×23 nm^2).

Figure 4.23a shows the IR spectra of acetophenone adsorbed on D-precovered surface recorded at 200 K for different coverages (1,3,5,7, gray). The IR spectra recorded on the pristine surface are shown correspondingly (2,4,6,8, black).

The IR spectra of acetophenone on the D-precovered surface reveal only vibrational bands that are related to the unperturbed ketone form of acetophenone, with no indication for vibrations characteristic of ketone-enol dimers (1203 and 1663 cm^{-1}). For comparison, the spectra recorded on the pristine surface show the prominent appearance of bands that are related to ketone-enol dimers in addition to that of the largely unperturbed ketone species (monomer and/or ketone-ketone dimer). Note that the results obtained for the pristine and precovered surfaces are strongly correlating for all data set. A similar trend can also be seen in the spectra of Figs. 4.13a and b obtained at 170 and 155 K for acetophenone and isotopically labelled acetophenone respectively. Figures 4.23b shows the STM image obtained on Pt surface saturated with hydrogen after adsorption of acetophenone at 200 K. We have shown in section 4.3 that at 200 K, acetophenone forms two types of dimers on the pristine surface (for details see Fig. 4.9; D1 and D2). Here, the majority of acetophenone molecules seems to form monomers on the surface. Clearly, dimers cannot be formed on this surface. Each of the acetophenone molecules appears as an elongated protrusion with a bright spot at one end. It becomes also apparent that the acetophenone monomers appear blurry and exhibit slightly different protrusion shape than that observed on the pristine surface (see Fig. 4.9 in section 4.3). It is very likely that the electronic structure of acetophenone adsorbed on H-precovered surface is different from that obtained on a pristine surface. Such differences may also arise from different binding sites of the molecule on the surface. Formation of structures that can be imaged with intramolecular resolution is due to the low mobility of the adsorbed surface species in the STM time scale. The fact that we were not able to obtain intramolecular resolution on the precovered surface might be interpreted as increased mobility of the acetophenone molecules compared to that one observed on the pristine surface at the same temperature. Note that STM images of acetophenone adsorbed on H/Pt(111) recorded as a function of bias voltage over the same spatial region of the Pt surface did not show any change in the image contrast. Therefore, it can be assumed that the physical topography, rather than the electronic structure is the dominant factor for the contrast in the STM image. Considering either the methyl or the C=O groups located much higher on the surface than the phenyl group, the delocalized π-electron system of the latter may appear as a dark protrusion in the STM image. This suggestion

is consistent with the flat-lying geometry of the aromatic ring reported previously in section 4.2 (Fig. 4.7).

In line with the STM observation showing no formation of dimers on the H-precovered surface, only vibrational bands related to the unperturbed ketone species of acetophenone were found, while the vibrations characteristic to ketone-enol dimers (1203 and 1663 cm^{-1}) did not appear. Obviously, formation of the enol form of acetophenone as well as of ketone-enol surface dimers stabilized by H-bonding does not occur at this surface. There are several reasons that can be invoked as a possible explanation for inhibition of dimer formation by co-adsorbed hydrogen. First, formation of any kind of dimers – either ketone-enol or ketone-ketone – requires formation of hydrogen bonds between the carbonyl group of the ketone and a hydrogen atom of the neighboring molecule, incorporated either into the OH-group in case of ketone-enol or into the CH_3-group in case of ketone-ketone species. If H is present on the surface, it might interact with the carbonyl groups via a bond similar to hydrogen bonding, thus preventing hydrogen bonding between neighboring molecules. Second, formation of ketone-enol species relies on H transfer from the CH_3-group to the O atom of the carbonyl group to form the enol part of the dimer. This process might require considerable perturbation of the molecule's electronic structure by the underlying metal, which might occur effectively on pristine Pt(111) but be hindered on the H-containing surface as a result of weaker interaction between acetophenone and H-precovered Pt. In this case, the inhibition of intramolecular H transfer in acetophenone by co-adsorbed H can be a potential reason for missing ketone-enol dimer formation. It should be noted, however, that the second phenomenon might explain the missing ketone-enol dimer formation but not the fact that the ketone-ketone dimers are also not formed. Therefore, the first explanation based on hindered intermolecular hydrogen bonding due to competition with adsorbed hydrogen seems to be a more likely scenario as it could account for the lacking formation of both types of dimers.

The low intensity band detected at 1820 cm^{-1} in spectrum (2) is assigned to the stretching vibration of CO molecules adsorbed on hollow sites of Pt(111)[81, 160]. Note that the intensity of this band is very low, corresponding to < ~0.02 CO molecules per Pt surface atoms (or < ~$2\cdot10^{13}$ CO molecules·cm^{-2}). The frequency of this band is red-shifted to 1765 cm^{-1} with increasing exposure of acetophenone.

During the time interval between the stabilization of the sample's temperature and the acquisition of the background IR spectrum, a small amount of background CO could be very well adsorbed. In fact, when adsorbing acetophenone on the Pt(111) surface during the measurement, changes in the frequencies region related to stretching vibrations of individual CO molecules occur. Fig. 4.24 shows the IR spectra of acetophenone on Pt(111) as a function of coverage in the frequencies range 1100-2250 cm^{-1}. It represents the spectra shown in Fig. 4.23 for the pristine surface and its spectra are correspondingly numbered. In spectrum (2), following acetophenone exposure of $2.1 \cdot 10^{14}$ molecules·cm^{-2}, the band at 2087 cm^{-1} is strongly attenuated. This band is assigned to CO molecules adsorbed on a top sites[81]. The intensity of this band indicates no significant change with increasing exposures of acetophenone (4,6,8). Also to be noted in spectrum (2) is that the attenuation of the band at 2087 cm^{-1} is accompanied with the appearance of a broad band at 1820 cm^{-1}. Thus, we suggest that upon adsorption of acetophenone, CO molecules are repelled from a top sites and are attracted to hollow sites. The same trend is noticed in spectrum (4), with the attenuation of the band at 2074 cm^{-1} and the band centered at ~1800 cm^{-1}. The former band is assigned to CO molecules adsorbed on a top site of a step-edge of Pt(111) in accordance to previously reported data.[81] It becomes also apparent that following the occupation of the background CO molecules on the hollow sites, the bands at 2087 and 2074 cm^{-1} show no significant change in intensities and peak position with increasing exposures of acetophenone (spectra 4,6,8). However, the frequency of the band related to the hollow sites at 1820 cm^{-1} is red shifted by 55 cm^{-1} when the acetophenone coverage increases from zero to saturation. Such a shift is likely a consequence of dipole-dipole interactions of adsorbed background CO with acetophenone molecules. The results reported herein show that acetophenone molecules possibly replace CO molecules on atop sites. This model could explain the infrared observation of three-fold hollow CO upon co-adsorption of acetophenone. The results thus suggest that the band at 1765 cm^{-1} is not related to any distinctive vibration of acetophenone molecules, but rather to individual CO molecules adsorbing from the background.
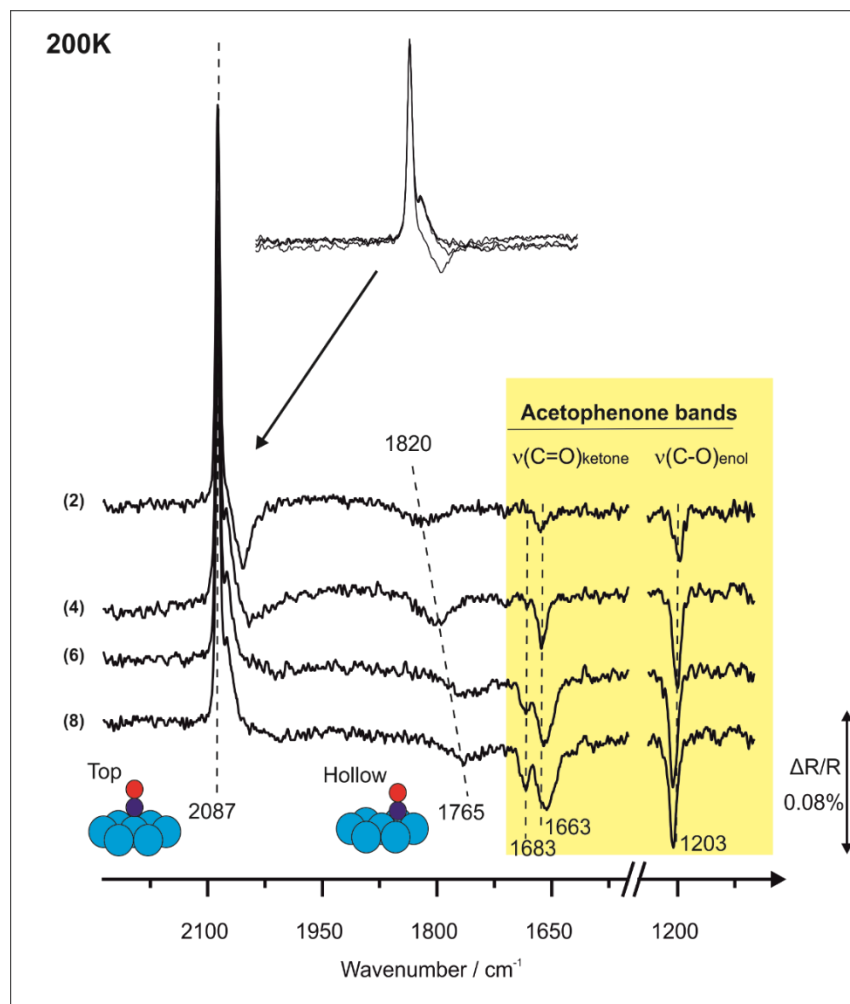
Figure 4.24: IR spectra of acetophenone adsorbed on pristine Pt(111) recorded at 200 K at different exposures: (2): $1.7 \cdot 10^{14}$, (4): $2.1 \cdot 10^{14}$, (6): $6.5 \cdot 10^{14}$, (8): $1.2 \cdot 10^{15}$ molecules·cm^{-2}. Inset: comparison of spectra (2)-(8) in the range 2250-1950 cm^{-1}.

In the next step, the acetophenone interaction with H(or D)-precovered surface containing only one type of hydrogen – strongly bound β_2-H species – was investigated.

Figures 4.25a shows the IR spectra of acetophenone on Pt(111) after saturation with hydrogen at 240 K. The grey spectra (1),(3) and (5) in Figure 4.25a are related to acetophenone adsorbed at different sub-monolayer coverages on the D-precovered surface, while the black spectra (2), (4) and (6) were recorded with acetophenone on the pristine surface and is shown for comparison at the same temperature. Note that on the pristine Pt(111) surface, only ketone-enol dimers are formed at 240 K, as evidenced by the presence of bands at 1203 and 1663 cm^{-1} and the absence of

a band at 1683 cm^{-1}. The STM image obtained on β_2-H-containing Pt(111) is displayed in Fig. 4.25b.
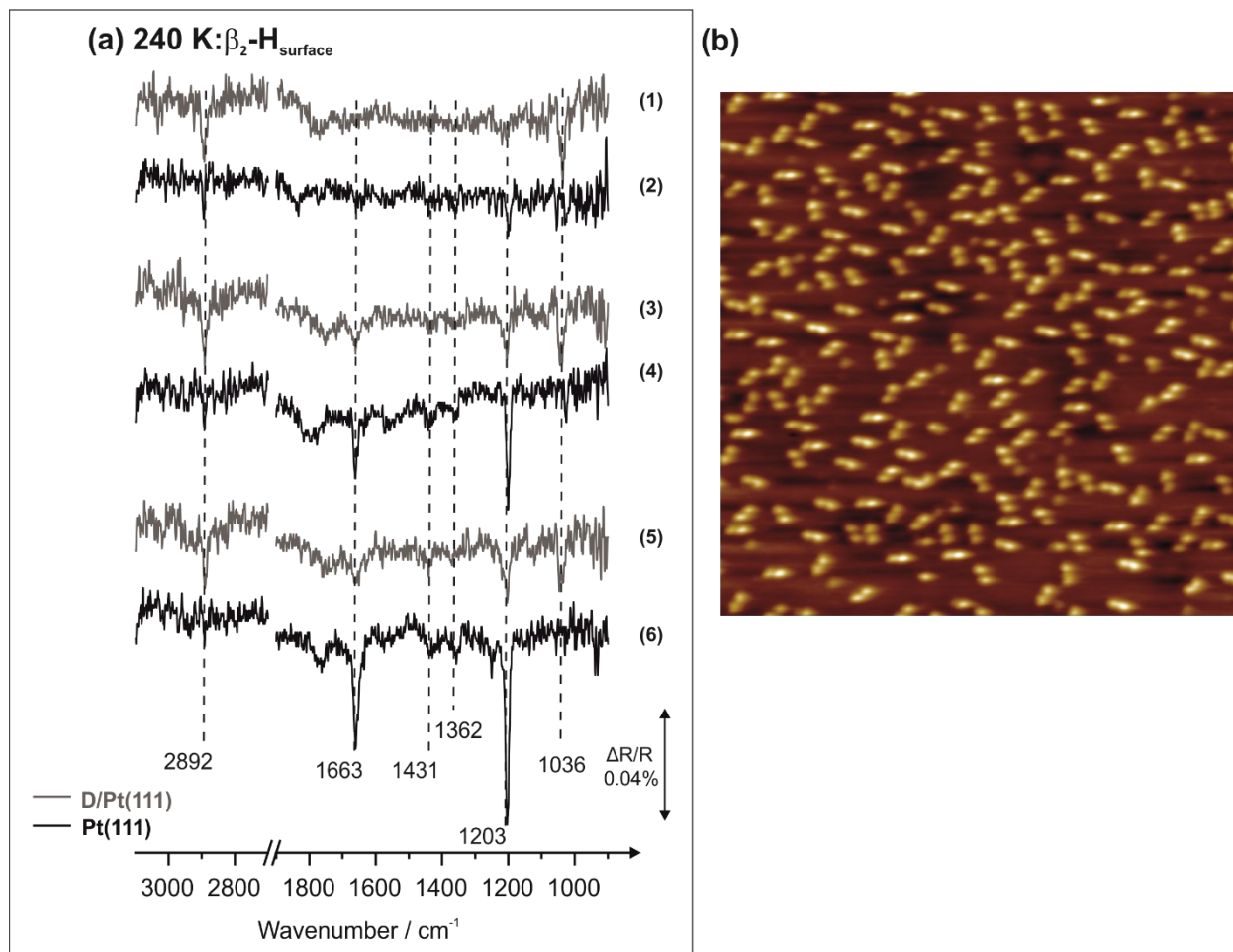
Figure 4.25: (a) IR spectra of acetophenone adsorbed on pristine (black lines) and D-precovered (gray lines) Pt(111) obtained at different sub-monolayer coverages recorded at 240 K. Acetophenone exposure (gray lines) (1): $2.7\cdot10^{14}$, (3): $4.0\cdot10^{14}$, (5): $5.4\cdot10^{14}$ molecules·cm^{-2}; (black lines) (2): $1.3\cdot10^{14}$, (4): $2.7\cdot10^{14}$,(6): $4.0\cdot10^{14}$ molecules·cm^{-2}; (b) STM image of acetophenone adsorbed on H-precovered Pt(111) (hydrogen exposure at 150 K; acetophenone exposure at 240 K; acquisition temperature 115 K, 1V, 0.29 nA, 30×30 nm^2);

It can be clearly seen that acetophenone dimers are formed on this surface again and most of the adsorbates are accommodated in dimer species (68% of the surface species).

The spectra obtained on the β_2-H-covered surface (1,3,5) show a prominent appearance of bands at 1203 and 1663 cm^{-1} which indicates the formation of ketone-enol dimers on this surface.

The spectrum (1) in Figure 4.25a, obtained on D-precovered surface, significantly differs from that of molecularly adsorbed acetophenone. A pronounced IR vibrational mode appears at 2896 cm^{-1} and a second mode at 1036 cm^{-1}. These bands are saturated already in spectrum (1) and are detected along the entire measurement with increasing exposure of acetophenone (3,5). The intense IR absorption band at 1036 cm^{-1} is present neither in the adsorbed molecular acetophenone on Pt(111) nor in the acetophenone ice (Fig. 4.17), and therefore cannot be related to any distinctive vibration of an intact acetophenone molecule. Additional demonstration for acetophenone on Pt(111) at 115 K has been shown earlier in this work (Figs. 4.1a, section 4.1), at which acetophenone does not undergo any chemical transformation, across a broad coverage range from the submonolayer to multilayer coverages. These observations are in agreement with the literature data obtained for liquid and gaseous acetophenone.[96] Note that the intensity of the band at 1036 cm^{-1} is comparable to the intensity of the C-O single bond in the ketone-enol dimers (1203 cm^{-1}), suggesting that noticeable amounts of the new species are formed. The vibrational range 1000-1200 cm^{-1} is typical for a single C-O bond, which was reported for gaseous species and a number of oxygenates on different surfaces.[128, 161] The frequency of the new band is approximately 150 cm^{-1} lower than that obtained for ketone-enol dimers at 1203 cm^{-1}, suggesting that the chemical environment of this bond strongly differs from that existing in the enol form. One explanation that can be accounted for this strong frequency shift is the fact that the C atom connected to O is not involved into the C=C double bond on the other side as it was the case for enol species. Indeed, typical C-O vibrational frequencies in saturated alcohols lye in the range 1000-1150 cm^{-1}.

Actually, the C-O(H) bond in the non-dissociated form of 1-phenylethanol – the hydrogenation product of acetophenone – exhibits a vibrational frequency at 1082 cm^{-1},[162] which is fairly close to our experimentally observed value at 1036 cm^{-1}. The band related to the new C-O single bond appears simultanously with a strong vibrational band at 2892 cm^{-1}, which is typically assigned to C-H stretching vibrations in methyl (–CH$_3$) or methylene-bridge (–CH$_2$–) groups[163, 164] and nearly coincides with the C-H stretching frequency of the methyl group in 1-phenylethanol[162] (2886 cm^{-1}). Importantly, this frequency is typical for C-H vibrations with the C atom participating in the C-C single bond. In contrast, had the C-atom been participating in the C=C bond, the =C–H

stretching vibration would be expected to appear at significantly higher frequencies, in the range 2960-3060 cm^{-1}.[163]

The simultaneous evolution of new intense vibrational bands that are related to *(i)* C-O single bond, and *(ii)* C-H single bonds with C-atom not participating in the C=C double bond, strongly suggests the formation of a new type of surface species, which most likely originates from a partial hydrogenation of acetophenone with one H atom. It should be emphasized that formation of hydrogenated species occurs in the temperature regime, at which the absolute majority of the adsorbates is associated into dimers. Therefore, at 240 K the pristine Pt(111) surface contains only ketone-enol dimers, rather than ketone-ketone dimers or monomers, as suggested by the appearance of the bands at 1203 and 1663 cm^{-1} and the absence of the band 1683 cm^{-1}. According to the spectroscopic observations, at a β_2 –H containing surface, a fraction of the dimers is still present in the ketone-enol form, whereas the remaining dimers, roughly of a similar amount as judged by the similar intensities of the two C-O single bonds (1203 vs 1036 cm^{-1}), undergoes partial hydrogenation, forming H-bonded dimer species consisting of one half-hydrogenated acetophenone molecule and one original acetophenone. Note that since the reactants – the ketone-enol dimers – and the products – the partly hydrogenated acetophenone forming a dimer with the original acetophenone molecule – are found on the surface only in the form of dimers, the hydrogenation step takes place most likely in dimers and not in monomers.

Based on the spectroscopic observations, the new species contains a C-O single bond as well as C-H bonds with C-atom not participating in the C=C double bond. If this is actually the case, then there are two possible formation mechanisms that can be responsible for a partially hydrogenated product which is consistent with all spectroscopic and microscopic observations: (1) H insertion into the C=C bond of the enol molecule, and (2) H insertion into the C=O bond of the ketone molecule, which participates in H-bonding with OH-group of enol. Figure 4.26 shows the feasible reaction mechanisms that can potentially result in the observed product. Note that H bonding between two halves of the product dimer should be possible to ensure the stability of the newly formed dimer species under the reaction conditions.
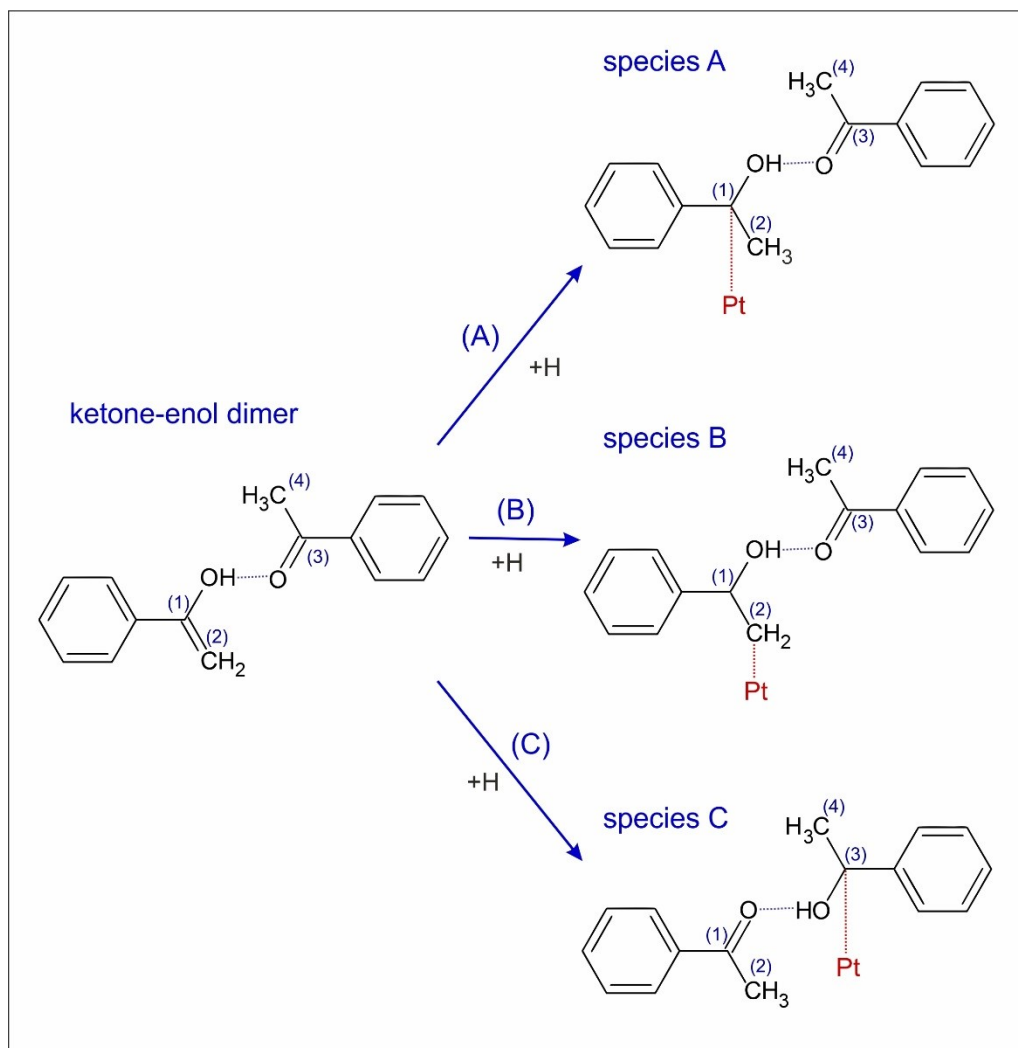
Figure 4.26: Proposed reaction mechanisms leading to H insertion into the ketone-enol dimer on Pt(111) surface.

(1)   Insertion of H into the C=C bond of enol can occur via two pathways: *(i)* if H attaches to the C(2) atom, a methyl group is formed, while the C(1) atom becomes connected to Pt atom (Figure 4.26, species A), and *(ii)* if H connects to C(1) atom, a –CH_2– bridge group is produced with C(2) being attached to the surface (Figure 4.26, species B). Both possible species should generally produce a similar spectroscopic pattern consistent with the spectroscopic observations. However, the species A seems more likely as its structure better explains the experimentally observed strong red-shift of the C-O single bond. If the involved carbon C(1) is directly attached to the metal, the reduced mass of the C-O entity

strongly increases, which should result in a noticeable decrease of the related vibrational frequency.[80] Also the newly formed $CH_3–$ group of species A should have high flexibility with respect to the surface, so that it can principally attain a close-to-upright configuration with respect to the surface, resulting in high intensity of the C-H stretching vibrations in accordance with the MSSR.[80] In species B, the C-H vibrations of the methylene-bridge group, in which a C(2) atom is connected to Pt, are expected to be more parallel with respect to the underlying metal surface, and therefore to exhibit low or no intensity in this vibrational region.

(2) The ketone part of the ketone-enol dimer can be principally hydrogenated on the C=O bond – either at the O or C(3) position – producing either Pt-C(3)-OH (species C in Figure 4.26) or -HC(3)-O-Pt (not shown) entities. In both cases the carbonyl group of the ketone molecule will be no longer available for H-bonding with the neighboring molecule, and the dimers should fall apart. At this stage, the enol form of the original dimer can possibly transfer back to ketone and build a dimer with the newly formed Pt-C(3)-OH entity to form species C. Note that species C is identical to species A and its structure is also consistent with the experimental observations. On the contrary, formation of the -HC(3)-O-Pt entity can be excluded since in this case the molecule has no possibility to form H-bonded dimers (between the C=O and HO- groups) and should appear as a monomer on the surface, in total contradiction to the experimental observations.

In both discussed cases, the dimer consisting of one ketone and one partly-hydrogenated molecule containing an OH- group is produced; however, it cannot be unambiguously deduced from our experimental observations if the H-atom is inserted into the C=C bond on the enol form or into the H-bonded C=O bond of the ketone form. H insertion into the enol form of acetophenone seems to be more likely based both on the theoretical predictions and frequently experimentally observed easier hydrogenation of olefins. However, the electronic structure perturbation of the C=O bond via H-bonding to the neighboring HO- group can be quite substantial, as indicated by the strong red-shift of the carbonyl frequency from 1683 to 1663 cm^{-1} upon H-bonding to enol. This strong interaction between an acidic hydrogen of the enol and the carbonyl group of the ketone part of the dimer weakens the C=O bond quite significantly and by that can potentially lower the activation barrier for H insertion into the carbonyl group. Therefore, both mechanisms can potentially lead to the spectroscopically observed reaction intermediates.

It should be pointed out, however, that formation of ketone-enol dimers appears to be crucial for the first hydrogenation step in this reaction, as both the reactants (ketone-enol dimers) and the products (dimers consisting of a ketone and partly hydrogenated acetophenone) are present on the surface in dimer form. The mechanisms described above can be realized only via dimer formation: *(i)* either due to formation and stabilization of the C=C bond, which can be hydrogenated with the low activation barrier, or *(ii)* due to weakening of the C=O bond as a result of strong hydrogen bonding with the acidic hydrogen of the enol species.

4.6 Conclusions

This chapter provides atomistic-level insights into the adsorption of simple carbonyl compound acetophenone over Pt(111) surface. Specifically, we present a mechanistic study on the details of intermolecular interactions between acetophenone adsorbates carried out under well-defined UHV conditions in the newly built experimental setup presented in Chapter 3.

The IR spectra of acetophenone on Pt(111) suggest the co-existence of two adsorption geometries on the surface which do not interconvert to each other. The species S1 exhibits a flat lying geometry of the aromatic ring with the -CH$_3$ group pointing away from the surface, and species S2 exhibits a tilted geometry of the aromatic ring, with a structure almost similar to that shown for the unperturbed molecule, i.e. multilayer or gas phase structures. The former is observed at low coverage and/or temperatures above 185 K, and its distorted geometry arises most likely from the combination of strong anchoring aromatic ring to the surface and the steric hindrance of the-CH$_3$ group while interacting with the surface. The molecular orientation of this species plays an important role in governing lateral interactions between two adjacent molecules on the surface, which trigger an important reaction of keto-enol tautomerization producing an enol reaction intermediate.

By combining IRAS, molecular beam techniques and STM, we found that several types of hydrogen-bonded oligomer species can be formed, including ketone-enol dimers and ketone-enol-enol trimers. We achieved a clear spectroscopic identification of the keto-enol dimers and of the ketone-enol-enol trimer, and showed that the enol can exists only if it is stabilized by the neighboring ketone molecule. This mechanism is proposed for mono-carbonyl compounds and

contradicts the commonly accepted view that the enol exists in the form of enol-enol oligomers. The evolution of the dimer and trimer species exhibits a strong temperature dependence, suggesting that oligomer formation promotes keto-enol tautomerization by lowering the activation barrier for hydrogen transfer from the methyl to the carbonyl group. Based on these observations, we conclude that this process occurs most likely in a concerted way, in which the energy barrier for hydrogen transfer can be compensated by formation of strong hydrogen bonds between enol and ketone species assembled in an oligomer. Also, based on the investigations of the co-adsorption behavior of acetophenone and hydrogen, we conclude that keto-enol tautomerization occurs in the intermolecular process. This suggestion is in contrast to the prevailing mechanistic tautomerization models of acetophenone on Pt(111) suggesting hydrogen transfer through the surface.

Importantly, we show that formation of more than one enol molecule per one ketone species through multiple hydrogen bonding can be achieved – a finding which might crucially contribute to the rational design of functionalized surfaces capable of enol formation and stabilization at high surface concentrations.

Additionally, hydrogen bonding between the ketone and enol parts of surface-adsorbed oligomers play an important role in stabilizing the enol species, making them accessible for further reaction steps. These ketone-enol dimers can attach a H atom forming a reaction intermediate consisting of a partly hydrogenated acetophenone species with a non-hydrogenated neighboring molecule. Based on the spectroscopic assignment of the chemical nature of the reaction intermediate, we conclude that H atom can be attached either to the C=C bond of the enol part, or to the C=O bond of the ketone part, which is strongly weakened due to H-bonding with the enol species. In both cases, formation of ketone-enol dimer species was found to be a crucial step in acetophenone hydrogenation.

Chapter 5

Adsorption of (R)-(+)-1-(1-naphtylethylamine) and CO on Pt(111)

While intermolecular interactions have been successfully employed in many homogeneous catalysts to control the selectivity towards individual reaction pathways[32, 33], e.g. via modification of an active metal site with specific organic ligands, only a limited number of studies on heterogeneous catalysts that utilizes this approach was reported. The most prominent examples are related to enantioselective heterogeneous catalysis on surfaces functionalized with chiral adsorbates, which exhibit enantiospecific interaction with a pro-chiral reactant and, by this, direct the catalytic process towards formation of only one enantiomeric form of the product.[5, 38-40]

Such catalysts, combining high catalytic activity and stereochemical control, may be produced by a variety of methods, including e.g. chiral templating by formation of long-range ordered patterns of chiral molecules on metal surfaces (chiral lattice templates),[34, 165] or adsorption of chiral organic molecules (chiral ligands) that build a 1:1 complex with a prochiral substrate.[36, 37] Among these methods, imparting chirality by adsorption of chiral ligands, seems to be one of the most promising.[166, 167] In the hydrogenation of C=O and C=C bonds, such chirally functionalized supported metal catalysts represent a successful approach with high synthetic potential demonstrated in batch and continuous-flow reactors.[168]

The greatest discoveries of asymmetric hydrogenation catalysts have often been based on fortuity and on its optimization by trial and error. While the underlying surface processes of asymmetric hydrogenation on chirally functionalized noble metal catalysts have been significantly better characterized, especially due to the use of systematic model approach,[14, 169] the current information about the enantiodifferentiating step and, in particular, regarding the structure of the enantiodifferentiating surface complex, is still incomplete.

At this stage, a molecular-level understanding of catalysis by the chirally functionalized surfaces strongly gains critical importance in order to further advance this field and to achieve rational designs of new chiral catalytic processes from first principles. Different structural aspects of the chirally-functionalized catalytic surfaces need to be understood at the atomistic level. These include details of the local bonding of the chiral ligand to the surface, and how the adsorption strength and geometry are affected by the small size of metallic nanoparticles, details of the interaction of the pro-chiral substrate with the chiral ligand (adsorption geometry, bonding,

reaction intermediates), particularly on hydrogen containing surfaces; possible reconstruction of the metal nanoparticles upon interaction with the chiral ligand and the substrate. On the other hand, quantitative kinetic and dynamic information needs to be obtained under well-defined isothermal reaction conditions that can be correlated with the different structural features of the catalytic surface.

Amongst the examples of enantioselective heterogenous catalysis on surfaces functionalized with chiral adsorbates, the synthetic ligand R-(1-naphthyl)ethylamine (NEA) gained a great deal of focus.[170-173]

Recent studies of NEA/Pt(111)[102, 174-177] and NEA/Pd(111) system[126] have proposed that an interacting NEA ligand comprises a combination of naphthyl/Pt π- and amine/Pt dative- bonding, a notion which is consistent with the current literature view that aromatic groups, such as cinchonidine or cinchonine, also function as chemical anchors lying flat on the catalyst surface. Nonetheless, recent evidences imply that neither cinchonine, nor NEA, are necessarily adsorbed with the aromatic groups π-bonded to the catalyst surface. Specifically, Meemken et al.[40] found an evidence for a strongly tilted cinchonine, occurring in the hydrogenation reaction on Pd/Al$_2$O$_3$ which is claimed to play a dominant role in the enantioselective step. Furthermore, Zaera and co-workers,[178] studied by IRAS the uptake of NEA and structurally related compounds from CCl$_4$ solutions onto a polycrystalline Pt surface. Relying on a comparative adsorption study that employed closely related compounds of different steric hindrance around the N atom, the authors of Ref. 178 concluded that chiral ligands such as NEA are bound to the surface, predominantly through their aminic N. This result complies with a former study of these authors on NEA/Pt(111),[54] suggesting that with increasing coverage, an adsorption geometry evolves, such that the naphthalene ring gradually tilts with its long axis out of the surface.

In contrast to the findings of Zaera et al,[54, 178] McBreen and co-workers have shown that π-bound NEA is prevalent on Pt(111).[101] An adequate summary regarding the different interpretations of the Zaera and Mcbreen groups, may be found in a recent review of Alfons Baiker on heterogenous asymmetric hydrogenation of hydrocarbon compounds on supported metal catalysts:[38] *".. this discrepancy may be explained by the vastly different conditions of measurements, that is, ultrahigh-vacuum (UHV) conditions employed by McBreen and co-workers versus CCl$_4$ solution employed by Zaera and co-workers. It is well-known that the solvent has a strong influence on the*

adsorption behavior of NEA as reflected by the very different catalytic performances observed with various solvents". It is hence clear that the mechanistic implications to practical catalysis should be carefully considered when comparing such spectroscopic results, because the catalytic solid-liquid interfaces are highly sensitive to the experimental conditions, e.g. choice of solvent and properties of the polycrystalline metal.

Motivated by the lack of conclusive experimental evidences that could help in resolving the above issue, we approach the problem by first revisiting the interaction behavior of R-NEA with Pt(111), and then, studying the adsorption of CO, being the simplest proxy of carbonyl-containing compounds, on the R-NEA functionalized Pt surface. Addressing the lateral interactions between R-NEA and CO molecules on a Pt(111) surface, is expected to provide valuable insights regarding the activity and selectivity of heterogeneously catalyzed reactions, and may, in turn, be employed for purposeful functionalization of surfaces aiming at optimizing their catalytic activity.

5.1 Vibrational bands assignment of R-NEA

To the best of our knowledge, at present, the existing assignments of the vibrational bands of NEA using isotope labeling experiments, are not available for the gas phase or on surfaces. Most of the vibrational bands of NEA are assigned in the literature by relying on reference studies of phenylethylamine,[179-181] naphthalene,[182] substituted naphthalene[183] and ethylamine.[184] The resulting assignments of some of the bands are nonetheless rather unclear. As an exemplifying case, one may consider the experimental band around 1600 cm^{-1}, which was prominently observed in all of the above mentioned studies, [54, 100-102, 178] and assigned solely to the C-C in-plane stretching mode of the naphthalene ring. Upon a closer inspection, however, one that relies on theoretical studies of phenylethylamine in the gas phase,[180, 181] it is found that this band may be assigned to the deformation mode of the -NH$_2$ group. Unambiguous assignments of the vibrational bands of NEA are thus of crucial importance. For that matter, the use of isotopically labeled R-NEA is very promising, however very costly, and hence not available in our lab. Our assignment procedure of the vibrational bands of R-NEA was thus based on gas phase calculations, as hereby explained.

In order to obtain reference values for the collection of R-NEA normal modes, the optimized structure and vibrations of isolated (gas phase) molecules were calculated, using the Gaussian 16

software package.[185] The calculation was carried out at the B3LYP/cc-aug-pVTZ level of theory in the gas phase[¥]. Experimentally, to obtain a reference spectrum for an unperturbed molecule, the IR spectra are first recorded at multilayer coverages at which most of the adsorbed molecules do not directly interact with the surface. The resulting experimental bands were then assigned by comparison to the theoretical spectra.

The experimental IR spectrum of R-NEA on Pt(111) at multilayer coverages, acquired at 160 K, is shown in Figure 5.1a, together with that calculated for the gas phase (Fig. 5.1b). The calculated frequencies were scaled by a factor of 0.967 for best fitting the experimental data. The assignments of the measured IR bands are presented in Table 5.1.
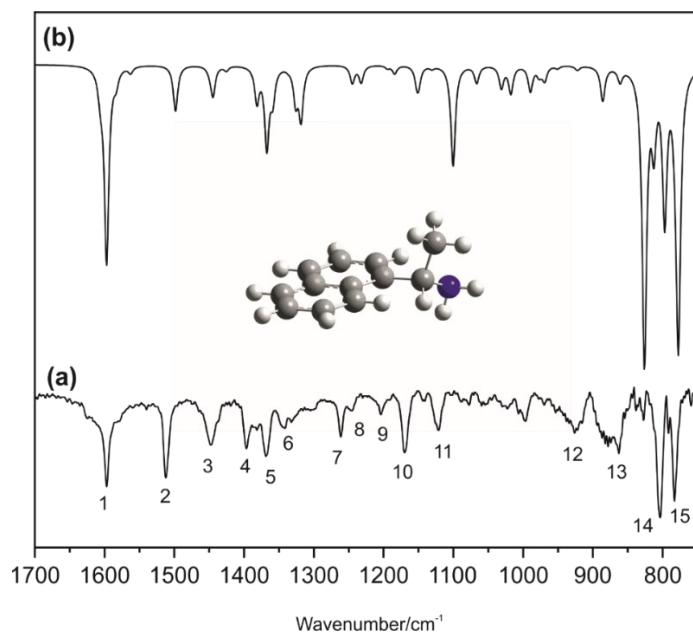
Figure 5.1: Experimental IR spectra of R-NEA on Pt(111) at multilayer coverages measured at 160 K (a) along with the calculated IR spectra at B3LYP/cc-aug-pVTZ level of theory (b). The frequencies were scaled by factor of 0.967 to obtain the best fit to the experimental data. The calculated bands are numerically labeled from 1-15 for the purpose of assignments (see Table 5.1). The optimized structure is given in the inset.

[¥] Several model chemistries have been used. The operational considerations for the presented model chemistry are given in Appendix II.

Mode number	Gas phase[a]	Pure liquid[b]	Multilayer[c]	B3LYP/aug-cc-pvTZ, scaled[d]	Assignment[e]
1	1597	1595	1597	1597	δ_s (NH$_2$)
2	1508	1510	1512	1510	ν_{ip}(CC)$_{ring-x}$
3	1453	1446	1448	1466	δ_{as} (CH$_3$)
4		1395	1397	1380	δ_{ip}(CH)$_{ring-y}$, δ(C*H)$_{ethylamine}$
5	1377	1368	1369	1367	δ_s (CH$_3$)
6	1329	1337	1342	1325	δ(C*H)$_{ethylamine}$
7		1259	1261	1245	δ(C*H)$_{ethylamine}$
8	1242	1242	1245	1232	ring breathing
9		1201	1204	1185	mix modes ω(NH$_2$)
10	1167	1167	1170	1151	mix modes ν(C-N)
11	1117	1119	1120	1100	mix modes
12	905	917	927	911	mix modes ρ(CH$_3$), ρ(NH$_2$)*, ν(C*-C)$_{ethylamine-ring}$
13	856	861	863	862	ω (NH$_2$)
14	795		804	790	δ_{oop}(CH)$_{ring}$
15	773		783	765	δ_{oop}(CH)$_{ring}$

Table 5.1: Vibrational frequencies (in cm^{-1}) of NEA and their assignments. Experimental frequencies of NEA multilayers are compared with harmonic frequencies calculated at the B3LYP/aug-cc-pvTZ (scaled by 0.967) level of theory. Labels 1-15 refer to Fig. 5.1. a- NIST gas phase values for S-NEA[162], b-values reported by Zaera for pure liquid NEA[54], c- experimental values for a multilayer of R-NEA on Pt(111) at 160 K as measured in the present work (Fig. 5.1a). Bands of <0.01% of max intensity are discarded. Band assignments rely on visual inspection of both calculated and multilayer spectra. For bands comprising a combination of vibrational modes, predominant vibration characters are indicated. Ring-x and ring-y labels correspond to ring vibrations at which the dynamic dipole moments are aligned along the long and short axes of the naphthalene ring respectively.

On a brief visual examination of Fig. 5.1, the measured and calculated spectra appear fairly similar. Going into details however, reveals small shifts in several absorbance bands (cf. Table 5.1). Note that computed intensity values should not be taken too literally. Rather, relative intensity values are more reliable. Hence the predicted intensities are more of qualitative than quantitative relevance. From the inspection of the 1600-1350 cm^{-1} vibrational range, the 1-6 calculated bands nicely reproduce the experimentally observed ice values. This allows for a tentative assignment of some of the bands in the experimental spectrum. In the following, we review in brief some important aspects of vibrational properties of R-NEA, which are of relevance for the present study. For the most part, a clear assignment to a localized bond or molecular sub-unit is not possible. Nevertheless, detailed inspection identifies various deformation and stretching modes with specific polarizations, i.e. along the long or short axes of the R-NEA. For instance, the 1510 cm^{-1} band is assigned to C-C in-plane stretching mode of the naphthalene ring. Its dynamic dipole moment is aligned along the long axis of the naphthalene ring in accordance with previously published data.[54, 100, 101, 186] The nature and orientation of the dynamic dipole moment of selected vibrational modes (labeled 1-5 in Fig. 5.1) are illustrated in Fig. 5.2.
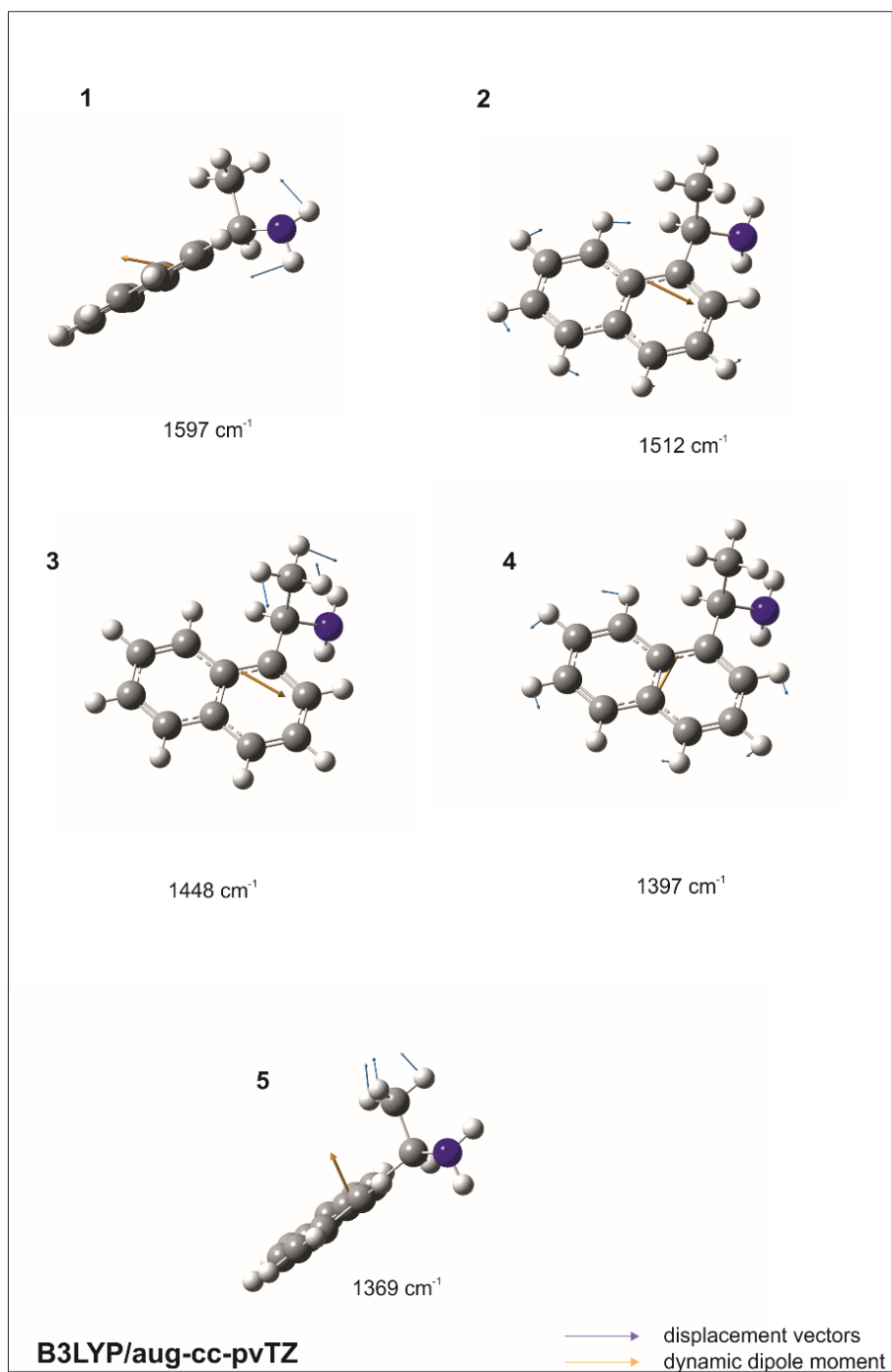
Figure 5.2: Visualization of selected vibrational modes of R-NEA, with labels 1-5 taken from Figure 5.1. The displacement vectors and the dynamic dipole moment for each mode are indicated in blue and orange respectively.

5.2 Adsorption of R-NEA on Pt(111) at sub-monolayer coverages

Once established the assignments of R-NEA at multilayer coverages (Table 5.1), we can now turn to study the interaction of R-NEA with Pt(111) at submonolayer coverages to investigate the perturbation of chemical bonds by the interaction with Pt(111) as well as obtaining insights regarding its adsorption geometry based on the MSSR. This was achieved by acquiring the IRAS spectra of R-NEA on Pt(111) surface at 160 K as a function of R-NEA exposure time. The thus obtained IRAS data is presented in Fig. 5.3. Assignments of the observed vibrational bands were made by accounting for those calculated for the gas phase, as well as by comparison to previously published theoretical data of phenylethylamine.[180, 181] Assigning the IR bands in the submonolayer relied on the multilayer and gas-phase spectra because the band positions in the submonolayer spectra occur in close proximity to those in the multilayer spectra, and also because the submonolayer and monolayer appear to be weakly adsorbed. It should be pointed out that our results are somewhat different from those published previously by Mcbreen and co-workers.[101]

It is clearly noted from Fig. 5.3 that increasing the coverage promotes marked changes in the IRAS spectrum. These changes are more clearly evident in Fig. 5.3b which focuses on a spectral region of interest. Spectroscopically, the difference between sub-monolayer and multilayer adsorption is generally reflected by small frequency shifts, however a much marked difference occurs in the relative intensities of the bands.
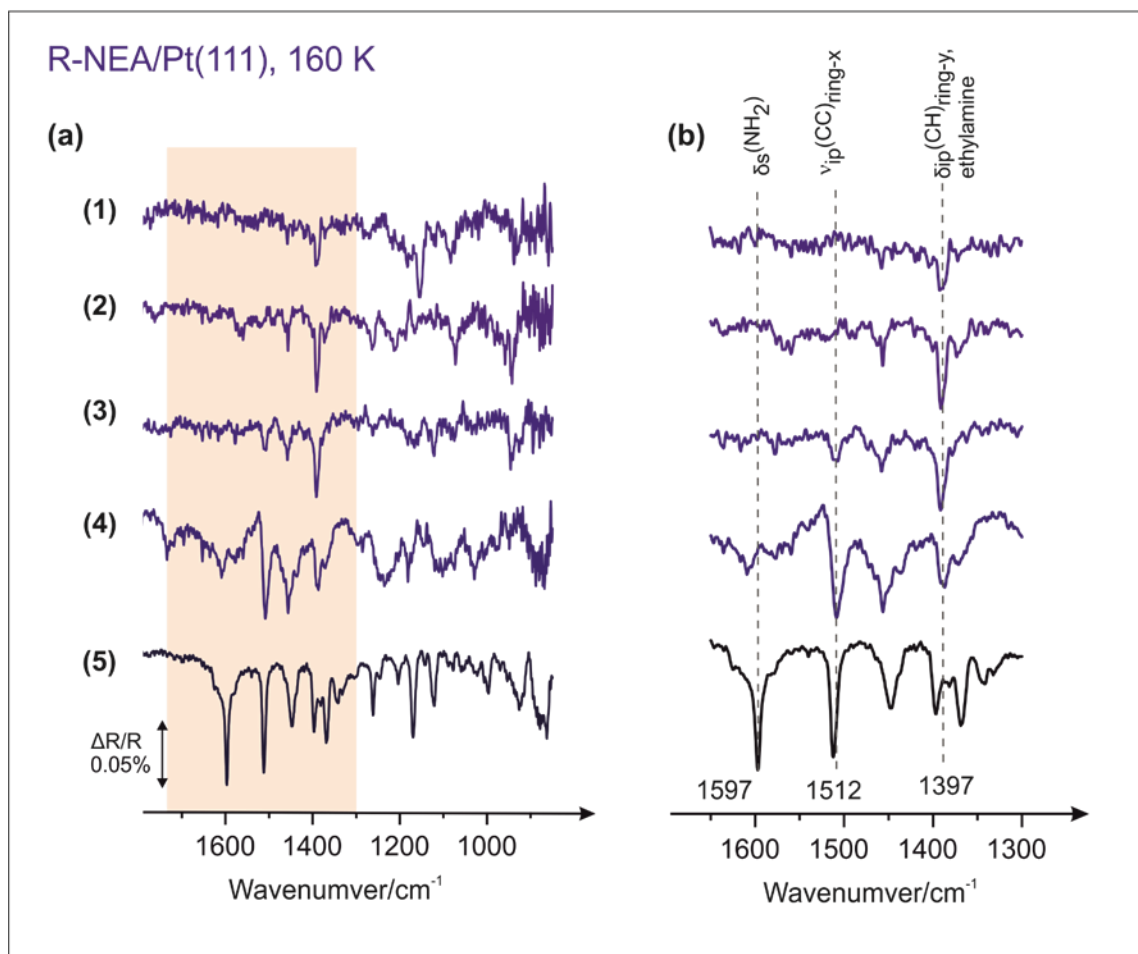
Figure 5.3: IRAS spectra of R-NEA on Pt(111) recorded at 160 K as a function of R-NEA exposure; $5 \cdot 10^{-8}$ mbar for (1)1, (2) 1.5, (3) 2, (4) 5, (5) 10 minutes at 155 K (b) Enlarged view in the region 1300-1650 cm^{-1}.

At the lowest coverage (1), a band at 1397 cm^{-1} is detected. This band is continuously growing with increasing coverage, and finally saturates (3). Further exposure shows the evolution of the bands at 1512 and 1448 cm^{-1} which then grow in intensity with increasing coverage (4). In spectrum (4), the band at 1597 cm^{-1} is detected as well. The latter band grows in intensity with increasing R-NEA exposure and finally dominates the spectra (5).

Under the basic assumption that the naphthyl ring of the R-NEA molecule largely preserves its gas phase structure upon adsorption, some preliminary conclusions may be drawn regarding its orientation relative to the surface. Such assumption may be justified by noting the relative small differences between the frequency positions in the adsorbed NEA spectra (Fig. 5.3) and those of pure liquid[54] or gas phase[95] (cf. Table 5.1), whereby it can be reasonably concluded that the

adsorption is molecular, at least at 160 K, and that it is rather weak and occurs with minimal distortion of the electronic structure.

According to the MSSR, only vibrations having a non-zero projection of the dynamic dipole moment along the direction perpendicular to the surface, are detectable by IRAS, whereas the vibrational components parallel to the surface are strongly attenuated due to the formation of an image dipole moment in the underlying metal surface.[80] The 1397 cm^{-1} band, detected at the lowest coverage (spectrum (1) in Fig. 5.3), is assigned mainly to in-plane C-H deformation modes of the naphthalene ring with the dynamic dipole moment aligned along its short axis (see Fig. 5.2 (4)). This indicates adsorption with the naphthalene ring standing up along its short axis on the surface, that is, bonded through its long side. This observation is consistent with the absence of the band at 1512 cm^{-1} which is assigned to C-C stretching vibrations of the naphthalene ring whose dynamic dipole moment is aligned along its long axis. A schematic representation of the suggested adsorbed structure is shown in Fig. 5.4. The band at 1597 cm^{-1} is assigned to the symmetric deformation of the amine group. The dynamic dipole moment of this latter vibrational mode, is aligned along the plane formed by the H-N-H bond (Fig. 5.2 (1)). The absence of this band in spectrum (1) of Fig. 5.3, indicates that the plane formed by the H-N-H bonds is practically aligned parallel to the surface. It should be pointed out that in the multilayer spectra, the intensities of the 1397 cm^{-1} and 1369 cm^{-1} bands (nos. 4 and 5) are comparable. The dynamic dipole moment of the latter, assigned to the symmetric deformation of the methyl group, is aligned along the bond of the chiral carbon and the CH$_3$ group (C$_{chiral}$-CH$_3$). In spectrum (1) of Fig, 5.3, the 1397 cm^{-1} band is detected whereas that of 1369 cm^{-1} is not. This indicates that the C$_{chiral}$-CH$_3$ bond is aligned parallel to the Pt surface. Exposing the Pt(111) surface to additional R-NEA, leads to development of few vibrational bands, notably that at 1512 cm^{-1}, which is assigned to in-plane skeletal stretching of the naphthalene ring (ν_{ip}(CC)$_{ring-x}$). This clearly indicates that a new adsorption arrangement is evolved, such that the aromatic ring is somewhat standing up on the surface along its long axis. Finally, spectrum (5) in Fig. 5.3b shows vibration characteristics of largely unperturbed R-NEA molecules with the most prominent band occurring at 1597 cm^{-1}. This indicates that all dipoles are inclined with respect to the surface.
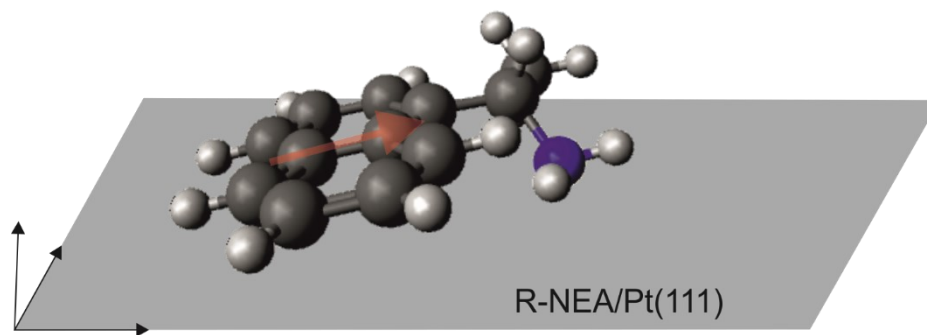
Figure 5.4: Schematic drawing of R-NEA adsorbed on Pt(111). The aromatic ring is tilted on the surface even at low coverage. The dynamic dipole moment of the band at 1397 cm^{-1} is shown schematically with respect to the surface plane.

Overall, the IR data provides a pretty strong indication that R-NEA is always adsorbed with its aromatic ring tilted with respect to the surface, even at low coverages. This observation is also consistent with a previously reported near edge X-ray absorption fine structure spectroscopy study by Lambert and co-workers,[36] as well as with the IRAS results of Zaera et al.[54] Considering the typical behavior observed for aromatic rings on single-crystal metal surfaces, where an initial flat adsorption geometry tilts up only above some threshold coverage,[187-190] the present results are somewhat surprising.

The interaction of R-NEA with Pt(111) as a function of coverage was additionally investigated by STM. STM images of adsorbed R-NEA molecules were collected at 300 and 160 K as a function of coverage. The STM images were collected at the Christian-Albrecht University and the Fritz-Haber-Institute by Marvin Schmidt and Evan Spadafora. The results are shown in Figs. 5.5a and 5.5b respectively.
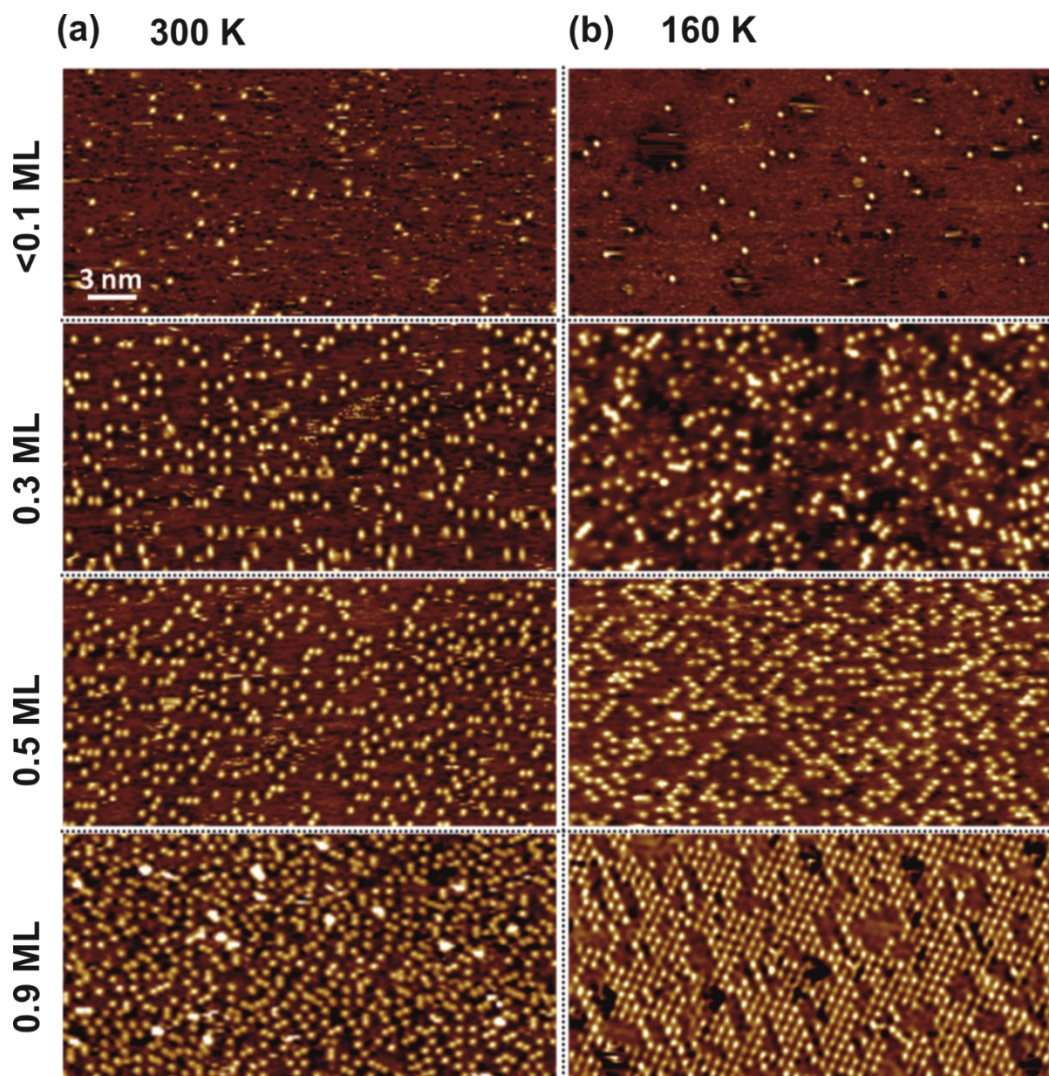
Figure 5.5: STM images of R-NEA adsorbed on Pt(111) as a function of coverage at 300 K (a) and 160 K (b).

It is clearly seen in Fig. 5.5.a that at room temperature the R-NEA molecules are practically randomly distributed on the surface, irrespective of the coverage. In strong contrast, at 160 K we observe a very interesting phenomenon, which to the best of our knowledge has not been described previously in the literature: formation of directed chains at intermediate coverages (Fig.5.5b, 0.5 ML) and self-assembled R-NEA overlayer at the near saturation coverage (Fig. 5.5b, 0.9 ML). Chains formation, with typical 3-4 members per chain, points to a directed intermolecular interaction between the individual R-NEA molecules. In combined, the present preliminary IRAS and STM results are indicative of inclined adsorption geometry for R-NEA molecules on Pt(111) with intermolecular interactions between the adsorbed molecules. Most likely, the observed

directed interaction results from hydrogen bonding between the amine group of a given molecule and the hydrogen of the naphthyl ring in a neighboring molecule. Such interaction is in agreement with previous studies showing that the hydrogens of the naphthyl ring are also capable of forming hydrogen bonds on Pt(111).[191-193] Worth pointing out in that regard, is the fact that the intermolecular interaction between the molecules can be also reinforced by additional CH--- π interactions between, for instance, an hydrogen atom in the chiral center of one molecule and a naphthyl ring in the neighboring molecule, as suggested previously for various complexes of chiral molecules.[194, 195] The driving force for the observed phenomenon can be also attributed to intermolecular π ---π stacking, although it is likely that the side group causes steric hindrance and thus prevents π ---π stacking.

Our preliminary spectroscopic results suggest a strongly inclined adsorption geometry of R-NEA molecules in the chains and strong intermolecular interaction between them. Two possible scenarios can be considered for the observed phenomenon: (i) chains formation takes place already at low coverages and consists of adsorbed R-NEA ligands having their naphthalene ring standing up along its short axis (as realized by the appearance of the δ(C-H)ring-y band at 1397 cm^{-1} and the absence of the ν(C-C)ring-x band at 1512 cm^{-1}; see Fig. 5.3b (1)), or (ii) chains are formed at intermediate coverages and comprise of R-NEA ligands adsorbed with the naphthalene ring tilted along its short and long axes with respect to the surface plane (as realized by the appearance of both characteristic bands at 1397 and 1512 cm^{-1}; see Fig. 5.3b(3)). Accounting for the former scenario, it is possible that each individual adsorbate simply rearranges on the surface to minimize the steric hindrance between the surface and the substituted group, most likely the terminal methyl group, resulting in the inclination of the naphthalene ring along its short axis with respect to the surface. In this case, the tilted adsorption geometry of the adsorbate can be stabilized by intermolecular H-bonding between adjacent R-NEA molecules, which can also explain the observed tilted geometry already at low coverage. This is in opposed to the adsorption of aromatic rings on single-crystal metal surfaces that typically lay flat on the surface up to a threshold coverage.[187-190] In the second scenario of chains consisting of R-NEA adsorbates oriented with the naphthalene ring tilted along its both axes, it is possible that the surface is already crowdedly populated with R-NEA molecules, which result in tilting of the naphthalene ring in order to minimize the steric repulsion between them. In that case, since individual molecules are found in close spatial proximity, they form directed chains via H-bonding in order to compensate for the

weak interaction of the naphthalene ring with the surface. It should be noted, however, that the STM image revealing the observation of directed chains ((Fig. 5.5, 160 K, 0.5 ML), is nonetheless also strongly indicative of a considerable unpopulated surface space, on which additional molecules are likely to be accommodated. It is therefore suggested that the formation of strips of 3-4 R-NEA molecules is favorably consistent with the spectroscopic observation at low coverage, and that it consists of R-NEA molecules oriented with the naphthalene ring tilted along its short axis with respect to the surface plane. The intermolecular interaction between the individual molecules in the chains most likely involves a main NH_2---HC_{ring} H-bonding and weak stabilizing CH_{chiral}--- π interactions, as suggested previously for various complexes of chiral molecules.[191, 192, 194, 195]

5.3 Interaction of CO with R-NEA on Pt(111)

In the previous section, we have addressed lateral interactions between R-NEA molecules on Pt(111). Such interactions are expected to have crucial effect on the activity and selectivity of heterogeneously catalyzed reactions, and therefore be employed for purposeful functionalization of surfaces to improve their catalytic activity.

Among the typical strategies of asymmetric hydrogenation catalysis, asymmetric hydrogenation of activated ketones on chirally modified Pt catalyst is probably the most studied chiral surface transformation.[38] And yet, the molecular scale details of the interaction of the pro-chiral substrate with the chiral modifier (adsorption geometry, bonding, reaction intermediates) are not well understood. To address this issue, and as a first step towards this goal, we chose CO as the simplest proxy for carbonyl-containing compounds and investigated its interaction with Pt surface functionalized with R-NEA.

Having characterized independently the interaction of R-NEA with Pt(111) (see section 5.2), and given the broadly investigated CO/Pt(111) model system,[81, 98, 196] it is now possible to characterize the adsorption behavior of R-NEA using CO as a probe molecule.

For this, the sample is first cleaned in the preparation chamber according to the procedure described in Chapter 3. Then, the R-NEA molecules are deposited onto the sample in the

deposition chamber which is then transferred to the reaction chamber. To measure the IR spectral changes arising from the exposure of the R-NEA-functionalized surface to CO, the spectrum of the adsorbed R-NEA is first collected and accounted for as background. Next, the surface, is exposed, at the same temperature, to varying exposures of CO using the effusive source, and the IR spectrum is acquired. By measuring the differential spectra, the NEA related bands that have not been altered by the interaction with CO, are eliminated. This procedure allows for easier interpretation of the CO-induced changes.

In addition, another set of experiments was carried out by dosing the surface with R-NEA and then saturating all surface sites available for CO adsorption, where the differential CO and R-NEA spectra were collected by IRAS. Our goal is to bring the CO close to the R-NEA, or even on top of it, in order to characterize the interaction of CO with R-NEA. This however may result in saturation of the metal vacant sites. In the following discussion, the surface sites that are available for CO adsorption can be attributed to (i) vacant metal sites on the surface which have not been populated by R-NEA, and/or (ii) adsorption sites which are sufficiently distant from the surface, e.g. adsorbed CO that seats on top of the R-NEA. The former type of surface sites includes CO molecules which are directly bonded to the metal but are either well distant from R-NEA ligands, or surrounded by an atmosphere of R-NEA ligands, whereby it can directly interact with the ligands. It should be pointed out that CO is generally used as a probe for estimating surface coverages. In IRAS, with increasing coverage of CO, the intensity of the corresponding absorbance bands does not scale linearly with the coverage due to dipole-dipole interactions. Obviously, on R-NEA functionalized surface, CO can interact with the ligand which, in turn, might affect the estimate of surface coverage. Nonetheless, comparing the relative integrals of the stretching bands of CO on the NEA-functionalized surface, with those of a bare surface, allows for a qualitative comparison regarding the fraction of the surface that is blocked by R-NEA/available for CO adsorption. In the following, the relative coverage of CO is referenced to the saturation coverage of CO per Pt atoms on the pristine 111 face at the same temperature.[98]

Figure 5.6 (spectra (1),(2)) shows the IR spectra of CO adsorbed on R-NEA/Pt(111) recorded at 155 K following exposure of $2.6 \cdot 10^{16}$ CO molecules cm^{-2}. Also shown for comparison, is the IRAS spectrum of CO on the pristine surface (spectrum (4)), for which two vibrational bands at 2104 cm^{-1} (on-top sites) and 1854 cm^{-1} (bridge sites) were detected; both the vibrational

frequencies and the intensities correspond to that recorded previously for a pristine Pt(111) surface.[98]
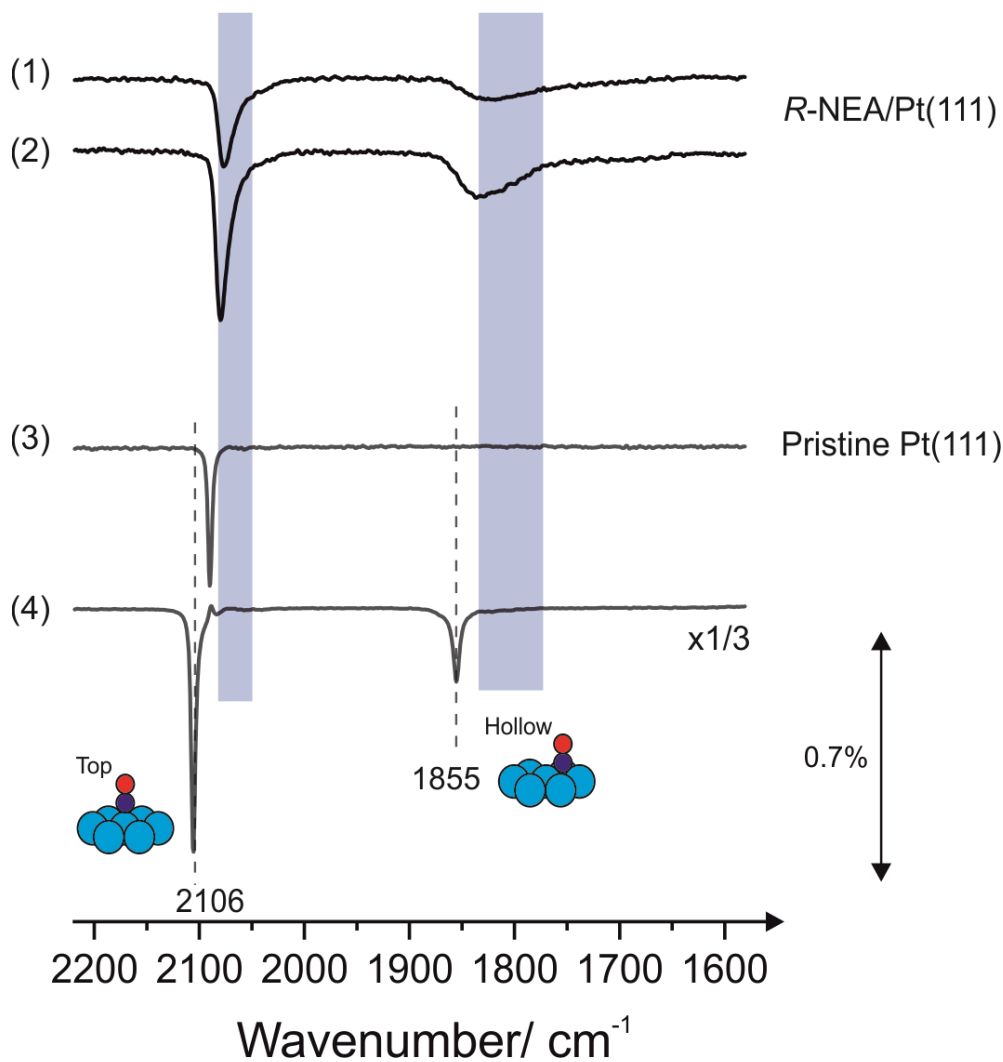
Figure 5.6: IRAS spectra of CO adsorbed on *R*-NEA/Pt(111) at two different sub-monolayer coverages recorded at 155 K (1),(2) and on pristine Pt(111) recorded at 115 K (3),(4). CO exposure: (1),(2) $2.6 \cdot 10^{16}$, (3) $2 \cdot 10^{13}$,(4) $8.5 \cdot 10^{14}$ molecules·cm^{-2}.

Spectra (1) and (2) which correspond to adsorbed CO on NEA-functionalized surface, show that the peaks of adsorbed CO are both shifted and broadened compared to those recorded for the pristine surface (spectrum (4)), with the CO adsorbed at the on-top sites, redshifted by 33 cm^{-1},

and the CO adsorbed at the bridge sites, shifted by 24 cm^{-1}, as compared to the pristine Pt(111) surface. In addition, the latter band shows a considerable broadening (FWHM = 100 cm^{-1}).

The shift in C-O stretching modes is coverage dependent: the vibrational frequency typically red-shifts to lower wavenumbers due to substrate-adsorbate interaction, while typically increases (blue-shifts) upon coverage increment, as a result of lateral interactions between adsorbed CO molecules. For a Pt(111) surface preliminary dosed with R-NEA, it is expected that the amount of vacant sites for CO adsorption will be smaller than that obtained on a pristine surface. Hence, one may interpret the observed red-shifted frequency of the CO molecules on the NEA-modified surface, as resulting from a low CO coverage. Spectrum (3) shows the IRAS spectra of CO on a clean Pt(111) surface following exposure of $2 \cdot 10^{13}$ molecules$\cdot$cm^{-2}. In this spectrum, CO is bonded exclusively to on-top sites with a characteristic vibrational band at 2090 cm^{-1}, whereas an absorption band due to C-O stretch at bridging sites is not obtained. This indicates a < 1/3 ML CO coverage, in accordance with previously published data.[98] Spectrum (2), on the other hand, depicts absorption bands at 2080 cm^{-1} and 1836 cm^{-1} arising from the C-O stretch at on-top and bridging sites respectively. Note that the intensities of the bands due to the on-top sites of spectra (2) and (3) are of comparable intensities, suggesting, *at least*, the same CO coverage on both pristine and R-NEA functionalized surfaces. The functionalized surface, however, exhibits a small, ~10 cm^{-1}, red shift of the CO on-top band. The trend of the red-shifted frequency of CO on the functionalized surface is even more pronounced while comparing the vibrational bands due to the C-O stretch on bridging sites (spectra (2) and (4)) which shows additionally a significant broadening. Given the strikingly different IR data, it is suggested that the CO is diluted in NEA ligands on the surface. These observations might point out for an intermolecular interaction of CO with the adsorbed R-NEA molecules.

In NEA, the amine group provides the major H-bonding donor in the molecule,[186] although it has also been suggested that the hydrogens of the naphthyl ring are also capable of forming hydrogen bonds on Pt(111).[191-193] This nicely agrees with the combined IRAS and STM data of the previous section, which suggested that the self-assembled molecular chains of NEA molecules are bonded to each other most likely by H-bonding between the amine group of a given molecule and an aromatic hydrogen in a neighboring molecule. Other H-bonded interactions such as between neighboring NH$_2$ groups or between NH$_2$ and chiral hydrogen of the ethyl amine substituent, cannot explain the formation of chains of typical 3-4 NEA units, neither the formation

of NEA overlayers. The suggestion seems to correlate with the observed tilted geometry of the molecules.

Primary amines can serve as H-bond donors or acceptors. Given the fact that carbonyl groups serve as H-bond acceptors,[197] the amine group likely serves as H-bond donor. As observed and discussed in chapter 4 for acetophenone, the stronger is the acidity of the hydrogen bond donor, the larger is the shift in frequency. Such red-shifted frequency of the CO stretch can thus be understood by the formation of H-bonds between the oxygen atom of the C=O group (the H-bond acceptor) and a constituent hydrogen of the NH_2 group in the R-NEA molecule (the H-bond donor). It should be pointed out that the aromatic H, as discussed previously in section 5.2, can also serve as an H-bond donor. The latter, however, is significantly less acidic than the H of the amine group, and therefore it is not expected that in case of CO interacting with aromatic H, the frequency shift of the C-O vibrational bands will be that substantial.

The CO/Pt(111) system follows a typical Blyholder picture state;[196, 198] the bond of the CO to the surface is formed through a donation from 5σ into the metal, and a backdonation from the metal d-band into the $2\pi*$, resulting in a red-shift of the CO vibrational bands as compared to the unperturbed molecules. As lateral interactions between CO molecules on the surface will likely result in higher frequencies due to dipole-dipole interactions, the frequency red-shift observed for CO on NEA-functionalized surface might also be indicative of an enhanced π backdonation from the d-band metal to the CO molecule, most likely into the $2\pi*$. The origin of this phenomenon is not clear and demands further theoretical studies in order to address this issue. Nevertheless, few possible scenarios and explanations may be considered. For instance, it is possible that the $-NH_2$ group is donating electrons to the surface, enhancing by that the electron backdonation to the antibonding orbital of CO. It is also possible that the lone pair electron (n) of the $-NH_2$ group is transferred directly to the antibonding orbital of CO. The inclusion of $n{\rightarrow}\pi^*$ interactions in the inventory of non-covalent forces has been shown previously in the literature in relation to force field of biomolecular modeling[199] and was found to contribute to the stability of proteins that involve NH_2---O=C H-bonds.

In the following we refer to the spectral changes occurring across two different vibrational regions: (i) bands related to the C-O stretch, i.e. 1800-2200 cm^{-1}, and (ii) bands related to R-NEA in the 1000-1650 cm^{-1} range.

Figure 5.7a shows the differential IR spectra at submonolayer coverage of R-NEA as a function of CO exposure at 155 K. The spectra of the R-NEA represent a surface coverage that corresponds to 70% saturation coverage of CO; the corresponding C-O stretching region is shown in Fig. 5.7b.

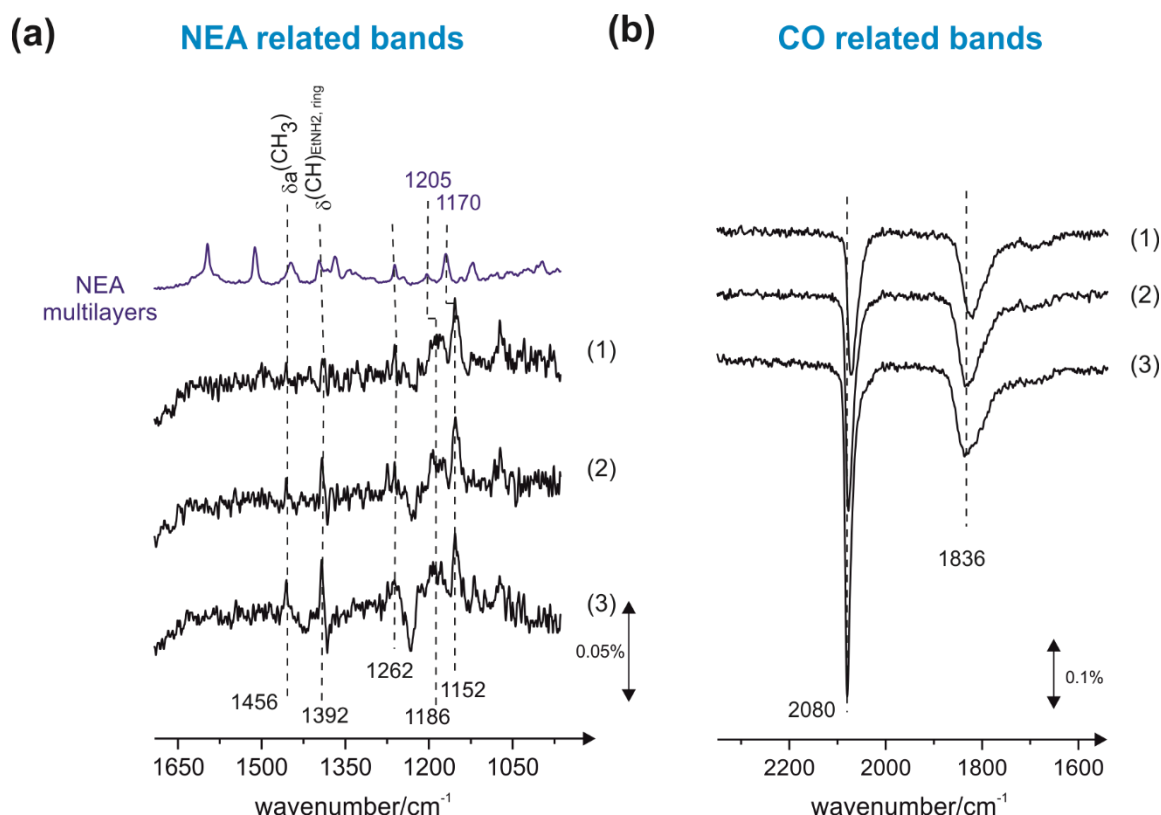**Figure 5.7:** Differential IRAS spectra of R-NEA on Pt(111) as a function of CO exposure recorded at 155 K. Two spectral regions are presented; the vibrational bands related to R-NEA (a) and those related to CO (b). The R-NEA-covered surface corresponds to *R*-NEA exposure of $5 \cdot 10^{-8}$ mbar for 1.5 minutes at 155 K. CO exposure: (1) $7.5 \cdot 10^{14}$, (2) $2.3 \cdot 10^{15}$, (3) $2.6 \cdot 10^{16}$ molecules·cm^{-2}.

The uppermost spectrum in Fig. 5.7a corresponds to R-NEA at multilayer coverages, and is used as a reference for the case of closely unperturbed molecules. Comparison of this spectrum with those obtained at sub-monolayer coverages, allows us to explore the perturbation of chemical bonds by the interaction of R-NEA with CO on Pt(111).

The spectral region of R-NEA reveals that the adsorbed R-NEA is strongly affected by CO. Upon CO adsorption, some vibrational bands are attenuated: 1456, 1392, 1262, 1186, 1152 and 1077 cm^{-1}. One plausible interpretation is that the adsorption geometry of R-NEA is affected by CO, such that the IRAS spectrum is significantly altered. A more striking and important finding is the attenuation of the band at 1392 cm^{-1}, which arises when both CO and R-NEA are present. We have earlier demonstrated that this band, which is assigned to δ_{ip}(C-H)$_{ring-x}$, was obtained on the pristine surface at low R-NEA coverage (see Fig. 5.3(1)). This observation enabled us to obtain some insights regarding the orientation of the molecule, and a tilted adsorption geometry bonded to the surface via the long axis of the naphthalene ring was consequently suggested. In line with these arguments, considering that the structure of the naphthalene ring of the R-NEA molecule is preserved on the surface while interacting with CO, further conclusions can be drawn regarding the orientation of the R-NEA. The dynamic dipole moment of the vibrational mode at 1392 cm^{-1} is aligned along the short axis of the naphthalene ring. Thus, attenuation of this band upon exposure of CO indicates a smaller projection of its dynamic dipole moment along the surface normal. One possible explanation for such observation is that the naphthalene ring, initially tilted with respect to the surface plane and bonded through its long axis, shifts back towards the surface, i.e. *via the short axis of the naphthalene ring.* Schematic illustration of this suggested phenomenon is shown in Fig. 5.8.
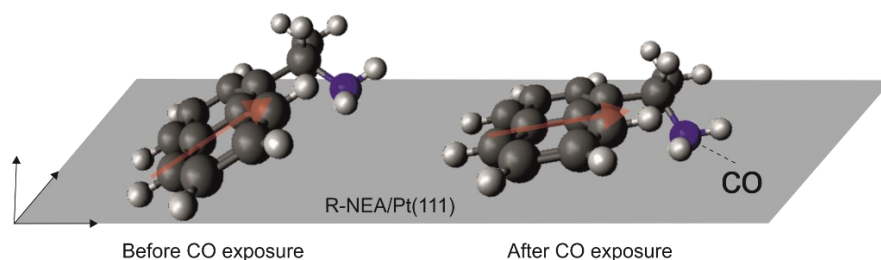
Figure 5.8: Schematic illustration of the structure of R-NEA on Pt(111) with (left) and without (right) CO on the surface, as could be suggested by the attenuation of the band at 1397 cm^{-1}. The orientation of the dynamic dipole moment of that vibration relative to the surface plane is indicated schematically by the red arrow.

The signals of the attenuated bands are easily identified by comparison with the multilayer spectra. Particularly, the two bands at 1186 and 1152 cm^{-1} seem to correlate with the bands recorded in the reference spectra at 1205 and 1174 cm^{-1} respectively (Fig. 5.7, uppermost spectrum, multilayer). These bands comprise vibrational characteristics of the entire molecule. Nevertheless, unlike the band at 1392 cm^{-1} which is assigned mainly to skeletal deformation modes, the two attenuated bands comprise contributions from stretching vibrations of the ethylamine moiety. Specifically, the band at 1170 cm^{-1} comprises stretching vibration of the C-N bond of the ethylamine moiety. The latter assignment is consistent with the typical vibrational bands in the region of 1250-1020 cm^{-1}, with medium to weak adsorption for unconjugated C-N linkage in primary amines.[200] Note that the vibrations responsible for these bands involve C-N stretching coupled with the stretching of adjacent bonds in the molecule. Additionally, the band at 1205 cm^{-1} comprises stretching vibration of the C_{ring}-C_{chiral} bond, as well as wagging deformation of the NH$_2$ group.

The spectra show that co-adsorption of CO and R-NEA on the surface results in: (i) red-shifted frequency of 18 cm^{-1} with respect to the unperturbed R-NEA molecule; and (ii) attenuation of the bands at 1186 and 1152 cm^{-1}. It is very likely that the electronic structure perturbation of the -N-H bond via H-bonding to the neighboring CO can be quite substantial, as indicated by the strong red shift of the band at 1205 to 1186 cm^{-1} upon H-bonding to the CO molecule. It is also possible that if H-bonding is formed between the NH$_2$ group and the CO molecule, it imposes a

geometrical constraint which results in a bond elongation (weakening) of the N-C bond. This phenomenon seems reasonable as both bands are attenuated upon CO interaction with the surface, which is likely an indication for a change in the adsorption geometry. The scenario proposed by the presented infrared data is still preliminary, and complementary DFT calculations for a more detailed assignment of the IR features will be performed in the near future.

5.4 Conclusions

R-(1-naphthyl)ethylamine (R-NEA) molecules adsorbed on Pt(111) at 160 K form directed chains at intermediate coverages and self-assembled onto R-NEA overlayer at the coverages close to saturation. Formation of chains, typically consisting of 3-4 members, points to a directed intermolecular interaction between individual R-NEA molecules. Our preliminary spectroscopic results suggest a strongly inclined adsorption geometry of R-NEA molecules in the chains, and strong intermolecular interaction between the amine group of one molecule and the naphthyl-ring of the neighboring molecule, which most likely lead to the observed directed interaction. CO was utilized as a simple proxy to study the interaction of simple carbonyl compounds with chiral modifiers. The IR spectrum clearly shows that the peaks of adsorbed CO on R-NEA-modified surface are both shifted and broadened compared to the pristine surface. These two observations could suggest that the CO is diluted in R-NEA ligands on the surface, pointing to intermolecular interaction between them. This interaction triggers a change in the adsorption geometry of the R-NEA, such that a less tilted aromatic ring anchor is observed. Considering that the molecular orientation of adsorbates plays a crucial role in asymmetric catalysis, e.g. the enantiospecific adsorption of the prochiral reactant determines the enantioselectivity, the present results could shed light in explaining enenatioselectivity of chirally modified metals. Yet, to reveal the surface coverage-molecular orientation-selectivity relationship, an extended mechanistic study with catalytically relevant materials such as acetophenone have to be carried out.

Chapter 6

Summary

The aim of this thesis was to investigate the reactivity of hydrocarbon compounds by employing ligand-functionalized model catalysts. This goal was approached in two ways:

Firstly, an essential step towards the connection of structural parameters of the underlying solid substrate, the chemical nature of the deposited ligands and the reactive properties, was the construction and implementation of a new experimental setup combining molecular beam techniques and in situ surface spectroscopy for reactivity measurements on complex nanostructured model surfaces. The setup, its components and performance, were presented in detail in Chapter 3. The experimental setup was specifically designed for studying the mechanisms, kinetics and dynamics of heterogeneously catalyzed reactions over well-defined model catalysts. With this setup, detailed reactivity studies can be performed on such complex nanostructured catalysts across a broad pressure range, from UHV up to ambient pressure conditions, and the reactivity behavior can be directly compared in the broad pressure range to trace down pressure-dependent changes in the mechanisms and kinetics of surface reactions. The setup allows model studies, in which controllable variation of two structural parameters – the structure of the underlying solid substrate (extended crystal vs. NPs, particle size and surface density, etc.) and the chemical nature of the deposited ligands – will allow to independently address different ligand-related effects in order to explore the most important working principles of ligand-directed heterogeneous catalysis.

The new apparatus consists of three chambers, which can be operated as independent UHV systems, and a unique combination of tools including two effusive and one supersonic molecular beams, IRAS for spectroscopic identification of adsorbed surface species, QMS for gas phase analyses, as well as tools required for preparation and structural characterization of complex nanostructured model catalysts based on thin oxide films epitaxially grown on metal single crystals. These tools include LEED/AES, TPD, metal evaporators and calibration methods. Additionally, a dedicated deposition chamber is implemented, allowing to functionalize the catalytic surface with low vapor pressure compounds. The apparatus also contains an ambient

pressure cell that provides the possibility to carry out reactivity studies in a broad pressure range of reaction conditions.

A particular challenge was to combine all required components- two effusive and one supersonic beams as well as the infrared setup- in one reaction chamber. Therefore, the molecular beams implemented in this setup comprise a compact size and allow for achieving high molecular fluxes typically required in reactivity studies.

Secondly, two test studies on catalytically relevant materials, adsorption of two different adsorbates – acetophenone and R-NEA – were investigated by employing IRAS, molecular beam techniques and STM. As a first step towards a better understanding of ligand-induced catalysis, it is shown that lateral interactions between coadsorbed molecules on surfaces might trigger specific reaction pathways and stabilize otherwise energetically unstable reaction intermediates. These phenomena can crucially affect the overall activity and selectivity of catalytic processes and can be employed for purposeful functionalization of surfaces to improve their catalytic efficiency. In chapter 4, intermolecular interactions between acetophenone adsorbates on Pt(111) were investigated. Their interaction on the surface triggers an important reaction of keto-enol tautomerization producing an enol reaction intermediate, which is envisaged to enable low-barrier hydrogenation of simple carbonyl compounds. This mechanism was predicted previously by several research groups and we provided for the first time an experimental evidence for it. By combination of IRAS and STM techniques, we found that several types of hydrogen-bonded oligomer species can be formed, including ketone−enol dimers and ketone−enol−enol trimers. Their evolution exhibits a strong temperature dependence, suggesting that oligomer formation promotes keto−enol tautomerization by lowering the activation barrier for hydrogen transfer from the methyl to the carbonyl group. This process occurs most likely in a concerted way, in which the energy barrier for hydrogen transfer can be compensated by the formation of strong hydrogen bonds between enol and ketone species assembled in an oligomer. Additionally, hydrogen bonding between the ketone and the enol parts of the surface-adsorbed oligomers stabilizes the otherwise unstable enol species, making them accessible for further reaction steps. Indeed, we show that the target process –hydrogenation of the carbonyl group – occurs not in monomers but rather in the ketone-enol dimers, and results in the formation of a partly hydrogenated acetophenone species attached via the hydrogen bonding to the second acetophenone molecule. The spectroscopically

derived reaction intermediates suggests that two possible mechanisms can be responsible for dimer-induced hydrogenation of the carbonyl group: (i) formation of a C=C bond in the enol part of the dimer, which exhibits a lower activation barrier for hydrogenation according to previously published theoretical predictions, and (ii) weakening of the C=O bond in the ketone part of the dimer due to the strong interaction with the acidic hydrogen of enol, which might result in the facilitation of H insertion into this highly perturbed carbonyl group. In both cases, formation of ketone-enol dimer species was found to be a crucial first step in acetophenone hydrogenation. Yet, theoretical support to the investigated system is still missing and should be addressed, such as which part of the dimer – the C=C bond in the enol or the C=O bond in the ketone– is hydrogenated.

The second study case involves coadsorption of chiral modifier, R-NEA and CO on Pt(111) (chapter 5). CO was utilized as a simple proxy to study the interaction of simple carbonyl compounds with chiral modifiers. Our preliminary spectroscopic results suggest a strongly inclined adsorption geometry of R-NEA molecules, which significantly changes upon adsorption of CO. The results also display changes in peak positions of the CO, suggesting an intermolecular interaction with the R-NEA-modified surface. These results highlight the importance of characterizing the molecular orientation of chiral modifiers and their potential role in asymmetric catalysis and can be employed to better emulate the reaction conditions. In the future, the catalytic performance of acetophenone hydrogenation on R-NEA functionalized surface should be studied with the new setup across a broad range of pressure conditions, from UHV and up to the near ambient pressure.

This thesis contributes to the understanding of lateral interactions between coadsorbed molecules on Pt(111) and their effect on the overall activity and selectivity of catalytic processes. This allows us to develop new concepts for a rational design of new catalytic materials. For instance, the metal surface can be modified, prior to the reaction, with stable ligand-like adsorbates containing a C=O group, which can serve as a counterpart required for the stabilization of the enol form via hydrogen bonding with the carbonyl group. By adjusting the chemical structure and the spatial distribution of these carbonyl ligands, we envisage a capability of fine tuning the properties of such functionalized surface toward stabilization of enols, and controlling by that their catalytic performance.

Examining nanostructured model surfaces as well as strong binding ligand-substrate combinations than the ones studied in this work is desirable in future studies to better understand industrially relevant processes. The design and implementation of molecular beam/IRAS experiment is an essential further step towards achieving this goal.

Bibliography

1.   Rideal, E. K. *Concepts in catalysis*. Academic P.:**1968**.

2.   Ertl, G.; Knözinger, H.; Weitkamp, J. *Environmental catalysis*. Wiley-VCH Weinheim: **1999**.

3.   Zaera, F. Outstanding mechanistic questions in heterogeneous catalysis. ACS Publications: **2002**.

4.   Somorjai, G. A.; Kliewer, C. J. Reaction selectivity in heterogeneous catalysis. *React. Kinet. Catal. Lett.* **2009**, 96 (2), 191-208.

5.   Mallat, T.; Orglmeister, E.; Baiker, A. Asymmetric Catalysis at Chiral Metal Surfaces. *Chem. Rev.* **2007**, 107 (11), 4863-4890.

6.   Ozkan, U. S. *Design of heterogeneous catalysts: new approaches based on synthesis, characterization and modeling*. John Wiley & Sons: **2009**.

7.   Zaera, F. Regio-, stereo-, and enantioselectivity in hydrocarbon conversion on metal surfaces. *Acc. Chem. Res.* **2009**, 42 (8), 1152-1160.

8.   Zaera, F. New challenges in heterogeneous catalysis for the 21st century. *Catal. Lett.* **2012**, 142 (5), 501-516.

9.   Sinfelt, J.; Cusumano, J. Bimetallic catalysts. *Sci. Am.* **1983**, 253 (3), 90-101.

10.   Rodriguez, J. Physical and chemical properties of bimetallic surfaces. *Surf. Sci. Rep.* **1996**, 24 (7-8), 223-287.

11.   Ertl, G. Engineering, Surface science and catalysis—studies on the mechanism of ammonia synthesis: the PH Emmett award address. *Catal. Rev.* **1980**, 21 (2), 201-223.

12.   Adesina, A. A. Hydrocarbon synthesis via Fischer-Tropsch reaction: travails and triumphs. *Appl. Catal. A* **1996**, 138 (2), 345-367.

13.   Somorjai, G. A. Surface science at high pressures. *Z. Phys. Chem.* **1996**, 197 (1-2), 1-19.

14.   Freund, H.-J.; Bäumer, M.; Libuda, J.; Risse, T.; Rupprechter, G.; Shaikhutdinov, S. Preparation and characterization of model catalysts: from ultrahigh vacuum to in situ conditions at the atomic dimension. *J. Catal.* **2003**, 216 (1-2), 223-235.

15.   Henry, C. R. Surface studies of supported model catalysts. *Surf. Sci. Rep.* **1998**, 31 (7-8), 231-325.

16.   Libuda, J.; Freund, H. -J. Molecular beam experiments on model catalysts. *Surf. Sci. Rep.* **2005**, 57 (7-8), 157-298.

17.   Zhdanov, V. P.; Kasemo, B. Simulations of the reaction kinetics on nanometer supported catalyst particles. *Surf. Sci. Rep.* **2000**, 39 (2-4), 25-104.

18.   Bäumer, M.; Freund, H. -J. Metal deposits on well-ordered oxide films. *Prog. Suf. Sci.* **1999**, 61 (7-8), 127-198.

19.   Clair, T. P. S.; Goodman, D. W. Metal nanoclusters supported on metal oxide thin films: bridging the materials gap. *Top. Catal.* **2000**, 13 (1-2), 5-19.

20.   Campbell, C. T.; Grant, A. W.; Starr, D. E.; Parker, S. C.; Bondzie, V. A. Model oxide-supported metal catalysts: energetics, particle thicknesses, chemisorption and catalytic properties. *Top. Catal.* **2000**, 14 (1-4), 43-51.

21.   Kwon, S. G.; Krylova, G.; Sumer, A.; Schwartz, M. M.; Bunel, E. E.; Marshall, C. L.; Chattopadhyay, S.; Lee, B.; Jellinek, J.; Shevchenko, E. V. Capping Ligands as Selectivity Switchers in Hydrogenation Reactions. *Nano Letters* **2012**, 12 (10), 5382-5388.

22.   Chen, G.; Xu, C.; Huang, X.; Ye, J.; Gu, L.; Li, G.; Tang, Z.; Wu, B.; Yang, H.; Zhao, Z.; Zhou, Z.; Fu, G.; Zheng, N. Interfacial electronic effects control the reaction selectivity of platinum catalysts. *Nature Materials* **2016**, 15, 564.

23.   Chen, M.; Goodman, D. The structure of catalytically active gold on titania. *Science* **2004**, 306 (5694), 252-255.

24.   Chen, M.; Goodman, D. W. Catalytically active gold on ordered titania supports. *Chem. Soc. Rev.* **2008**, 37 (9), 1860-1870.

25.   Ertl, G. Reactions at surfaces: from atoms to complexity (Nobel Lecture). *Angew. Chem. Int. Ed.* **2008**, 47 (19), 3524-3535.

26.   Park, J. B.; Graciani, J.; Evans, J.; Stacchiola, D.; Senanayake, S. D.; Barrio, L.; Liu, P.; Sanz, J. F.; Hrbek, J.; Rodriguez, J. A. Gold, copper, and platinum nanoparticles dispersed on CeOx/TiO2 (110) surfaces: high water-gas shift activity and the nature of the mixed-metal oxide at the nanometer level. *J. Am. Chem. Soc.* **2009**, 132 (1), 356-363.

27.   Heiz, U.; Bullock, E. J. Fundamental aspects of catalysis on supported metal clusters. *J. Mater. Chem.* **2004**, 14 (4), 564-577.

28.   Ludwig, W.; Savara, A.; Schauermann, S.; Freund, H. -J. Role of Low-Coordinated Surface Sites in Olefin Hydrogenation: A Molecular Beam Study on Pd Nanoparticles and Pd (111). *Chem. Phys. Chem.* **2010**, 11 (11), 2319-2322.

29.   RonáShen, Y. SFG and STM studies of the Pt (111) crystal face at atmospheric CO and oxygen pressures: preparation of platinum nanocluster arrays. *Faraday Discuss.* **1996**, 105, 263-274.

30.   Somorjai, G. A.; Rupprechter, G. Molecular Studies of Catalytic Reactions on Crystal Surfaces at High Pressures and High Temperatures by Infrared− Visible Sum Frequency Generation (SFG) Surface Vibrational Spectroscopy. *J. Phys. Chem. B* **1999**, 103 (10), 1623-1638.

31.   Cremer, P. S.; Su, X.; Shen, Y. R.; Somorjai, G. A. Ethylene hydrogenation on Pt (111) monitored in situ at high pressures using sum frequency generation. *J. Am. Chem. Soc.* **1996**, 118 (12), 2942-2949.

32.   Collman, J. P.; Wang, Z.; Straumanis, A.; Quelquejeu, M.; Rose, E. An Efficient Catalyst for Asymmetric Epoxidation of Terminal Olefins. *J. Am. Chem. Soc.* **1999**, 121 (2), 460-461.

33.   Taylor, M. S.; Jacobsen, E. N. Asymmetric Catalysis by Chiral Hydrogen-Bond Donors. *Angew. Chem. Int. Ed.* **2006**, 45 (10), 1520-1543.

34.   Roth, C.; Parschau, M.; Ernst, K. H. Chiral reconstruction of a metal surface by adsorption of racemic malic acid. *Chem. Phys. Chem.* **2011**, 12 (8), 1572-1577.

35.   Mark, A. G.; Forster, M.; Raval, R. Recognition and Ordering at Surfaces: The Importance of Handedness and Footedness. *ChemPhysChem* **2011**, 12 (8), 1474-1480.

36.   Bonello, J. M.; Williams, F. J.; Lambert, R. M. Aspects of enantioselective heterogeneous catalysis: structure and reactivity of (S)-(−)-1-(1-naphthyl) ethylamine on Pt(111). *J. Am. Chem. Soc.* **2003**, 125 (9), 2723-2729.

37.   Augustine, R. L.; Taneilyan, S. K.; Doyle, L. K. Enantioselective heterogeneous catalysis I. A working model for the catalyst: modifier: substrate interactions in chiral pyruvate hydrogenations. *Tetrahedron: Asymmetry,* **1993**, 4 (8), 1803-1827.

38.   Meemken, F.; Baiker, A. Recent Progress in Heterogeneous Asymmetric Hydrogenation of C═O and C═C Bonds on Supported Noble Metal Catalysts. *Chem. Rev.* **2017**, 117 (17), 11522-11569.

39.   Gellman, A. J.; Tysoe, W. T.; Zaera, F. Surface Chemistry for Enantioselective Catalysis. *Catal. Lett.* **2015**, 145 (1), 220-232.

40.   Rodríguez-García, L.; Hungerbühler, K.; Baiker, A.; Meemken, F. The Critical Role of Tilted Cinchona Surface Species for Enantioselective Hydrogenation. *ACS Catal.* **2017**, 7 (6), 3799-3809.

41.   McCue, A. J.; McKenna, F.-M.; Anderson, J. A. Technology, Triphenylphosphine: a ligand for heterogeneous catalysis too? Selectivity enhancement in acetylene hydrogenation over modified Pd/TiO$_2$ catalyst. *Catal. Sci. Thecnol.* **2015**, 5 (4), 2449-2459.

42.   Lee, K. Y.; Lee, Y. W.; Lee, J.-H.; Han, S. W. Effect of ligand structure on the catalytic activity of Au nanocrystals. *Colloid Surface A.* **2010**, 372 (1-3), 146-150.

43.   Snelders, D. J.; Yan, N.; Gan, W.; Laurenczy, G.; Dyson, P. J. Tuning the chemoselectivity of Rh nanoparticle catalysts by site-selective poisoning with phosphine ligands: The hydrogenation of functionalized aromatic compounds. *ACS Catal.* **2012**, 2 (2), 201-207.

44.   Marshall, S. T.; O'Brien, M.; Oetter, B.; Corpuz, A.; Richards, R. M.; Schwartz, D. K.; Medlin, J. W. Controlled selectivity for palladium catalysts using self-assembled monolayers. *Nat. Mater.* **2010**, 9 (10), 853-858.

45.   Wu, B.; Huang, H.; Yang, J.; Zheng, N.; Fu, G. Selective Hydrogenation of α,β-Unsaturated Aldehydes Catalyzed by Amine-Capped Platinum-Cobalt Nanocrystals. *Angew. Chem. Int. Ed.* **2012**, 51 (14), 3440-3443.

46.   Dostert, K.-H.; O'Brien, C. P.; Mirabella, F.; Ivars-Barceló, F.; Attia, S.; Spadafora, E.; Schauermann, S.; Freund, H. -J. Selective Partial Hydrogenation of Acrolein on Pd: A Mechanistic Study. *ACS Catal.* **2017**, 7 (8), 5523-5533.

47.   O'Brien, C. P.; Dostert, K.-H.; Schauermann, S.; Freund, H. -J. Selective Hydrogenation of Acrolein Over Pd Model Catalysts: Temperature and Particle-Size Effects. *Chem. Eur. J.* **2016**, 22 (44), 15856-15863.

48.   O'Brien, C. P.; Dostert, K. H.; Hollerer, M.; Stiehler, C.; Calaza, F.; Schauermann, S.; Shaikhutdinov, S.; Sterrer, M.; Freund, H. -J. Supports and modified nano-particles for designing model catalysts. *Faraday Discuss.* **2016**, 188, 309-21.

49.   Dostert, K.-H.; O'Brien, C. P.; Ivars-Barceló, F.; Schauermann, S.; Freund, H. -J. Spectators Control Selectivity in Surface Chemistry: Acrolein Partial Hydrogenation Over Pd. *J. Am. Chem. Soc.* **2015**, 137 (42), 13496-13502.

50.   Yang, B.; Wang, D.; Gong, X.-Q.; Hu, P. Acrolein hydrogenation on Pt (211) and Au (211) surfaces: a density functional theory study. *Phys. Chem. Chem. Phys.* **2011**, 13 (47), 21146-21152.

51.   Rasmussen, A. M.; Groves, M. N.; Hammer, B. Remote activation of chemical bonds in heterogeneous catalysis. *ACS Catal.* **2014**, 4 (4), 1182-1188.

52.   Bandyopadhyay, B.; Pandey, P.; Banerjee, P.; Samanta, A. K.; Chakraborty, T. CH··· O Interaction Lowers Hydrogen Transfer Barrier to Keto–Enol Tautomerization of β-Cyclohexanedione: Combined Infrared Spectroscopic and Electronic Structure Calculation Study. *J. Phys. Chem. A* **2012**, 116 (15), 3836-3845.

53.   Demers-Carpentier, V.; Laliberte, M. -A.; Lavoie, S.; Mahieu, G.; McBreen, P.H. Two-Dimensional Self-Assembly and Catalytic Function: Conversion of Chiral Alcohols into Self-Assembled Enols on Pt (111). *J. Phys. Chem. C* **2009**, 114 (16), 7291-7298.

54.   Lee, I.; Ma, Z.; Kaneko, S.; Zaera, F. 1-(1-Naphthyl) ethylamine adsorption on platinum surfaces: On the mechanism of chiral modification in catalysis. *J. Am. Chem. Soc.* **2008**, 130 (44), 14597-14604.

55.   Rettner, C.; Auerbach, D.; Tully, J.; Kleyn, A. Chemical dynamics at the gas− surface interface. *J. Phys. Chem.* **1996**, 100 (31), 13021-13033.

56.   Kleyn, A. Molecular beams and chemical dynamics at surfaces. *Chem. Soc. Rev.* **2003**, 32 (2), 87-95.

57.   King, D. A. *The chemical physics of solid surfaces and heterogeneous catalysis*. Elsevier: **2012**; Vol. 5.

58.   Kolasinski, K. W., *Surface science: foundations of catalysis and nanoscience*. John Wiley & Sons: **2012**.

59.   Weinberg, W.; Merrill, R. Technology, A Simple Classical Model for Trapping in Gas−Surface Interactions. *J. Vac. Sci. Thecnol.* **1971**, 8 (6), 718-724.

60.   Cassuto, A.; King, D. A. Rate expressions for adsorption and desorption kinetics with precursor states and lateral interactions. *Surf. Sci.* **1981**, 102 (2-3), 388-404.

61.   Christmann, K. *Introduction to surface physical chemistry*. Springer Science & Business Media: **2013**; Vol. 1.

62.   Böttcher, S.; Vita, H.; Weser, M.; Bisti, F.; Dedkov, Y. S.; Horn, K. Adsorption of water and ammonia on graphene: evidence for chemisorption from X-ray absorption spectra. *J. Phys. Chem. Lett.* **2017**, 8 (15), 3668-3672.

63.   Kisliuk, P. The sticking probabilities of gases chemisorbed on the surfaces of solids. *J. Phys. Chem. Solids* **1957**, 3 (1-2), 95-101.

64.   Levy, D. H. The spectroscopy of very cold gases. *Science* **1981**, 263-269.

65.   Christen, W.; Rademann, K. Cooling and slowing in high-pressure jet expansions. *Phys. Rev. A* **2008**, 77 (1), 012702.

66.   Campbell, W. C.; Tsikata, E.; Lu, H.-I.; van Buuren, L. D.; Doyle, J. M. Magnetic Trapping and Zeeman Relaxation of NH (X $^3\Sigma$-). *Phys. Rev. Lett.* **2007**, 98 (21), 213001.

67.   Narevicius, E.; Libson, A.; Riedel, M.; Parthey, C.; Chavez, I.; Even, U.; Raizen, M. Coherent slowing of a supersonic beam with an atomic paddle. *Phys. Rev. Lett.* **2007**, 98 (10), 103201.

68.   Dumesic, J. A. *The microkinetics of heterogeneous catalysis*. An American Chemical Society Publication: **1993**.

69.   Scoles, G. *Atomic and molecular beam methods. Vol. 1 Vol. 1*. Oxford University Press: New York; Oxford, **1988**.

70.   Levine, R. D. *Molecular reaction dynamics and chemical reactivity*. Oxford University Press, USA: **1987**.

71.   Barker, J. A.; Auerbach, D. J. Gas—surface interactions and dynamics; Thermal energy atomic and molecular beam studies. *Surf. Sci. Rep.* **1984**, 4 (1-2), 1-99.

72.   Libuda, J.; Meusel, I.; Hartmann, J.; Freund, H. -J. A molecular beam/surface spectroscopy apparatus for the study of reactions on complex model catalysts. *Rev. Sci. Instrum.* **2000**, 71 (12), 4395-4408.

73.   Jacobs, D. C. The role of internal energy and approach geometry in molecule/surface reactive scattering. *Condens. Mater.* **1995**, 7 (6), 1023.

74.   Comsa, G.; David, R. Dynamical parameters of desorbing molecules. *Surf. Sci. Rep.* **1985**, 5 (4), 145-198.

75.   Atkins, P. W.; Friedman, R. S. *Molecular quantum mechanics*. Oxford university press: 2011.

76.   Sakuri, J. Modern Quantum Mechanics, revised edition. Addison-Wesley: **1994**.

77.   Zaera, F. New advances in the use of infrared absorption spectroscopy for the characterization of heterogeneous catalytic reactions. *Chem. Soc. Rev.* **2014**, 43 (22), 7624-7663.

78.   Zaera, F. Infrared and molecular beam studies of chemical reactions on solid surfaces. *Int. Rev. Phys. Chem.* **2002**, 21 (3), 433-471.

79.   Ryczkowski, J. IR spectroscopy in catalysis. *Catal. Today* **2001**, 68 (4), 263-381.

80.   Hoffmann, F. M. Infrared reflection-absorption spectroscopy of adsorbed molecules. *Surf. Sci. Rep.* **1983**, 3 (2-3), 107-192.

81.   Hayden, B.; Bradshaw, A. The adsorption of CO on Pt (111) studied by infrared-reflection-adsorption spectroscopy. In *Studies in Surface Science and Catalysis*, Elsevier: **1983**; Vol. 14, p 51.

82.   Hollins, P.; Pritchard, J. Infrared studies of chemisorbed layers on single crystals. *Prog. Suf. Sci.* **1985**, 19 (4), 275-349.

83.   Genzel, L.; Martin, T. Infrared absorption by surface phonons and surface plasmons in small crystals. *Suf. Sci.* **1973**, 34 (1), 33-49.

84.   Griffiths, P. R.; De Haseth, J. A. *Fourier transform infrared spectrometry*. John Wiley & Sons: **2007**; Vol. 171.

85.   Francis, S. A.; Ellison, A. H. Infrared spectra of monolayers on metal mirrors. *J. Opt. Soc. Am.* **1959**, 49 (2), 131-138.

86.   Dawson, P. H. *Quadrupole mass spectrometry and its applications*. Elsevier: **2013**.

87.   Gross, J. H. *Mass spectrometry: a textbook*. Springer Science & Business Media: **2006**.

88.   De Hoffmann, E. Stroobant, V. *Mass spectrometry*. Principles and Applications, Third Edition, John Wiley & Sons: **2007**.

89.   Argoti, D. *Liquid chromatography-mass spectrometry for detection and characterization of DNA biomarkers and reactive metabolites*. Northeastern University: **2008**.

90.   Binnig, G.; Rohrer, H.; Gerber, C.; Weibel, E. Surface studies by scanning tunneling microscopy. *Phys. Rev. Lett.* **1982**, 49 (1), 57.

91.   Binnig, G.; Rohrer, H. Scanning tunneling microscopy. *Surf. Sci.* **1983**, 126 (1-3), 236-244.

92.   Chen, C. J. *Introduction to scanning tunneling microscopy*. Oxford University Press on Demand: **1993**; Vol. 4.

93.   Attia, S.; Spadafora, E. J.; Hartmann, J.; Freund, H. -J.; Schauermann, S. Molecular beam/infrared reflection-absorption spectroscopy apparatus for probing heterogeneously catalyzed reactions on functionalized and nanostructured model surfaces. *Rev. Sci. Instrum.* **2019**, 90 (5), 053903.

94.   Reisinger, T.; Bracco, G.; Rehbein, S.; Schmahl, G.; Ernst, W. E.; Holst, B. Direct images of the virtual source in a supersonic expansion. *J. Phys. Chem. A* **2007**, 111 (49), 12620-12628.

95.   Stein, S.; Mallard, W.; Linstrom, P. NIST/EPA gas-phase infrared database. *NIST Chemistry WebBook, NIST Standard Reference Database Number*, National Institute of Standards and Technology: **2003**; Vol. 69.

96.   Gambi, A.; Giorgianni, S.; Passerini, A.; Visinoni, R.; Ghersetti, S. Infrared studies of acetophenone and its deuterated derivatives. *Spectrochim. Acta A* **1980**, 36 (10), 871-878.

97.   Chen, M.; Maeda, N.; Baiker, A.; Huang, J. Molecular insight into Pt-catalyzed chemoselective hydrogenation of an aromatic ketone by in situ modulation–excitation IR spectroscopy. *ACS Catal.* **2012**, 2 (9), 2007-2013.

98.   Steininger, H.; Lehwald, S.; Ibach, H. On the adsorption of CO on Pt (111). *Surf. Sci.* **1982**, 123 (2-3), 264-282.

99.   Ni, Y.; Gordon, A. D.; Tanicala, F.; Zaera, F. Correlation between Chiral Modifier Adsorption and Enantioselectivity in Hydrogenation Catalysis. *Angew. Chem. Int. Ed.* **2017**, 129 (27), 8071-8074.

100.   Meemken, F.; Steiger, T.; Holland, M. C.; Gilmour, R.; Hungerbühler, K.; Baiker, A. Technology, Adsorption and stability of chiral modifiers based on 1-(1-naphthyl)-ethylamine for Pt catalysed heterogeneous asymmetric hydrogenations. *Catal. Sci. Thecnol.* **2015**, 5 (2), 705-715.

101.   Zeng, Y.; Masini, F.; Rasmussen, A. M.; Groves, M. N.; Albert, V.; Boukouvalas, J.; McBreen, P.H. The most stable adsorption geometries of two chiral modifiers on Pt (111). *Surf. Sci.* **2018**, 676, 17-22.

102.   Demers-Carpentier, V.; Goubert, G.; Masini, F.; Lafleur-Lambert, R.; Dong, Y.; Lavoie, S.; Mahieu, G.; Boukouvalas, J.; Gao, H.; Rasmussen, A. M. Direct observation of molecular preorganization for chirality transfer on a catalyst surface. *Science* **2011**, 334 (6057), 776-780.

103.   Attia, S.; Schmidt, M. C.; Schröder, C.; Pessier, P.; Schauermann, S. Surface-Driven Keto–Enol Tautomerization: Atomistic Insights into Enol Formation and Stabilization Mechanisms. *Angew. Chem. Int. Ed.* **2018**, 130 (51), 16901-16906.

104.   Attia, S.; Schmidt, M. C.; Schröder, C.; Schauermann, S. Formation and Stabilization Mechanisms of Enols on Pt through Multiple Hydrogen Bonding. *ACS Catal.* **2019**, 9, 6882-6889.

105.   Attia, S.; Schauermann, S. Coverage-dependent adsorption geometry of acetophenone on Pt(111). Submitted to *J. Phys. Chem. C* **2019**.

106.   Chen, C.-S.; Chen, H. -W.; Cheng, W. -H. Study of selective hydrogenation of acetophenone on Pt/SiO$_2$. *Appl. Catal.* **2003**, 248 (1-2), 117-128.

107.   Gordy, W. Spectroscopic evidence for hydrogen bonds: Effects of chelation on the carbonyl frequency. *J. Chem. Phys.* **1940**, 8 (7), 516-519.

108.   Fried, S. D.; Bagchi, S.; Boxer, S. G. Measuring electrostatic fields in both hydrogen-bonding and non-hydrogen-bonding environments using carbonyl vibrational probes. *J. Am. Chem. Soc.* **2013**, 135 (30), 11181-11192.

109.   Frisch, M.; Trucks, G.; Schlegel, H.; Scuseria, G.; Robb, M.; Cheeseman, J.; Scalmani, G.; Barone, V.; Mennucci, B.; Petersson, G. J. Gaussian Inc. Wallingford CT, **2009**.

110.   Lagunov, O.; Drenchev, N.; Chakarova, K.; Panayotov, D.; Hadjiivanov, K. Isotopic Labelling in Vibrational Spectroscopy: A Technique to Decipher the Structure of Surface Species. *Top. Catal.* **2017**, 60 (19-20), 1486-1495.

111.   Cattanach, C.; Mooney, E.F. The infrared spectra of benzyl and substituted benzyltin compounds. *Spectrochim. Acta A* **1968**, 24 (4), 407-415.

112.   Mohr, S.; Xu, T.; Döpper, T.; Laurin, M.; Görling, A.; Libuda, J. Molecular Orientation and Structural Transformations in Phthalic Anhydride Thin Films on MgO (100)/Ag (100). *Langmuir* **2015**, 31 (28), 7806-7814.

113.   Cicoira, F.; Miwa, J. A.; Melucci, M.; Barbarella, G.; Rosei, F. Ordered Assembly of α-Quinquethiophene on a Copper Oxide Nanotemplate. *Small* **2006**, 2 (11), 1366-1371.

114.   Rahe, P.; Nimmrich, M.; Nefedov, A.; Naboka, M.; Woll, C.; Kuhnle, A. Transition of molecule orientation during adsorption of terephthalic acid on rutile TiO2 (110). *J. Phys. Chem. C* **2009**, 113 (40), 17471-17478.

115.   Malherbe, F.; Bernstein, H. J. Infrared spectra of rapidly solidified vapors. *J. Chem. Phys.* **1951**, 19 (12), 1607-1608.

116.   Avery, N. R. EELS identification of the adsorbed species from acetone adsorption on Pt (111). *Surf. Sci.* **1983**, 125 (3), 771-786.

117.   Delbecq, F.; Sautet, P. Adsorption of aldehydes and ketones on platinum and palladium: influence of steps, open faces and metal nature: A theoretical study. *Surf. Sci.* **1993**, 295 (3), 353-373.

118.   Jeffery, E. L.; Mann, R. K.; Hutchings, G. J.; Taylor, S. H.; Willock, D. J. A density functional theory study of the adsorption of acetone to the (1 1 1) surface of Pt: implications for hydrogenation catalysis. *Catal. Today* **2005**, 105 (1), 85-92.

119.   Vannice, M.; Erley, W.; Ibach, H. A RAIRS and HREELS study of acetone on Pt (111). *Surf. Sci.* **1991**, 254 (1-3), 1-11.

120.   Vargas, A.; Bürgi, T.; Baiker, A. Adsorption of activated ketones on platinum and their reactivity to hydrogenation: a DFT study. *J. Catal.* **2004**, 222 (2), 439-449.

121.   Davis, J.; Barteau, M. The influence of temperature and surface composition upon the coordination of acetone to the Pd (111) surface. *Surf. Sci.* **1989**, 208 (3), 383-403.

122.   Liu, Z.; Vannice, M. The surface chemistry of acetone on a Pt foil. *Surf. Sci.* **1994**, 316 (3), 337-348.

123.   De Vrieze, J. E.; Thybaut, J. W.; Saeys, M. Role of Keto–Enol Tautomerization in the Copper-Catalyzed Hydrogenation of Ketones. *ACS Catal.* **2019**, 9 (5), 3831-3839.

124.   Schulz, K. H.; Cox, D. F. Surface reactions of acrolein and propionaldehyde on cuprous oxide (100): nonselective oxidation and enolate-mediated side reactions to C3 products. *J. Phys. Chem.* **1993**, 97 (14), 3555-3564.

125.   Sim, W.-S.; Li, T.-C.; Yang, P.-X.; Yeo, B.-S. Isolation and identification of surface-bound acetone enolate on Ni (111). *J. Am. Chem. Soc.* **2002**, 124 (18), 4970-4971.

126.   Mahapatra, M.; Burkholder, L.; Garvey, M.; Bai, Y.; Saldin, D. K.; Tysoe, W. T. Enhanced hydrogenation activity and diastereomeric interactions of methyl pyruvate co-adsorbed with R-1-(1-naphthyl) ethylamine on Pd (111). *Nature* **2016**, 7, 12380.

127.   Mitchell, W. J.; Xie, J.; Jachimowski, T. A.; Weinberg, W. H. Carbon monoxide hydrogenation on the Ru (001) surface at low temperature using gas-phase atomic hydrogen:

spectroscopic evidence for the carbonyl insertion mechanism on a transition metal surface. *J. Am. Chem. Soc.* **1995**, 117 (9), 2606-2617.

128.   Weldon, M. K.; Friend, C. M. Probing surface reaction mechanisms using chemical and vibrational methods: alkyl oxidation and reactivity of alcohols on transitions metal surfaces. *Chem. Rev.* **1996**, 96 (4), 1391-1412.

129.   Jones, T.; Baddeley, C. Influence of modification conditions on the interaction of methylacetoacetate with (R, R)-Tartaric acid-modified Ni (111). *J. Phys. Chem. C* **2007**, 111 (47), 17558-17563.

130.   Xu, M.; Huai, X.-L.; Liu, H. Role of Keto–Enol Isomerization on Surface Chemistry and Hydrogenation of Acetone on Pt (111): A DFT study. *Ind. Eng. Chem. Res.* **2014**, 53 (13), 5451-5454.

131.   Garvey, M.; Bai, Y.; Boscoboinik, J. A.; Burkholder, L.; Sorensen, T. E.; Tysoe, W. T. Identifying molecular species on surfaces by scanning tunneling microscopy: methyl pyruvate on Pd (111). *J. Phys. Chem. C* **2013**, 117 (9), 4505-4514.

132.   Jones, T.; Baddeley, C. Investigating the mechanism of chiral surface reactions: the interaction of methylacetoacetate with (S)-glutamic acid modified Ni (111). *Langmuir* **2006**, 22 (1), 148-152.

133.   Skliar, D.; Gelmi, C.; Ogunnaike, T.; Willis, B. Interaction of 2, 2, 6, 6-tetramethyl-3, 5-heptanedione with the Si (1 0 0)-2× 1 surface: Scanning tunneling microscopy and density functional theory study. *Surf. Sci.* **2007**, 601 (14), 2887-2895.

134.   Ontaneda, J.; Nicklin, R. E.; Cornish, A.; Roldan, A.; Grau-Crespo, R.; Held, G. Adsorption of methyl acetoacetate at Ni (111): Experiment and theory. *J. Phys. Chem. C* **2016**, 120 (48), 27490-27499.

135.   Trivella, A.; Roubin, P.; Theule, P.; Rajzmann, M.; Coussan, S.; Manca, C. UV and IR photoisomerization of acetylacetone trapped in a nitrogen matrix. *J. Phys. Chem. A* **2007**, 111 (16), 3074-3081.

136.   Belova, N. V.; Oberhammer, H.; Girichev, G. V. Tautomeric and conformational properties of methyl acetoacetate, CH3OC (O)− CH2− C (O) CH3: Electron diffraction and quantum chemical study. *J. Phys. Chem. A* **2004**, 108 (16), 3593-3597.

137.   Matrosov, E.; Kabachnik, M. Characteristics of the cis and trans enolic structures in the IR spectra. *Spectrochim. Acta A* **1972**, 28 (2), 191-196.

138. Nolasco, M. M.; Ribeiro-Claro, P. J. C-H··· O Hydrogen Bonds in Cyclohexenone Reveal the Spectroscopic Behavior of C_{sp2}-H and C_{sp3}-H Donors. *Chem. Phys. Chem.* **2005**, 6 (3), 496-502.

139. Lord, R.; Nolin, B.; Stidham, H. J. Quantitative Study of the Bonding of Chloroform-d in Various Solvents by Infrared Spectrometry1. *J. Am. Chem. Soc.* **1955**, 77 (5), 1365-1368.

140. Daniel, D. C.; McHale, J. L. Hydrogen Bonding in $CHCl_3$/DMSO-d_6 and $CDCl_3$/DMSO-h_6 Mixtures. *J. Phys. Chem. A* **1997**, 101 (17), 3070-3077.

141. Lavoie, S.; McBreen, P. H. Evidence for C− H---OC Bonding in Coadsorbed Aromatic− Carbonyl Systems on Pt (111). *J. Phys. Chem. B* **2005**, 109 (24), 11986-11990.

142. Hadjiivanov, K.; Knözinger, H. J. Low-Temperature CO Adsorption on Ag+/SiO2 and Ag− ZSM-5: An FTIR Study. *J. Phys. Chem. B* **1998**, 102 (52), 10936-10940.

143. Falk, M.; Whalley, E. Infrared spectra of methanol and deuterated methanols in gas, liquid, and solid phases. *J. Chem. Phys.* **1961**, 34 (5), 1554-1568.

144. Christmann, K.; Ertl, G. Interaction of hydrogen with Pt (111): the role of atomic steps. *Surf. Sci.* **1976**, 60 (2), 365-384.

145. Christmann, K.; Ertl, G.; Pignet, T. Adsorption of hydrogen on a Pt (111) surface. *Surf. Sci.* **1976**, 54 (2), 365-392.

146. Humblot, V.; Bingham, C.; Le Roux, D.; Marti, E. M.; McNutt, A.; Nunney, T.; Lorenzo, M. O.; Roberts, A.; Williams, J.; Surman, M. Synchrotron far-infrared RAIRS studies of complex molecules on Cu (1 1 0). *Surf. Sci.* **2003**, 537 (1-3), 253-264.

147. Ghosh, A. K.; Chatterjee, P.; Chakraborty, T. J. *J. Chem. Phys.* Keto-enol tautomerization and intermolecular proton transfer in photoionized cyclopentanone dimer in the gas phase. **2014**, 141 (4), 044303.

148. Fosser, K. A.; Nuzzo, R. G.; Bagus, P. S.; Wöll, C. The origin of soft vibrational modes of alkanes adsorbed on Cu: An experimental and theoretical investigation. *J. Chem. Phys.* **2003**, 118 (11), 5115-5131.

149. Rappaport, Z. *The chemistry of enols*. John Wiley & Sons: **1990**.

150. Tureček, F. 1-Phenylethenol: The enol form of acetophenone. Preparation, ionization energy and the heat of formation in the gas phase. *Tetrahedron Lett.* **1986**, 27 (35), 4219-4222.

151. Keeffe, J.; Kresge, A.; Toullec, J. Acid-catalyzed enolization of acetophenone: catalysis by bisulfate ion in sulfuric acid solutions. *Can. J. Chem.* **1986**, 64 (6), 1224-1227.

152.   Madsen, F.; Terpager, I.; Olskær, K.; Spanget-Larsen, J. Ultraviolet-visible and infrared linear dichroism spectroscopy of 1, 8-dihydroxy-9, 10-anthraquinone aligned in stretched polyethylene. *Chem. Phys.* **1992**, 165 (2-3), 351-360.

153.   Pihko, P. M. Activation of carbonyl compounds by double hydrogen bonding: An emerging tool in asymmetric catalysis. *Angew. Chem. Int. Ed.* **2004**, 43 (16), 2062-2064.

154.   Christmann, K. Interaction of hydrogen with solid surfaces. *Surf. Sci. Rep.* **1988**, 9 (1-3), 1-163.

155.   Lee, J.; Cowin, J.; Wharton, L. He diffraction from clean Pt (111) and (1× 1) HPt (111) surface. *Surf. Sci.* **1983**, 130 (1), 1-28.

156.   Papoian, G.; Nørskov, J. K.; Hoffmann, R. A comparative theoretical study of the hydrogen, methyl, and ethyl chemisorption on the Pt (111) surface. *J. Am. Chem. Soc.* **2000**, 122 (17), 4129-4144.

157.   Bădescu, Ş.; Jacobi, K.; Wang, Y.; Bedürftig, K.; Ertl, G.; Salo, P.; Ala-Nissila, T.; Ying, S.-C. Vibrational states of a H monolayer on the Pt (111) surface. *Phys. Rev. B* **2003**, 68 (20), 205401.

158.   Xu, L.; Ma, Y.; Zhang, Y.; Teng, B.; Jiang, Z.; Huang, W. Revisiting H/Pt (111) by a combined experimental study of the HD exchange reaction and first-principles calculations. *Sci. China Chem.* **2011**, 54 (5), 745.

159.   Jo, S. K. Weakly-bound hydrogen on defected Pt (111). *Surf. Sci.* **2015,** *635*, 99-107.

160.   Mate, C.; Somorjai, G. A. Carbon monoxide induced ordering of benzene on Pt (111) and Rh (111) crystal surfaces. *Surf. Sci.* **1985**, 160 (2), 542-560.

161.   Bellamy, L. *The infra-red spectra of complex molecules*. Springer Science & Business Media: **2013**.

162.   Linstrom, P. J.; Mallard, W. NIST Chemistry webbook; NIST standard reference database No. 69. **2001**.

163.   Kliewer, C. J.; Bieri, M.; Somorjai, G. A. Hydrogenation of the α,β-Unsaturated Aldehydes Acrolein, Crotonaldehyde, and Prenal over Pt Single Crystals: A Kinetic and Sum-Frequency Generation Vibrational Spectroscopy Study. *J. Am. Chem. Soc.* **2009**, 131 (29), 9958-9966.

164.	Weldon, M. K.; Friend, C. M., Probing Surface Reaction Mechanisms Using Chemical and Vibrational Methods: Alkyl Oxidation and Reactivity of Alcohols on Transitions Metal Surfaces. *Chem. Rev.* **1996**, 96 (4), 1391-1412.

165.	Mark, A. G.; Forster, M.; Raval, R. Recognition and ordering at surfaces: the importance of handedness and footedness. *Chem. Phys. Chem.* **2011**, 12 (8), 1474-1480.

166.	Toukoniitty, B.; Roche, O.; Mikkola, J.-P.; Toukoniitty, E.; Klingstedt, F.; Eränen, K.; Salmi, T.; Murzin, D. Y. Ethyl pyruvate hydrogenation under microwave irradiation. *Chem. Eng.* **2007**, 126 (2-3), 103-109.

167.	Bürgi, T.; Baiker, A. Heterogeneous enantioselective hydrogenation over cinchona alkaloid modified platinum: mechanistic insights into a complex reaction. *Acc. Chem. Res.* **2004**, 37 (11), 909-917.

168.	Diezi, S.; Ferri, D.; Vargas, A.; Mallat, T.; Baiker, A. The origin of chemo-and enantioselectivity in the hydrogenation of diketones on platinum. *J. Am. Chem. Soc.* **2006**, 128 (12), 4048-4057.

169.	Freund, H. -J. Models for heterogeneous catalysts: studies at the atomic level. *Rendiconti Lincei* **2017**, 28 (1), 5-18.

170.	Szori, K.; Balazsik, K.; Cserenyi, S.; Szollosi, G.; Bartok, M. Inversion of enantioselectivity in the 2, 2, 2-trifluoroacetophenone hydrogenation over Pt-alumina catalyst modified by cinchona alkaloids. *Appl. Catal. A* **2009**, 362 (1-2), 178-184.

171.	Holland, M. C.; Meemken, F.; Baiker, A.; Gilmour, R. J. Chiral imidazolidinone and proline-derived surface modifiers for the Pt-catalysed asymmetric hydrogenation of activated ketones. *J. Mol. Catal. A* **2015**, 396, 335-345.

172.	Diezi, S.; Mallat, T.; Szabo, A.; Baiker, A. Fine tuning the "chiral sites" on solid enantioselective catalysts. *J. Catal.* **2004**, 228 (1), 162-173.

173.	Margitfalvi, J. L.; Tálas, E. Anomalous behavior of rigid cinchona alkaloids in the enantioselective hydrogenation of ethyl pyruvate in an aprotic solvent. *Appl. Catal. A* **2006**, 301 (2), 187-195.

174.	Dong, Y.; Goubert, G.; Groves, M. N.; Lemay, J.-C.; Hammer, B.; McBreen, P. H. Structure and Dynamics of Individual Diastereomeric Complexes on Platinum: Surface Studies Related to Heterogeneous Enantioselective Catalysis. *Acc. Chem. Res.* **2017**, 50 (5), 1163-1170.

175.   Dong, Y.; Svane, K.; Lemay, J.-C.; Groves, M. N.; McBreen, P. H. STM Study of Ketopantolactone/(R)-1-(1-Naphthyl) ethylamine Complexes on Pt (111): Comparison of Prochiral and Enantiomeric Ratios and Examination of the Contribution of CH⋯ OC Bonding. *ACS Catal.* **2017**, 7 (3), 1757-1765.

176.   Goubert, G.; Dong, Y.; Groves, M. N.; Lemay, J.-C.; Hammer, B.; McBreen, P. H. Monitoring interconversion between stereochemical states in single chirality-transfer complexes on a platinum surface. *Nat. Chem.* **2017**, 9 (6), 531.

177.   Goubert, G.; McBreen, P. H. Surface Diastereomeric Complexes Formed by Methyl Benzoylformate and (R)-1-(1-Naphthyl) ethylamine on Pt (111). *ACS Catal.* **2014**, 4 (3), 847-854.

178.   Gordon, A. D.; Zaera, F. Adsorption of 1-(1-Naphthyl) ethylamine from Solution onto Platinum Surfaces: Implications for the Chiral Modification of Heterogeneous Catalysts. *Angew. Chem. Int. Ed.* **2013**, 52 (12), 3453-3456.

179.   Freedman, T. B.; Balukjian, G. A.; Nafie, L. A. Enhanced vibrational circular dichroism via vibrationally generated electronic ring currents. *J. Am. Chem. Soc.* **1985**, 107 (22), 6213-6222.

180.   Pollok, C. H.; Merten, C. Conformational distortion of α-phenylethyl amine in cryogenic matrices–a matrix isolation VCD study. *Phys. Chem. Chem. Phys.* **2016**, 18 (19), 13496-13502.

181.   Merten, C.; Amkreutz, M.; Hartwig, A. VCD study of α-methylbenzyl amine derivatives: Detection of the unchanged chiral motif. *Chirality* **2010**, 22 (8), 754-761.

182.   Lippincott, E. R.; O'Reilly Jr, E. J. Vibrational Spectra and Assignment of Naphthalene and Naphthalene-d-8. *J. Chem. Phys.* **1955**, 23 (2), 238-244.

183.   Hawkins, J.; Ward, E.; Whiffen, D. Characteristic infra-red absorption frequencies of substituted naphthalenes. *Spectrochim. Acta A* **1957**, 10 (1), 105-109.

184.   Hamada, Y.; Hashiguchi, K.; Hirakawa, A. Y.; Tsuboi, M.; Nakata, M.; Tasumi, M.; Kato, S.; Morokuma, K. Vibrational analysis of ethylamines: trans and gauche forms. *Spectrochim. Acta A* **1983**, 102 (1), 123-147.

185.   Frisch, M. J.; Trucks, G. W.; Schlegel, H. B.; Scuseria, G. E.; Robb, M. A.; Cheeseman, J. R.; Scalmani, G.; Barone, V.; Petersson, G. A.; Nakatsuji, H.; Li, X.; Caricato, M.; Marenich, A. V.; Bloino, J.; Janesko, B. G.; Gomperts, R.; Mennucci, B.; Hratchian, H. P.; Ortiz, J. V.; Izmaylov, A. F.; Sonnenberg, J. L.; Williams; Ding, F.; Lipparini, F.; Egidi,

F.; Goings, J.; Peng, B.; Petrone, A.; Henderson, T.; Ranasinghe, D.; Zakrzewski, V. G.; Gao, J.; Rega, N.; Zheng, G.; Liang, W.; Hada, M.; Ehara, M.; Toyota, K.; Fukuda, R.; Hasegawa, J.; Ishida, M.; Nakajima, T.; Honda, Y.; Kitao, O.; Nakai, H.; Vreven, T.; Throssell, K.; Montgomery Jr., J. A.; Peralta, J. E.; Ogliaro, F.; Bearpark, M. J.; Heyd, J. J.; Brothers, E. N.; Kudin, K. N.; Staroverov, V. N.; Keith, T. A.; Kobayashi, R.; Normand, J.; Raghavachari, K.; Rendell, A. P.; Burant, J. C.; Iyengar, S. S.; Tomasi, J.; Cossi, M.; Millam, J. M.; Klene, M.; Adamo, C.; Cammi, R.; Ochterski, J. W.; Martin, R. L.; Morokuma, K.; Farkas, O.; Foresman, J. B.; Fox, D. J. *Gaussian 16 Rev. C.01*, Wallingford, CT, 2016.

186.   Stacchiola, D.; Burkholder, L.; Tysoe, W. T. Enantioselective Chemisorption on a Chirally Modified Surface in Ultrahigh Vacuum: Adsorption of Propylene Oxide on 2-Butoxide-Covered Palladium(111). *J. Am. Chem. Soc.* **2002,** *124* (30), 8984-8989.

187.   Ma, Z.; Zaera, F. Organic chemistry on solid surfaces. *Surf. Sci. Rep.* **2006**, 61 (5), 229-281.

188.   Zaera, F. An organometallic guide to the chemistry of hydrocarbon moieties on transition metal surfaces. *Chem. Rev.* **1995**, 95 (8), 2651-2693.

189.   Netzer, F. P.; Ramsey, M. G. Structure and orientation of organic molecules on metal surfaces. *Crit. Rev. Solid State* **1992**, 17 (5), 397-475.

190.   Hoffmann, H.; Zaera, F.; Ormerod, R. M.; Lambert, R. M.; Wang, L. P.; Tysoe, W. T. Discovery of a tilted form of benzene chemisorbed on Pd (111): As NEXAFS and photoemission investigation. *Surf. Sci.* **1990**, 232 (3), 259-265.

191.   Lavoie, S.; Mahieu, G.; McBreen, P. H. Chemisorption-Induced Double Hydrogen Bonding, Self-Assembly, and Stereoselection. *Angew. Chem. Int. Ed.* **2006**, 45 (44), 7404-7407.

192.   Lavoie, S.; Laliberté, M.-A.; Temprano, I.; McBreen, P. H. A generalized two-point H-bonding model for catalytic stereoselective hydrogenation of activated ketones on chirally modified platinum. *J. Am. Chem. Soc.* **2006**, 128 (23), 7588-7593.

193.   Lavoie, S.; Laliberté, M.-A.; McBreen, P. H. Adsorption States and Modifier− Substrate Interactions on Pt (111) Relevant to the Enantioselective Hydrogenation of Alkyl Pyruvates in the Orito Reaction. *J. Am. Chem. Soc.* **2003**, 125 (51), 15756-15757.

194.   Scuderi, D.; Le Barbu-Debus, K.; Zehnacker, A. The role of weak hydrogen bonds in chiral recognition. *Phys. Chem. Chem. Phys.* **2011**, 13 (40), 17916-17929.

195.   Le Barbu-Debus, K.; Broquier, M.; Mahjoub, A.; Zehnacker-Rentien, A. Chiral recognition in jet-cooled complexes of (1R, 2S)-(+)-cis-1-amino-2-indanol and methyl lactate: on the importance of the CH··· π interaction. *Phys. Chem. Chem. Phys.* **2009**, 11 (35), 7589-7598.

196.   Ertl, G.; Neumann, M.; Streit, K. Chemisorption of CO on the Pt (111) surface. *Surf. Sci.* **1977**, 64 (2), 393-410.

197.   Desiraju, G. R. The C− H··· O hydrogen bond: structural implications and supramolecular design. *Acc. Chem. Res.* **1996**, 29 (9), 441-449.

198.   Doyen, G.; Ertl, G. Theory of carbon monoxide chemisorption on transition metals. *Surf. Sci.* **1974**, 43 (1), 197-229.

199.   Bartlett, G. J.; Newberry, R. W.; VanVeller, B.; Raines, R. T.; Woolfson, D. N. Interplay of hydrogen bonds and n→ π* interactions in proteins. *J. Am. Chem. Soc.* **2013**, 135 (49), 18682-18688.

200.   Silverstein, R. M.; Webster, F. X.; Kiemle, D. *Spectrometric Identification of Organic Compounds, 7th Edition*. Wiley: **2005**.

Appendix I

Ultra-High Vacuum Scanning Tunneling Microscope Setup

To obtain the atomistic-level understanding of ligand-directed catalysis, our research group links the detailed spectroscopic, kinetic and dynamic studies with the real space microscopic information on the structure of the functionalized surfaces. For this purpose, we designed and built an additional apparatus comprising a combination of well-controlled preparative techniques and STM. Fig. A1.1 shows both a schematic and picture of such apparatus. The setup consists of four UHV chambers: preparation chamber (Fig. A1.1a (1)), deposition chamber (not visible), STM chamber (2) and a load-lock chamber (3). The chambers are interconnected, and the sample can be transferred in situ between the chambers via a portable transfer system containing two manipulators (4,5), a magnetic transfer rod (6) and a wobble stick (7). The design and assembly of the preparation and deposition chambers are replicas chambers of the newly built molecular beam/IRAS setup, which was previously described in chapter 3 (see for instance Fig. 3.6). It also contains the same preparation and characterization techniques for different types of catalytic surfaces by means of standard surface science tools. The samples that be prepared in situ range from single crystals to more complex nanostructured systems consisting of metallic nanoparticles supported on well-defined single crystalline thin oxide films, epitaxially grown on single crystalline metal supports. Additionally, the designs of the sample manipulator, the magnetic transfer rod and the sample holder (Fig.3.8d) is also identical to the one previously described in Chapter 3.

The STM and the load-lock chambers are separated from the preparation chamber by a gate valve (8) and equipped with a pumping station so that it can be vented and pumped down to a vacuum independently, if necessary. The STM chamber is also equipped with as an ion getter pump (9) to achieve a base pressure better than $1 \cdot 10^{-10}$ mbar. The sample is handled via the manipulator of the preparation chamber and the transfer rod to the rack of the load-lock, and then transferred to the STM stage via the manipulator of the load-lock chamber and a wobble stick. A photograph of the STM setup is shown in Fig. A1.1b.
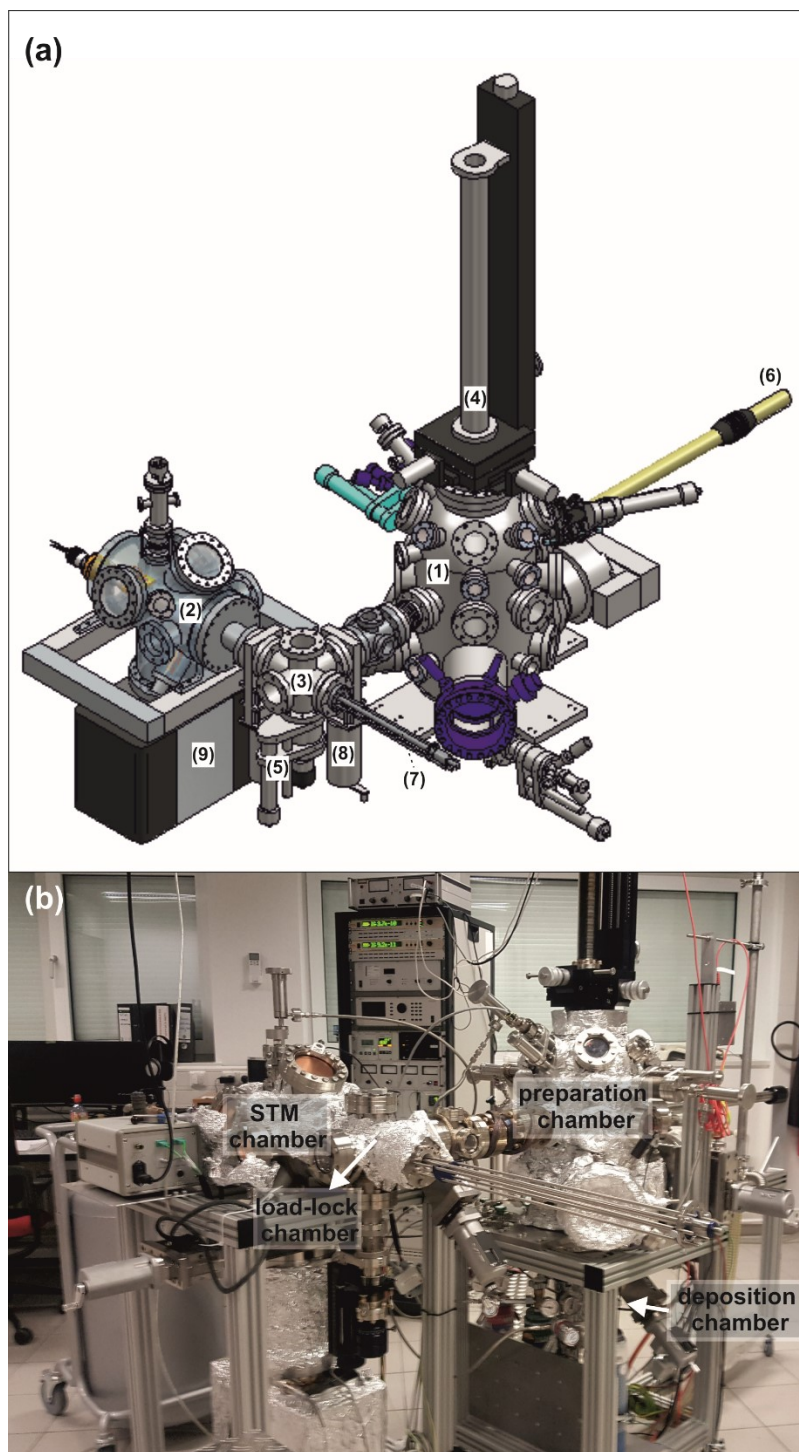
Figure A1.1: (a) Schematic drawing of the STM experimental setup. The labeled components are: (1) preparation chamber, (2) STM chamber, (3) load-lock chamber, (4) sample manipulator in the preparation chamber, (5) sample manipulator in the load-lock chamber, (6) magnetic transfer rod, (7) wobble stick, (8) gate valve, (9) ion getter pump. (b) A photograph of the experimental setup.

Movable sample plate- design and considerations

Due to the requirements for the sample's dimensions to fit into the STM assembly (Aarhus 150 SPM (SPECS), the design of the movable sample plate (the movable compartment that is directly attached to the sample) has been altered. The requirements from SPECS dictates that the sample cannot rise above the sample plate more than 0.7 mm, making it hard to use a normal sample plate with no cutout because samples are usually thicker. One way to easily overcome it is to use the sample plates with a cutout. The working or polished side of the sample fits through an appropriately sized cutout of the top-side and is held in place by a counter plate that is either screwed together with the top-plate or spot welded. A front view photograph of the movable sample plate, already inserted into the sample holder of the manipulator in the preparation chamber is shown in Fig. A1.2a. The back view of the movable sample plate inserted in the STM stage is shown in Fig. A1.2b.
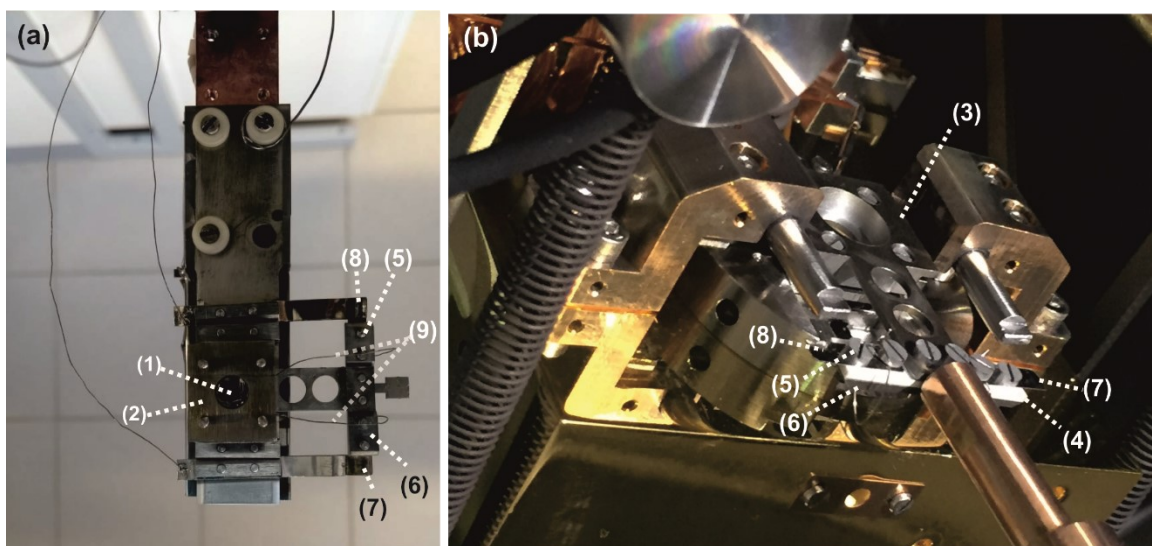

Figure A1.2: (a) A photograph of the *movable sample plate* (front view) and the *sample holder* mounted on the manipulator of the preparation chamber. (b) A photograph of the *movable sample plate* (back view) inserted in the STM clasp. The labeled components are: (1) single crystal (sample), (2) Mo sample supporting plate (front side), (3) Mo sample supporting plate (back side), (4) insulating rectangular plate containing six in-line holes, (5) screws, (6) trapezoid pins, (7),(8) thermocouple thin sheets installed on the ceramic plate, (9) thermocouple wires which are spot welded together close to the sample surface.

The sample (1) is Pt(111) single crystal which has a hat-like shape and it is positioned in between two Mo sample plates with 6 mm diameter central opening and fixed with Mo screws (2,3). Accessing the back side of the sample is provided by a 6 mm diameter central opening in the Mo supporting plate. A rectangular ceramic plate containing six in-line holes (4) is attached at its center (its two central holes) to the front side of the supporting plate by molybdenum screws (5) and a trapezoid pin (6). The remaining two pairs of holes are used for the installation of type-K thin thermocouple sheets from both front sides of the supporting plate (7),(8) via additional screws and trapezoid pins. The ceramic plate ensures an electric insulation between the thermocouple pair and the Mo supporting plate. The trapezoid shape of the pins was carefully chosen to provide a sandwich-like arrangement, in which the probability of unwanted electrical contact caused by thermal expansion of individual trapezoid pins during heating, is minimized.

Thermocouple wires (9) are pressed with molybdenum screws against the K-type thermocouple sheets (7),(8) and are spot welded to the edge of the single crystal. The design of the sample holder in the preparation chamber of the STM setup is identical to that of the molecular beam setup (for details on the sample holder design see section 3.6 in chapter 3). Also, in both designs electron beam heating is used for temperature control.

The construction of this setup was performed by me and by Evan J. Spadafora at the Fritz-Haber-Institute (FHI) in Berlin which was later moved to the Christian-Albrecht-University (CAU) in Kiel. The STM measurements presented in this thesis were carried out by Marvin C. Schmidt at the CAU and by Evan J. Spadafora at the FHI. All measurements were carried out in a constant current mode and the bias voltage U_T was applied to the sample. The etched W-Tip was commercially produced by SPECS and in-situ sharpened by 3 keV Ar+ -bombardment with 5·10 -6 mbar back pressure for 5 min.

The fact that we built the same preparation chamber with the same preparation and characterization tools ensures preparation of the same well-defined conditions of the model catalyst so the microscopic data can be correlated with the spectroscopic data obtained by the IRAS/molecular beam setup. This approach is applied to study ligand-directed catalysis over model catalytic surfaces and allows us to obtain deep atomistic-level insights into the related surface process.

Appendix II

Calculated IR spectrum of R-NEA in the gas phase

We performed a relaxed Potential Energy Surface (PES) scan for R-NEA in the gas phase, rotating the ethylamine group with respect to the naphthalene ring, through the C-C bond connecting them. The scan was performed using the smaller 6-31G (d,p) basis set to minimize computer requirements while exploring the conformation space, which provides a sufficient level of accuracy for this purpose. Figure A2.1 displays the results of the relaxed PES in the gas phase, where the (ethylamine)C-C-C-C(naphthalene) dihedral angle was incremented with steps of 20°. The scan calculation shows that the minimum energy structure occurs at dihedral angle of about 90° (shown by the purple arrow) corresponding to the structure shown in the inset. It should be pointed out that there are other structures that exhibit local minima, such as the one with a dihedral angle of about 300° which lies approximately 0.7 kcal/mol higher in energy than the 90° conformer. Nevertheless, the energy barrier between the two conformers is rather high and conversion is not likely to occur at room temperature. It should be kept in mind that a set of conformers can contribute significantly to the IR spectrum in the gas phase, and conformational averaging taking into account the relative abundance of the conformers should be performed. Such calculations, however, are beyond the scope of this thesis. The main goal of this section is to predict an IR spectrum of R-NEA in the gas phase, which is in reasonable agreement with the experimental results - the IR spectra of R-NEA on the Pt(111) surface at multilayer coverages. Such comparison allows us to better assign the vibrational bands of R-NEA, which then can be used to shed light on the perturbation of the chemical bonds at sub-monolayer coverages by the interaction with the Pt(111) surface, as well as to obtain insight regarding the geometry of the molecule on the surface, based on the MSSR. Obviously, in order to investigate the interaction of the molecule with the surface, geometry optimization of the molecule close to the surface should be carried out. A collaboration with a theoretical group to perform the corresponding calculation is being currently carried out. Nevertheless, first conclusions related to the geometry of the molecule can be very convincingly drawn based on the combination of the spectroscopic experimental data at sub-monolayer coverages with respect to largely unperturbed molecule, i.e the multilayer coverages. By comparing the spectra of the latter to the calculated gas phase spectra, the bands can be assigned

based on their similarity. Deriving the nature of the vibrational modes can also serve as a benchmark for further theoretical calculations of the molecule adsorbed to the surface.
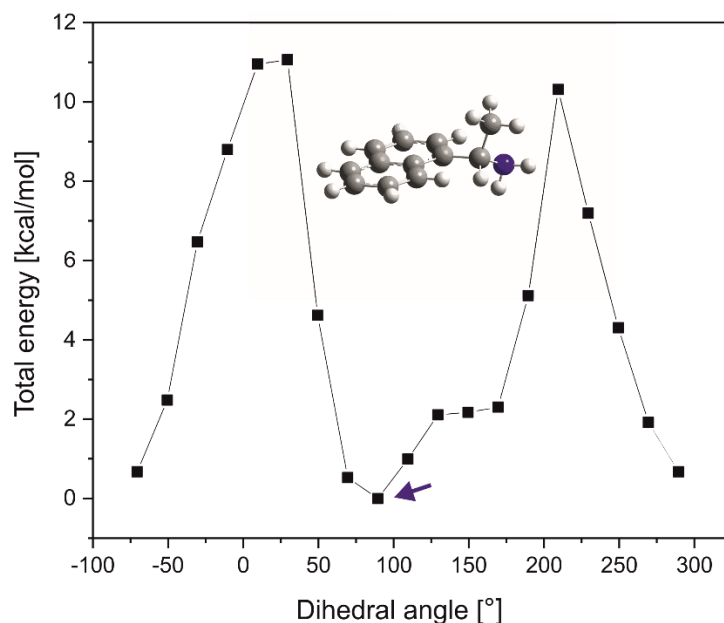

Figure A2.1: Relaxed PES of rotational conformations of R-NEA. The angle between the naphthalene ring and the ethylamine group was varied. The energy of the most stable conformer, corresponding to dihedral angle of 90°, is defined as zero total energy. Its structure is shown in the inset.

Next, starting with the obtained lowest energy structure (see inset of Fig. A2.1) we performed optimization and frequency calculations using the MP2 and B3LYP methods with various basis sets. For the DFT calculations with the B3LYP functional, several basis sets of the same family were used, and basis functions were added until energy convergence was achieved. Figure A2.2 shows the energy of the optimized structure as a function of the number of basis functions (the basis set names are marked in the figure). This plot shows that the difference in energy is decreasing as the basis set size is increasing. The small energy difference between the 6-311++G(3d,3p) and 6-311+G(3d,2p) basis sets of about 0.2 kcal/mol suggests that the former basis set is a suitable candidate for predicting the IR spectrum of the structure. The calculated IR spectrum is shown at the bottom trace of Fig. A2.3, and the corresponding vibrational frequencies are shown in Table A2.1. Note that the frequencies are unscaled by the commonly used scaling factor. These factors were applied in the main text of the thesis while comparing the calculated spectra with the experimental spectra (see chapter 5, section 5.1). Another basis set which was

used for optimization and frequency calculation is the aug-cc-pVTZ, using the B3LYP functional and the MP2 level of theory. The calculated IR spectrum is shown in the middle and upper traces of Fig. A2.3 respectively, and selected vibrational bands are given in Table A2.1. Comparison of the three computed model chemistries reveal a fair similarity between the bands position in the spectral region of 1700-1000 cm^{-1} (cf. Table A2.1). Closer inspection of Table A2.1 shows that the bands position in the region of 1000-775 cm^{-1}, are very similar while comparing MP2/aug-cc-pVTZ with B3LYP/aug-cc-pVTZ theories and are slightly different from that calculated with B3LYP/6-311++G(3d,3p) theory. Note, however, that the calculated IR frequencies for the optimized structure at the MP2/aug-cc-pVTZ level of theory have shown a different intensity distribution from that obtained with the B3LYP/aug-cc-pVTZ level of theory (cf. Fig. A2.3, upper spectrum and middle spectrum). Most likely, a complete basis set analysis at the same level of theory or rather a higher level of theory (such as MP3,MP4) with the same basis (aug-cc-pVTZ) should be used in order to improve these results.
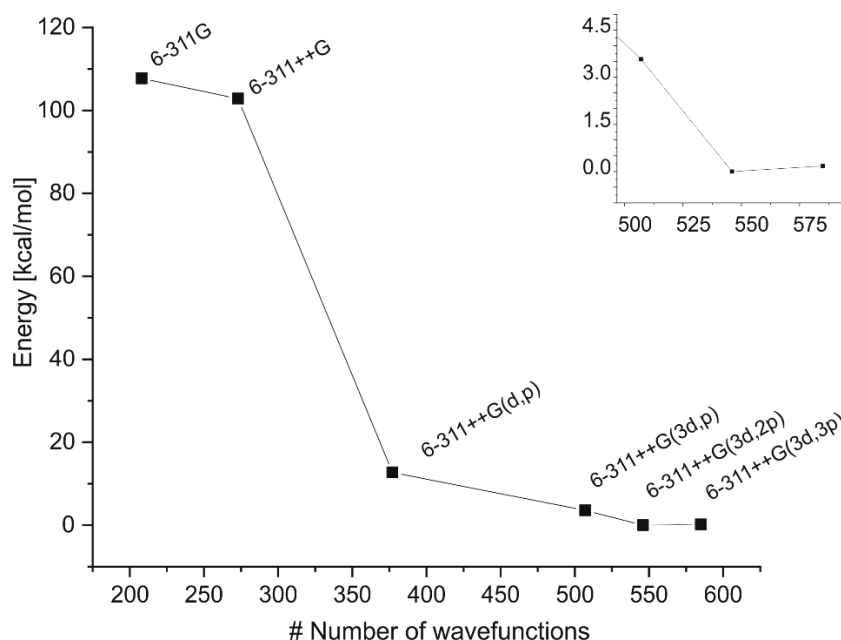

Figure A2.2: Calculated total energy of the optimized structure of R-NEA as a function of the number of basis functions of the same type. A DFT calculation was performed with the B3LYP exchange-correlation functional. The inset shows an enlarged view in the region of basis sets containing 500-600 basis functions.
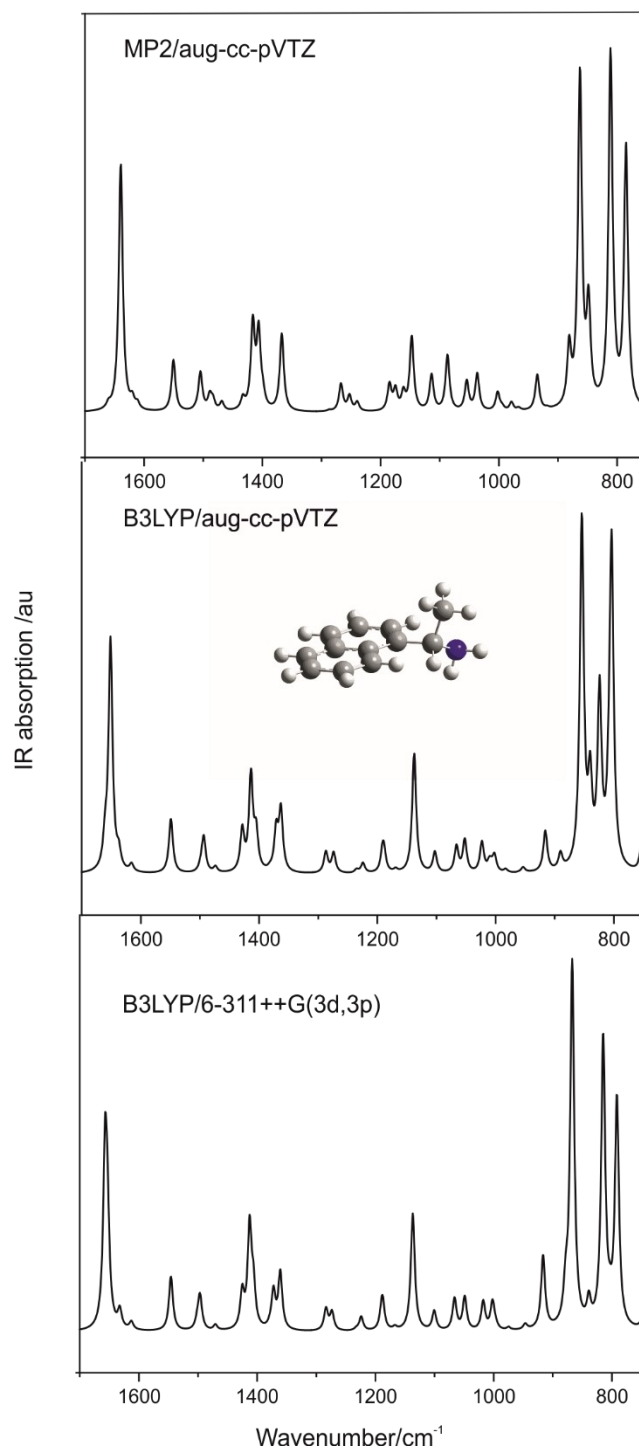
Figure A2.3: Calculated IR spectrum at the MP2/aug-cc-pVTZ (upper), B3LYP/aug-cc-pVTZ (middle) and B3LYP/6-311++G(3d,3p) (bottom) levels of theory. The optimized structure calculated at the B3LYP/aug-cc-pVTZ is shown in the middle panel.

B3LYP		MP2
6-311++G(3d,3p)	aug-cc-pVTZ	aug-cc-pVTZ
1651	1657	1639
1549	1545	1550
1494	1497	1505
1414	1416	1416
1363	1361	1367
1138	1137	1147
854	867	863
824	815	811
804	792	785

Table A2.1: Vibrational frequencies (in cm^{-1}) as calculated by MP2/aug-cc-pVTZ, B3LYP/aug-cc-pVTZ and B3LYP/6-311++G(3d,3p). Only the nine most intense bands are presented. The corresponding spectra are shown in Fig. A2.3. Notice that the frequencies are unscaled by any scaling factor.

To summarize, the IR spectrum calculated at the B3LYP/aug-cc-pVTZ level of theory is in good qualitative agreement with the experimental multilayer spectra (see Figure 5.1 in section 5.2). Also, it can be concluded from the data in this appendix that the common practice of running a high-level single point energy calculation at a geometry optimized with a less expensive method is just as good as performing the calculations at the higher level of theory. Using geometries computed with more expensive models do not necessarily lead to more accurate results.

List of Publications

1. <u>S. Attia</u>, E. J. Spadafora, M. C. Schmidt and S. Schauermann. Adsorption geometry and self-assembling of chiral modifier (R)-(+)-1-(1-naphtylethylamine) on Pt(111). In preparation.

2. M. C. Schmidt; <u>S. Attia</u>, C. Schröder; A.-Katrin Baumann, S. Schauermann. Temperature dependent formation of acetophenone oligomers accompanied by keto-enol tautomerization: real space distribution. In preparation.

3. <u>S. Attia</u>, M. C. Schmidt, C. Schröder, J. Weber, A.-Katrin Baumann, S. Schauermann. Keto-enol tautomerization as a first step in hydrogenation of carbonyl compounds. Submitted to *J. Phys. Chem. C*.

4. <u>S. Attia</u>, S.Schauermann. Coverage-dependent adsorption geometry of acetophenone on Pt(111). Submitted to *J. Phys. Chem. C*.

5. <u>S. Attia</u>, M. C. Schmidt, C. Schröder, S. Schauermann. Formation and Stabilization Mechanisms of Enols on Pt through Multiple Hydrogen Bonding. *ACS Catal.* **2019**, 9(8), 6882-6889.

6. <u>S. Attia</u>, E. J. Spadafora, J. Hartmann, H. -J. Freund, S. Schauermann. Molecular beam/infrared reflection-absorption spectroscopy apparatus for probing heterogeneously catalyzed reactions on functionalized and nanostructured model surfaces. *Rev. Sci. Instrum*. **2019**, 90, 053903.

7. <u>S. Attia</u>, M. C. Schmidt, C. Schröder, P. Pessier, S. Schauermann. Surface-Driven Keto–Enol Tautomerization: Atomistic Insights into Enol Formation and Stabilization Mechanisms. *Angew. Chem. In. Ed*. **2018**, 57 (51), 16659-16664.

8. K.-H. Dostert, C. P. O'Brien, F. Mirabella, F. Ivars-Barceló, <u>S. Attia</u>, E. Spadafora, S. Schauermann and H. -J. Freund. Selective Partial Hydrogenation of Acrolein on Pd: A Mechanistic Study. *ACS Catal*. **2017**, 7(8), 5523-5533.

Selbstständigkeitserklärung

Hiermit erkläre ich, die Dissertation selbstständig und nur unter Verwendung der angegebenen Hilfen und Hilfsmittel angefertigt zu haben. Ich habe mich nicht anderwärts um einen Doktorgrad in dem Promotionsfach beworben und besitze keinen entsprechenden Doktorgrad. Die Promotionsordnung der MathematischNaturwissenschaftlichen Fakultät, veröffentlicht im Amtlichen Mitteilungsblatt der Technische Universität Berlin, habe ich zur Kenntnis genommen.

15.10.2019